



UNIVERSITAT DE
BARCELONA

Development of 3D in vitro platforms for the study of muscle function and axonal growth and regeneration

Karen Isabel Wells Cembrano

ADVERTIMENT. La consulta d'aquesta tesi queda condicionada a l'acceptació de les següents condicions d'ús: La difusió d'aquesta tesi per mitjà del servei TDX (www.tdx.cat) i a través del Dipòsit Digital de la UB (diposit.ub.edu) ha estat autoritzada pels titulars dels drets de propietat intel·lectual únicament per a usos privats emmarcats en activitats d'investigació i docència. No s'autoritza la seva reproducció amb finalitats de lucre ni la seva difusió i posada a disposició des d'un lloc aliè al servei TDX ni al Dipòsit Digital de la UB. No s'autoritza la presentació del seu contingut en una finestra o marc aliè a TDX o al Dipòsit Digital de la UB (framing). Aquesta reserva de drets afecta tant al resum de presentació de la tesi com als seus continguts. En la utilització o cita de parts de la tesi és obligat indicar el nom de la persona autora.

ADVERTENCIA. La consulta de esta tesis queda condicionada a la aceptación de las siguientes condiciones de uso: La difusión de esta tesis por medio del servicio TDR (www.tdx.cat) y a través del Repositorio Digital de la UB (diposit.ub.edu) ha sido autorizada por los titulares de los derechos de propiedad intelectual únicamente para usos privados enmarcados en actividades de investigación y docencia. No se autoriza su reproducción con finalidades de lucro ni su difusión y puesta a disposición desde un sitio ajeno al servicio TDR o al Repositorio Digital de la UB. No se autoriza la presentación de su contenido en una ventana o marco ajeno a TDR o al Repositorio Digital de la UB (framing). Esta reserva de derechos afecta tanto al resumen de presentación de la tesis como a sus contenidos. En la utilización o cita de partes de la tesis es obligado indicar el nombre de la persona autora.

WARNING. On having consulted this thesis you're accepting the following use conditions: Spreading this thesis by the TDX (www.tdx.cat) service and by the UB Digital Repository (diposit.ub.edu) has been authorized by the titular of the intellectual property rights only for private uses placed in investigation and teaching activities. Reproduction with lucrative aims is not authorized nor its spreading and availability from a site foreign to the TDX service or to the UB Digital Repository. Introducing its content in a window or frame foreign to the TDX service or to the UB Digital Repository is not authorized (framing). Those rights affect to the presentation summary of the thesis as well as to its contents. In the using or citation of parts of the thesis it's obliged to indicate the name of the author.



Doctoral thesis
Universitat de Barcelona

**Development of 3D *in vitro*
platforms for the study of muscle
function and axonal growth and
regeneration**

Karen Isabel Wells Cembrano
Director: Prof. Dr. José Antonio del Río
Molecular and Cellular Neurobiotechnology group
Institute for Bioengineering of Catalonia

Universitat de Barcelona
Facultat de Biologia
Departament de Biologia Cel·lular, Fisiologia i Immunologia
Programa de Doctorat en Biomedicina

Institute for Bioengineering of Catalonia (IBEC)
Parc Científic de Barcelona (PCB)

Development of 3D *in vitro* platforms for the study of muscle function and axonal growth and regeneration

PhD thesis report presented by Karen Isabel Wells Cembrano to apply for a PhD degree from the Universitat de Barcelona. This doctoral thesis is inscribed in the **Programa de Doctorat en Biomedicina** of the **Universitat de Barcelona**.

Experimental work and the editing of the present thesis have been performed in the **Institute for Bioengineering of Catalonia (IBEC)**, under the direction and tutoring of **Prof. Dr. José Antonio del Río Fernández**, Professor of Cell Biology in the **Departament de Biologia Cel·lular, Fisiologia i Immunologia of the Universitat de Barcelona**.

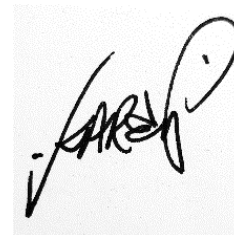
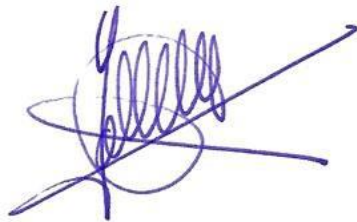
Barcelona, 2023

Thesis director and tutor

Prof. Dr. José Antonio del Río Fernández

PhD candidate

Karen Isabel Wells Cembrano



UNIVERSITAT DE
BARCELONA



Institute for Bioengineering of Catalonia



Parc Científic de Barcelona
UNIVERSITAT DE BARCELONA

ABSTRACT

The use of *in vitro* models in biomedical research offers an invaluable tool for exploring biological processes of health and disease. While animal models remain highly informative and necessary to ensure clinical research safety, laboratory models are essential for reducing animal experimentation and enabling fine manipulation and high-throughput analysis. However, there is a concern that traditional *in vitro* models, based on two-dimensional cultures of mammalian cells and relying on primary culture and non-human cell lines, could lead to inaccurate or misleading results, ultimately jeopardizing the success of novel therapies in clinical trials. Thankfully, exponential advancements in biomedical and biotechnological research have facilitated the creation of increasingly complex and biomimetic models, leading to a paradigm shift in this field. The first pillar of this shift is the use of three-dimensional culture to recapitulate the extracellular matrix environment, through the use of scaffold-based models, lab-on chip devices, and organotypic slice cultures. The second pillar involves transitioning to human cell-derived models to achieve clinically relevant outcomes. The combination of these models with optical techniques such as optogenetics and calcium imaging enables precise manipulation and analysis of cell activity, opening new possibilities for relevant biomedical research.

In this work, our general objective was to develop and utilize 3D *in vitro* models of excitable tissues for two main purposes. On the one hand, our objective was to develop a 3D platform for studying muscle physiology, utilizing human immortalized myoblasts as a clinically relevant cell source. Our next focus was to use this system to model the autoimmune neuromuscular disease myasthenia gravis (MG). On the other hand, we were interested in studying the effect of neuronal activity on axonal regeneration in central nervous system (CNS) neurons. For this, we sought to develop a 3D axotomy platform which could complement previous results obtained in 2D culture. In parallel, we wished to investigate the effect of neuronal activity in a previously established 3D model, namely entorhino-hippocampal organotypic slice cultures (OSCs). In both models, we were interested in applying optogenetic stimulation to Channelrhodopsin-2 (ChR2)-modified neurons.

In the first chapter, we show the validation of *in vitro* culture systems for human myoblast differentiation. First, we used 2D cultures with hydrogel overlays as an approach for

comparing differentiation and functionality of human myoblast cell lines, as well as for evaluating MG serum antibody binding to *in vitro* endplates. Later, we developed an anchored 3D *in vitro* platform for the culture of aligned, differentiated, and contractile human muscle, which responded to electrical, chemical, and optogenetic stimulation. Muscle function was analyzed using motion analysis algorithms or by calcium imaging. Treatment with MG patient serum recapitulated endplate destruction observed *in vivo*, and some functional effects were observed, although further experiments are needed.

In the second chapter, we developed a 3D axotomy platform using embryonic cortical explants cultured in collagen gels. This model provided a reliable source of axonal projections for axotomy, in contrast to stem-cell derived cultures, which were also evaluated as potential neuronal sources. Using this axotomy platform, we observed that optogenetic stimulation was detrimental to axonal regeneration.

In the third chapter, we used entorhino-hippocampal OSCs for a similar purpose, benefitting from our research group's experience in this area. This model recapitulates key neurobiological processes and forms near-*in vivo* glial scars after lesion; making it a biologically relevant model of CNS development and lesion. We applied optogenetic stimulation on developing connections and axotomized cultures, to study the effect of neuronal activity on axonal pathfinding and regeneration after lesion. We observed that increased neuronal activity resulted in loss of target specificity in developing axons, which could affect regenerative potential in lesioned neurons. In line with the second chapter, optical stimulation was also found to impair axonal regeneration in this model.

TABLE OF CONTENTS

LIST OF ABBREVIATIONS	7
GENERAL INTRODUCTION	11
Overview on <i>in vitro</i> models	11
Current trends in <i>in vitro</i> models	12
The importance of architecture: Goodbye to flat biology	12
Human models and reduction of animal experimentation	15
Excitable cells	15
Optogenetics	17
Optogenetic tools	18
Channelrhodopsin-2	20
Calcium analysis	21
Calcium indicator dyes	21
Genetically encoded calcium indicators	22
All-optical assays	24
GENERAL OBJECTIVES	25
CHAPTER 1. Development of human 3D models of muscle function and their application to proof-of-concept modeling of the neuromuscular disease myasthenia gravis	26
INTRODUCTION	27
Skeletal muscle: anatomy and development	27
Muscle contraction and the neuromuscular junction	27
Overview of the state of the art in muscle tissue modeling	34
Myasthenia gravis	39
<i>In vitro</i> models of myasthenia gravis	44
OBJECTIVES	48
MATERIALS AND METHODS	49
Human myoblast cell lines and maintenance	49
2D differentiation protocol with hydrogel overlays	50
Generation of ChR2 ⁺ and GCaMP6 ⁺ stable cell lines	53
3D free-floating platform	54
3D anchored platform for muscle cell culture	56
Treatments of muscle constructs with MG serum	69
RESULTS	71
2D differentiation of human myoblasts	71
3D differentiation of free-floating muscle strips	78
3D anchored platform for muscle cell culture	81

Modeling myasthenia gravis <i>in vitro</i> : Proof-of-concept	95
DISCUSSION	107
Muscle <i>in vitro</i> models	107
Myasthenia gravis modeling	108
CHAPTER 2. Development of a 3D scaffold-based axotomy model and application of optogenetic stimulation to evaluate its potential in axonal regeneration	111
INTRODUCTION.....	112
Neuronal regeneration in the central nervous system	112
Cellular and molecular events after CNS injury	113
<i>In vitro</i> axotomy models	117
Sources of cells for <i>in vitro</i> neuronal models.....	120
Scaffolds for neuronal tissue modeling	121
Strategies for treating CNS injuries.....	123
OBJECTIVES	126
MATERIALS AND METHODS	127
Cell lines: maintenance and differentiation protocols	127
Hydrogel sandwich technique	130
Embryonic cortical neuron cultures	131
Axotomy of cortical explants	133
Calcium imaging and analysis.....	135
Optical stimulation of cortical explants.....	136
Immunostaining.....	137
RESULTS	140
C17.2-eGFP differentiation.....	140
hNS1 differentiation.....	144
Primary cortical explant cultures.....	148
DISCUSSION	156
CHAPTER 3. Potential of optical modulation of neuronal activity to enhance axon regeneration after axotomy in entorhino-hippocampal organotypic slice co-cultures.....	160
INTRODUCTION.....	161
Organotypic slice cultures as relevant <i>in vitro</i> models of neural tissue	161
Organotypic slice culture methodologies	162
Organotypic slice cultures recapitulate key aspects of brain anatomy and regeneration after axotomy.....	163
OBJECTIVES	166
METHODS	167

Entorhino-hippocampal culture (EHC) experiments.....	167
<i>In vitro</i> optogenetic stimulation of EC projecting neurons	168
Calcium imaging in AAV9-Syn-ChR2 and AAV9-Syn-jRCaMP1b double-infected EC neurons	168
EHC labeling with biocytin.....	169
Immunohistochemical procedures.....	170
EHC treatments	170
RESULTS	171
Analysis of the regenerative properties of lesioned entorhino-hippocampal projections in organotypic slice cultures.....	171
Target ablation of EC axons by domoic acid impairs axon development of the EHP, but target transplantation is unable to overcome the absence of EHP regeneration after axotomy in aged OSCs.....	174
Development of an optogenetic stimulation setup of the EC neurons in EHCs.....	176
Optogenetic stimulation of developing EHP largely impairs their development in OSC. .	178
Optogenetic stimulation of axotomized EHP does not enhance axon regeneration in aged EHC	178
DISCUSSION	182
GENERAL DISCUSSION	185
CONCLUSIONS	187
REFERENCES	188

LIST OF ABBREVIATIONS

Abbreviation	Full name
6-ACA	6-aminocaproic acid
AAV	Adeno-associated virus
ACh	Acetylcholine
AChE	Acetylcholine esterase
AChR	Acetylcholine receptor
ALS	Amyotrophic lateral sclerosis
AM	Acetoxymethyl group
AMPA/KA	alpha-amino-3-hydroxy-5-methylisoxazole-4-propionic acid / kainate
AT	Axon terminal
ATP	Adenosine triphosphate
BBB	Blood-brain barrier
BDNF	Brain-derived neurotrophic factor
BF	Brightfield
bHLH	Basic helix-loop-helix transcription factor
BR	Bacteriorhodopsin
BSA	Bovine serum albumin
BTX	α -Bungarotoxin
BTX-555	α -Bungarotoxin Alexa Fluor™ 555 conjugate
CA1-2	Hippocampal regions, previously named cornu Ammonis (CA) regions
CaM	Calmodulin
cAMP	Cyclic adenosine monophosphate
Ca _v	Voltage-gated calcium channels
CEEA	Ethical Committee for Animal Experimentation
ChR	Channelrhodopsin
ChR1	Channelrhodopsin-1
ChR2	Channelrhodopsin-2
CMCMA	Methacryloyl-carboxymethyl cellulose methacrylate
CNS	Central nervous system
Col.	Collagen
cpGFP	Circularly permuted green fluorescent protein
CR	Cajal-Retzius
CSPG	Chondroitin sulfate proteoglycans
DAB	3,3'-Diaminobenzidine
DAG	Diacylglycerol
DAL	Days after lesion
DAT	Days after treatment
DG	Dentate gyrus
DMD	Duchenne muscular dystrophy
DMEM	Dulbecco's modified Eagle's Medium

DNA	Deoxyribonucleic acid
DRG	Dorsal root ganglion
E	Embryonic day
EC	entorhinal cortex
ECM	Extracellular matrix
EDTA	Ethylenediamine tetraacetic acid
EGF	Endothelial growth factor
EH	Entorhino-hippocampal
EHC	Entorhino-hippocampal connection
EHP	Entorhinal-hippocampal projections
ESC	Embryonic stem cells
eYFP	Enhanced yellow fluorescent protein
Fab	Fragment antigen-binding region
FACS	Fluorescence-activated cell sorting
FBS	Fetal bovine serum
Fc	Constant fragment crystallizable domain
FcRn	Neonatal Fc receptor
FRET	Fluorescence resonance energy transfer
GCL	Granule cell layer
GDNF	Glial cell-derived neurotrophic factor
GECI	Genetically encoded calcium indicator
GelMA	Gelatin methacrylate
GFAP	Glial fibrillary acidic protein
GFP	Green fluorescent protein
GPCR	G protein-coupled receptor
H	Hilus
HA	Hyaluronic acid
HDAC5	Histone deacetylase 5
hFGFb	Human fibroblast growth factor basic
HR	Halorhodopsin
HRP	Horseradish peroxidase
IGF-1	Insulin-like growth factor
IgG	Immunoglobulin G
IP3	Inositol triphosphate
iPSC	Induced pluripotent stem cells
ISX9	Isoxazole 9
Kv1.4	Potassium voltage-gated channel subfamily A member 4
LGMD	Limb girdle muscular dystrophy
LRP4	Lipoprotein receptor-related protein 4
LV	Lentivirus
MAC	Membrane attack complex
MAG	Myelin-associated glycoprotein
Matrigel GFR	Matrigel Growth Factor Reduced (GFR) Basement Membrane Matrix

MEM	Minimum Essential Medium
MFD	Microfluidic device
MG	Myasthenia gravis
MHC	Myosin heavy chain
MICM	Membrane interface culture method
ML	Molecular layer
MN	Motor neuron
MRF	Myogenic regulatory factor
MuSK	Muscle-specific kinase
NA	Numerical aperture
nAChR	Nicotinic acetylcholine receptor
Na _v	Voltage-gated sodium channels
NG2	Neural/glial antigen 2
NGF	Nerve growth factor
NHS	Normal horse serum
NT-3	Neurotrophin-3
O/N	Overnight
Olig2	Oligodendrocyte transcription factor 2
OoC	Organ-on-chip
OptoXR	Rhodopsin-GPCR chimera
OSC	Organotypic slice culture
P	Postnatal day
P/S	Penicillin/Streptomycin solution
PBS	Phosphate-buffered saline 0.1 M
PCB	Parc Científic de Barcelona
PEG	Polyethylene glycol
PEG-NHS	O,O'-Bis[2-(N-Succinimidyl-succinylamino)ethyl]polyethylene glycol
PNS	Peripheral nervous system
PTFE	Polytetrafluoroethylene
RAG	Regeneration-associated gene
RNA	Ribonucleic acid
ROS	Reactive Oxygen Species
RT	Room temperature
RT-qPCR	Real-time quantitative polymerase chain reaction
RyR	Ryanodine receptor
SAA	Sarcomeric alpha-actinin
SB	Subiculum
SC	Stem cell
SCI	Spinal cord injury
SDS	Sodium dodecyl sulfate
SDS-PAGE	Sodium dodecyl sulfate - polyacrylamide gel electrophoresis
SGM	Skeletal muscle cell growth medium
SKM	Skeletal muscle

SKMSC	Skeletal muscle stem cell, also known as satellite cell
SLM	Stratum lacunosum-moleculare
slm/ml	Stratum lacunosum-moleculare / molecular layer
SN	Seronegative
SR	Sarcoplasmic reticulum
Triton	Triton X-100 detergent
TTBS	Tris-buffered saline supplemented with 0.1% Tween 20
TTL	Tubulin tyrosine ligase
TUJ1	Neuron-specific class III beta-tubulin
WB	Western Blot
$\Delta F/F_0$	Increase in fluorescence versus background fluorescence (F_0) divided by F_0

GENERAL INTRODUCTION

Overview on *in vitro* models

Since the dawn of human curiosity, scientists, both official and unofficial, have been eager to understand living organisms by extracting parts of the whole, to obtain a more detailed view of specific processes. This practice eventually led to what we know today as primary cultures, in which organs, tissues, or isolated cells are artificially maintained outside of their natural context. These were the first established *in vitro* cultures, named after scientists of yesteryear trying their best to keep cells alive in a glass dish; just enough time so they could use them to answer their burning existential questions. Laboratory models have allowed humanity to gain invaluable insight on countless biological mechanisms, which would have been impossible to elucidate using whole organisms.

In addition to keeping cells alive during experimentation, an especially important characteristic of *in vitro* cultures was the ability to obtain more cells from an initial sample, by allowing subsequent cell division in the laboratory. Thus, the idea of creating human-made models for research became a possibility: expansion of the original cells could eliminate the need to use new animals for each experiment. Unfortunately, cells do not survive and divide indefinitely in a lab, as stripping them from their natural environment results in unwanted phenotypic changes and reduced viability over time. Luckily, advancements in genetic manipulation gave a solution to this issue, which was to generate so-called “immortalized” cell lines with altered expression of oncogenes, telomerase, or other cell division-associated genes (Shay et al., 1991). These immortalized cell lines have the ability to divide (almost) indefinitely in the laboratory, providing an everlasting source of cells for scientific exploration.

In many cases, adult cells are terminally differentiated and non-proliferative, meaning that creating an immortalized cell line is not a viable strategy. This is true for both muscle cells and neurons, which do not proliferate in their differentiated state. Instead, in the body, these cells are periodically regenerated from stem cells (SC). SCs are undifferentiated or partially differentiated cells, characterized by their self-renewal capability (S. He et al., 2009) and their multi- or pluripotentiality (ability to give rise to several cell types or all cell types in the body, respectively). The only naturally pluripotent stem cells are embryonic stem cells (ESC), while other SC types residing in tissues are multipotent, as they are specialized in the generation of cell types from a certain tissue.

SCs can be extracted and maintained in the laboratory, and then differentiated into the desired cell type by using specially formulated cell culture media. Immortalized stem cell lines can also be generated, as some primary SC lines are also subject to senescence and have limited self-renewal capabilities (Gong et al., 2011).

Apart from natural stem cells, modern biotechnology brought forth a breakthrough in stem cell research. This historic discovery by Dr. Shinya Yamanaka and colleagues was that adult, differentiated cells (in their case, fibroblasts) could be turned into induced pluripotent stem cells (iPSCs), opening the path to obtaining all imaginable cell types from a single patient biopsy. This was achieved by the overexpression of only four defined transcription factors, now known as the Yamanaka factors (Takahashi & Yamanaka, 2006). iPSCs display properties similar to ESCs, but have the advantage of enabling the generation of personalized models, as the retrieval of patient fibroblasts does not require invasive procedures.

Current trends in *in vitro* models

Numerous discoveries have been made using simple culture models and limited technology. Nowadays, however, there are considerable efforts aimed at increasing the complexity and clinical relevance of *in vitro* models, thanks to the exponential advancements seen in bioengineering and its related disciplines (Loewa et al., 2023). As the Springer journal describes, *in vitro* models have recently experienced a paradigm shift based on two main pillars. The first is “a goodbye to flat biology”, or in other words, a transition towards 3D models of tissues, organs, and their interfaces. The second is a reduction or elimination of animal experimentation, combined with an endeavor to use human-derived cells instead of animal cells (*In vitro models / Home*, 2022).

The importance of architecture: Goodbye to flat biology

Until recently, most biological models have cultured cells or tissue explants on 2D surfaces, as the majority of mammalian cells have the ability to grow as adherent cells. Alternatively, suspension cultures are also used for certain cell types, in which cells grow in flotation inside liquid media. However, these cultures are missing one of the most important components of a living tissue, which is its architecture. In general, tissues are structured in three-dimensional space and form interactions with their surrounding extracellular matrix (ECM), which significantly influences their functionality. Indeed, it

has been increasingly noted that 2D cultures fail to recapitulate *in vivo* physiology, leading to a lack of translation between *in vitro* results and *in vivo* studies. Gene and protein expression patterns are markedly different when comparing the two approaches, which has prompted researchers to abandon 2D culture in favor of more realistic models (C. Jensen & Teng, 2020). A wide variety of strategies have been explored, as will be outlined in the following subsection.

3D culture strategies: Scaffolds, organoids, organotypic cultures, and microfluidics

A relevant component of many *in vitro* models is a suitable scaffold that can mimic the tissue ECM, giving mechanical support and reinforcing chemical signaling pathways. ECM stiffness has been previously shown to play an important role in determining cell fate (Engler et al., 2006). Therefore, choosing an appropriate scaffold stiffness is crucial for supporting optimal development of the desired cell type.

One commonly used type of scaffold are hydrogels, which can be natural or synthetic. Hydrogels are aqueous solutions of polymers with the ability to form a water-based gel, similar to the natural ECM. Natural hydrogels can be composed of mammalian ECM extracts (i.e., Matrigel (Orkin et al., 1977) and similar products), or composed of purified natural ECM proteins (i.e. collagen (Gil & Del Río, 2012), hyaluronic acid, or fibrin-based gels). Alternatively, decellularized ECMs from the tissue of interest have also been used to better recapitulate the tissue environment (Blanco-Fernandez et al., 2022). The main advantage of natural hydrogels is their inherent cell adhesion and signaling properties, making them highly biocompatible. However, they are limited by batch-to-batch variability and non-defined composition.

Synthetic hydrogels, in turn, are characterized by a fully defined formulation and a high tunability in terms of chemical and mechanical properties. These gels often incorporate chemical groups aimed at enabling specific crosslinking mechanisms, cell adhesion signaling, controlled release of growth factors, or fine-tuned biodegradability (Madduma-Bandarage & Madihally, 2021). Depending on their composition and crosslinking mechanism, some natural and synthetic hydrogels can be used for 3D bioprinting, which allows precise fabrication of detailed morphologies, potentially enabling reproducible, high-throughput 3D culture (Gungor-Ozkerim et al., 2018). For stiffer tissues, such as bone or cartilage, solid microporous scaffolds (i.e. poly-lactic acid scaffolds) are often

used. Specific architectures can also be generated by advanced fabrication techniques such as bioprinting (Yazdanpanah et al., 2022) or electrospinning (Zeng et al., 2003).

Despite the widespread applications of scaffold-based culture, some 3D culture methods are scaffold-free. A recently popularized example are organoids, which are self-organized 3D tissues typically derived from stem cells. These structures can reach a level of complexity similar to real organs, hence the name “organoid” (Z. Zhao et al., 2022). A more traditional approach to modeling organs *in vitro* are organotypic cultures, which are cultures of an organ or part of an organ derived from primary sources. Despite the long-standing nature of this technique, it is still relevant today as a tool for studying certain biological mechanisms and disease processes, especially in neuroscience (Croft et al., 2019). This is due to the fact that organotypic cultures conserve all the relevant three-dimensional structures and cell types of the organ, thus constituting a physiologically relevant yet easily manipulable model (J. A. del Río & Soriano, 2010; Humpel, 2015). A summary of all these models is presented in **Figure 1**.

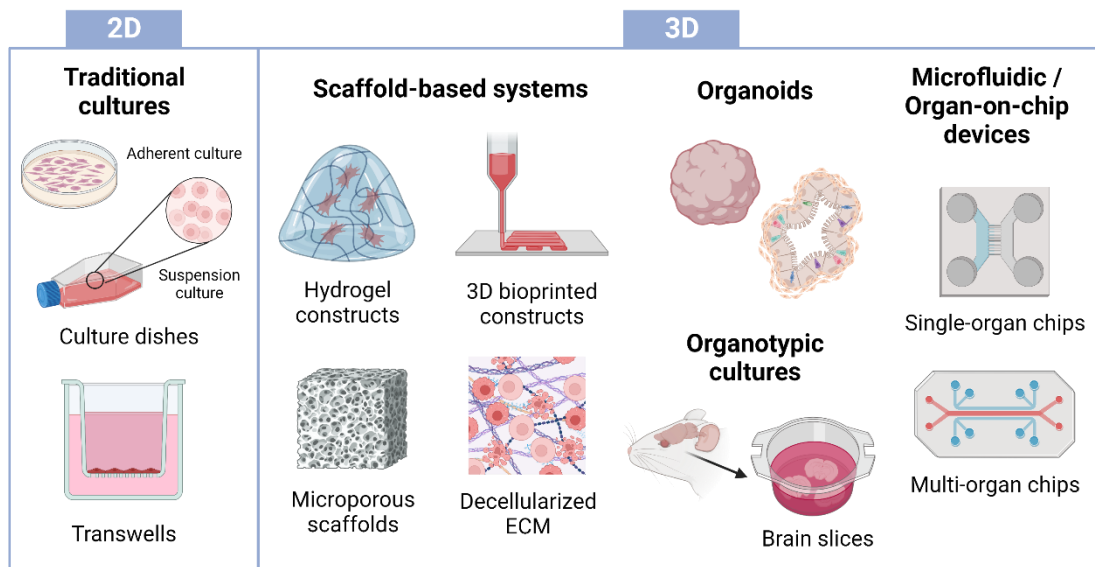


Figure 1. Summary of currently available *in vitro* models, showing relevant types of 2D and 3D configurations.

Last but not least, a promising tool for increasing the complexity of *in vitro* models are microfluidic devices (MFDs) or organ-on-chip (OoC) models. As the name implies, these devices enable miniaturization of cell culture, as they require low amounts of cells and microliter-range fluid volumes. The design of these systems is generally based on polydimethylsiloxane (PDMS) chips with specialized compartments, which are bonded to glass coverslips to enable cell imaging. MFDs allow the design of specific culture

configurations for studying particular processes (J. R o & Ferrer, 2020), and can also be used to model interactions between different tissues or organs (Fern andez-Costa et al., 2023). Their only disadvantage is the complexity of their microfabrication process and manipulation, which means they are not always suited to high-throughput applications (Loewa et al., 2023).

Human models and reduction of animal experimentation

Another equally important factor in the relevance of preclinical results is the origin of cells used for *in vitro* models. Mammalian model organisms share a fair amount of conserved biological mechanisms with humans, but one must not forget they present fundamental differences with them as well. Due to these insurmountable dissimilarities, animal-based models often paint an incomplete or misleading picture of human reality. Therefore, to increase the clinical relevance of the models we use today, there have been considerable efforts directed at increasing our independence from animal models, through the use of human cell lines, stem cells, and iPSCs (Moysidou et al., 2021). In some cases, primary human cells are also used (commercial or obtained from biopsy samples), due to their superior phenotypic properties.

Apart from the lack of clinical translation of animal-based results, the scientific community has become increasingly conscious of the ethical considerations surrounding animal experimentation. Although the “3R” (reduction, refinement, and replacement) guidelines for humane experimental technique were introduced more than 60 years ago (Russell & Burch, 1959), animal experimentation has continued to increase, raising concerns about the need to update these guidelines to reflect our current options in scientific research (Ferdowsian & Beck, 2011). While elimination of animal studies is also currently unethical due to reduced safety guarantees for human study participants, *in vitro* models are moving in the direction of at least partially substituting animal models and animal-sourced *in vitro* models.

Excitable cells

A common thread throughout this thesis is the use of excitable cells, namely muscle cells and neuronal cells. Excitable cells are characterized by their ability to generate and transmit electrical impulses along their cell membrane. Although the aforementioned cell types are the most common excitable cells, some endocrine cells also share this property

(J. A. Williams, 1981). The membrane of excitable cells contains voltage-gated ion channels and chemical receptors, which allow them to respond to chemical and electrical stimuli by altering the flow of ions across the membrane. This results in an alteration of membrane voltage, which can be used for cell-cell communication in the case of neurons, or contractile activity in the case of muscle cells.

All cells have a resting membrane potential, determined by concentrations of ions on either side of the membrane. While in most cells this potential remains relatively stable, neurons and muscle cells can experience rapid changes in potential in response to stimuli. In the case of voltage-gated ion channels, electrical stimuli cause opening of the channel; while in the case of neurotransmitter receptors, binding of the neurotransmitter molecule causes ionic flow through the receptor. Apart from having a defined resting potential, cells also have a characteristic threshold potential at which a generalized and rapid depolarization response is initiated. For example, in neurons, the resting potential is typically around -70 mV and the threshold potential is -55 mV. A signal amplification response occurs when the threshold voltage activates voltage-gated sodium channels present on the membrane, leading to additional ionic flow alterations. The depolarization resulting from surpassing the threshold potential causes an action potential, which is first generated locally and subsequently propagated along the membrane.

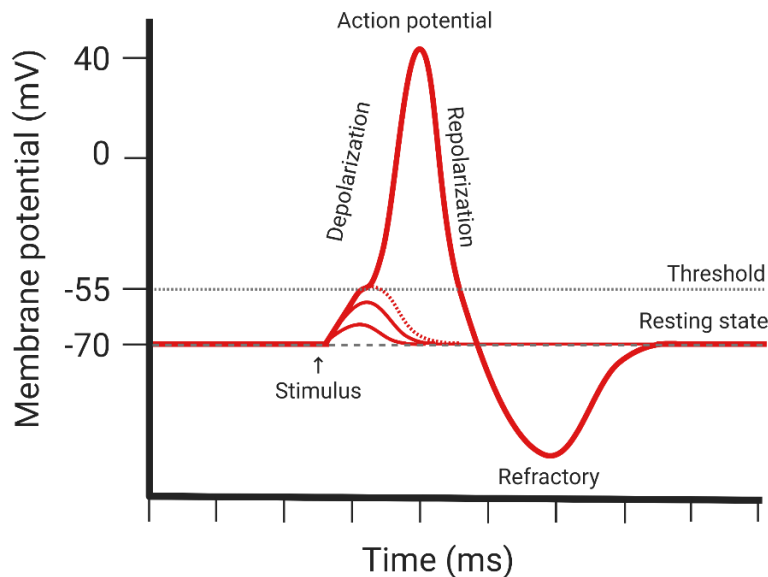


Figure 2. Diagram of an action potential and its phases. The example shows the resting potential value of a typical neuronal cell.

After maximum depolarization is reached, ion channels are closed again, and membrane potential is gradually restored; often involving an overcompensation (hyperpolarization) response. During this period, action potentials are hindered by the increased difficulty in reaching the threshold potential due to hyperpolarization. This is the second part of the refractory period, termed the relative refractory period. The absolute refractory period, however, spans from the depolarization to partially through the repolarization phase. This is defined as the absolute refractory period due to the fact that voltage-gated sodium channels are completely open during this period, making them insensitive to new depolarizations (Kandel et al., 2013).

Optogenetics

Until scarcely two decades ago, stimulation of neurons and other excitable cells was mainly achieved by using chemical factors such as neurotransmitters and depolarizing agents, or by applying electrical stimulation (Ditterich et al., 2003; Kandel et al., 1961; Salzman et al., 1990). In a 1979 *Scientific American* article, Nobel laureate Francis Crick mentioned that a major challenge faced by neuroscience was the need to be able to manipulate specific populations of cells in the brain while leaving others unaltered. Electrical stimulation was too indiscriminate for this task, as well as incapable of silencing neural activity. Similarly, drugs had excessively slow kinetics compared to the speed of brain functions. Crick later speculated that infrared-range light may possess the properties needed to accomplish fast and targeted stimulation, but the appropriate technology for this had not been discovered.

Some optical techniques had been developed by the beginning of the 21st century, but they were only able to control neuronal activity in timescales of seconds to minutes, which was roughly 1000 times slower than needed to control individual spikes (Banghart et al., 2004; Lima & Miesenböck, 2005; Zemelman et al., 2002, 2003). Alternatively, some researchers used laser photostimulation to specifically activate or inactivate molecules at a target region, thus causing a localized change in activity. A relevant example of this is glutamate uncaging, in which caged glutamate (modified with a photoremovable protecting group) is activated by light at specific regions (Dalva & Katz, 1994; Pettit et al., 1999; Shepherd et al., 2003; Yoshimura et al., 2005).

However, in 2005, a revolutionary finding was published. Researchers from the group of Karl Deisseroth reported the use of a light-sensitive algal cation channel,

Channelrhodopsin-2 (ChR2), to control the activity of neuronal populations at millisecond timescales (Boyden et al., 2005). They combined lentiviral gene delivery of ChR2 with high-speed optical switching, thus achieving an exquisite control of activity. The clear advantages of this method were its reliability, non-invasiveness, and temporal and spatial precision (**Figure 3**). In the following years, this discovery led to many improvements in the original techniques, as well as and protein engineering of different ion channel variants.

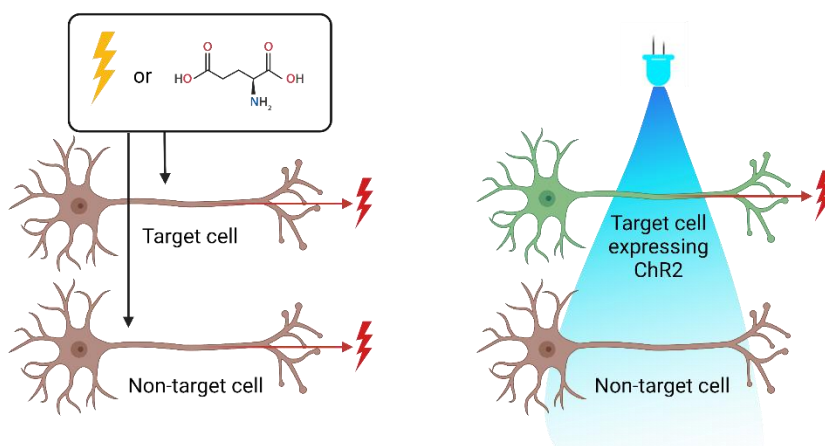


Figure 3. The unprecedented specificity of optogenetics. Target cell populations expressing ChR2 can be exclusively stimulated, unlike with electrical or chemical stimulation (glutamate is shown as an example).

Stemming from Boyden’s seminal paper in 2005, the term “optogenetics” was coined to describe these techniques. The term was originally intended to include processes of optically controlling and imaging neuronal activity by the use of genetically encoded elements (Deisseroth et al., 2006). Presently, according to its most common usage in literature, it predominantly refers to the control aspect of light manipulation in neurons and other cells, mainly through light-sensitive ion channels. Optogenetics has revolutionized scientific research, providing an invaluable toolbox to explore and modulate the activity of excitable cells, both *in vitro* and *in vivo* (Adamantidis et al., 2015).

Optogenetic tools

Opsins are a family of heptahelical membrane proteins that can be found in all domains of life, which enable organisms to harvest light for various survival purposes (Fenno et al., 2011; F. Zhang et al., 2011). There are two primary categories of opsins: Type I, which are found in prokaryotes, algae, and fungi; and Type II, which are found in animals. The

opsins commonly employed in optogenetics primarily belong to the Type I category, although certain Type II opsins have also been used. Type I opsins are known as rhodopsins, which means that they include both an opsin protein with seven transmembrane domains as well as the light-sensitive chromophore retinal.

There are several families of rhodopsins that have been applied to optogenetic techniques. Some relevant examples can be seen in **Figure 4**. The most widely used type of rhodopsin is Channelrhodopsin (ChR), which is naturally found in the alga *Chlamydomonas reinhardtii*. ChRs are light-gated cation channels, which cause depolarization and can thus be used to excite cells upon light stimulation. Bacteriorhodopsins (BR) are proton pumps found in haloarchaea, which generate a proton gradient that can be used for ATP synthesis. Although native bacteriorhodopsins are not commonly used in optogenetics, some variants such as ArchT have been genetically engineered to silence neuronal activity (Han et al., 2011). Halorhodopsins (HR) are yellow light-driven chloride pumps, which can be used as a tool to inhibit neuronal activity by hyperpolarization (F. Zhang et al., 2007). To expand the horizons of optogenetics beyond ion channels, chimeric rhodopsins have been engineered to precisely control intracellular signaling. A family of proteins named OptoXRs incorporates intracellular GPCR signal transduction domains, with the ability to control diacylglycerol (DAG), inositol triphosphate (IP3) and cyclic adenosine monophosphate (cAMP) signaling pathways (Airan et al., 2009).

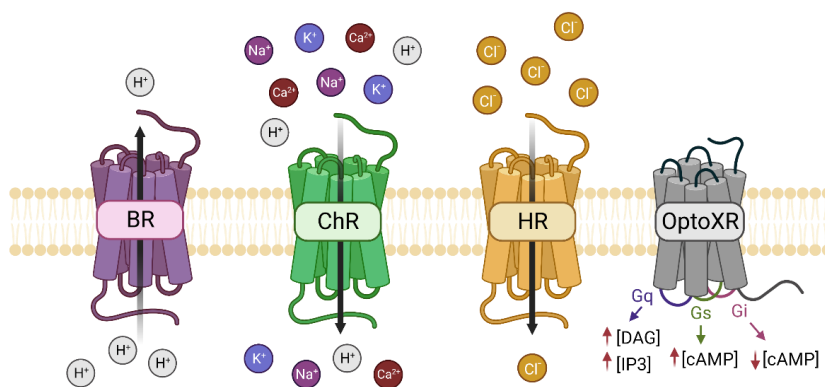


Figure 4. Some common optogenetic tools. The proton pump Bacteriorhodopsin (BR), the cation channel Channelrhodopsin (ChR), the chloride anion channel Halorhodopsin (HR), and the rhodopsin-GPCR chimera OptoXR.

Over the past decades, rhodopsins have been extensively optimized and modified through protein engineering, giving rise to a plethora of variants with different wavelength specificities, ion selectivity, light sensitivity, or kinetics. Optogenetics has entered a new

era that some call "optogenetics 2.0," which expands its scope beyond simply controlling ion transport. This new era involves the exploration of various instrumental proteins, modifying photoreceptors, and utilizing different types of light to regulate intricate biochemical reactions within cells. Optogenetics has also extended its reach beyond animal models to encompass plants and microorganisms. As a result, the current era of optogenetics offers a potent problem-solving approach not only in neuroscience but also in fields like plant science, cell biology, and molecular biology (Tan et al., 2022; H. Zhang et al., 2022).

Channelrhodopsin-2

ChR2 was discovered at the beginning of the century in conjunction with ChR1, a similar protein from the same algal species (Nagel et al., 2003). ChR2 is preferred over ChR1 because ChR2 has higher conductance at physiological pH and is correctly targeted to the cell membrane (*Addgene: Optogenetics Guide, 2023*). The wild-type form of this protein is sensitive to blue light, with a maximum excitation peak at 470nm. Current viral vectors for delivery of ChR2 frequently incorporate a fluorescent reporter. In our case, the reporter present in the viral constructs was enhanced yellow fluorescent protein (eYFP), incorporated as a fusion at the C-terminal domain. This reporter is excited by green light and emits yellow light, although it does exhibit some absorption of 470 nm light and emission of green light (**Figure 5**). Therefore, if needed, the same light source used to excite ChR2 can be used to visualize eYFP expression.

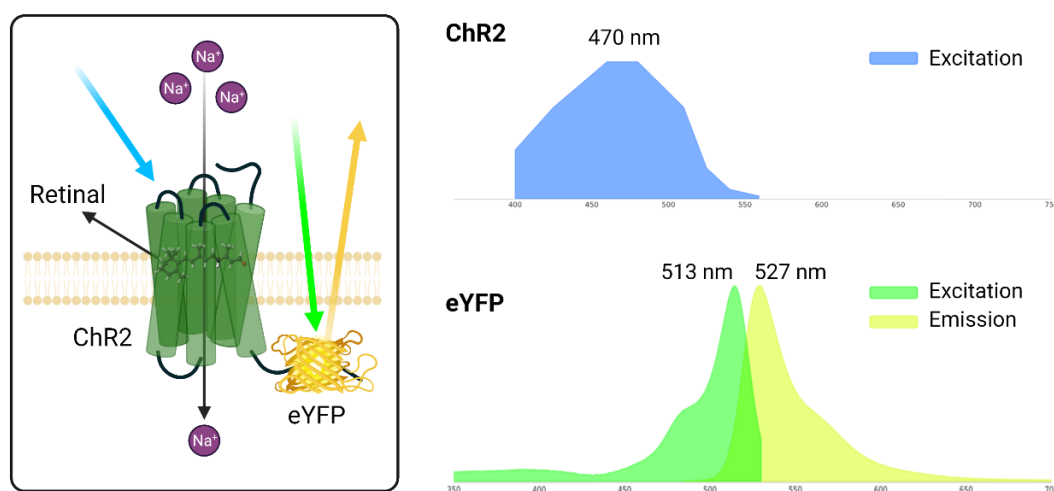


Figure 5. ChR2-eYFP fusion protein. Diagram of protein structure and function, showing light colors used to excite each part of the fusion protein. Spectra adapted from Fluorescent Protein Database, Lambert, 2023.

In previous works from our research group, the ChR2-eYFP fusion has been successfully used for stimulation of mouse cortical neurons and DRG neurons (Mesquida-Veny et al., 2022), mouse spinal cord motor neurons (Sala-Jarque et al., 2020), and the mouse muscle cell line C2C12 (Sala-Jarque et al., 2020). In this work, ChR2-eYFP is used in two different applications. Firstly, this channel is used to optically stimulate stable ChR2-eYFP⁺ human muscle cells as a way of proving the contractile functionality of a bioengineered 3D muscle model. Secondly, it is introduced in neurons of cortical explants and organotypic slices to modulate neuronal activity in developing or lesioned neurons.

Calcium analysis

The importance of calcium in nervous system and muscle function was discovered by Sydney Ringer in 1887 (Ringer & Buxton, 1887). As we now know, calcium plays an indispensable role in the activity of excitable cells, such as neurons and muscles, which exhibit transient increases in intracellular calcium upon depolarization (also known as calcium transients). This feature can be exploited to measure and quantify cell activity as a function of intracellular calcium concentration, without recurring to direct measurements of electrical currents. In contrast with electrophysiology, calcium imaging is non-invasive, as it does not require direct contact with cells. It also allows for population-level analysis of calcium dynamics, providing information on the activity of many individual cells at the same time. Thanks to optimized indicators, this method has a potential for high spatial and temporal resolution, which makes it suitable for detecting fast and localized changes in activity.

Calcium indicator dyes

In short, calcium dyes are fluorescent molecules which change their fluorescence intensity and/or wavelength upon calcium binding. The objective of these dyes is to provide quantitative information on the cytosolic concentration of calcium in cells containing the dye. Roger Tsien, known for the discovery of green fluorescent protein (GFP), was also one of the pioneers of calcium imaging. Some of the first calcium dyes were developed in Tsien's group, such as the first widely used calcium dye fura-2 (Grynkiewicz et al., 1985), based on the stilbene chromophore and a tetracarboxylate calcium chelating site. Other dye families derived from the group were rhod- dyes (rhodamine-based) and fluo- dyes (fluorescein-based) (Minta et al., 1989).

Nowadays, there is a greater variety of calcium dyes on the market, exhibiting different absorption and emission wavelengths, calcium selectivity, and fluorescence changes upon calcium binding. Most calcium dyes can be purchased as cell-impermeable or cell-permeable variants. Some moieties such as acetoxymethyl (AM) improve uptake of the dye, making the molecule hydrophobic and able to cross the membrane by diffusion. The AM group is then cleaved by intracellular esterases, releasing the dye and trapping it inside the cell (Jobsis et al., 2007). Most dyes (i.e., fluo-4) are non-ratiometric, meaning that they can only provide relative or qualitative information on calcium concentration. However, some ratiometric dyes (i.e., fura-2) can be calibrated to measure absolute calcium concentrations. It must be noted that calcium dye assays are endpoint experiments, meaning that longitudinal analysis is not possible with this method.

Genetically encoded calcium indicators

Despite the versatility and usefulness of calcium dyes, genetically encoded calcium indicators (GECIs) offer several advantages. For one, they allow the expression of calcium indicators in specific cell types by using cell-specific promoters, which prevents confusion when imaging mixed cultures (for example, glial cells present in neural cultures also have calcium transients, albeit with different kinetics). Another advantage is the ability to create stable cell lines that homogeneously express the indicator, eliminating issues with uneven loading that often occur with dyes. Lastly, calcium imaging with GECIs is not a destructive procedure, while calcium dyes can alter cell function and viability, rendering the culture unusable after several hours.

In broad terms, GECIs can be classified into two types: (1) fluorescence resonance energy transfer (FRET)-based and (2) single-fluorophore-based (Oh et al., 2019). The first GECIs, named were FRET-based, and were also developed by Tsien's research group (Miyawaki et al., 1997). These indicators utilized tandem fusions of a blue- or cyan-emitting mutant of the green fluorescent protein (GFP), calmodulin (CaM), the calmodulin-binding peptide M13, and an enhanced green- or yellow-emitting GFP. Upon calcium binding to CaM, this portion experimented a conformational change, which reduced the distance between the flanking GFPs and increased the FRET between them (**Figure 6**). The name given to these GECIs was "cameleons", based on the "CaM" abbreviation of calmodulin and the chameleon-like activity of the sensor protein.

Single-fluorophore GECIs such as the well-known GCaMP (Nakai et al., 2001) are based on the use of a modified version of GFP, which is circularly permuted (cpGFP). This circularly permuted variant has its N- and C- termini fused together by a linking sequence, and the GFP sequence is split into two parts, creating two artificial N- and C- termini that are connected to the M13 and CaM domains (**Figure 6**). In the absence of Ca^{2+} , the GFP chromophore exists in a protonated state due to being exposed to water. This protonated form of cpGFP exhibits minimal fluorescence. When calcium binds CaM, this domain undergoes a conformational change and tightly binds to the M13 domain alpha helix, preventing water molecules from accessing the chromophore. This causes rapid deprotonation and converts cpGFP into an anionic form that has a bright fluorescence comparable to that of native GFP (Wang et al., 2008).

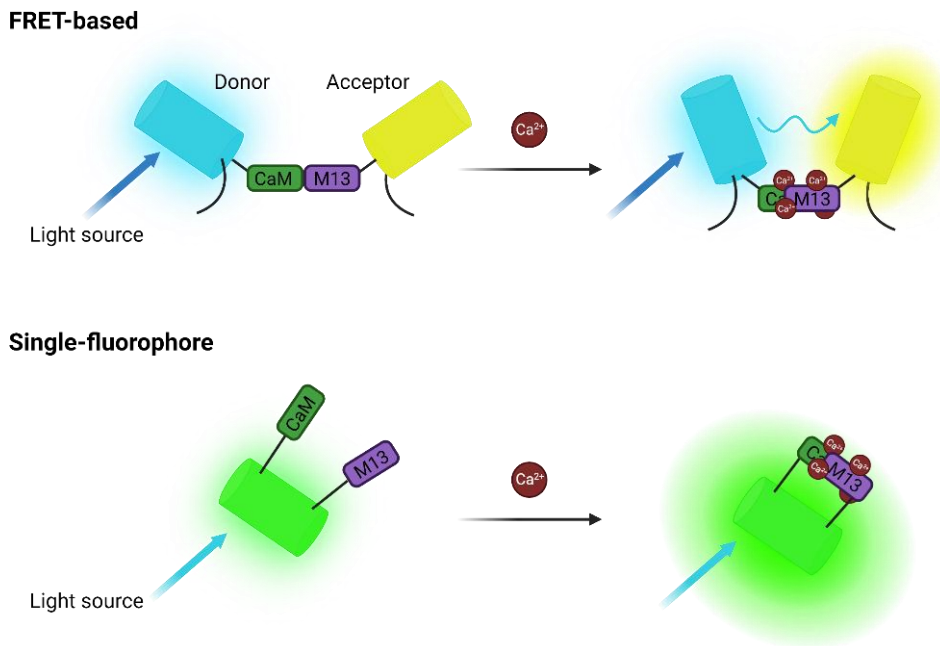


Figure 6. Types of GECIs based on mechanism of fluorescence increase. FRET-based GECIs use two GFP variants. The donor transfers energy by FRET to the acceptor in the presence of calcium, due to the conformational change that occurs in the M13 peptide upon calcium binding to CaM. In single-fluorophore GECIs, the CaM and M13 are bound to a circularly permuted GFP that has minimal fluorescence in its protonated, water-exposed state. The chromophore of cpGFP undergoes deprotonation and regains native fluorescence upon conformational change of CaM and M13. Adapted from (Oh et al., 2019).

The original GCaMP1 has been optimized in terms of signal, sensitivity, and dynamic range of Ca^{2+} detection. The most common variants today are GCaMP6 and GCaMP7, which exist in fast (GCaMP6f, GCaMP7f) and slow isoforms (GCaMP6s, GCaMP7s). The fast isoforms show a faster fluorescence response, but the slow variants are comparably more sensitive due to exhibiting a larger fluorescence increase upon calcium

binding. Alternatively, there exists a medium variant, GCaMP6m, with intermediate properties. Red-shifted indicators such as RCaMP (Akerboom et al., 2013) are also available, enabling more combinations of fluorophores in multiplexed analyses. jRCaMP1a and jRCaMP1b use a circular permutation of the red fluorescent protein mRuby instead of GFP (Dana et al., 2016).

All-optical assays

Thanks to the vast assortment of fluorescent tools available for cell biology research, researchers now have the option to integrate cell manipulation and analysis into a single experiment, utilizing only optical techniques. These innovative experimental designs are generally referred to as all-optical assays (Afshar Saber et al., 2018; Hochbaum et al., 2014). For example, researchers may choose to stimulate cells with an optogenetic tool while imaging the resulting calcium transients with a calcium indicator. The requirements for undertaking this type of experiment are mainly to choose proteins with non-overlapping fluorescent spectra, and to use an appropriate optical setup to perform stimulation and imaging at the same time.

A straightforward way to achieve this is to co-transform cells with two different vectors, i.e., one encoding an optogenetic tool such as Chr2, and another encoding a calcium indicator of a different wavelength such as RCaMP. In fact, RCaMP was developed specifically with this application in mind (Akerboom et al., 2013). Alternatively, calcium dyes could be used in combination with optically stimutable cells (Renault et al., 2015). Another more elegant approach is to integrate the optogenetic tool and the calcium indicator into a single vector, such as the OptoCaMP construct proposed by Afshar Saber et al., 2018. In this work, Chr2 and jRCaMP1b have been combined to demonstrate activation of neurons upon optical stimulation.

GENERAL OBJECTIVES

In our group, models of muscle function and axonal growth and regeneration had been established, but they required improvements to their clinical relevance, as well as some additions to the repertoire of techniques available for their manipulation and analysis.

In the former case, 3D models with mouse myoblasts, but not with human myoblasts, had been previously used (Sala-Jarque et al., 2020; other unpublished data). These models still showed some issues with reproducibility, as will be explained in Chapter 1. Although optogenetics had been used in Sala-Jarque et al., 2020, muscle function was analyzed in terms of contraction recordings, and appropriate calcium imaging protocols had not been established. Also, these systems had not yet been applied to muscular disease modeling.

In the latter case, 2D axotomy models (Tong et al., 2014) and organotypic cultures (Del Río et al., 2002; Solé et al., 2004) had been used to study axonal regeneration. However, although 3D scaffold-based neuronal cultures had been applied for other objectives (Gil & Del Río, 2012), they had not yet been applied to axotomy studies, which is one of the improvements we incorporated in this thesis. While optogenetic stimulation had been evaluated in 2D primary cultures as a potential promoter of axonal growth and regeneration (Mesquida-Veny et al., 2022), it had not been used in 3D scaffold-based cultures or organotypic cultures.

In sum, our **two main objectives** for this thesis were:

- 1) To implement improvements to our existing *in vitro* muscle and axotomy models, both in terms of a transition to 3D models and a transition to human cell sources.
- 2) To increase the versatility of our models in terms of optical techniques for manipulation and analysis; namely, optogenetics and calcium imaging.

With these objectives in mind, the content of this thesis is organized in **three chapters**:

- 1) Development of human 3D models of muscle function and their application to proof-of-concept modeling of the neuromuscular disease myasthenia gravis.
- 2) Development of a 3D scaffold-based axotomy model and application of optogenetic stimulation to evaluate its potential in axonal regeneration.
- 3) Potential of optical modulation of neuronal activity to enhance axon regeneration after axotomy in entorhino-hippocampal organotypic slice co-cultures.

**CHAPTER 1. Development of human 3D models of
muscle function and their application to proof-of-
concept modeling of the neuromuscular disease
myasthenia gravis**

INTRODUCTION

Skeletal muscle: anatomy and development

Skeletal muscle (SKM), the tissue responsible for voluntary movements, constitutes 30-40% of body weight in humans, therefore constituting the most abundant tissue type. Each individual cylindrical skeletal muscle cell constitutes a myofiber or muscle fiber, composed of hundreds or thousands of myofibers, which are aligned and tightly bundled together into fascicles. Different connective tissue layers provide additional mechanical support for withstanding contraction forces: these are the epimysium which surrounds whole muscles, the perimysium which surrounds fascicles, and the endomysium which envelops individual myofibers. Muscle cells are multinucleated cells that originate from the fusion of their progenitors, myoblasts, into large units of 2-3 mm wide and 100 μm wide in an adult human (Alberts et al., 2008). The minimum contractile unit inside these cells is called a sarcomere, formed from a precisely ordered array of thin and thick filaments. Thin filaments are composed of actin and associated proteins, and they are attached at their (+) ends to a Z-disc, a structure that delineates the lateral ends of a sarcomere. The (-) ends of the actin filaments extend in toward the middle of the sarcomere, where they overlap with thick filaments formed from specific muscle isoforms of myosin II.

The mechanism by which muscle cells align and assemble their sarcomeres into organized repetitive structures is thought to be driven by mechanical forces. In the body, skeletal muscle tissue is attached by tendons to bones of the skeleton. Except for the tongue, all muscles are connected to bone at both ends. The presence of two attachment sites contributes to the generation of mechanical tension during development of the muscle. Evidence suggests that mechanical tension precedes the self-assembly of sarcomeres into organized arrays. (Luis & Schnorrer, 2021; Mao et al., 2022; Weitkunat et al., 2014). Therefore, when seeking to model muscle tissue, including mechanical tension is a relevant point to consider.

Muscle contraction and the neuromuscular junction

To contract, muscles must receive signals from motor neurons (MN), which can innervate different muscle fibers at the same time. The group of myofibers innervated by a single

motor neuron is called a motor unit. The synaptic connection between a motor neuron and a muscle cell is called the neuromuscular junction, which possesses a specialized microstructure and assembly of proteins. Motor neurons release the neurotransmitter acetylcholine (ACh) to elicit contraction in the muscle. ACh released to the synaptic cleft binds to ACh receptors (AChRs) present on the muscle membrane, which form clusters specifically at the NMJ. The binding of ACh initiates a depolarization response, which generates an action potential that travels along the muscle cell. This depolarization ultimately leads to a release of calcium stores from a specialized organelle, the sarcoplasmic reticulum (SR), into the cytoplasm. Finally, calcium binding to proteins in the sarcomere results in sarcomere contraction (**Figure 7**).

Neuromuscular junction structure and function

The first part of muscle contraction depends on the release and reception of ACh signaling at the NMJ. The specialized region of the muscle membrane (sarcolemma) that is innervated by a motor neuron is termed the “endplate” (Kandel et al., 2013). This region presents with deep invaginations called junctional folds, which increase the postsynaptic surface area available for AChR clusters to maximize signal transmission. These clusters are assembled through a cascade of protein interactions initiated by the presynaptic neuron. Initially, agrin released by the nerve terminal binds to lipoprotein receptor-related protein 4 (LRP4), activating its ability to form a complex with muscle-specific kinase (MuSK). Consequently, MuSK dimerizes and autophosphorylates, thus initiating a signaling cascade in which rapsyn mediates AChR clustering on the muscle membrane (Lazaridis & Tzartos, 2020) (see diagram in **Figure 7**).

In the body, there are two main types of AChRs, nicotinic or muscarinic receptors, which receive their name from their ability to specifically bind the alkaloids nicotine or muscarine, respectively. The receptors present at the NMJ are nicotinic AChRs (nAChRs), which comprise three similar and two identical polypeptide chains, circularly arranged around a narrow membrane pore. Therefore, this receptor has a heteropentameric transmembrane structure, as revealed by electron microscopy (Karlin, 1993; Unwin, 1993). In human muscle, two isoforms of nAChRs exist. During prenatal stages, the fetal isoform of the acetylcholine receptor is actively involved in the development of the neuromuscular system. Later, following the prenatal period, the adult isoform is predominant except in cases of denervation, where the fetal form is once again

expressed throughout the muscle (Cetin et al., 2020). The pentamer is composed of two α -, one β -, and one δ -subunit, as well as a γ -subunit in the fetal AChR isoform that is replaced by an ϵ -subunit in the adult AChR isoform (Kalamida et al., 2007).

Depolarization and calcium release

To elicit contraction, motor neurons release ACh contained in synaptic vesicles to the synaptic cleft of the NMJ (**Figure 7**). The nAChRs present at the NMJ are ligand-gated ion channels, meaning that the binding of ACh results in the opening of the transmembrane pore to exchange ions. In skeletal muscle, nAChR channels allow influx of cations into the cell, mainly Na^+ ions, causing a decrease in the membrane potential (depolarization). This depolarization normally exceeds the threshold voltage required to activate voltage-gated sodium channels (Na_v), which leads to an additional influx of Na^+ . In sum, this generates an action potential that travels along the cell, eventually reaching an anatomical region called the transverse tubule or T-tubule.

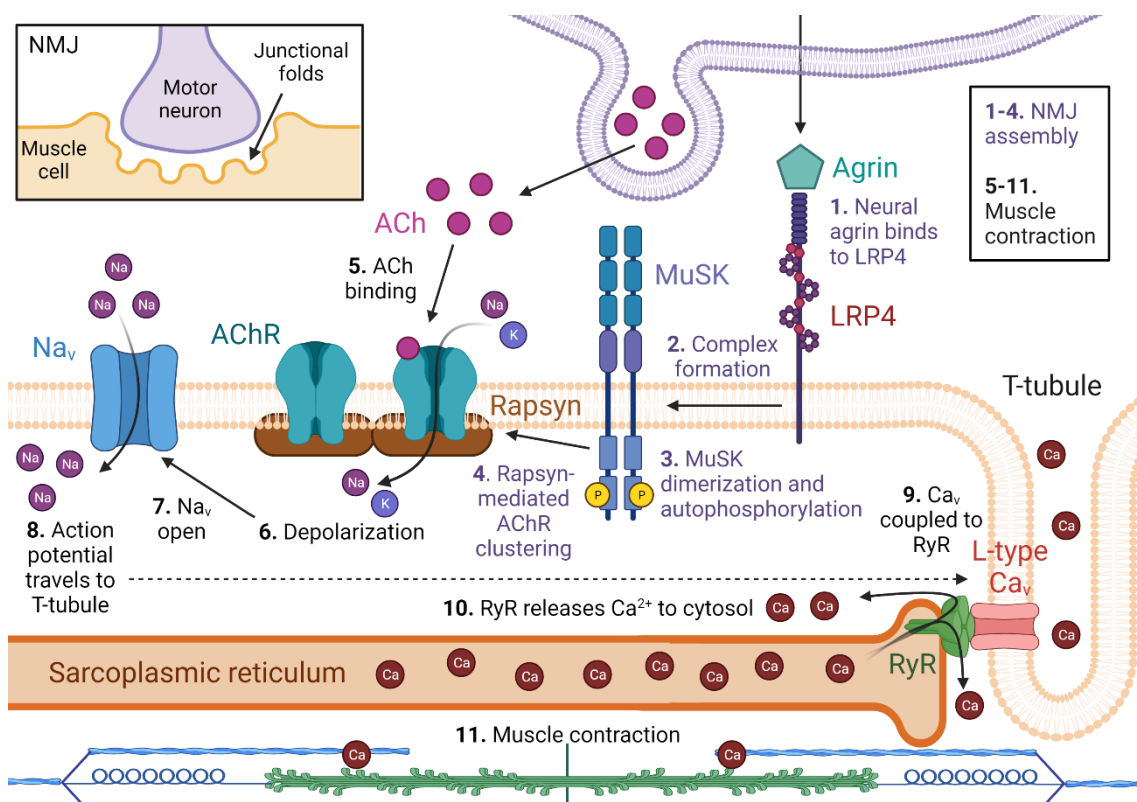


Figure 7. Diagram of NMJ assembly and ACh-mediated muscle depolarization and contraction.

T-tubules are invaginations of the cell membrane that extend deep into the interior of the muscle fiber. They form a network of tubular structures that are in close proximity to the

sarcoplasmic reticulum, a specialized form of endoplasmic reticulum found in muscle cells. T-tubules are necessary for excitation-contraction coupling, which is the process by which the action potential is translated into a contraction response. At the T-tubule, there is a higher density of voltage-gated calcium channels (Ca_v), that open in response to the depolarization. Ca_v are mechanically coupled to ryanodine receptors (RyR) on the SR membrane, which open in conjunction with Ca_v . The opening of RyRs leads to the massive release of calcium stores in the SR, which dramatically increases the intracellular Ca^{2+} concentration. Calcium is a key element in allowing sarcomere contraction, as will be explained in the following subsection.

The sliding filament model of muscle contraction

After depolarization and calcium release, muscle cell contraction relies on sarcomeres, which consist of myosin, troponin, actin, and tropomyosin. The sliding filament model (A. F. Huxley & Niedergerke, 1954; H. Huxley & Hanson, 1954) suggests that contraction occurs as actin filaments slide over myosin filaments. Actin forms a complex with tropomyosin and troponin molecules, and myosin has projections called "myosin heads" with binding sites for actin and ATP. The sliding filament theory involves the cross-bridge cycle, where ATP binds to myosin heads, causing detachment from actin. ATP hydrolysis moves the myosin head into a cocked position for actin binding. In the resting state, tropomyosin partially blocks actin binding sites, but upon calcium release, the troponin- Ca^{2+} complex displaces tropomyosin, fully exposing myosin binding sites. Myosin strongly binds to actin, initiating a "power stroke" that shortens the sarcomere by moving actin filaments inwards. A diagram of this process is shown in **Figure 8**.

The cross-bridge cycle relies on available ATP and Ca^{2+} for muscle contraction. When calcium is actively pumped back into the sarcoplasmic reticulum (SR), cross-bridge cycling ends. This reuptake of Ca^{2+} is achieved by ATP-driven calcium pumps on the SR membrane (Hasselbach, 1964). Additionally, to completely stop contraction, excess ACh (acetylcholine) released into the synaptic cleft is hydrolyzed by acetylcholine esterase (AChE) on the postsynaptic membrane when action potentials cease. This combination of intracellular Ca^{2+} depletion and ACh degradation rapidly terminates contraction.

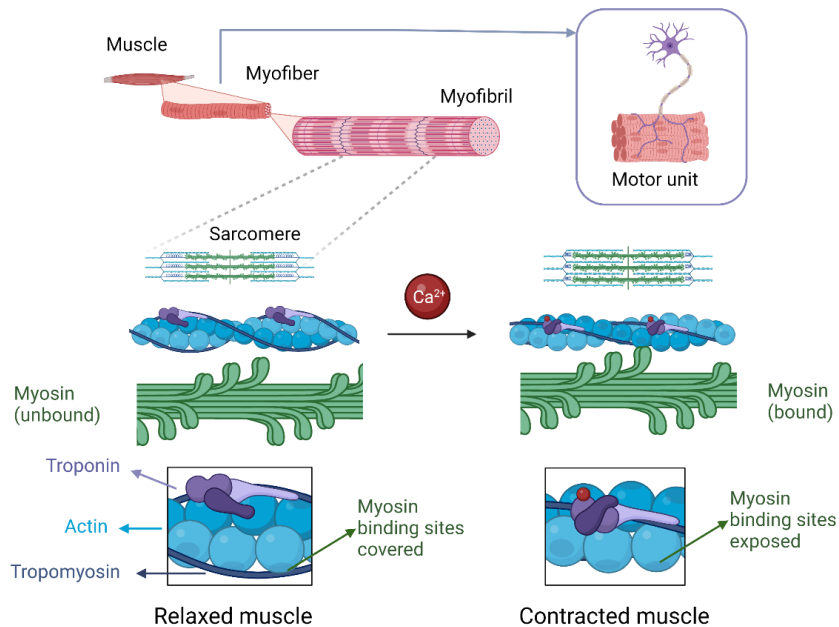


Figure 8. Sliding filament model of contraction. Inside myofibrils, sarcomeres regulate shortening of muscle cells through a process involving calcium binding in an ATP-dependent reaction.

Action potentials and modulation of muscle contraction force

When a single action potential is sent from a neuron to a muscle cell, a twitch contraction is initiated. Then, when signaling is terminated (through ACh degradation and calcium reuptake), muscle relaxation begins. The duration of a contraction is notably longer than the duration of an action potential. Muscles can exhibit different patterns of contraction depending on the frequency of the action potentials they receive (**Figure 9**). If action potentials are spaced out to allow relaxation in between, a series of individual twitch contractions are produced. However, one twitch is often not enough to produce a useful muscle contraction. Therefore, action potentials are delivered closer together to cause the summation of contraction waves, resulting in increased contraction (I. C. Smith et al., 2020). As the next contractions begin at higher baselines, they also reach higher peaks than the first contraction. With further increases in frequency, the relaxation phase shortens even more, resulting in an increasing contraction force wave known as tetanus. Maximum contraction force is achieved in smooth tetanus, in which action potentials are sufficiently frequent as to completely impede relaxation in between.

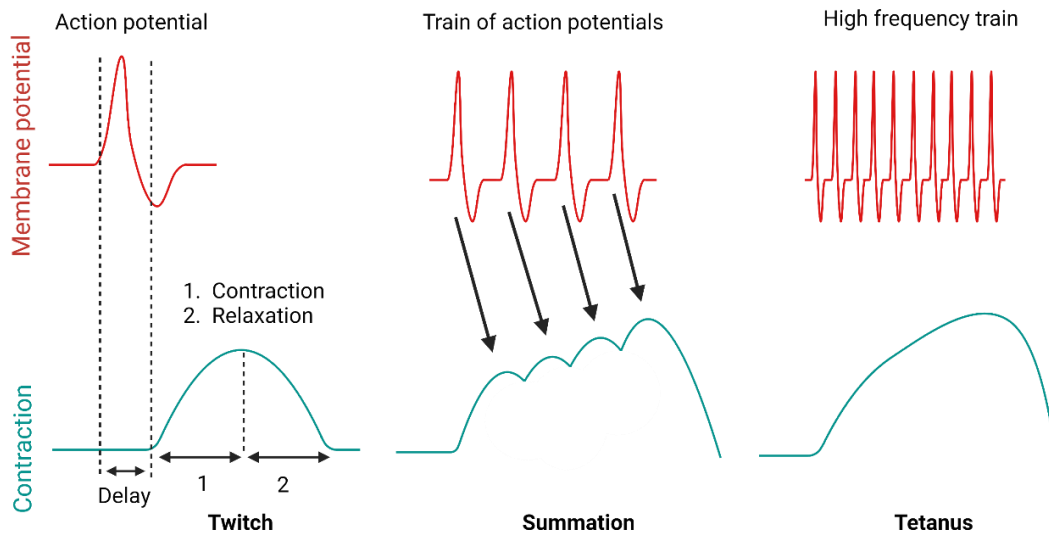


Figure 9. Action potentials and their relationship to the phases of muscle contraction. Different types of muscle contraction result from increasing frequency of action potentials.

If it is desired to depolarize cells *in vitro* to induce contractions, several methods are available. One method would be to use ACh in solution, which effectively activates AChR channels and causes depolarization (Afshar Bakooshli et al., 2019; Afshar et al., 2020). However, it must be noted that degradation of acetylcholine cannot occur as it would *in vivo*, as the ACh is added in large amounts to the cell culture medium instead of being confined to a synaptic cleft. Therefore, ACh *in vitro* causes sustained tetanic contractions unless it is removed from the medium using a perfusion system. As an alternative method to chemical stimulation, electrical stimulation is frequently used, as it can deliver precisely timed pulses to induce twitch or tetanic contractions (Guix et al., 2021; Hinds et al., 2011; Osaki et al., 2020). The disadvantage of this method is that it is more indiscriminate than the *in vivo* pathway of depolarization, and its lack of tissue specificity in co-culture models. Finally, as a more cell-specific and gentle mechanism, muscle cells expressing optogenetic tools such as ChR2 can be depolarized by optical stimulation (Osaki, Sivathanu, et al., 2018; Sala-Jarque et al., 2020; Vila et al., 2021) to produce different kinds of contractions. The latter two methods can also be used for training to improve muscle maturation (Ito et al., 2014; Langelaan et al., 2011; Powell et al., 2002).

Muscle differentiation markers

Adult skeletal muscle tissue possesses a highly efficient regenerative mechanism, which is essential for meeting the repair demands that arise from everyday activities such as growth or exercise (Schmidt et al., 2019). Skeletal muscle stem cells (SKMSC), also known as satellite cells, reside under the basal lamina of the muscle in a quiescent state (Mauro, 1961). In this state, SKMSCs express Sprouty1, a receptor tyrosine kinase signaling inhibitor, which is a key regulator in maintaining reversibility of SKMSC quiescence (Shea et al., 2010). They also express the paired box transcription factor Pax7, which is required for SKMSC specification (Seale et al., 2000). The myogenic potential of SKMSCs depends on the expression of Pax genes as well as myogenic regulatory factors (MRFs) such as MyoD, Myf5, Myogenin, and MRF4 (**Figure 10**). These MRFs are part of a family of class II basic helix-loop-helix (bHLH) transcription factors, and therefore share a similar protein structure (Zammit, 2017).

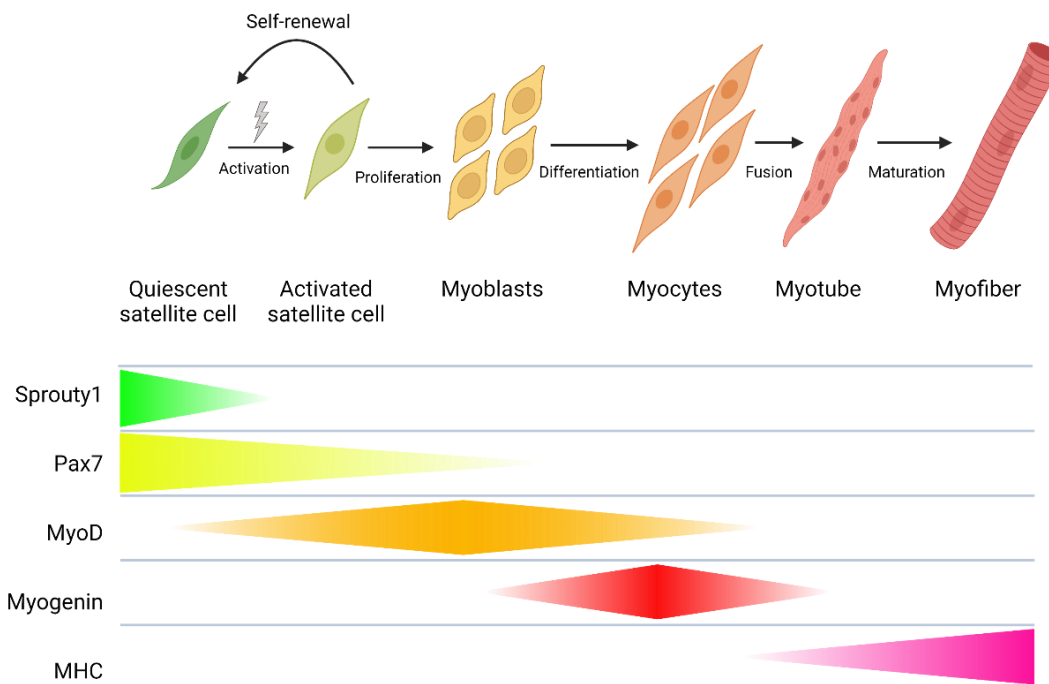


Figure 10. Muscle differentiation *in vivo* and expression of associated markers at each stage. Adapted from Schmidt et al., 2019.

Upon activation in response to muscle damage or growth requirements, satellite cells co-express Pax7 and MyoD, an early marker for myogenic commitment, which causes them to leave the quiescent state and further differentiate into myocytes. MyoD induces expression of myogenin, which initiates terminal differentiation of myoblasts (myogenic

progenitor cells) (Hernández-Hernández et al., 2017). This is accompanied by downregulation of MyoD expression in differentiated myocytes. Finally, myocytes undergo cell fusion into multinucleated myotubes, which begin to assemble sarcomeric structures. At this stage, myosin heavy chain (MHC) expression starts to increase and reaches a plateau in mature myofibers. When differentiating myoblasts *in vitro*, the markers MyoD, myogenin and MHC are widely used markers for following myogenesis and maturation of muscle fibers. In addition to MHC, other sarcomere-associated proteins such as sarcomeric alpha-actinin (SAA) can be useful for evaluating *in vitro* muscle maturity.

Overview of the state of the art in muscle tissue modeling

In recent years, *in vitro* modeling of the muscle has gained relevance. This is in response to the growing need to find alternatives to animal models that are more ethical, scalable, and amenable to fine manipulations and detailed functional analysis. A relevant advancement in the field has been the development of functional *in vitro* NMJ models. The first *in vitro* culture of the NMJ dates to the early 1900s, when it was observed that a co-culture of frog spinal cord and surrounding muscle tissue produced spontaneously contractile muscle fibers with motor neuron innervation (Harrison et al., 1907). Since then, models have evolved to use human muscle and neural cell sources, and to rely less on primary sourcing of cells (Leng et al., 2022). In addition, important advances have been made in engineering specific tissue architectures, through the use of compartmentalized microfluidic devices (MFD) or organ-on-chip (OoC) technologies, as well as organoids and bioprinted constructs (as reviewed in Ajalik et al., 2022; Carraro et al., 2022; Jalal et al., 2021; Leng et al., 2022; Raffa et al., 2021).

Apart from motor neurons, muscle tissue includes several other relevant cell types, which have been included in different studies according to each desired clinical application. For example, muscles are highly vascularized, which has prompted the development of models that include vascularization (Kim et al., 2022; Osaki, Sivathanu, et al., 2018; Pinton et al., 2023). Another relevant interaction could be the cross-talk between muscle cells and adipocytes (Kudoh et al., 2018; Shahin-Shamsabadi & Selvaganapathy, 2020), which is relevant for understanding metabolic disorders such as obesity. Other metabolic diseases have been modeled by including fatty hepatocytes (De Chiara et al., 2022) to study non-alcoholic fatty liver disease, or pancreatic cells (Fernández-Costa et al., 2023)

to study insulin resistance in diabetes. Other supporting cell types have also been modeled, such as pericytes (Maffioletti et al., 2018; Pinton et al., 2023) or tenocytes (Laternser et al., 2018). These protocols from the Maffioletti group use an innovative multilineage differentiation to obtain several cell types at once from an iPSC source.

Despite the broadening horizons in the field *in vitro* NMJ modeling, one of the most limiting factors in human NMJ co-culture models is motor neuron derivation. While primary spinal cord explants and 2D dissociated cultures provide a straightforward solution for obtaining mouse motor neurons (Happe et al., 2017; Sala-Jarque et al., 2020; Tong et al., 2014), human models cannot circumvent the need for a stem cell source of neurons. The main challenges associated with MN differentiation are low efficiency and low purity of the resulting MN population, as well as long-term maintenance of cultures to achieve functional maturity. Currently available protocols use iPSCs (Osaki, Uzel, et al., 2018; Vila et al., 2021) or embryonic stem cells (ES) such as the WA09 cell line (Afshar Bakooshli et al., 2019; Du et al., 2015). Some of the most successful methods for MN induction have lately been the use of small molecules or transcription factors, which have been highly optimized to achieve more consistent results (Castillo Bautista & Sternecker, 2023). Despite considerable success with these protocols, the lack of reproducibility still remains problematic when applying the same differentiation protocol to different iPSC cell lines (Hu et al., 2010; Volpato et al., 2018), and there is also significant batch-to-batch variability due to the effect of cell passages and shelf life of induction factors (Afshar Bakooshli et al., 2019).

Although there has been considerable focus on increasing the complexity of muscle and NMJ models, there are also influential studies that have used monocultures of muscle cells as platforms for analyzing muscle function (Afshar et al., 2020; Hinds et al., 2011; Madden et al., 2015; Van Der Schaft et al., 2013). In some applications, a more simplistic approach may be beneficial, as co-culturing motor neurons and muscle cells presents several technical difficulties. This muscle-only type of model is suitable for studies of muscular diseases that are unrelated to the motor neuron, muscle-specific injuries (Fleming et al., 2020; Rajabian et al., 2021), and studies of muscle function in response to therapies targeting the muscle (Madden et al., 2015; Mestre et al., 2021).

Human muscle cell sources

In broad terms, human skeletal muscle models use either primary cells from muscle biopsies, immortalized myoblasts, iPSCs, or transdifferentiated patient-derived cells. For primary cells, the main advantage is their physiological relevance, as the cells retain the most *in vivo* muscle cell markers and functionality. However, the main drawback is the limited availability of cell sources, as well as the limited number of passages that the cells can undergo. Therefore, immortalized myoblasts have been developed to solve this issue. One of the most prominent research groups in Europe is the group of Dr. Vincent Mouly (Institut de Myologie, Paris), which has successfully immortalized multiple healthy and pathological human myoblast cell lines (Mamchaoui et al., 2011). One of the most widely cited murine skeletal muscle cell lines is C2C12, which is also an immortalized myoblast cell line. The main drawback of these cells is that they show some differences in functionality and maturity compared to primary cells, such as reduced spontaneous contractility (Macpherson et al., 2004; N. Rose et al., 2023). Nevertheless, immortalized myoblasts are still an excellent choice for *in vitro* skeletal muscle models, especially during protocol optimization phases. Newer *in vitro* setups with more biomimetic differentiation conditions can promote the formation of contractile tissue from immortalized cell sources (Shima et al., 2018).

As in many fields of biomedical research, iPSCs have been gaining relevance in SKM modeling in the past years, as they provide the unique opportunity to develop personalized models of numerous muscle diseases (Iberite et al., 2022). Some iPSC-derived muscle models have started to be published, for diseases such as amyotrophic lateral sclerosis (ALS) (Osaki, Uzel, et al., 2018) and Duchenne muscular dystrophy (DMD) (Yoshioka et al., 2021), among others. Finally, another method for generating patient-specific models is to transdifferentiate patient fibroblasts into myocytes, using genetic modification with lentiviruses (Almeida et al., 2021), myogenic factor overexpression (Fernández-Garibay et al., 2021) or small molecule induction (Abdel-Raouf et al., 2021).

Scaffolds for muscle tissue engineering

As it has been shown for most mammalian tissues, 2D culture lacks many relevant aspects of muscle tissue microenvironment and architecture, and thus does not successfully recapitulate *in vivo* phenotypes. A common problem when differentiating myoblasts in

2D is the detachment of myotubes from the substrate following spontaneous contractions, which limits long-term maintenance of the culture (Toral-Ojeda et al., 2018). Also, myofiber alignment does not naturally occur, although it can be guided by the use of surface modification (Das et al., 2010). Consequently, recent efforts have been focused on developing 3D models of the muscle. Many 3D models rely on the use of hydrogel scaffolds for culturing muscle cells, which must be mechanically appropriate to support differentiation and contraction.

Natural hydrogels are a common choice in muscle tissue modeling, due to their ease of use and their biomimetic composition. The most commonly used natural hydrogels are combinations of Matrigel and collagen I (Van Der Schaft et al., 2013) or Matrigel and fibrin (Afshar Bakooshi et al., 2019; Guix et al., 2021; Hinds et al., 2011; Madden et al., 2015; Mestre et al., 2021). The latter hydrogel has been shown to have excellent mechanical and biological properties for skeletal muscle differentiation, according to the comparative analysis of ECM composition in Hinds et al., 2011 and supported by its widespread use in literature. In contrast, Matrigel-collagen I hydrogels have shown excessive compaction and stiffness, leading to breakage of muscle constructs and poor oxygen diffusion. In fact, Matrigel has been shown to maintain *in vitro* myogenic potential in satellite cells, while collagen I does not (Grefte et al., 2012).

Synthetic hydrogels such as gelatin methacrylate (GelMA) hydrogels with methacryloyl-carboxymethyl cellulose methacrylate (CMCMA) have also been used in several publications. The main feature of methacrylated hydrogels is their ability to be crosslinked by UV light, which makes them amenable to bioprinting applications (García-Lizarribar et al., 2018), although UV curing can also be applied when using molds or stamps (Fernández-Garibay et al., 2021; Hosseini et al., 2012). These hydrogels have a high degree of tunability and reproducibility, but lack biological cues for differentiation present in natural hydrogels. A novel hybrid hydrogel alternative to animal-sourced hydrogels for skeletal muscle could be the xeno-free platelet lysate-derived hydrogels developed in the laboratory of Dr. Javier Ramon-Azcón (Fernández-Garibay et al., 2022), which could be useful for drug testing applications.

Anchored 3D models of muscle tissue

As a way to improve muscle maturation, alignment, and mechanical properties, an important advantage of 3D muscle culture is the ability to use anchors to mimic the way that tendons anchor muscles to bone. For this, muscle cells embedded in 3D hydrogels are seeded between two anchoring points and are allowed to detach from the culture substrate at their central region. An illustration of this concept is shown in **Figure 11**.

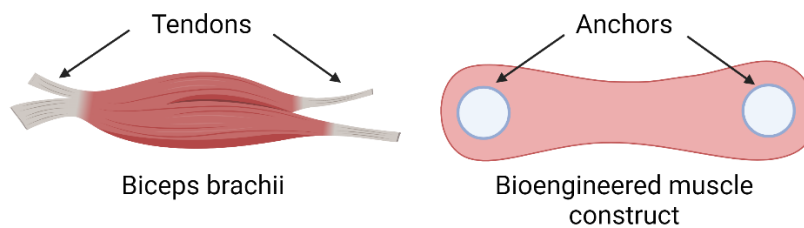


Figure 11. Anchors in bioengineered muscle constructs can mimic the function of in vivo tendon anchors. An effective method to achieve this is to use pillars or posts to serve as anchors. One of the pioneers of this method is the application described by Vandenburg et al., 2008. An especially interesting methodology presented in this article is the use of flexible PDMS pillars that can be deflected by muscle cell contraction. This method offers the advantage of enabling the quantification of muscle contractile force through measurements of pillar deflection, provided that the elastic modulus of the pillars is known (Afshar et al., 2020; Kajzar et al., 2008; Osaki et al., 2020). However, the microscale fabrication of these PDMS-based pillars is complex and time-consuming, often requiring use of cleanroom facilities for fabrication of molds by soft lithography, although some 3D printed molds have also been proposed (Afshar et al., 2020; Iuliano et al., 2020). The micro-posts must include caps or curved ends to avoid detachment of muscle constructs from them during contraction, which make the molding and demolding process more delicate, regardless of the molding technique. Different support morphologies such as internal flexible skeletons (Guix et al., 2021) or rings (H. Zhao et al., 2021) are used in some publications, also allowing the formation of highly aligned contractile tissue.

As a simplified yet effective alternative, several studies have utilized VELCRO™ fabric pieces as anchors for bioengineered muscle constructs (Afshar Bakooshli et al., 2019; Hinds et al., 2011; Madden et al., 2015; Van Der Schaft et al., 2013). This material

effectively entraps the hydrogel-cell mixture within the loops of the fabric, forming a robust anchoring site. Attaching the VELCRO™ fragments to cell culture supports can be easily achieved by gluing them using PDMS glue, as described in Van Der Schaft et al., 2013. The main limitation of VELCRO™ anchors is that they do not allow direct quantification of muscle force. Nevertheless, muscle contraction can also be evaluated using motion analysis algorithms. Alternatively, some studies (Afshar Bakooshli et al., 2019; Afshar et al., 2020) have successfully used calcium imaging to quantify muscle function.

Myasthenia gravis

Neuromuscular diseases are conditions that involve injury or dysfunction of peripheral nerves or the muscle. Myasthenia gravis (MG), a neuromuscular disease, is a rare autoimmune disorder of neuromuscular junction transmission which is estimated to affect 0,015-0,02% of the world population (Dresser et al., 2021). The hallmarks of MG are muscle weakness and fatigability, with severities that tend to vary between different patients. This disease is more common in women under 40 years old, and in men over 60 years old; with a generally higher incidence in women and in the Black population (Bubuioc et al., 2021). However, symptoms can appear at any age, gender, and ethnicity.

Antibody targets in myasthenia gravis

According to the current body of knowledge, myasthenia gravis is recognized as having an autoimmune origin, meaning that symptoms are directly related to elevated levels of serum autoantibodies directed at key proteins in the NMJ. This disease fulfils the Witebsky postulates that determine the autoimmune origin of a disease (N. R. Rose & Bona, 1993; Witebsky et al., 1957). These are the presence of pathogenic autoantibodies or reactive T cells, the reproduction of disease symptoms by passive transfer of pathogenic antibodies or T cells to animals, and circumstantial evidence from clinical cues.

MG autoantibodies were discovered in patients shortly after an unintended passive transfer experiment, which led to a rapid fulfilment of the first two requirements of the postulates. The detection of anti-acetylcholine receptor (AChR) antibodies in patients with MG was first reported by Lindstrom et al. in 1976. This finding followed an unexpected observation made three years earlier, where immunization of rabbits with

AChR resulted in a myasthenia gravis-like response (Patrick & Lindstrom, 1973) (Deymeer, 2020). As reported in the original publication, these antibodies were not found to be directed at the acetylcholine binding site of the receptor, which implied alternative pathogenic mechanisms not based on competitive inhibition.

Around 85% of MG patients are positive for anti-AChR autoantibodies. Each subunit of AChR has four transmembrane domains, a highly structured extracellular domain, and a partly structured intracellular domain. MG antibodies target the extracellular domain and are very heterogeneous, but half of them bind to the α subunit at a specific region called the main immunogenic region (MIR). The MIR is formed by several epitopes centered around amino acids 67-76 of the $\alpha 1$ subunit extracellular domain. These antibodies are significantly more pathogenic than those directed at other subunits (Kordas et al., 2014).

Anti-AChR antibodies are mainly of the IgG1 and IgG3 subclasses. Importantly, this means that they are able to activate complement, which is implicated in complement-mediated destruction of AChRs (Koneczny & Herbst, 2019). Once pathogenic IgGs bind to AChRs, C1q binds to the Fc region of the antibodies, which initiates the complement cascade. During this process, C3 is cleaved to C3a and C3b, after which the formation of the membrane attack complex (MAC) ensues. Complement attack results in membrane lysis and destruction of NMJ structure, causing the loss of junctional folds and drastically reducing the density of AChRs and Na_v at the synapse. C3 can be found colocalized with AChRs in patients (Engel et al., 1977) and *in vitro* (Afshar Bakooshli et al., 2019).

However, two other mechanisms of AChR functional impairment have been described. In the second mechanism, bivalent binding of anti-AChR antibodies can cross-link AChRs and induce their endocytosis (Kao & Drachman, 1977; C. W. Lee et al., 2014). This unnaturally increases their turnover and degradation rate, leading to reduced AChR densities at the synapse. Finally, a third mechanism involves direct block of function by preventing the binding of ACh (Gomez & Richman, 1983; F. M. Howard et al., 1987). A diagram of these mechanisms can be found in **Figure 12**.

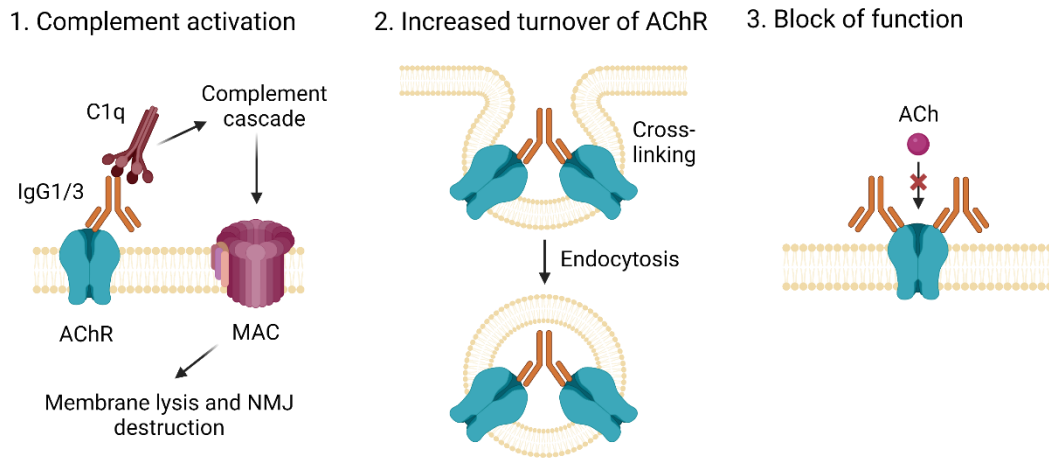


Figure 12. Pathogenic mechanisms of MG anti-AChR antibodies. Adapted from Koneczny & Herbst, 2019.

A smaller percentage of patients (around 6%) has antibodies against MuSK (Hoch et al., 2001). In this case, however, antibodies are mostly IgG4 subclass, which are unable to cause complement activation. A particular characteristic of IgG4 is their ability to generate bi-specific antibodies, which are unable to crosslink two antigens of the same kind as observed in anti-AChR antibodies. In this scenario, monovalent binding of IgG4s to MuSK is known to impair binding of LRP4 to MuSK, which impairs the agrin-LRP4-MuSK signaling axis and retrograde signaling of LRP4 to the motor neuron (Huijbers et al., 2013; Koneczny et al., 2013). In the case of the infrequent IgG1/3 subtypes, divalent binding to MuSK results in MuSK dimerization, causing unwarranted dimerization and autophosphorylation of MuSK. This induces activation of AChR recruitment independent of agrin, which enables the formation of ectopic AChR clusters (Huijbers et al., 2019). Both of these mechanisms are represented in **Figure 13**.

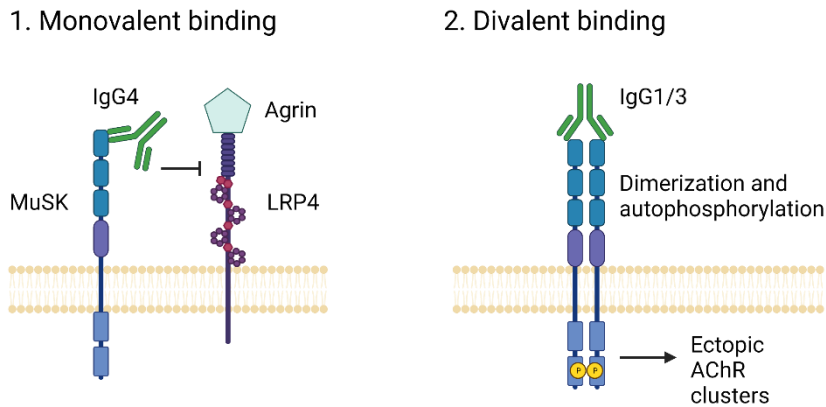


Figure 13. Pathogenic mechanisms of MG anti-MuSK antibodies depending on the IgG subclass. Adapted from Koneczny & Herbst, 2019.

Patients with MG symptoms that lack both AChR and MuSK antibodies are referred to as double-seronegative patients. However, some of these patients may simply have low-affinity AChR antibodies (Leite et al., 2008). Furthermore, around 2% of MG patients have recently been found to be positive for anti-LRP4 antibodies (Higuchi et al., 2011; Zisimopoulou et al., 2014). One theory of their pathogenic mechanism is that they inhibit binding of LRP4 to agrin, impairing recruitment of AChRs at the NMJ (Pevzner et al., 2012). Also, these antibodies predominantly belong to the IgG1 or IgG3 subclass, which as mentioned before, are complement activators.

Additional antibodies of interest for MG have been detected, directed against agrin, titin, Kv1.4 (a potassium channel subunit), ryanodine receptors, collagen Q, and cortactin (Gilhus et al., 2019). All these molecules are relevant for muscle contraction, despite not being solely located at the NMJ as in the case of the three most typical antigens. MG with LRP4 or other alternative antibodies still does not fulfil the Witebsky postulates of autoimmune disease, due to lack of sufficient understanding of pathogenic mechanisms and adequate passive transfer animal models (Koneczny & Herbst, 2019). Identification of novel targets in seemingly seronegative (SN) patients is still ongoing, aiming to shed light on the mechanism behind a higher number of MG cases and guide specific treatment options.

Symptoms of myasthenia gravis

Depending on the case, MG symptoms may be restricted to specific muscle groups or present a more widespread manifestation (generalized MG). It is especially common for

MG patients to develop drooping of eyelids (ptosis) and weakness of the eye muscles, which can result in double vision. This is a frequent form of focal MG, known as ocular myasthenia. In other cases, patients may experience abnormal muscle fatigue after exercise, especially in the upper limbs. Additionally, facial muscles are often affected, causing impaired speech, difficulties with chewing and swallowing. About 10% of affected individuals could develop severe impairment of muscles used for breathing, which causes a life-threatening event named a myasthenic crisis (*Myasthenia Gravis - Symptoms, Causes, Treatment | National Organization for Rare Disorders, 2023*).

The severity of symptoms varies greatly across patients, even in those with the same antibody specificity. Also, physical manifestations of the disease can experience peaks at different moments in a patient's lifetime. Perplexingly, symptom severity is not directly correlated to autoantibody titers (Lazaridis & Tzartos, 2020; Lindstrom et al., 1976), which suggests that the specific affinities of different antibodies are an important aspect of the pathophysiology of this disease. Also, due to complex immune interactions and compensation mechanisms in individual patients, antibody levels are not an accurate predictor of symptoms over time.

Patients with AChR MG frequently have thymic abnormalities, such as thymic hyperplasia (frequently associated with early onset of disease) or thymoma. It is thought that the thymus plays a role in pathogenesis. In fact, there is a correlation between higher anti-AChR antibody levels and thymic hyperplasia (Truffault et al., 2017). The presence of thymic disorders is also correlated with the presence of anti-striated muscle antibodies directed against proteins such as alpha-actin, myosin, titin, and RyRs, among others.

Currently available treatments

Considering that the majority of MG cases are anti-AChR-mediated, and acetylcholinesterase (AChE) inhibitors like pyridostigmine are commonly used to increase the amount of available ACh at the synaptic cleft, providing symptomatic relief (Farmakidis et al., 2018). However, this treatment is less effective for anti-MuSK patients or ocular MG (Hatanaka et al., 2005). Many patients with generalized MG or non-AChR MG require additional immune modulation or suppression, often in combination with corticosteroids, both of which can have significant side effects (Warmolts & Engel, 1972). Thymectomy is a beneficial option for MG patients with thymic abnormalities

(Wolfe et al., 2016), but it is limited to specific subsets of patients and is not considered a standalone treatment (Clifford et al., 2019). Emerging therapies under investigation include monoclonal antibodies targeting T-cell activation, B-cell molecules, and the fragment crystallizable neonatal receptor (FcRn) receptor (Ward et al., 2003). Efgartigimod, an antibody drug that acts as an FcRn blocker, has been approved for the treatment of generalized MG (J. F. Howard et al., 2021). Inhibiting components of the complement system, such as with eculizumab, is another approach for patients with moderate or severe MG symptoms (J. F. Howard et al., 2013). Although treatment outcomes for MG have improved, some evidence is still lacking for newer treatments, and there is room for improvement, especially in refractory cases (Mantegazza & Antozzi, 2018). The diversity in the etiologies of this disease points at the need to design target-specific therapies. For this, it is imperative to continue the search for novel antibody targets and elucidate their exact mechanisms to guide rational drug design (Schneider-Gold & Gilhus, 2021).

***In vitro* models of myasthenia gravis**

Traditionally, autoimmune diseases have mainly been studied using cell-based assays or passive transfer animal models. However, more clinically relevant and highly sensitive *in vitro* models are needed to fully understand the disease, both for research and diagnostic purposes. In terms of research on disease mechanisms, current animal models are limited by the profound differences between human NMJs and murine NMJs or those derived from other mammalian species. In addition, studying changes in *in vivo* neuromuscular junction architecture and functionality is notably complex.

Diagnosis of MG is classically performed by radioimmunoprecipitation assay (RIA) or enzyme-linked immunoassay (ELISA). Although RIA is the gold standard for diagnosis due to its high sensitivity, these techniques have limitations regarding antibody detection, as some antibodies may bind poorly to recombinant or soluble antigens but could have a higher affinity to their antigen in its NMJ membrane-bound form. This is why cell-based assays have been developed, to provide a platform for exposing clustered AChRs on a cell membrane (Leite et al., 2008). A recent cell-based assay with a high detection rate of AChR antibodies (Cai et al., 2021) still uses a modified HEK cell line (as originally proposed in Leite et al., 2008), which expresses adult AChR and the clustering protein rapsyn. Nevertheless, this model would not be appropriate for detection of novel antigens,

as it does not express other NMJ or skeletal muscle proteins or possess contractile activity. Thus, use of human muscle cells for both diagnosis and research would be preferable to better mimic *in vivo* conditions.

A concern in the field of muscle cell-based models is the lack of ACh ϵ subunit in *in vitro* non-innervated muscle cultures or rhabdomyosarcoma cultures, which generates false negative diagnoses from these assays (Zisimopoulou et al., 2014). For this, one solution is to use a rhabdomyosarcoma cell line, TE671, that is modified to express the epsilon subunit (Beeson et al., 1996). However, TE671 rhabdomyosarcoma is after all a cancer cell line, which limits the clinical relevance of this model.

The effect of MG serums *in vitro* has been studied using 2D myoblast cultures but has mainly been applied to mouse or rat myoblasts cultured in 2D (Burges et al., 1990; Luckman et al., 2006). A few recent publications have tested the effect of MG patient serums or purified autoantibodies on muscle function in *in vitro* human NMJ models using primary or immortalized human myoblasts. These human models, which are clinically more relevant, are hereby discussed in more detail.

Summary of relevant publications

In a study published by Smith et al., 2021, primary human myoblasts were co-cultured in 2D with iPSC-derived motor neurons, and treated with a commercial anti-AChR antibody (not a patient autoantibody). Another questionable part of this study is the use of “direct” and “indirect” electrical stimulation in two fluidically connected microfluidic chambers. Although the methods state that electrical leakage into the opposite chamber was ruled out before electrophysiological testing, this methodology does not seem ideal. In addition, the target subunit or protein region of the commercial antibody is unknown, meaning that the clinical relevance of this antibody is not guaranteed. Despite these considerations, the model demonstrated a decrease in NMJ connections after only 3 hours of antibody treatment, as well as increased receptor internalization. With complement treatment, C3C deposition and reduced NMJ functionality after electrical stimulation were observed.

Another study by Vila et al., 2021 reported the use of an optogenetically controllable, iPSC-derived NMJ microfluidic model, which could be treated with purified IgGs from MG patients. Reduced muscle function in response to optical stimulation of neurons was seen in these cultures. Interestingly, in this study, seronegative patient serum was used to demonstrate the ability of the model to replicate pathology of some seronegative patients,

albeit at a very high concentration (equivalent to adding 40% serum to the medium), and with no effect in one of the tested sera. Unfortunately, the IgG purification methodology is not explained in detail, which limits the reproducibility of their treatment conditions. Similar results were reported in a previous study that also used optogenetically controllable NMJs (Steinbeck et al., 2016) treated with AChR MG serum.

In the 3D NMJ model developed by (Afshar Bakooshi et al., 2019), human immortalized myoblasts were co-cultured with WA09-derived motor neuron spheroids. In this case, the model was not compartmentalized, as it used VELCRO™ anchors and mixed MN spheroids into the myoblast-hydrogel suspension to generate direct MN-SKM contacts. IgGs purified from three different AChR MG patient serums were applied to the muscle constructs at a normalized concentration of 300 nM. Muscle function in response to acetylcholine stimulation was evaluated by calcium imaging using GCaMP6⁺ immortalized myoblasts (also immortalized as described in Mamchaoui et al., 2011), after 3 days of treatment with patient IgGs. A decrease in muscle function was observed, as well as C3C deposition upon addition of human complement, which colocalized with AChRs stained with α -bungarotoxin.

Another relevant feature of this platform was that the AChR γ to ϵ subunit switch (fetal to adult isoforms of nAChR) was observed in their co-culture model, indicating maturity of the endplates. The lack of ϵ subunit is a common limitation of simpler cell-based assays. Of note, this was only demonstrated with primary myoblasts, but not with immortalized myoblasts. In addition to the AChR subunit switch, proof was shown in this article that the addition of agrin to cell culture medium could successfully induce endplate formation in muscle cells in the absence of motor neurons. The maturity of these endplates was said to be comparable to those obtained in co-culture experiments. Therefore, this could be an appropriate alternative to co-culture in myasthenia gravis studies, as all the currently known autoantibodies are directed against the postsynaptic cell. In all, this article is currently one of the most detailed accounts of reproduction of MG hallmarks *in vitro*. The only caveat of this article is that it does not compare the effects of different autoantibody types, such as anti-MuSK or other antibodies.

In all, we can conclude that current humanized *in vitro* models of MG have provided valuable advances in replicating MG pathogenesis, that could be used for research and diagnostic purposes with the necessary adaptations. The main challenges that arise for

future development of models are the possibility to model other described MG subtypes, such as MuSK MG, and the ability to use these models for diagnostic purposes in MG patients classified as seronegative. For this, adequate methods for quantifying changes in muscle function and NMJ architecture must be developed.

OBJECTIVES

The general objective for this chapter was to develop platforms for the differentiation and analysis of human muscle cells, which could sustain long-term culture and give rise to mature muscle fibers with contractile activity. The final application of these platforms is to be able to measure differences in muscle function and associated biomarkers when modeling the conditions of muscular diseases such as myasthenia gravis.

1. First, we sought to optimize 2D culture of human myoblast cell lines using a system with hydrogel overlays to improve maturation and reduce myotube detachment.
 - 1.1. Determine the best hydrogel composition for differentiation in terms of sarcomere formation.
 - 1.2. Determine the best hydrogel composition in terms of contractile functionality.
2. Next, we wanted to obtain a 3D culture system that could sustain long-term culture of human myoblasts and promote maturation and alignment of muscle cells.
 - 2.1. Reproduce results of a previously established 3D model with C2C12 cells, which uses free-floating muscle constructs in PDMS devices, and use it for culturing human myoblasts.
 - 2.2. Develop a simple 3D platform with VELCRO™ fabric anchors, as an alternative to PDMS pillars which are more difficult to manufacture.
 - 2.2.1. Optimize culture conditions and hydrogel composition for optimal alignment, expression of differentiation markers, and contractile ability of the muscle cells in response to electrical stimulation.
 - 2.2.2. Establish a suitable calcium analysis method to quantify muscle function in response to chemical stimulation.
 - 2.2.3. Use ChR2⁺ human myoblasts to enable optical stimulation.
3. Finally, we wanted to use the established culture platforms to evaluate the effect of myasthenia gravis patient autoantibodies on muscle function and endplate presence.
 - 3.1. Demonstrate that patient autoantibodies colocalize with endplates in 2D and 3D cultures.
 - 3.2. Determine whether anti-AChR and anti-MuSK antibodies present in patient serum or isolated IgG fractions can alter muscle function when analyzed by calcium imaging. Functional analysis should be combined with microscopic analysis of endplates after treatment.

MATERIALS AND METHODS

Human myoblast cell lines and maintenance

All immortalized human myoblast cell lines (**Table 1**) were maintained in Skeletal Muscle Cell Growth Medium (C-23160, PromoCell, abbreviated as SGM) supplemented with 1% penicillin/streptomycin (P/S, ThermoFisher), in a humidified 37°C 5% CO₂ cell culture incubator. Cells were defrosted by thawing quickly in a 37°C water bath and adding the contents of the cryovial to 9 ml of room temperature (RT) cell culture medium. Then, cells were centrifuged for 5 minutes at 800 rpm, and the pellet was resuspended in 1 ml of SGM and seeded in a T-75 flask containing 12 ml of SGM. Defrosting was performed in the afternoon and medium was replaced the next morning. Thereafter, cells were passaged into new T-75 flasks when a maximum of 60-70% confluence was reached, to avoid differentiation by contact. Cell passaging was performed by washing cells in sterile PBS (without Ca²⁺ and Mg²⁺) and incubating with 1X trypsin-EDTA solution (Gibco) for 2-3 minutes inside the incubator. Then, trypsin was inactivated using myoblast inactivation medium, prepared with Dulbecco's Modified Eagle Medium, high glucose, pyruvate (DMEM 41966-029, Life Technologies) containing 10% FBS (10500064, Invitrogen) and 1% P/S. Cells were centrifuged at 800 rpm for 5 minutes, and the pellet was resuspended in fresh SGM for replating into new flasks. Medium was changed every 2-3 days.

Table 1. Immortalized human myoblast cell lines

Cell line	Origin	Provided by	Citations
LHCN-M2	Healthy human pectoralis major muscle	Adolfo López de Munain (Grupo de Enfermedades Neuromusculares, Biodonostia Health Research Institute, Donostia)	(Zhu et al., 2007)
AB1079	Healthy human quadriceps muscle	Eduard Gallardo (Neuromuscular BCN, Hospital de Santa Creu i Sant Pau, Barcelona)	(Bruge et al., 2022; Mamchaoui et al., 2011)

8220	Healthy human paraspinal muscle	Adolfo López de Munain (Grupo de Enfermedades Neuromusculares, Biodonostia Health Research Institute, Donostia)	(N. Rose et al., 2023)
------	---------------------------------	---	------------------------

C2C12 myoblast maintenance

C2C12 (ATCC) cells are an immortalized myoblast line derived from mouse satellite cells. Cells were maintained for no more than 14 passages, in a 37°C 5% CO₂ cell culture incubator. Growth medium was composed of DMEM (11965, Gibco) which was supplemented with 10% fetal bovine serum (FBS), 1M HEPES, 100 units/mL penicillin, and 100 µM streptomycin. Cells were passaged into new T-75 flasks when a maximum of 70-80% confluence was reached, to avoid differentiation by contact. Cell passaging was performed by washing cells in sterile PBS (without Ca²⁺ and Mg²⁺) and incubating with 1X trypsin-EDTA solution (Gibco) for 2-3 minutes inside the incubator. Then, trypsin was inactivated using maintenance medium. For differentiation experiments, the differentiation medium consisted of DMEM (11965, Gibco) containing 2% normal horse serum (NHS, 26050088, ThermoFisher), 100 units/mL penicillin, 100 µM streptomycin, and 1M HEPES.

2D differentiation protocol with hydrogel overlays

2D differentiation was performed by adapting a protocol published in Toral-Ojeda et al., 2018. Myoblasts were seeded on glass coverslips coated with 0.5% gelatin and allowed to reach maximum confluence. Then, an overlay of soft hydrogel about 1 mm in height was applied on top of the cells. For a 24-well or 4-well plate, 200 µl of hydrogel were added to each well. The tested hydrogels were the following: Corning® Matrigel® Growth Factor Reduced (GFR) Basement Membrane Matrix, 8 mg/ml (354230, Corning) diluted 1:3 in DMEM, ECM gel GF reduced (E6909, Sigma Aldrich) 1:3 in DMEM, or VitroGel® 3D (TWG001, The Well Biosciences) 1:3:1. Then, differentiation medium is added according to the cell type. Myotubes begin to emerge around day 3-4 and contractile activity is observed after 13-21 days, depending on the cell line. In **Figure 14**, a general overview of relevant stages in the differentiation process can be found.

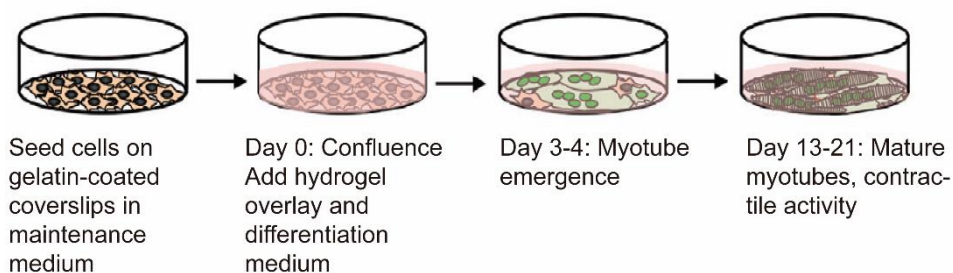


Figure 14. 2D differentiation protocol and relevant timepoints.

LHCN-M2 and 8220 differentiation protocol

After reaching maximum confluence (necessary for cell fusion), cells were switched to a first differentiation medium, DM1. This medium was replaced by DM2 upon the first observation of myotube formation, which usually occurred after 3-4 days. Then, DM2 was used until day 13 of differentiation, at which contraction started to be visible. Half of the medium was changed every 3 days. Composition of DM1 and DM2 can be seen in **Table 2** and **Table 3**, respectively.

Table 2. DM1 medium composition.

Component	Final concentration
DMEM (41966-029 Life Technologies)	-
Insulin (I6634, Sigma Aldrich)	10 μ g/ml
ApoTransferrin (T1147, Sigma)	100 μ g/ml
Gentamycin (15750-037, Life Technologies)	50 μ g/ml

Table 3. DM2 medium composition.

Component	Final concentration
Neurobasal A (10888-022 Life Technologies)	-
B27 (17504-044 Life Technologies)	1x
GlutaMAX (35050-038 Life Technologies)	1x
BDNF (450-02 Peprtech)	20ng/ml
Shh (1845-SH-025 R&D systems)	50ng/ml
IGF-1 (4326-RG-050 R&D systems)	10ng/ml
CNTF (557-NT-010 R&D systems)	5ng/ml
NT-3 (450-03-A Peprtech)	20ng/ml
Laminin (23017-015 Life Technologies)	4 μ g/ml
Agrin (550-AG-100 R&D systems)	100ng/ml
Gentamycin (15750-037 Life Technologies)	50 μ g/ml

AB1079 differentiation protocol

AB1079 myoblasts were differentiated in the medium shown in **Table 4**. Half of the medium was changed every 3 days for 2D differentiation or every 2 days for 3D differentiation. In 2D, contraction was observed at 19-21 days, which is longer than the necessary time for LHCN-M2 in the same culture system.

Table 4. AB1079 differentiation medium composition

Component	Final concentration
DMEM (41966-029 Life Technologies)	3 parts
M199 (BE12-119F, Cultek)	1 part
Glutamine 200 mM (25030-024, Invitrogen)	1%
Insulin (I6634, Sigma Aldrich)	10 μ g/ul
FBS (10500064, Invitrogen)	2%
Agrin (550-AG-100, R&D systems)	100 ng/ml
P/S (15140122, Invitrogen)	0,9%
Fungizone (15290-026, Invitrogen)	0,1%

Electrical stimulation of 2D differentiated muscles

Coverslips with myotubes and hydrogel were carefully transferred to a 35 mm \varnothing Petri dish with differentiation medium. The outline of the coverslip was cut out using a pipette tip before seizing the coverslip with fine tweezers, in order to avoid detachment of the hydrogel from the coverslip. The lid of the Petri dish was modified to incorporate two graphite electrodes in parallel disposition. Electrodes were sterilized in 70% EtOH for 15 minutes and washed in sterile Milli-Q® water. Then, electrodes were connected to a pulse generator (Aim-TTi, TG2512A) using alligator clips, and the pulse generator was coupled to an oscilloscope. An image of the stimulation setup can be seen in **Figure 20**. The Petri dish was positioned on the stage of an inverted microscope (Olympus IX71) to record videos lasting 1 minute, at 40 fps and 20x magnification. Pulses were applied at 5-10 V with 5-10 ms of pulse duration. Different frequencies were tested (1 Hz, 2Hz, 5 Hz), as well as monophasic or biphasic pulses. Time-lapse videos were analyzed using the MUSCLEMOTION plugin for ImageJ (Sala et al., 2017), or with MotionGUI software for Matlab (Huebsch et al., 2015).

Immunostaining of 2D muscles

For immunostaining of 2D samples, cells were fixed by addition of one volume of 4% paraformaldehyde solution in PBS (PFA 4%) to the cell culture medium. If samples had a hydrogel overlay, fixation was performed at room temperature to avoid depolymerization of Matrigel. Otherwise, fixation was performed on ice. After 5 minutes in a final concentration of 2% PFA, liquid was aspirated carefully to avoid detaching cells and 4% PFA was added. Cells were fixed for a further 25-30 minutes and washed three times with PBS for 5 minutes each. Then, cells were permeabilized for 15 minutes using PBS with Triton X-100 0.1% (PBS-Triton 0.1%). For blocking, cells were blocked for 1 hour at room temperature (RT) in PBS-gelatin 0.2% containing 10% FBS and 0.1% Triton with gentle shaking. Then, cells were washed 3 x 5 minutes in PBS-Triton 0.1% and incubated with primary antibody solution overnight (O/N) at 4°C with gentle shaking. The primary antibody was diluted in PBS-gelatin 0.2% containing 10% FBS and 0.1% Triton. Primary antibody dilutions can be seen in **Table 7**. The next day, cells were washed 3 x 5 minutes in PBS-Triton 0.1% and incubated for 2 hours with a secondary antibody and fluorescent marker solution composed of the same buffer as the primary antibody solution. This step was performed at RT with shaking and protected from light thereafter. A list of fluorescent markers and secondary antibodies can be seen in **Table 6** and **Table 8**. Finally, cells were washed 3 x 5 minutes in PBS-Triton 0.1% and 3 x 5 minutes in PBS. Coverslips were mounted on microscope slides using Mowiol® 4-88 (475904, Calbiochem) and allowed to harden at least for 48 hours at 4°C.

MG serum stainings using 2D cultures

For evaluating binding of patient autoantibodies to endplates, patient serum was added as if it were primary antibody, at a 1:50 dilution. The rest of the 2D staining protocol was performed as described above. Staining of human autoantibodies was performed using fluorescent anti-human antibodies from **Table 8**, and combined with BTX staining to counterstain endplates.

Generation of ChR2⁺ and GCaMP6⁺ stable cell lines

For stable transfection of muscle cell lines, the following lentiviral vectors (LV) were employed: For ChR2 expression, the vector pLenti-EF1 α -hChR2(H134R)-EYFP-WPRE (Addgene Plasmid #20942) was used, which contains an enhanced yellow fluorescent

protein (eYFP) reporter. For GCaMP6s expression, pRRL-MHCK7-GCaMP6 (Addgene Plasmid #65042) was chosen as it encodes a muscle-specific promoter, MHCK7. Lentiviral particles were produced with the packaging plasmids psPAX2 (Addgene Plasmid #12260) and pMD2.G (Addgene Plasmid #12259), using HEK293FT as a viral production cell line. Lentiviral production was performed in the virus room of the PCB (Parc Científic de Barcelona) cell culture facilities. Appropriate virus concentration for infection was determined by testing different dilutions in myoblast cultures and choosing the minimum amount of virus required to observe GFP fluorescence.

Human muscle cell lines (AB1079, LHCN-M2, and 8220) were infected with LV (1:500 dilution) for 24 h. Cells were maintained and passaged for 7 days to allow for visible expression of eYFP or GCaMP6, and subsequently sorted using fluorescence-activated cell sorting (FACS) from the Scientific services of the University of Barcelona. Sorting was performed at room temperature, with the goal to obtain approximately 100.000 positive cells for reseeded in each sort. Positive cells were amplified and stored in liquid nitrogen for future use. Presence of GFP in GCaMP6⁺ cell lines was confirmed by Western Blot using rabbit anti-GFP antibody (A11122, Invitrogen).

3D free-floating platform

A free-floating muscle construct method based on the protocol from Osaki, Sivathanu, et al., 2018 had been previously established in our laboratory to culture C2C12 myoblasts in combination with spinal cord explants. This method uses polydimethylsiloxane (PDMS) (Sylgard 184, Dow Corning) devices with a seeding channel and a central opening. The dimensions of the device are 2 x 2 cm (long x wide), and 0.8 cm high. The central opening is 7 mm in diameter, and the seeding channel is formed by introducing a 21G hypodermic needle into the mold during PDMS casting. PDMS were adhered to round glass coverslips by oxygen plasma bonding and sterilized by autoclaving. On the day of seeding, the central opening was filled with a 5% gelatin (G9391, Sigma Aldrich) solution (prepared in C2C12 maintenance medium and filter sterilized), while introducing a new 21G needle into the channel. The devices were left on ice to solidify the gelatin solution during trypsinization of myoblasts (**Figure 15**).

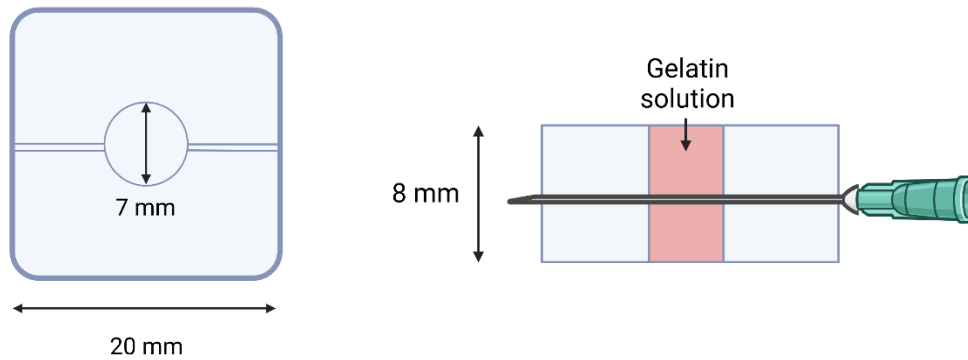


Figure 15. PDMS device dimensions and addition of gelatin solution or cell culture medium into the central opening.

Myoblasts were trypsinized and counted. Then, they were seeded into the channel at a density of $3.5 \cdot 10^6$ cells/ml in a plasma clot mixture. The plasma clot was made using Chicken Plasma (P3266, Sigma Aldrich) and Thrombin from bovine plasma (T4648, Sigma Aldrich). Cell pellets were resuspended in 200 μ l of chicken plasma and kept on ice thereafter. Then, 200 μ l of thrombin solution was added and quickly mixed. Thrombin solution was previously diluted from 100 U/ml to 30U/ml using Hank's balanced salt solution (14175053, ThermoFisher). Shortly after mixing the thrombin solution, a small needle and 1 ml syringe were used to aspirate the mixture. Then, the needle was removed and exchanged for the 21G needle inside the PDMS device. The syringe was slowly retracted from the seeding channel while expelling the cell-plasma mixture, in order to fill the whole channel. Remaining cell suspension was used to create small caps at the ends of the channel to fix the construct during differentiation (**Figure 16**).

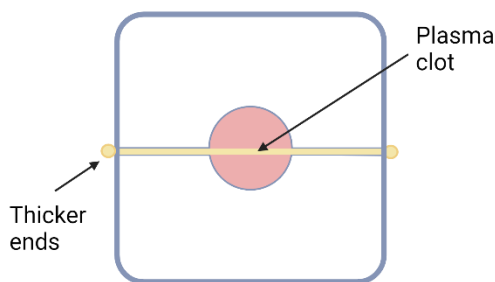


Figure 16. Plasma clot with myoblasts inside the PDMS device. Note the thicker ends on the sides of the channel.

The plasma mixture was allowed to clot for 5 minutes at room temperature inside the solidified gelatin channel. Then, devices were transferred to the incubator for at least 10 minutes to liquefy the gelatin solution. This solution was removed and exchanged for

C2C12 differentiation medium. Devices were placed inside 35 mm Ø Petri dishes and cell culture medium was added to the outside of the device as well. Cells were maintained for 3 days as a free-floating construct, and then pure Matrigel was added to the central opening to embed the construct. Following this, cells were maintained for as long as the constructs remained intact, or until spontaneous contraction was observed. Differentiation medium was exchanged every other day.

3D anchored platform for muscle cell culture

A detailed, step-by-step version of the protocol for this method can be found in Wells-Cembrano et al., 2022.

Culture device preparation

First, the VELCRO™ anchors were prepared and adhered to cell culture dishes as shown in **Figure 17**. Anchors had an arrow shape, with different dimensions according to the size of the cell culture dish. For 35 mm Ø Petri dishes, the dimensions of the square portion were 4 x 4 mm with 2 cm of arrow length. For 4-well plates, the arrows were 3 x 3 mm with 1.5 cm of arrow length. To draw the region in which the anchors were to be adhered, lines were drawn with a permanent marker on the underside of the dish, using a stencil for comfort. For 35 mm Ø Petri dishes, this distance was 1.2 cm, and for 4-well plates it was 0.6 cm. The anchors were adhered as shown in **Figure 17C**, using PDMS glue (Sylgard 184, Dow Corning). The PDMS glue was prepared by mixing elastomer and curing agent at a 10:1 ratio, with degassing for 1 hour in a vacuum dessicator to remove bubbles. PDMS glue was applied using a small spatula, and anchors were aligned to the markings on the Petri dish. Plates were left to cure O/N at minimum. Excess PDMS glue was stored at -20°C for future use.

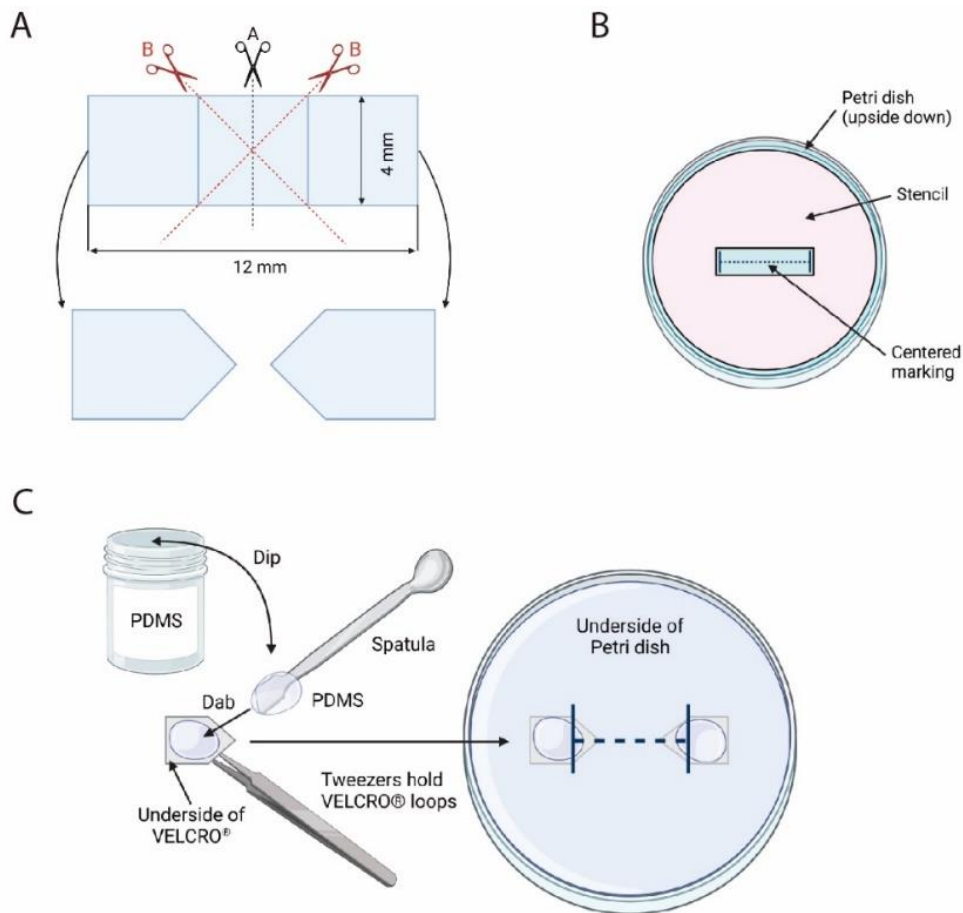


Figure 17. Preparation of VELCRO™ devices. A. Cutting of VELCRO™ pieces. B. Marking of Petri dish with a centered 1.2 cm line using a stencil. C. Adhesion of VELCRO™ pieces to Petri dishes with PDMS glue.

Sterilization and coating

Plates were sterilized on the day of cell seeding by submerging the whole plate or well in 70% EtOH for 15 minutes. After that time, plates were washed 3 times with PBS. Without aspirating the last PBS wash, UV light was applied to the plates for 15 minutes. Then, PBS was aspirated, and plates were left to dry in the incubator for approximately 1 hour to dry them completely before coating. Then, plates were coated with filtered 0.2% Pluronic® F-127 solution in Milli-Q® water (P2443, Sigma Aldrich). To perform the coating, a fine flat paintbrush was used, which was sterilized by submerging in 70% EtOH for 15 minutes and drying by evaporation or aspiration with the vacuum. The paintbrush was dipped in Pluronic® solution and the region between both anchors was covered in a layer of liquid (**Figure 18**). Plates were left in the incubator for a minimum of 1 hour. After this time, the coating solution has evaporated, and does not require washing.

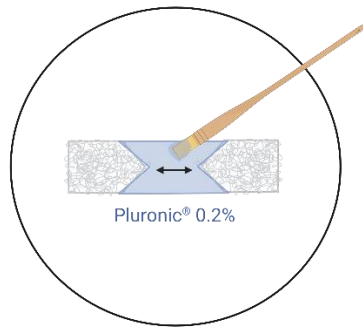


Figure 18. Pluronic® coating procedure using a fine paintbrush.

Preparation of hydrogel components

For Matrigel-Fibrin constructs, the necessary components were prepared as follows. First, fibrinogen (F8630, Sigma Aldrich) solution (8 mg/ml) was prepared in sterile PBS by adding fibrinogen powder layered over an appropriate volume of warm PBS in a Falcon tube. The tube was left to rest in a 37°C water bath until fibrinogen was dissolved, and the solution was sterile-filtered and kept on ice until use. This solution was prepared fresh for every seeding. Thrombin from bovine plasma (T4648, Sigma Aldrich) was prepared as a 100 U/ml stock solution according to the manufacturer's instructions and stored at -20°C. On the day of seeding, a use solution was prepared by diluting the stock solution 1:5 in HBSS (14175046, ThermoFisher) and kept on ice thereafter. This yielded a use concentration of 20 U/ml. Matrigel Growth Factor Reduced (GFR) Basement Membrane Matrix (356230, Corning) was defrosted O/N on ice kept at 4°C.

Cell seeding procedure

For amplification of human myoblasts in larger amounts for seeding, T-175 flasks were used. Cells were harvested by trypsinization and pooled in a T-175 flask for counting with a hemocytometer. The seeding density was $1 \cdot 10^6$ cells/ml of hydrogel solution. Therefore, for each 35 mm Ø Petri dish construct, $3 \cdot 10^6$ cells were needed (300 µl hydrogel), compared to $1 \cdot 10^6$ cells per 4-well construct (100 µl hydrogel). Cell suspension was added to separate Falcon tubes (in amounts sufficient for seeding one or two constructs at a time) and centrifuged at 800 rpm for 5 minutes. The supernatant was aspirated, and cells were kept on ice thereafter. Then, Matrigel-Fibrin hydrogel was prepared as shown in **Table 5**. Fibrinogen and Matrigel GFR were mixed by gently pipetting 10 times, and thrombin was added quickly with a small pipette and quickly mixed with a larger volume pipette.

Table 5. Matrigel-Fibrin hydrogel preparation

Component	Stock solution	Order of addition	% of final volume
Fibrinogen	8 mg/ml	1	50%
Matrigel GFR	7.2-9.4 mg/ml	2	40%
Thrombin	20 U/ml	3	10%

For Matrigel-Collagen constructs, the composition and preparation instructions detailed in (Van Der Schaft et al., 2013) were used. In our laboratory, we used Rat tail collagen I solution in 0.02% acetic acid acetic acid (354236, Corning), which had a stock concentration of 3.3mg/ml. The amount of NaOH 1M needed to adjust the pH was modified according to the datasheet for this product.

For seeding of the hydrogel onto VELCRO™ anchors, the order of pipetting shown in **Figure 19** was used to correctly distribute the mixture. First, hydrogel-cell mixture was pushed into VELCRO™ loops. Second, anchors were connected using more hydrogel-cell mixture, and finally the outer edges of the anchors were covered in the mixture as well. The seeded constructs were left to rest at RT for 5 minutes and gelified in the incubator for a minimum of 10 minutes and a maximum of 30 minutes. Fibrin-thrombin clot formation is rapid, but an additional time was allowed to ensure complete gelification. Then, SGM was carefully added to the plates and they were returned to the incubator.

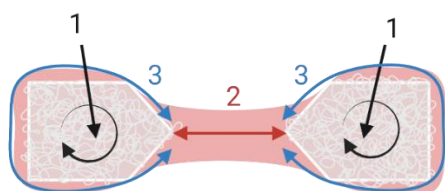


Figure 19. Cell-hydrogel mixture seeding procedure, with order of pipetting shown as numbered steps.

Differentiation protocol

For differentiation of muscle constructs, cells were kept in SGM for 2 days before adding differentiation medium, to allow distribution and proliferation of cells inside the gel. Then, differentiation medium was added and changed 3 times per week. Before and after weekends, medium was completely changed, while on Wednesdays only half of the medium was changed. In the case of AB1079 cells, differentiation was performed for 14

days, up to a maximum of 21 days. All differentiation media contained 1 mg/ml 6-aminocaproic acid (6-ACA) as a fibrinolysis inhibitor (A2504, Sigma Aldrich). 100 mg/ml 6-ACA stock solution was prepared and frozen at -20°C .

Electrical stimulation

For muscle constructs generated with VELCRO™ anchors in 35 mm Ø Petri dishes, electrical stimulation was performed using the same setup used to stimulate myotubes on 2D coverslips. The lid of the muscle construct dish was replaced by the lid modified with graphite electrodes, as shown in **Figure 20**. Electrical pulses were applied at 10 V, with a 10 ms pulse duration and 1 Hz frequency. Videos were recorded using an inverted microscope (Olympus IX71). Recordings were 1 minute long, at a 40 fps frame rate and 20x magnification. Stimulation was initiated at $t = 10$ s. Contraction data was processed using the MUSCLEMOTION plugin for ImageJ (Sala et al., 2017).

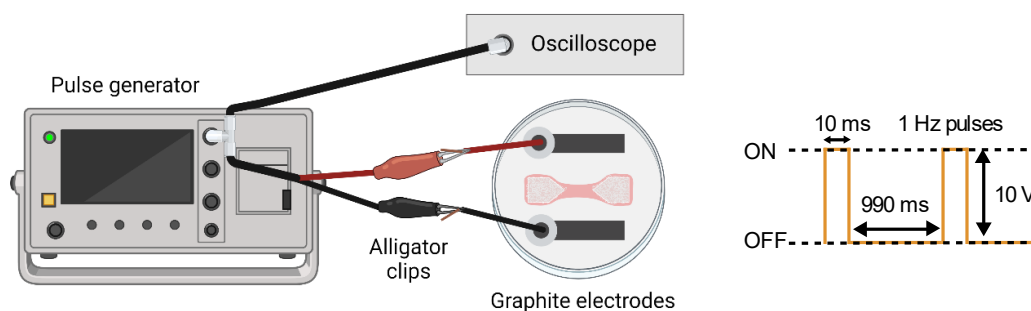


Figure 20. Electrical stimulation setup with graphite electrodes connected to a pulse generator and an oscilloscope. Pulse parameters shown on the right side.

ChR2⁺ constructs were stimulated using a coolLED pE-300 illumination system coupled to an inverted microscope (i.e., Olympus IX71) to visualize the muscle contraction. The TTL control of the illumination system allows for the delivery of precisely timed sequences of light. The TTL can be directed to an Arduino-UNO™ microcontroller pulse generator or alternatively a PulserPlus generator and Pulser v3.1 software (Prizmatix, Israel). The average light intensity with this setup is $\approx 20\text{-}25$ W/cm², measured at the culture dish with a Newport 1919 optical power meter (Newport Photonics, USA). Pulses of 5 ms at a frequency of 20 Hz were delivered in trains of 1 s ON and 1 s OFF for a total duration of 1 minute (**Figure 21**). Contractions were imaged in brightfield and processed using the MUSCLEMOTION plugin for ImageJ.

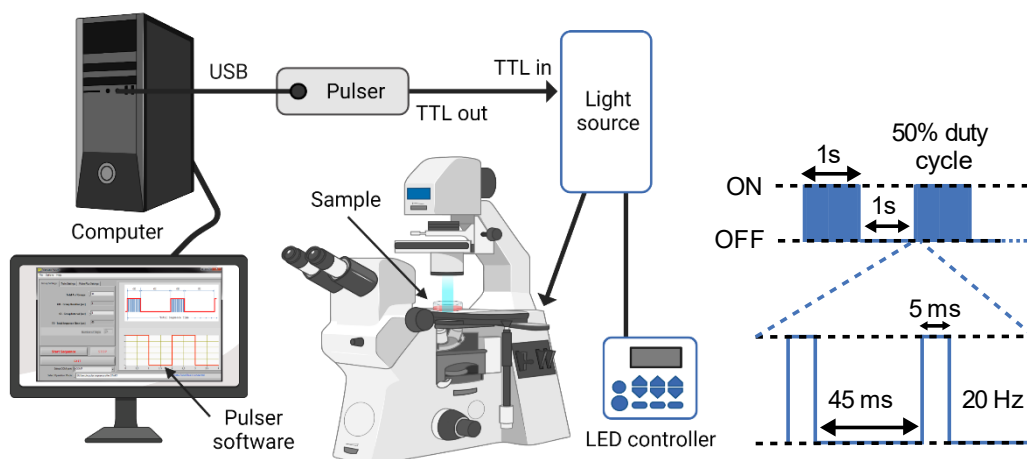


Figure 21. Optical stimulation setup and pulse regimen.

Fluo-4 AM loading

Fluo-4 AM (F14217, Thermo Fisher) was prepared according to the manufacturer's instructions. On the day of imaging, cells were washed with pre-warmed phenol red-free DMEM (21063029, Thermo Fisher) three times. Then, 10 μ M fluo-4 AM in phenol red-free DMEM was added, using just enough solution to cover the muscle bundle. Loading was performed in the incubator for 1 hour. After loading, cells were washed 3 more times in phenol red-free DMEM. For deesterification of fluo-4, cells were allowed to sit at RT for 15 minutes and in the incubator for 15 more minutes. Imaging was performed as quickly as possible after deesterification to maintain cell viability and fluorescence intensity. If performing multiple replicates in the same day, staggered loading and imaging would be recommended.

Calcium recordings and chemical stimulation

For calcium imaging in muscle constructs stained with fluo-4, magnification was set to 20X to distinguish individual cells, and the acquisition time was set to 100 ms (10 fps). For GCaMP6⁺ constructs, imaging was performed at 5 fps (200 ms/frame) to account for the lower basal fluorescence, and 4x magnification to view global calcium increases in the whole construct. In both cases, the resolution was 1024 x 1024 px, 16-bit. Recordings were typically 2-10 minutes long, consisting of a 10-30 second period in which spontaneous activity was recorded, followed by the addition of 100 μ M ACh to elicit calcium release. This induced activity was recorded for the remaining time of the video. In some cases, 100 mM KCl was added in the last 30 seconds of video as a positive

control of non-ACh-dependent depolarization. ACh solution was prepared on the same day of recording, at 100x concentration in DMEM 41966-029 (Life Technologies) from acetylcholine chloride (A6625, Sigma) and sterile filtered. Recordings were performed at room temperature; therefore, when using 4-well plates, plates were alternated between recordings to ensure each plate was only outside the incubator for 5-minute periods. If it was necessary to maintain the cells after recording, the plates were washed once in DMEM 41966-029 to remove excess ACh, and new differentiation medium was added.

Immunostaining of muscle constructs

Muscle constructs were fixed by adding an equal volume of 4% paraformaldehyde (PFA) to the cell medium (thus obtaining a final concentration of 2% PFA) for 5-10 minutes. Then, liquid was aspirated and 4% PFA solution was added, and fixation was performed at room temperature for 30-60 minutes (to avoid depolymerization of Matrigel on ice). Cells were washed with phosphate-buffered saline 0.1 M (PBS) 3x10 minutes. Then, blocking was performed using PBS-gelatin 0.2% containing 10% FBS and 0.5% Triton X-100 (Triton) for 5-6 hours at RT on a shaker. Constructs were then detached from VELCRO™ anchors with a scalpel and transferred to a 12-well or 24-well plate (**Figure 22**).

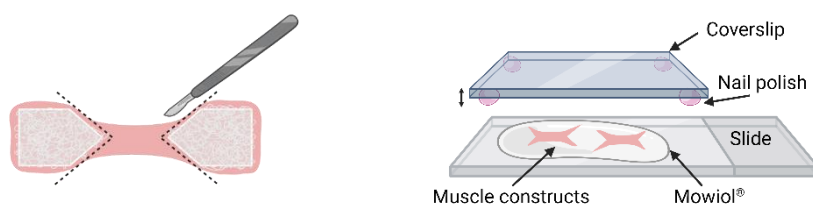


Figure 22. Detachment of muscle bundles from VELCRO™ anchors using a scalpel, and mounting procedure with nail polish-modified coverslips.

Construct fragments were washed twice in PBS-Triton 0.5% before adding primary antibody solution, prepared in PBS-gelatin 0.2% containing 5% FBS and 0.5% Triton. The primary antibody was incubated for 3 overnights (O/N) at 4°C with gentle shaking. Then, washing was performed in PBS-Triton 0.5% for 3x10 minutes. Then, secondary antibody solution and other fluorescent markers were added, diluted in the same antibody buffer as the primary antibody. Incubation was performed for 5-6 hours at RT on a shaker, protected from light. Constructs were washed 3x10 minutes in PBS-Triton 0.5% and 3x10 minutes in PBS. Finally, constructs were mounted using a fine paintbrush to transfer them to a microscope slide, and excess buffer was dried off with filter paper. Mowiol® 4-88

(475904, Calbiochem) was added on top of the constructs and slides were sealed with 24x50 mm coverslips modified with nail polish drops on the corners to create space for the construct height (**Figure 22**). Slides were allowed to harden for at least 48 hours before imaging.

Table 6. Fluorescent markers used for muscle cell staining

Fluorescent marker	Dilution	Reference
α -Bungarotoxin, Alexa Fluor™ 555 conjugate (BTX 555)	1:500	B35451, ThermoFisher
Hoechst 34580 nuclear dye	1:200	H21486, Life Technologies

Table 7. Primary antibodies used for muscle cell staining

Primary antibody	Origin	Dilution	Reference
Anti-MuSK	Rabbit polyclonal	1:50	PA1-1741, Invitrogen
Anti-Myosin heavy chain (Skeletal Fast)	Mouse monoclonal	1:400	M4276, Sigma Aldrich
Anti-Sarcomeric alpha-actinin (SAA)	Mouse monoclonal	1:200	A7811, Sigma Aldrich

Table 8. Secondary antibodies used for muscle cell staining

Secondary antibody	Origin	Dilution	Reference
Anti-mouse 488	Goat	1:500	A11029, Invitrogen
Anti-mouse 568	Goat	1:500	A11031, Invitrogen
Anti-mouse 633	Goat	1:500	A21052, Life Technologies
Anti-rabbit 633	Goat	1:500	A21070, Life Technologies
Anti-Human IgG (H+L) 488	Goat	1:500	A11013, Life Technologies
Anti-Human IgG (H+L) 633	Goat	1:500	A21091, Life Technologies

Processing of fluo-4 calcium recordings with ImageJ

For fluo-4 recordings, which were performed at 20X magnification focusing on individual cells, ROIs and fluorescence information were analyzed using ImageJ. First, recordings were opened in ImageJ and cells that responded to stimulation were visually identified. Using the ROI manager tool, 5-10 ROIs were defined using the polygon selection tool, as shown in **Figure 23**.

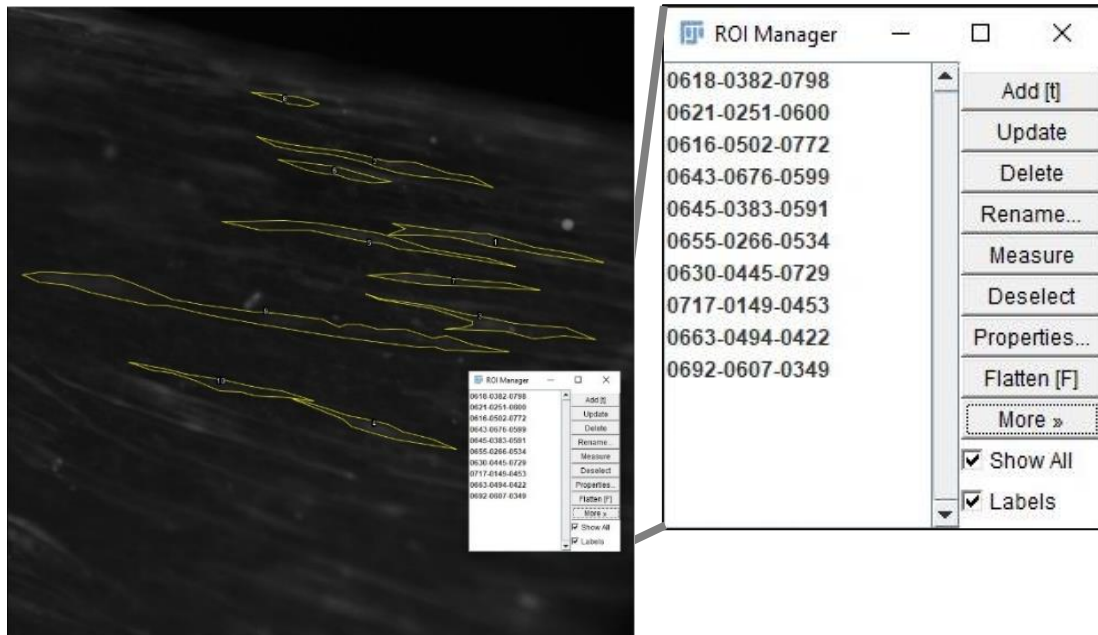


Figure 23. Example of 10 ROIs selected with the ImageJ ROI manager.

Next, the mean intensity of each ROI was measured over time using Analyze > Set Measurements > “Mean gray value” and the More > Multi Measure option of the ROI manager. Menus are shown in **Figure 24**. Results were copied to an Excel file for analysis.

To obtain the background fluorescence (F_0), the time lapse recording was converted to an average intensity projection using the Image > Stacks > Z project and selecting “Average Intensity”. This Z projection (or time projection) was used to select a ROI containing only background, with any of the ROI selection tools. The Analyze > Measure option was used to measure the mean gray value of the background ROI, and this value was saved as F_0 (**Figure 25**).

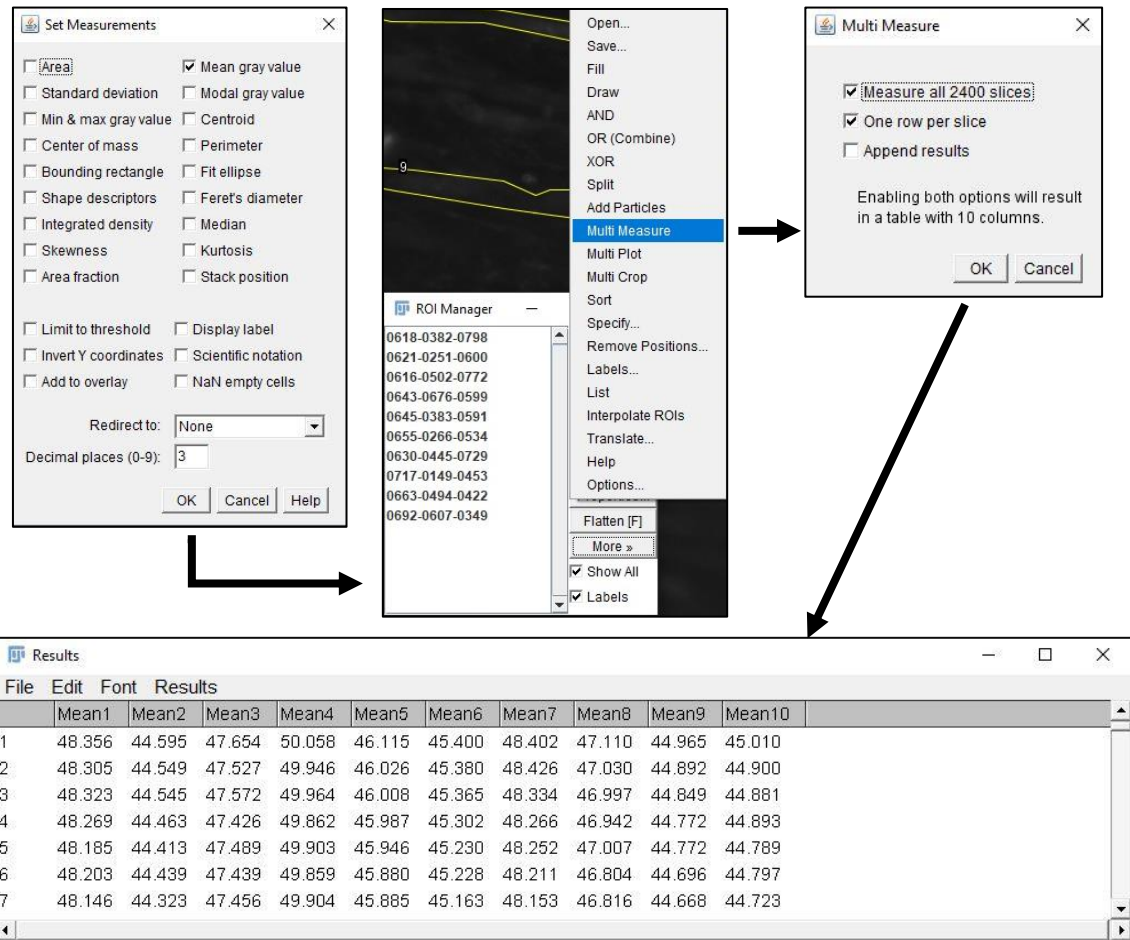


Figure 24. Measurement options, multi measure tool and options, and results of mean gray value measurement.

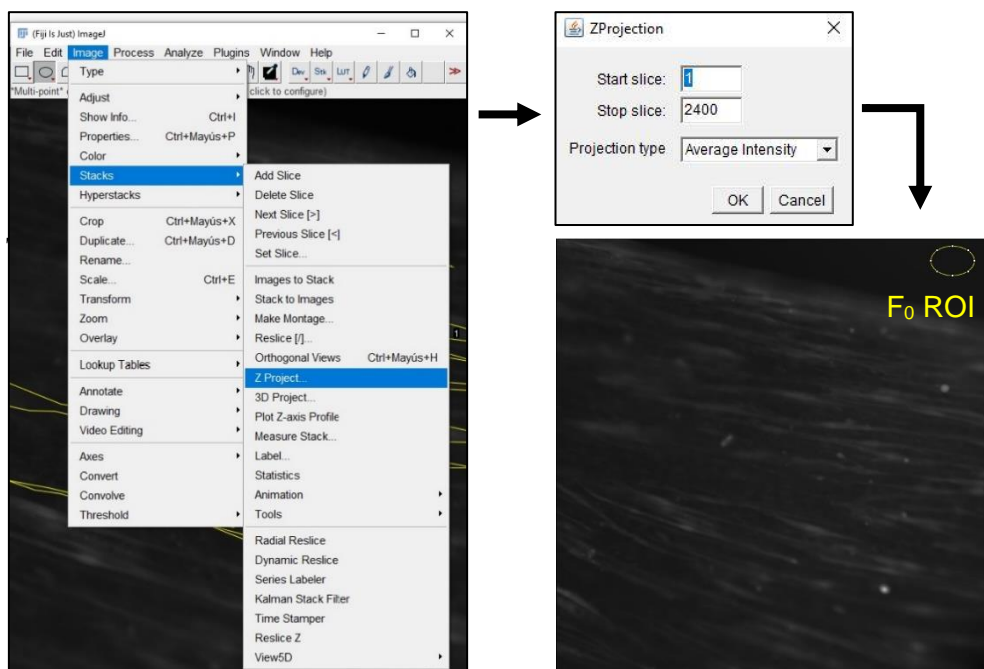


Figure 25. Options to select for generating an average intensity Z Project and selecting a background ROI to extract F_0 .

Once all the fluorescence data was extracted for each timepoint, normalized fluorescence was calculated for each timepoint and each ROI. Background fluorescence (F_0) was subtracted from each fluorescence (F) value to calculate the increase in fluorescence in relation to background fluorescence (ΔF). Then, this value was normalized to F_0 as shown in **Figure 26**.

$$\frac{\Delta F}{F_0} = \frac{F - F_0}{F_0}$$

Figure 26. Formula for calculation of normalized fluorescence.

The $\Delta F/F_0$ data was then plotted using GraphPad Prism 8.4.3 to show calcium traces over time.

Processing of GCaMP6 calcium recordings with Netcal

Calcium recordings were saved as uncompressed .avi files at 5 fps and processed using Netcal for Matlab (Orlandi et al., 2017). In Netcal, Preprocessing was set to standard with “Fast” settings, and ROIs were defined using the Supervised ROI detection mode. Using this mode, a 2x2 grid was defined to separate the image into 4 ROIs (**Figure 27**). Then, traces were extracted and smoothed. Finally, traces were exported into a .csv file, which contained $100 \times \Delta F/F_0$ data for each timepoint and each ROI. The maximum $100 \times \Delta F/F_0$ was extracted for each ROI, and the mean of all ROIs was calculated for each construct. The means before treatment and after treatment were divided to obtain the after/before fold change ratio of maximum $100 \times \Delta F/F_0$.

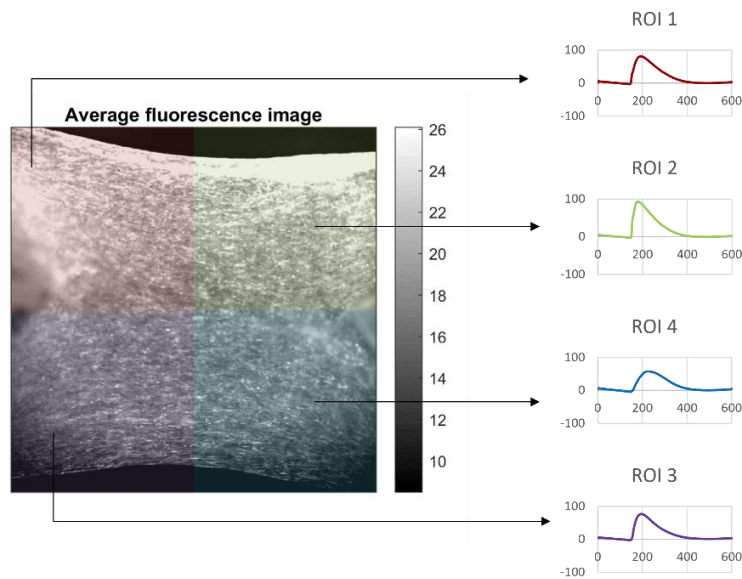


Figure 27. Separation of images into 4 ROIs to account for wave propagation of calcium transients.

Western blot of muscle constructs

Muscle constructs were separated from VELCRO™ anchors using a scalpel and transferred to an eppendorf tube. Constructs were frozen at -80°C until lysis, which was carried out using $100\ \mu\text{l}$ of RIPA buffer ($0.01\ \text{M}$ Tris-HCl $\text{pH}=7.3$, 10% SDS, 0.2% Triton X-100, $0.15\ \text{M}$ NaCl) for each 4-well size construct, or $300\text{-}400\ \mu\text{l}$ for each $35\ \text{mm}$ \varnothing dish-size construct. Lysis was allowed to proceed for $30\text{-}60$ minutes on ice, on a shaker. Then, the muscle fragments were pooled to reach a minimum of $200\ \mu\text{l}$ for sonication. Sonication was performed using four 2-second pulses at 50% amplitude and repeating once after 5 minutes of waiting to reduce bubble formation. After sonication, the lysate was centrifuged at $16000\times g$ for 20 minutes at 4°C , and the supernatant was recovered in a new eppendorf tube. Protein concentration was measured by Pierce™ BCA assay (23227, ThermoFisher) using a $1:10$ dilution of each sample. Western blot samples were prepared by adding Laemmli Buffer 2x (S3401, Sigma Aldrich) to the lysate and denaturing for 5 minutes at 95°C . Then, $20\ \mu\text{g}$ of protein were loaded onto SDS-PAGE gels. As an alternative and more rapid lysis method, muscle constructs were lysed directly in Laemmli Buffer 2x and boiled for 10 minutes at 95°C . Lysates were centrifuged at $14000\ \text{rpm}$ for 5 minutes prior to loading to prevent loading of viscous components such as DNA or remaining hydrogel. This method also allowed for more complete recovery of muscle proteins compared to RIPA-based lysis and centrifugation.

For Western Blot, samples were loaded on 8 or 10% acrylamide SDS-PAGE gels and electrophoresis was performed at a constant voltage. 90 V were applied during the stacking gel phase and 120 V during the resolving gel period. Then, proteins were transferred to nitrocellulose membranes using wet transfer in methanol-containing transfer buffer, keeping the cassettes at 4°C during transfer (100 V applied for 1 hour). The membranes were then blocked in 5% fat-free milk in Tris-buffered saline supplemented with 0.1% Tween 20 (TTBS) and 2% FBS for 1 hour at RT. Membranes were probed with primary antibodies diluted in TTBS, overnight at 4°C on a shaker (see antibodies in **Table 9**). The next day, membranes were rinsed in TTBS three times and incubated with the appropriate secondary antibody conjugated with horseradish peroxidase (HRP) in 5% fat-free milk in TTBS for 1 hour at room RT (see antibodies in **Table 10**). Then membranes were washed three times with TTBS for 10 minutes each. Finally, signal was developed with the ECL-plus chemiluminescence Western blot kit (Amersham-GE Healthcare).

Table 9. Primary antibodies used for Western blot of muscle constructs.

Primary antibody	Origin	Dilution	Reference
Anti-GFP	Rabbit	1:1000	A11122, Invitrogen
Anti-GAPDH	Mouse	1:1000	AM4300, Life Technologies
Anti-tubulin	Mouse	1:1000	T0198, Sigma Aldrich
Anti-actin	Mouse	1:1000	MAB1501, Millipore
Anti-MHC (fast)	Mouse	0.5 µg/ml	A4.74, DSHB
Anti-MHC (slow)	Mouse	0.5 µg/ml	A4.951, DSHB
Anti-AChR	Rabbit	1:500	NBP2-19540, Novus Biological
Anti-MuSK	Rabbit	1:500	PA1-1741, Life Technologies
Anti-Myogenin	Mouse	1:200	sc-12732, Santa Cruz Biotechnology

Table 10. Secondary antibodies (HRP-conjugated) used for Western blot.

Secondary antibody	Origin	Dilution	Reference
Anti-mouse HRP	Horse	1:1000	7076, Cell Signaling
Anti-rabbit HRP	Goat	1:1000	7074, Cell Signaling

Treatments of muscle constructs with MG serum

Serum from MG patients was obtained from the group of Eduard Gallardo (Neuromuscular BCN, Hospital de Santa Creu i Sant Pau, Barcelona). In some cases, treatments were performed by directly adding MG serum at 20% into the cell medium (volume and concentration of growth factors was adjusted). In other cases, serum was decontaminated at 56°C for 30 minutes before adding it to cells. This serum was not assumed to be sterile but was always opened in a biological safety hood when preparing cell medium. Serums used for treatments are listed in **Table 11**.

Finally, some experiments were performed with purified IgGs, which were extracted using the Melon™ Gel IgG Spin Purification Kit (45206, ThermoFisher). The advantage of this method is that it uses a gentler elution buffer than Protein A or G-based methods, as well as its simple procedure. Serum was diluted 1:10 in purification buffer; starting from 50 µl of serum, around 500 µl of purified IgGs were recovered. The resulting purified IgGs were quantified with a Nanodrop™, using the IgG quantification setting. This setting measures absorbance at 280 nm and considers all protein to be IgG, which has an extinction coefficient of $\sim 210,000 \text{ cm}^{-1}\text{M}^{-1}$ and a molecular weight of 150 KDa. Typical range of IgG concentration was between 0.5 and 6 mg/ml. To obtain a more concentrated solution of IgGs, the solution was concentrated using Amicon® Ultra-0.5 mL Centrifugal Filters with a molecular weight cutoff (MWCO) of 50 KDa. These filters also allow for buffer exchange, and therefore the Purification Buffer (pH=6.5-7) was exchanged for sterile phosphate-buffered saline (PBS, pH=7.3). Centrifugation was performed for 30 min at 14000xg. The resulting concentrated solution was around 25 times more concentrated than the initial solution (**Figure 28**).

Statistics

Statistical analysis was performed in GraphPad Prism. Due to the small sample sizes used for most experiments, a non-parametric Kruskal-Wallis test was chosen, to account for the potential non-normality of the data. We compared the medians of all groups by enabling the option of Multiple Comparisons between all columns. A confidence interval of 95% was chosen, ($p < 0.05$ was considered significant).

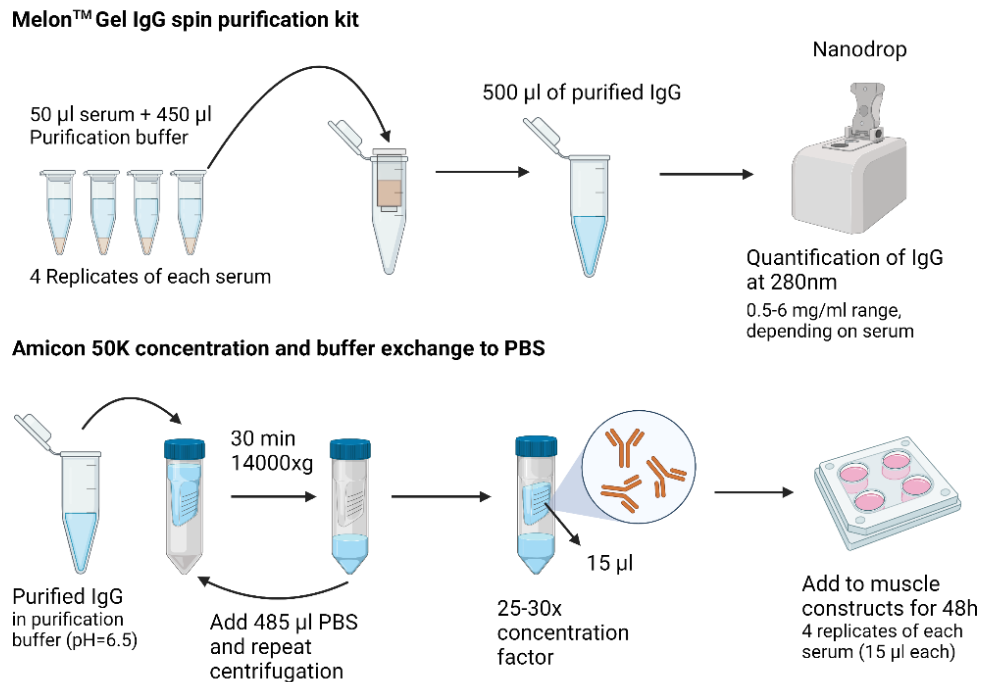


Figure 28. Diagram showing steps for purifying IgGs from human serum using the Melon™ Gel IgG spin purification kit, and subsequent concentration using Amicon® centrifugal filters.

Table 11. Serums used in MG serum treatments.

Serum code	Diagnosis	Autoantibody titer (nM)	Used in
Healthy-23yo	Healthy	-	Figure 51, Figure 57
Healthy-E	Healthy	-	Figure 52, Figure 53, Figure 54, Figure 55, Figure 56
Healthy-C	Healthy	-	Figure 54, Figure 55, Figure 56
19-299	MG AChR	~900 (very high titer)	Figure 50, Figure 51, Figure 57
09-4177	MG AChR	98 (high titer)	Figure 51, Figure 57
19-0454	MG AChR	0,6 (low titer)	Figure 51, Figure 57
18-0842	MG AChR	1918	Figure 52
JC	MG AChR	Not reported	Figure 53, Figure 54, Figure 55, Figure 56
17-0442	MG MuSK	60	Figure 51, Figure 57
18-0959	MG MuSK	44	Figure 52
OS35	MG MuSK	Not reported	Figure 53, Figure 54, Figure 55, Figure 56

RESULTS

2D differentiation of human myoblasts

As a first step in optimizing the culture of human myoblasts, a 2D differentiation protocol was adapted from Toral-Ojeda et al., 2018. As explained in the Methods section, this protocol utilizes a soft hydrogel overlay on 2D-cultured myoblasts. This prevents a common issue that arises in 2D cultures, which is the detachment of myotubes from the substrate due to spontaneous contractions. The hydrogel overlay allowed for only partial detachment of myotubes and provided mechanical support to contraction.

First, the objective was to compare different hydrogel compositions, in terms of how well they supported myotube differentiation and contraction. The original publication utilized Extracellular Matrix Gel (ECM gel), which has the same origin as Matrigel, but had been reported to produce less background fluorescence in immunostainings by the group of Adolfo López de Munain. Therefore, we compared Matrigel, ECM gel, and a third hydrogel (VitroGel) that had been previously used in the laboratory.

VitroGel is a polysaccharide-based hydrogel that polymerizes in the presence of Na^+ and Ca^{2+} ions that are naturally present in cell culture medium. It has the advantage of being highly transparent and xeno-free, which reduces the batch-to-batch variability that is inevitable with ECM-derived products. However, this product does not contain any binding motifs such as RGD peptides and is devoid of biomimetic components such as laminin and other biologically relevant mammalian ECM components. Still, as the objective of the gel overlay was mainly to provide mechanical support to contractile myotubes, and not necessarily to mimic the muscle ECM, this gel could be a potential alternative to ECM gel or Matrigel.

LHCN-M2 2D differentiation

The first cell line that was tested was LHCN-M2, which was the one used in the original publication of the culture protocol. We compared the expression of MHC at different timepoints, corresponding with the three different stages of differentiation: Day 0 (addition of hydrogel overlay), DM1 (emergence of myotubes and change from DM1 to DM2), and DM2 (after maturation in DM2). In **Figure 29**, a comparison of the expression of MHC and an actin counterstain can be seen.

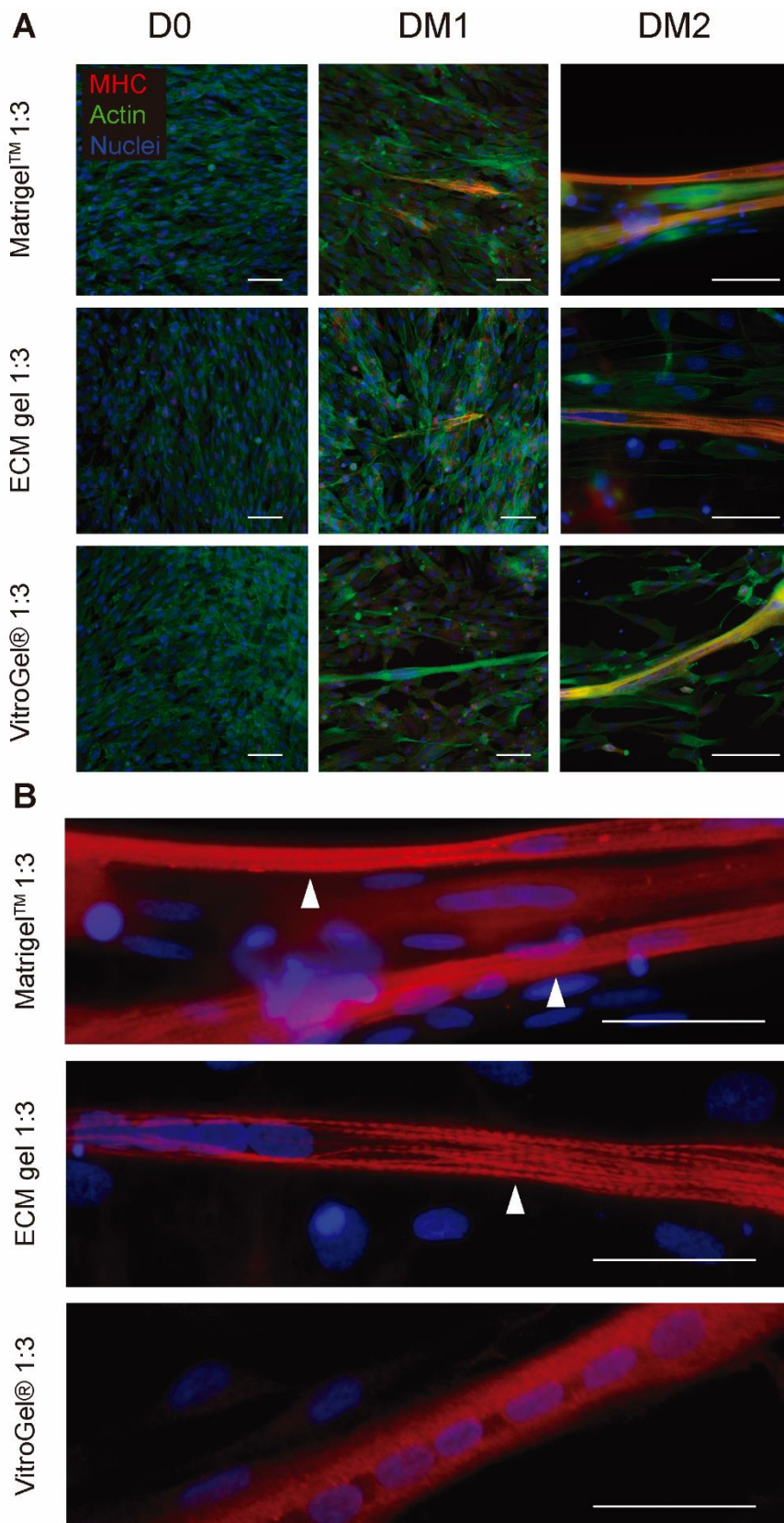


Figure 29. Sarcomere formation in LHCN-M2 at different stages of differentiation. DM1 stands for Day 4 in DM1, and DM2 stands for 13 days of differentiation (9 days in DM2). A. MHC staining (Alexa fluor 568) with actin counterstain (Phalloidin-FITC), nuclei stained with Hoechst 34580. B. Close-up view of sarcomeres in DM2 for each hydrogel. Arrows show sarcomeric banding patterns. Scale bars: 50 μ m.

As observed in the figure, myotubes began to emerge at the DM1 stage, and MHC expression was present in Matrigel and ECM gel but not in VitroGel. At the DM2 stage, MHC expression was visible on myotubes but only showed a sarcomeric pattern in the case of ECM gel and Matrigel.

These results from immunostaining are useful to complement simple brightfield images along the culture, as they provide information on the maturity of the myotubes. By observing the cultures in brightfield, as shown in **Figure 30**, it could seem that VitroGel is a good condition for myotube differentiation; as myocyte fusion is notably high after the first days in DM1 and continues to improve after several days in DM2. However, the maturity of these myotubes in terms of MHC expression was clearly inferior to that of myotubes obtained in ECM Gel or Matrigel, which were the only ones showing sarcomeric structures.

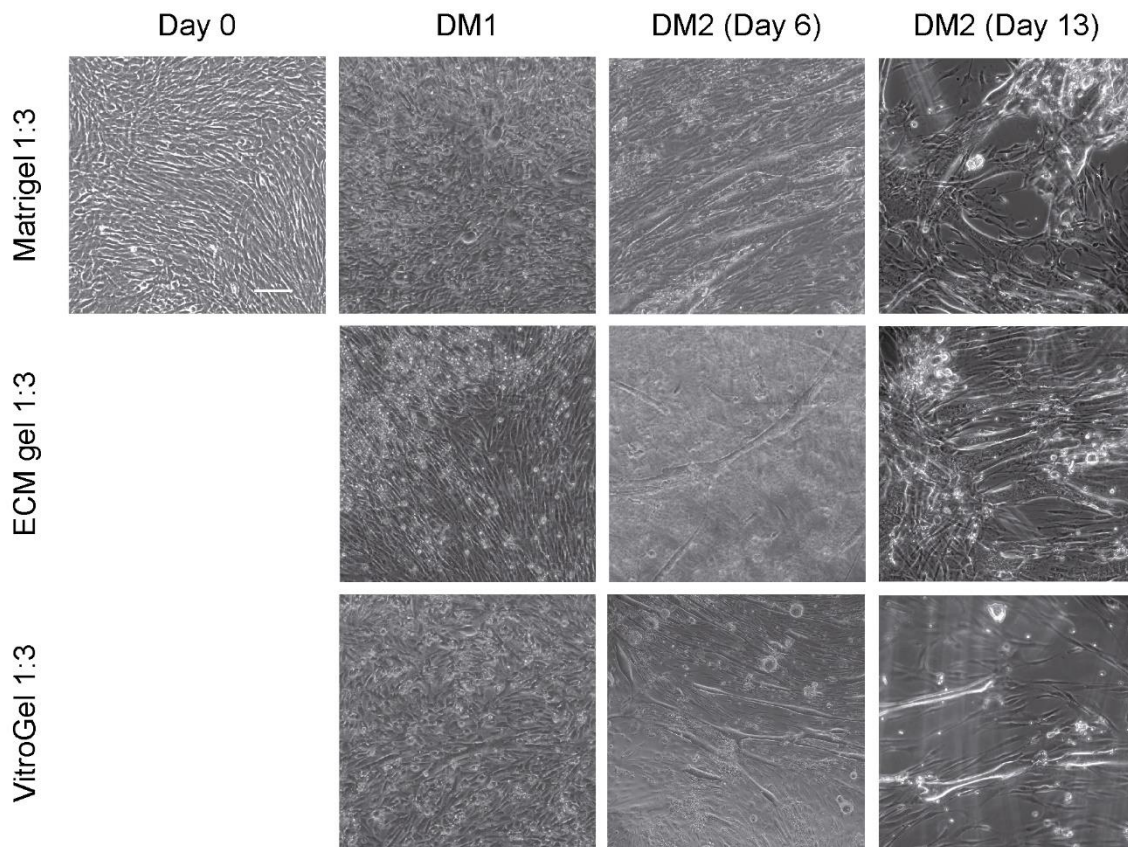


Figure 30. Brightfield images of LHCN-M2 myotube formation and maturation in different hydrogels at different timepoints. Scale bar: 100 μ m.

In parallel, we also compared the three hydrogels in terms of contractile ability of mature myotubes. In order to evaluate both the spontaneous and induced activity, recordings were performed without stimulation for 10 seconds and with electrical stimulation for 50

seconds. Monophasic 10V pulses at 1 Hz were applied in all hydrogels to compare twitch contractility. Biphasic pulses of increasing frequency were applied in Matrigel constructs to evaluate which frequency would induce tetanization. In **Figure 31**, representative contraction graphs can be seen.

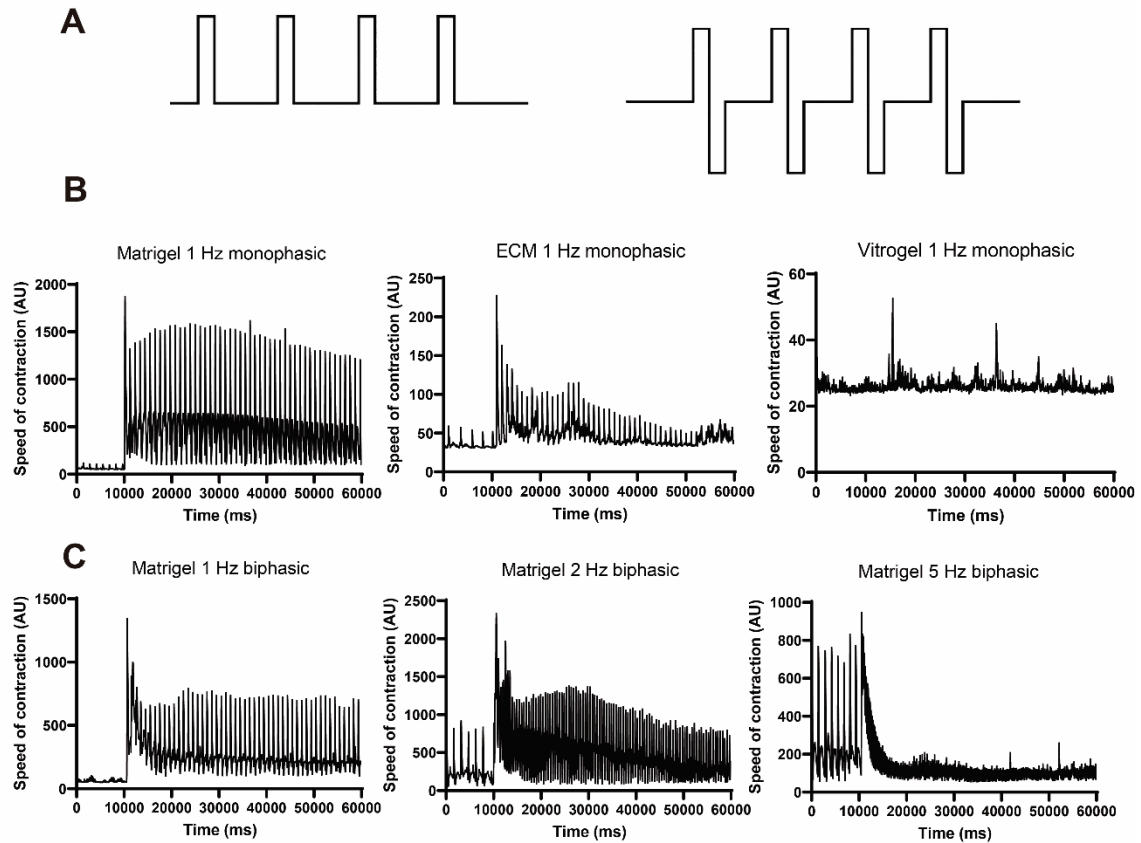


Figure 31. Analysis of contractile ability of LHCN-M2 in response to electrical stimulation. **A.** Pulse waveforms used for **B** (monophasic) and **C** (biphasic), respectively. **B.** Comparison of different hydrogel overlays at 1 Hz, monophasic 5 ms pulses of 10V. **C.** Contraction of cells in Matrigel at increasing frequencies using 5 ms biphasic pulses of +/- 5V. Cells were unstimulated for the first 10 s in all graphs.

Matrigel was the hydrogel that showed the highest contraction speed, which was about 10-fold higher than in ECM gel and 50-fold higher than in VitroGel. When testing different frequencies of biphasic pulses in Matrigel, it was observed that the cells were able to contract and relax in response to pulses of up to 2 Hz, but experienced tetanization at 5 Hz. There was a noticeable amount of spontaneous rhythmic contraction in both Matrigel and ECM Gel myotubes, which was roughly 0.5 Hz in frequency.

AB1079 2D differentiation

After receiving the LHCN-M2 cell line, we also established a collaboration with the group of Eduard Gallardo, who provided us with another immortalized myoblast cell line (AB1079). Therefore, we also tested the ability of this cell line to differentiate in the 2D hydrogel overlay system (**Figure 32**). In this case, cells exhibited some spontaneous contractions after 19-21 days of differentiation, instead of 13 days as seen in the case of LHCN-M2.

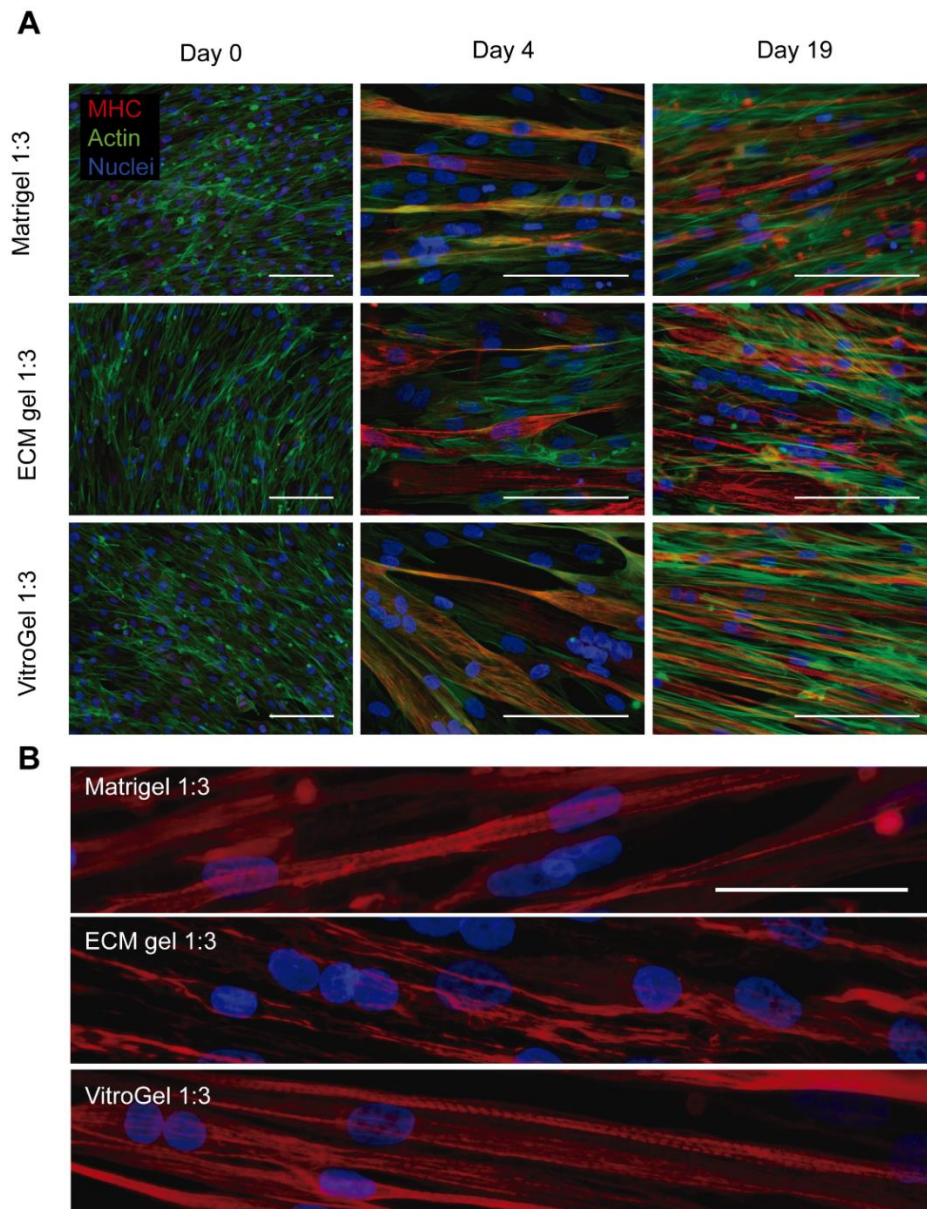


Figure 32. Sarcomere formation in AB1079 at different stages of differentiation. **A.** MHC staining (Alexa fluor 568) with actin counterstain (Phalloidin-FITC), nuclei stained with Hoechst 34580. **B.** Close-up view of sarcomeres at Day 19 for each hydrogel. Scale bars: **A.** 100 μm . **B.** 50 μm .

MHC staining revealed that AB1079-derived myotubes tended to become thinner and more elongated at the end of differentiation, which created spaces between them. In comparison, LHCN-M2 myotubes were thicker and more compacted, especially in Matrigel. In contrast with the data obtained in LHCN-M2, ECM Gel did not produce sarcomeric structures, but VitroGel did. The only hydrogel that produced consistent results in terms of sarcomere formation in both cell lines was Matrigel.

Myotube formation was also evident in brightfield images. In this case, cell fusion occurred in the first 2 days of differentiation, which was notably faster than in the case of LHCN-M2 cells. An example of the differentiation progression in Matrigel can be seen in **Figure 33**. Consistent with MHC stainings, brightfield images show a progressive alignment and thinning of myotubes over time.

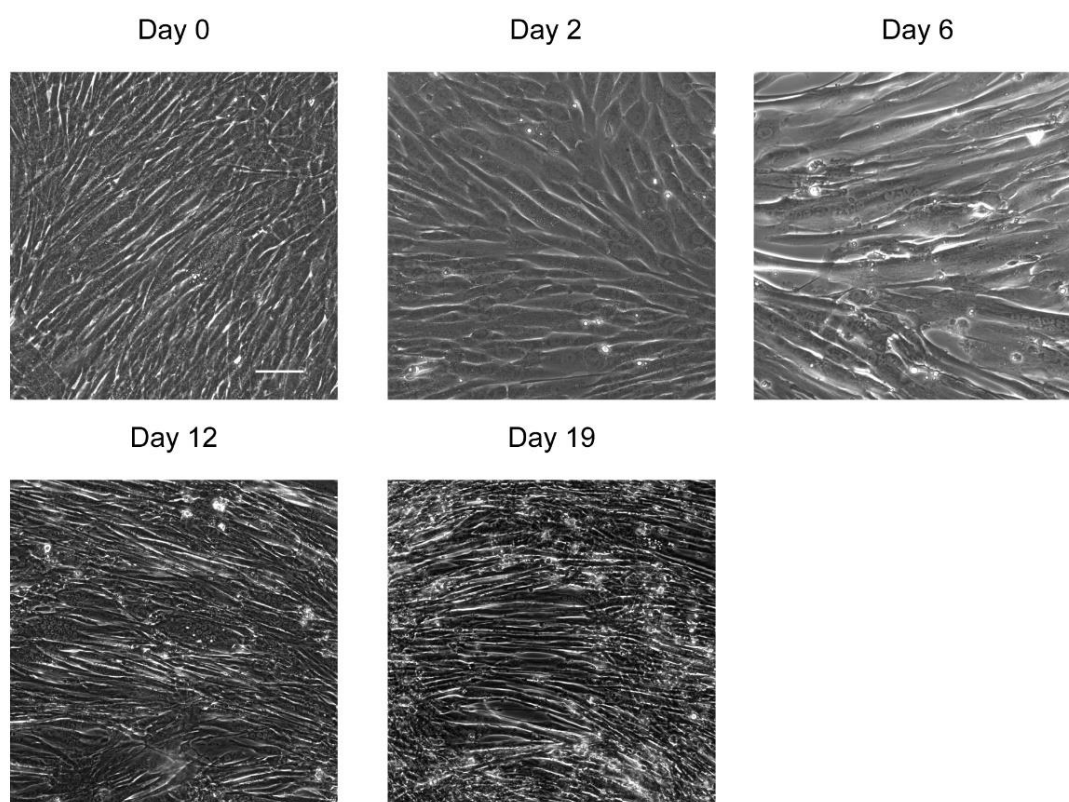


Figure 33. Brightfield images of AB1079 myoblasts at different timepoints of differentiation with Matrigel 1:3 overlay. Scale bar: 100 μ m.

As in the case of LHCN-M2, the contractility of AB1079 differentiated myotubes was evaluated. As seen in **Figure 34**, only Matrigel and VitroGel overlays were suitable to support contractile activity. Very little spontaneous activity was visible even after 19-21 days of differentiation, and the induced activity was about 10-fold lower than that observed in LHCN-M2. However, the cells responded to the stimulation with synchronic

pulses, which is correlated to the presence of functional sarcomeres. ECM Gel-differentiated cells did not exhibit any contraction, neither spontaneous nor induced. This is consistent with the lack of sarcomeric structures observed by MHC staining.

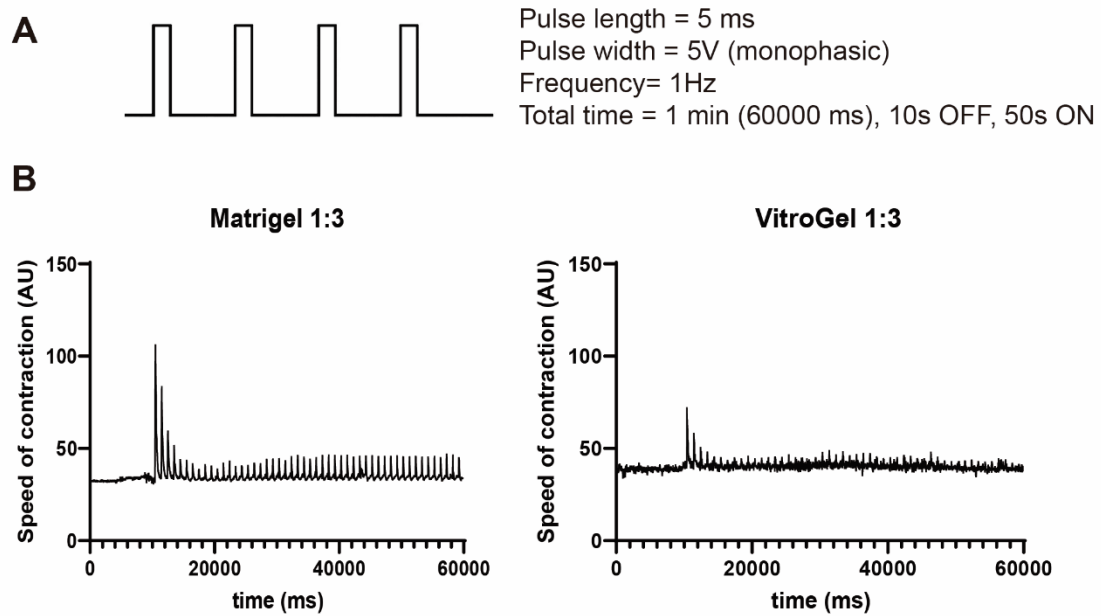


Figure 34. Analysis of contractile ability of AB1079 myoblasts in response to electrical stimulation. **A.** Pulse waveform used for stimulation of AB1079 myoblasts. **B.** Comparison of contraction speeds of AB1079 differentiated for 19 days in Matrigel 1:3 or VitroGel 1:3. ECM 1:3 hydrogel not shown due to lack of contractile activity.

3D differentiation of free-floating muscle strips

Before the beginning of this thesis project, a system based on had been developed in our laboratory to culture mouse C2C12 myoblasts in combination with spinal cord explants. This culture system does not use anchors, and instead relies on the use of additional hydrogel-cell mixture at the ends of a channel to generate anchoring sites. This model had already been optimized in a master's thesis project to set up the ideal culture conditions. At the beginning of this project, we decided to replicate this model using C2C12 myoblasts and the LHCN-M2 cell line. The model maintains free-floating muscle strips generated by embedding cells in a plasma clot, and at Day 3, adds Matrigel to mechanically support the construct.

Originally, the protocol was intended to be able to maintain cells for around 20 days. However, in our experience, the constructs did not last longer than 3-4 days due to breakage or detachment of the muscle strips from their anchors, as illustrated in **Figure 35**.

LHCN-M2 muscle strips

When we applied this protocol to the LHCN-M2 myoblast cell line, we used the DM1 / DM2 differentiation timepoints that had been used in 2D culture, but maintained the cell density and the day at which the Matrigel is added (day 3). In the C2C12 protocol, the addition of Matrigel was performed at Day 3 to avoid spreading of cells to the gel when it was added at Day 0. However, with LHCN-M2 myoblasts, spreading occurred despite adding Matrigel on day 3. In addition to this, only 25% of the constructs survived without breakage until Matrigel addition, meaning that prolonging the addition of the mechanical support would not have been possible. In this case, the constructs that resisted the Matrigel embedding experienced progressive migration from the original plasma clot, which resulted in a lack of cell alignment (**Figure 36**). Contractile activity was monitored, but was not observed even after performing electrical stimulation.

Despite the issues we experienced with reproducing this culture method, its main advantage is that it allows a rapid alignment and differentiation of myoblasts, as observed in the first 4 days in **Figure 35**. In the original development of this protocol, contractile activity and sarcomere formation were reported, as well as NMJ formation and evoked muscle response upon optogenetic stimulation of connected spinal cord explants.



Figure 35. Free-floating muscle constructs of C1C12 myoblasts. **A.** Image showing a PDMS device used for culturing the constructs. **B.** Schematic representation of the plasma clot (yellow) and surrounding gelatin, medium, or hydrogel in pink. **C.** Brightfield images of constructs at different stages of culture. Most constructs did not last longer than Day 4 without experiencing one of the issues shown in the last two images. Scale bar: 200 μm .

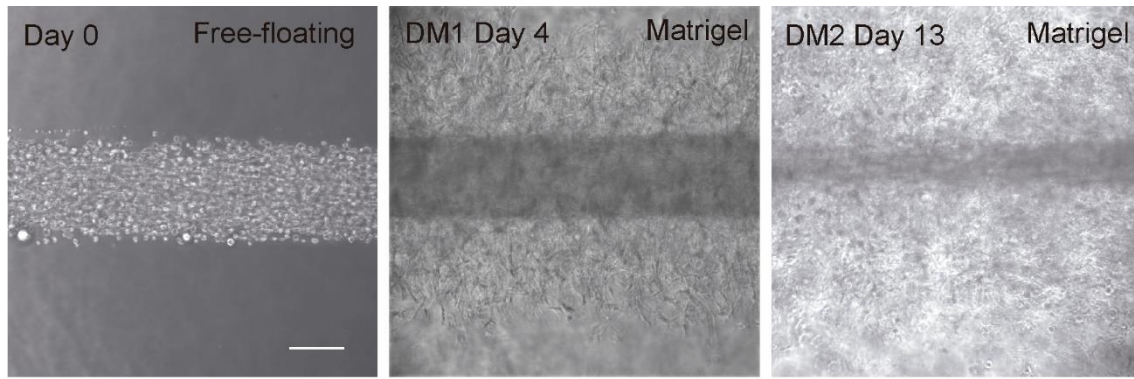


Figure 36. LHCN-M2 myoblasts cultured in the free-floating muscle strip system exhibit spreading upon addition of Matrigel. Scale bar: 200 μ m.

We believe that incorrect anchoring at the ends of the channel caused an increase in lateral retraction. More careful monitoring of anchors and addition of extra hydrogel on subsequent days might be needed to avoid this effect. Chicken plasma batch-to-batch variability had also been previously reported to affect the reproducibility of this method in terms of integrity of the constructs.

Regarding the spreading observed upon Matrigel addition, different cell lines may exhibit different behaviors in the same conditions. Other supporting hydrogels (ECM Gel, VitroGel) were tested in C2C12 hydrogels, but their influence in muscle maturation could not be evaluated due to the breakage of the constructs before or around the time of hydrogel addition. Another strategy that was tested was the use of VitroGel instead of gelatin during seeding of cells, which would eliminate the need to maintain the constructs as free-floating structures and would also impede cell spreading due to its lack of cell binding motifs. Nevertheless, the lower stiffness of this gel in comparison to gelatin resulted in issues with leakage of plasma-cell mixture from the channel during seeding, due to puncturing of the gel. A stiff gelatin support is needed during seeding but would probably hinder differentiation at later stages. So, the priority would be to improve integrity of the constructs before Matrigel addition. Notwithstanding, we consider that using a system with anchors would guarantee better maintenance of longitudinal tension.

3D anchored platform for muscle cell culture

The first iteration of our 3D muscle platforms for muscle cell differentiation was based on the method presented in Hinds et al., 2011. In this article, VELCRO™ fragments were fixed to a tubular silicone mold using metal pins (**Figure 37A**). Molds were coated with a hydrophobic Pluronic® solution prior to seeding of cells, and the best hydrogel was determined to be a Matrigel-Fibrin mixture. We attempted to replicate this culture system, by using cut syringe needles as pins (**Figure 37B**) and using the AB1079 myoblast cell line. The setup of the molds and placement of the pins was notably difficult, and detachment of the pins was common. This excessive manipulation probably contributed to the contamination of 75% of the cultures. In the cultures that were uncontaminated, we encountered difficulties with microscopic imaging. To evaluate contractile activity, the original publication indicated that it was necessary to detach muscle constructs from the opaque silicone tubing and pin them to a new culture dish (**Figure 37C**). The manipulation for this step was unnecessarily complex and risked damaging the muscle construct, which prompted us to discontinue the optimization of this protocol.

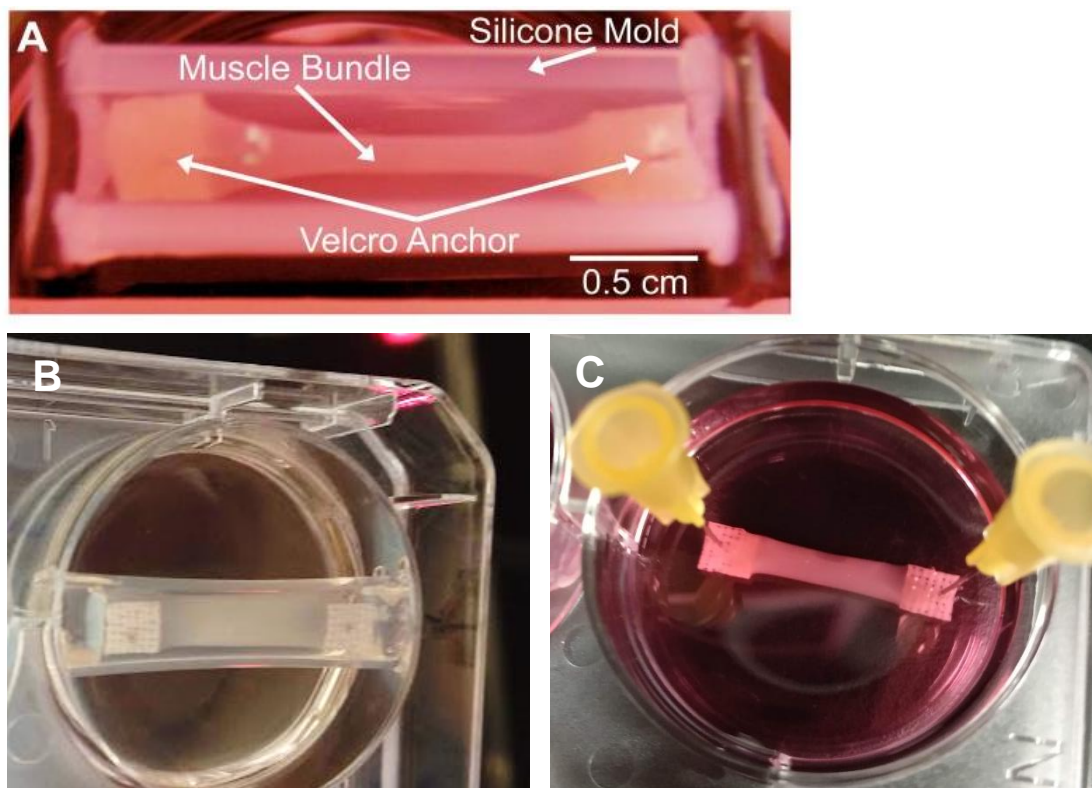


Figure 37. Attempt to replicate the culture protocol described in Hinds et al., 2011. **A.** Image of the muscle constructs taken from the original publication. **B.** Replicated constructs seen from below. **C.** Muscle construct moved from the tubular mold to a new culture dish using syringe needles.

As an alternative to the previous method, we thought that the protocol in Van Der Schaft et al., 2013 was more straightforward, as it did not use any opaque molds and firmly glued the VELCRO™ pieces to culture dishes using PDMS glue. This model uses a Matrigel-Collagen hydrogel and no specific hydrophobic coating for causing detachment of muscle constructs. As we had observed that many recent publications used Matrigel-Fibrin hydrogels, and pure Matrigel was found to be the optimal hydrogel for 2D overlays, we decided to compare all three hydrogel compositions in this setup.

The main observation that we made was that Matrigel and Matrigel-Fibrin hydrogels did not detach from treated culture dishes, but the Matrigel-Collagen constructs did, as seen in the original publication (**Figure 38**). We believe this was due to the increased degree of compaction that occurred in Matrigel-Collagen, which probably detached the constructs by generation of tension. The lack of detachment in the other hydrogels also resulted in poor cell alignment, especially in the case of Matrigel. Despite some increased alignment and myotube formation in Matrigel-Fibrin gels after more than one week in differentiation medium, the constructs did not form the compacted bundle that was desired.

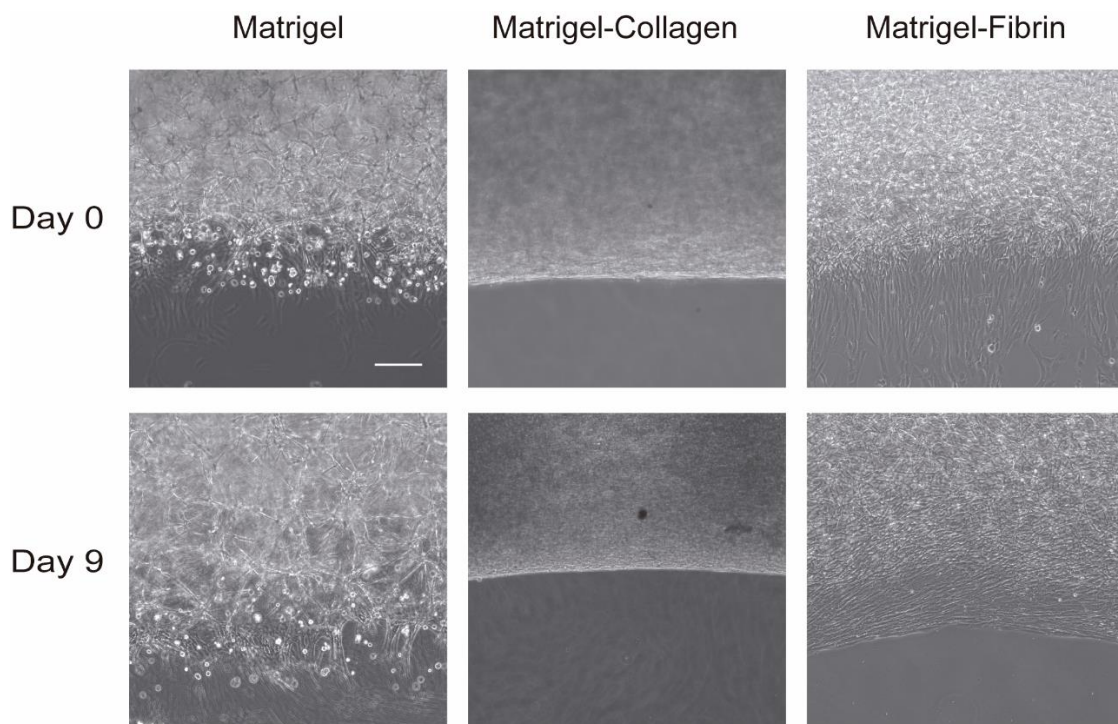


Figure 38. Lack of detachment in Matrigel and Matrigel-Fibrin gels at day 0 and day 9 in differentiation medium. Scale bar: 200 μm .

To solve this issue, we decided to use Pluronic® 0.2 % coating to increase cell detachment. As a way to coat only the region underneath the central part of the construct, we used a fine paintbrush to paint the region of interest with the solution, as explained in the Materials and Methods section. We realized that the thin layer of liquid evaporated after 1 hour in the incubator, so we decided to test seeding the cells directly on top of the dry coating. As seen in **Figure 40**, all the constructs detached from the plates, regardless of the hydrogel composition. Nevertheless, we still observed a lack of cell alignment in Matrigel hydrogels, even after 14 days of differentiation. In the Matrigel-Fibrin hydrogels, the alignment was now comparable to that of Matrigel-Collagen gels, despite the lower degree of compaction. Alignment was analyzed with the Directionality plugin for ImageJ and the Fast Fourier Transform (FFT) tool.

Even though the greater degree of compaction observed in Matrigel-Collagen could be considered a positive indicator of muscle maturation, the constructs started to show regions with breakage as early as Day 7 of differentiation (**Figure 39**). This did not occur in the case of Matrigel-Fibrin hydrogels, even after 14 days of differentiation. The holes observed in the first week of differentiation progressed until there was complete breakage of some constructs after 2 weeks. In addition, darker hypoxic regions were observed in these highly compacted constructs, indicating that this was not an ideal hydrogel composition to maintain cell viability.

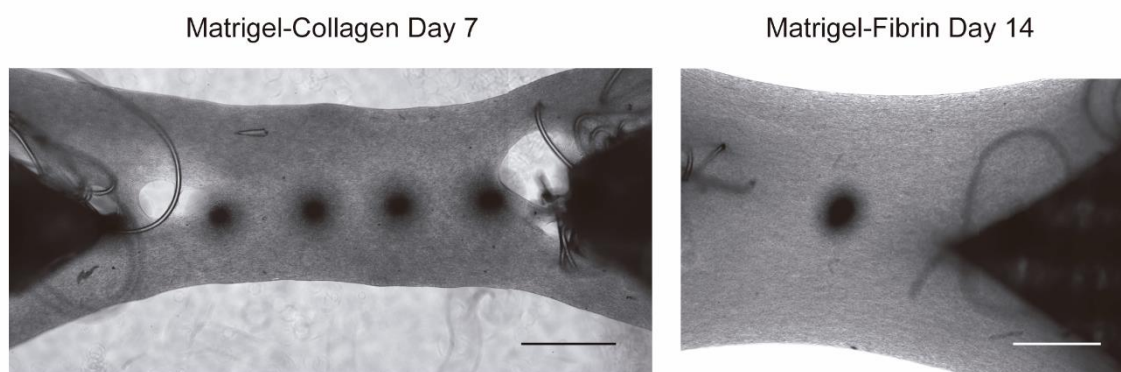


Figure 39. Breakage of Matrigel-Collagen constructs after 7 days, compared to a 14-day differentiated Matrigel-Fibrin construct with no breakage. Black dots are permanent marker guides on the underside of the Petri dish. Scale bar: 1 mm.

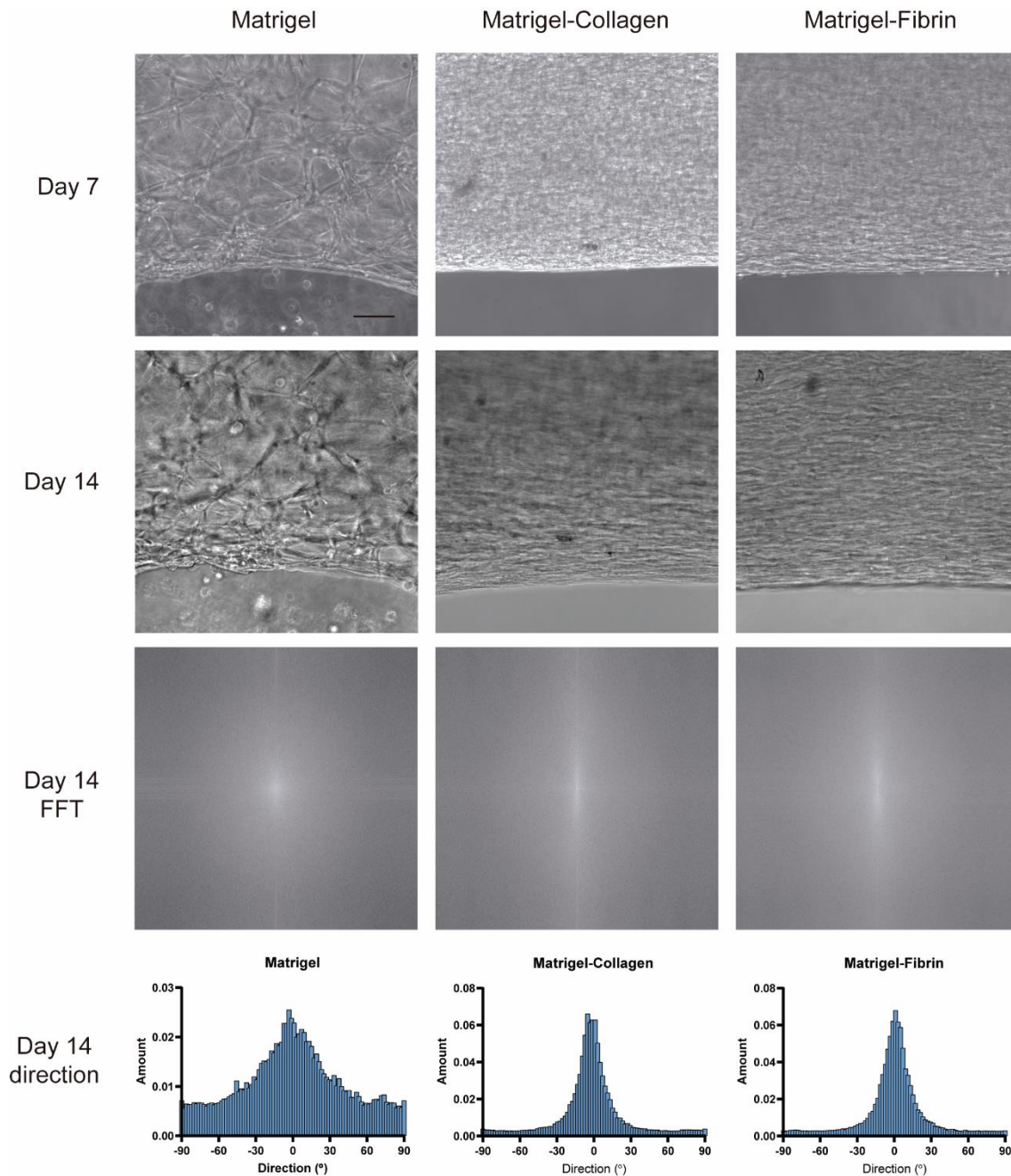


Figure 40. Alignment of AB1079 cells in different anchored hydrogels with Pluronic® coating at Day 7 and Day 14 of differentiation. Fast Fourier transform (FFT) and directionality histograms at day 14 are shown for comparison of alignment. Scale bar: 100 μm .

Once the detachment of the constructs was achieved, we did not observe major improvements in alignment and maturation after Day 14 of differentiation. Therefore, we decided to evaluate contractile activity at Day 14 in all three hydrogels. The results of this analysis can be seen in **Figure 41**. Confirming the results seen by microscopy imaging, the optimal hydrogel mixture in terms of contraction was Matrigel-Fibrin. At about half the contraction speed, Matrigel hydrogels also showed some induced contraction,

meaning that despite the lack of alignment of myotubes in this gel, they were still functionally mature. Finally, the lowest contraction speed of all three conditions was seen in Matrigel-Collagen gels. The best condition was an important improvement from the contraction of this cell line in 2D conditions.

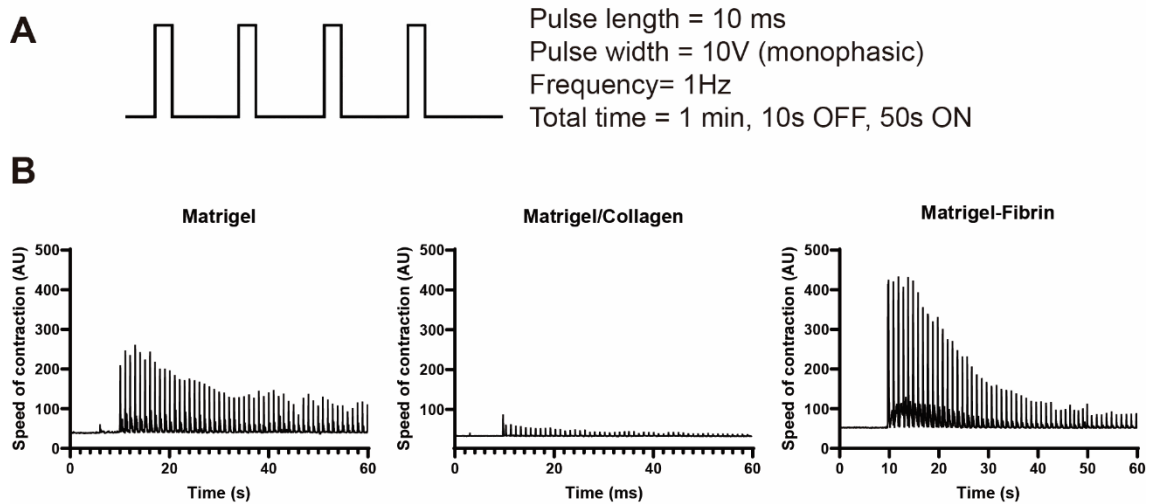


Figure 41. Speed of contraction of 3D muscle constructs with different hydrogel compositions after 14 days of differentiation in response to electrical stimulation.

After establishing the optimal hydrogel composition and optimizing cell culture conditions, we performed some immunostaining of differentiation markers, followed by confocal imaging. To stain sarcomeric structures, we used MHC and also sarcomeric alpha-actinin (SAA), which is more specific for fully differentiated sarcomeres. In parallel, we stained endplates using fluorescent BTX (**Figure 42**). Aligned sarcomeric structures were visible both by MHC staining and SAA staining, confirming the maturity of the contractile machinery. We also observed multiple AChR clusters in the constructs, which indicated that agrin signaling was exerting its expected effect.

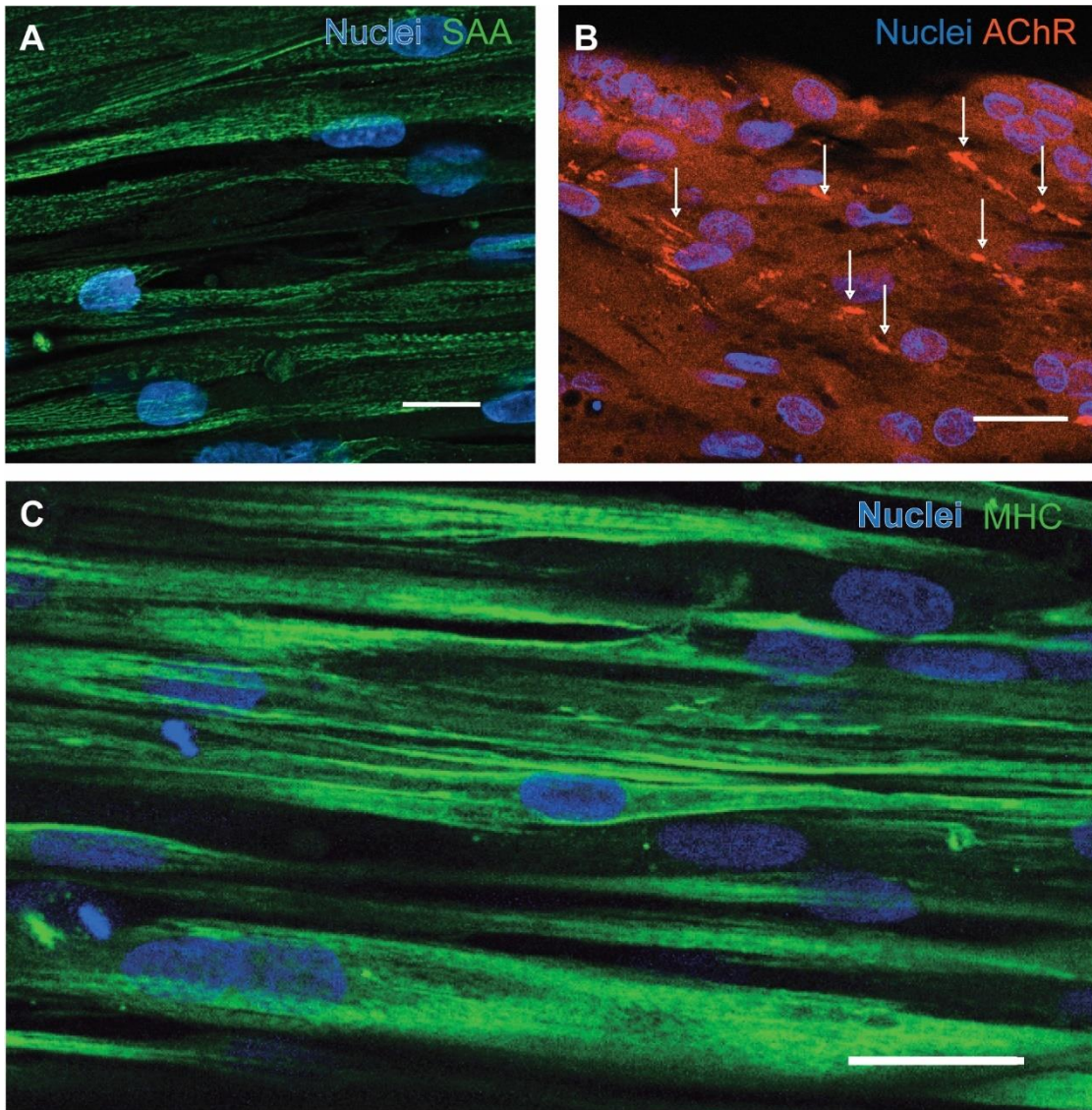


Figure 42. Confocal images of differentiation markers in AB1079 Matrigel-Fibrin constructs. **A.** SAA staining showing a sarcomeric pattern. **B.** AChR staining with BTX-555 reveals multiple AChR clusters. **C.** MHC staining showing a sarcomeric pattern. Nuclei stained with Hoechst 34580. Scale bar: 15 μm .

Optical stimulation of ChR2⁺ muscle constructs

To make this model amenable to optical stimulation, we generated stable myoblast cell lines expressing ChR2-eYFP under the EF1 α promoter. These cells were differentiated for 14 days and then stimulated with blue light pulses using an LED light source, as explained in the Materials and Methods section. We observed synchronic contractions in response to the applied pulses, which indicates that ChR2 expression and functionality was achieved. In **Figure 43**, it can be noted that contraction shows a summation pattern, and speed of contraction decreased over time, as had been observed in electrically stimulated constructs.

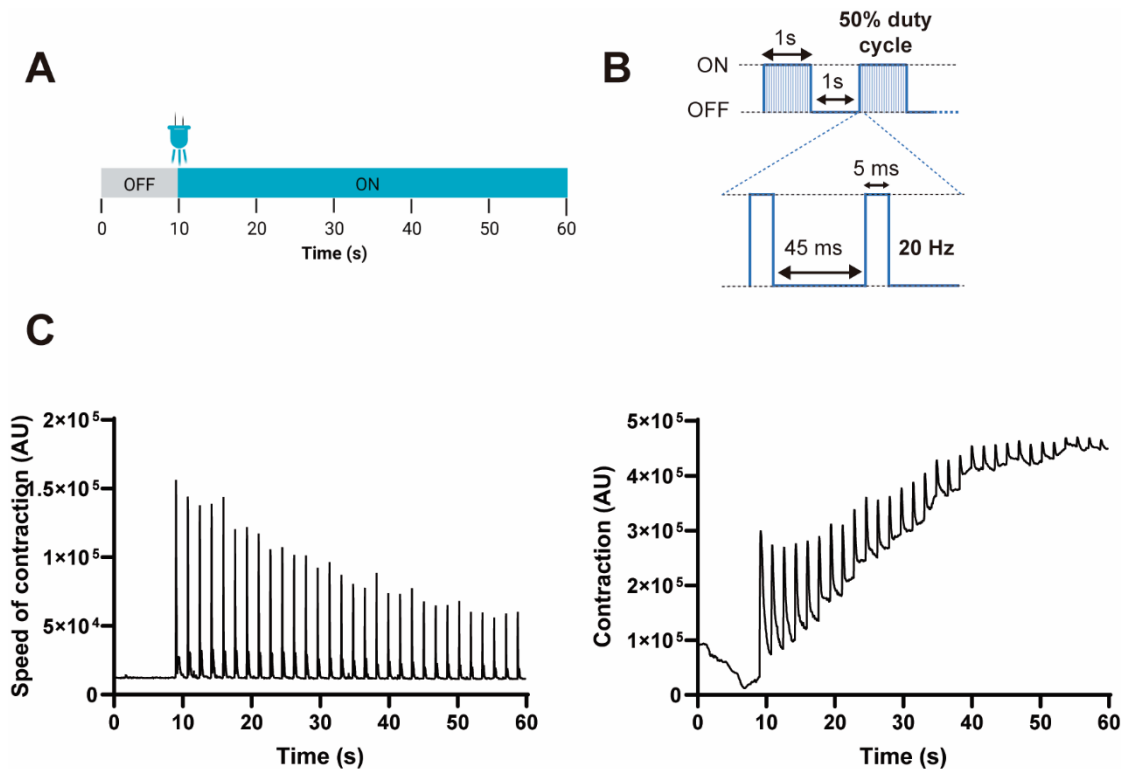


Figure 43. Optical stimulation of ChR2+ AB1079 constructs differentiated for 14 days. A. Stimulation regimen. B. Pulse parameters. C. Speed of contraction and contraction graphs generated with MUSCLEMOTION.

Response of muscle constructs to acetylcholine stimulation

With the previously mentioned data, we had demonstrated that the constructs could respond to electrical and optical pulses. However, considering that one of our main goals with the 3D muscle constructs was to use them to model myasthenia gravis, we wanted to demonstrate that the cells could respond to a more physiological, ACh-mediated stimulation. For this, we decided on a concentration of 100 μM of acetylcholine, as it was reported to be an appropriate concentration to stimulate *in vitro* muscle cells (Afshar Bakooshi et al., 2019, Weng et al., 2018, Vianney et al., 2014). This concentration was also on the higher end of the range used to stimulate muscles *ex vivo* (Shieh et al., 1995; Trailovic et al., 2021).

In our first experiments with ACh stimulation, we aimed to measure the contraction response as we had done with electrical stimulation, using the MUSCLEMOTION plugin. Stimulation with ACh resulted in a single tetanic contraction, as would be expected when ACh is not removed from the medium (**Figure 44**). Therefore, in the speed of contraction graphs, the speed had an initial peak and later stabilized at low values, as the muscle remained in a contracted state. If the initial 20 seconds of the graph are eliminated to

visualize the tetanic phase more clearly, small fluctuations in contraction speed can be observed. This can be attributed to individual cells contracting at different rates due to diffusion of acetylcholine. Contraction graphs, on the other hand, showed a contraction plateau that lasted at least 9 minutes (recording was stopped after 10 minutes).

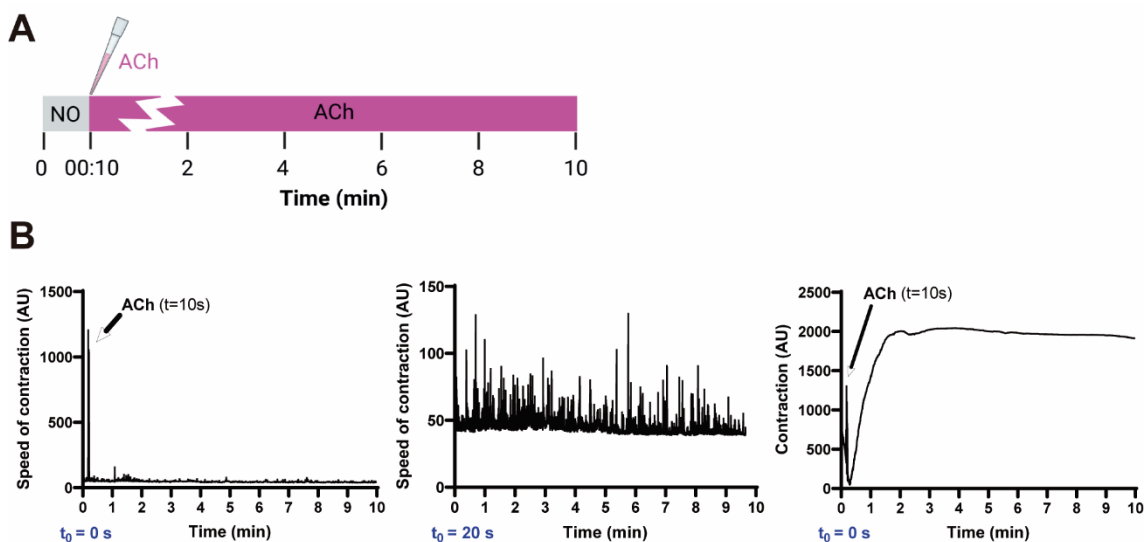


Figure 44. Contraction of AB1079 muscle constructs in response to acetylcholine stimulation. **A.** Stimulation regimen. **B.** Contraction and speed of contraction graphs. Speed of contraction graphs show a high peak upon ACh addition that obscures the smaller contractions of individual cells, which can be visualized more clearly by omitting the first 20 seconds of recording.

Ideally, we would have been interested in modeling the relaxation phase of muscle contraction that occurs when ACh is removed, as well as the contraction phase. For this, we attempted to use a batch perfusion system to continuously perfuse muscle cells during recording of contraction. The goal was to add acetylcholine as a spike, by using an injection port on a modified cell culture dish, and then slowly wash it out while recording the muscle response. As depicted in **Figure 45**, the inlet flow was controlled by a peristaltic pump, and the outlet flow was controlled by a syringe pump set to ejection mode. Although this setup is technically feasible, we encountered issues with movement of the muscle constructs due to the flow of cell culture medium, which created artifacts in contraction measurements.

We believe that one of the causes of flow disturbances was that the volume of medium inside the cell chamber was not constant due to inaccurate calibration of the inlet and outlet flow rates. The units of flow measurement were not equal for both devices, and so manual calibration of flow rate was performed. To solve this, it would be advisable to use two peristaltic pumps or two syringe pumps that could be calibrated to function at the exact same flow rate and set to a rate that ensures laminar flow to avoid disturbances to

the muscle construct. Syringe pumps are comparatively less likely to experience flow rate alterations due to wear and tear, due to their propulsion mechanism. Peristaltic pump tubing tends to become stretched due to use or autoclaving, which influences the effect of the propulsion mechanism used in this type of pump. Ultimately, we decided to discontinue these experiments, as the complexity of the flow setup limited our ability to study muscle function in larger sample sizes.

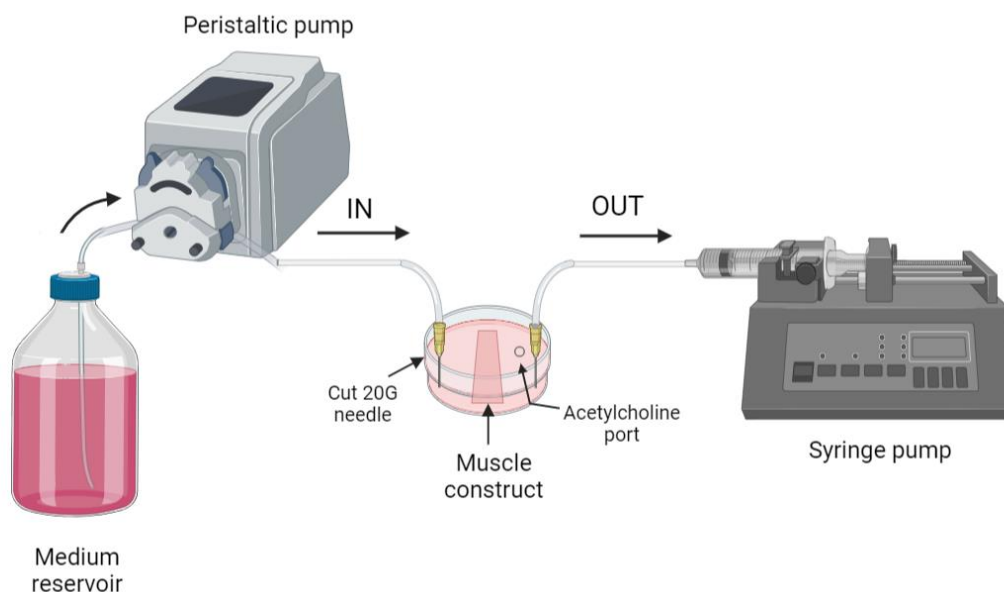


Figure 45. Batch perfusion system used for acetylcholine stimulation and washout.

Calcium imaging combined with chemical stimulation

Although ACh stimulation contraction graphs obtained with MUSCLEMOTION showed the expected tetanic contraction pattern, an issue that we detected was the difficulty in determining the exact moment at which muscle response begins after addition of ACh. The first seconds of the graph after ACh addition are subject to artifacts from the movement of the medium, and contraction builds up gradually as different muscle fibers receive the diffused ACh. To visualize the ACh response more clearly, we decided to use calcium imaging as a way to visually determine the initiation of the contractile response.

Fluo-4 for calcium imaging in muscle constructs

As a straightforward method to perform calcium imaging directly in our current muscle constructs without the need for genetic modification, we used the calcium dye fluo-4 AM. The staining protocol was adapted for 3D constructs by increasing the loading time. Usually, calcium imaging measures calcium transients in individual cells, which is why

we decided to record calcium transients at a higher magnification (20x) to visualize individual myoblasts. This method was also more appropriate when using fluo-4, as loading in a 3D construct was predicted to be incomplete, and in this manner, we would be able to select only the ACh-responsive cells for analysis. As a positive control of depolarization, we used a high concentration of potassium chloride (KCl) at the end of the stimulation. An example of this experiment is shown in **Figure 46**.

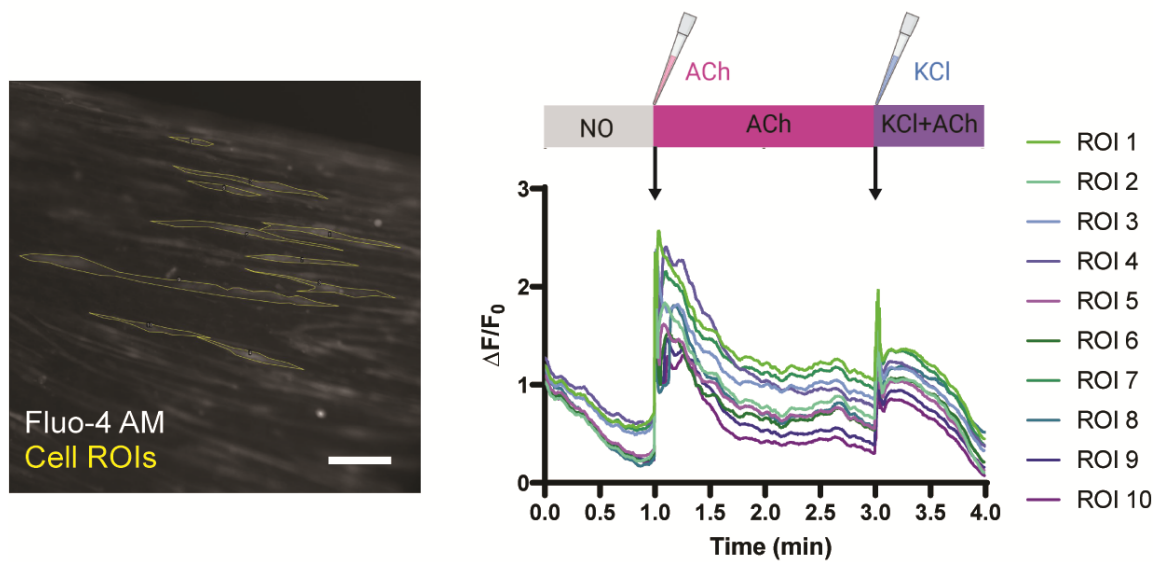


Figure 46. Calcium transients in muscle constructs loaded with fluo-4 AM and stimulated with ACh and KCl. 10 ACh-responsive cell ROIs were selected from the field of view and calcium transients were analyzed with ImageJ, resulting in the traces shown on the right. ACh was added at $t=1$ min, and KCl was added at $t=3$ min. Scale bar: 100 μm .

It must be noted that, in the case that most of the cells have been depolarized by ACh (as would be desired), the response to KCl would logically be lower, due to the inability to further depolarize the membrane of these cells. This is what we observed in this example. Another relevant comment is that the initial peak in fluorescence at the time when ACh is added is also an artifact, which occurs due to a temporary change in cell culture medium birefringence when adding the ACh spike. However, after this initial peak, a wider and more sustained calcium release wave can be seen for all ROIs.

The main drawbacks of fluo-4 in this system were the following: 1) Inconsistent loading across samples and across the construct; 2) Loss of fluorescence over time during recording of several samples; and 3) Inability to maintain cultures after fluo-4 loading and recording. Apart from these issues that stemmed from the calcium dye itself, we also encountered problems with the calcium analysis in individual cells. In the example shown in **Figure 46**, the construct also contracted in response to ACh, but the cells in focus did

not experience significant displacements over time. However, in other recordings, cell ROIs could not be defined as fixed regions due to contraction-induced displacement. Nevertheless, we realized that other publications relied on global calcium analysis to quantify muscle response to ACh stimulation, but they used a GECI to ensure homogeneous distribution of the indicator. Due to these reasons, we decided to generate GCaMP6⁺ myoblast cell lines in future experiments to analyze global calcium transients.

GCaMP6⁺ muscle constructs

To obtain GCaMP6⁺ myoblasts, we generated lentiviral vectors from a plasmid containing GCaMP6s under a muscle promoter, MHCK7. After infecting and FACS sorting all human myoblast cell lines, we confirmed that all of them expressed GFP from GCaMP6 at different stages of differentiation (**Figure 47**). Although the actin loading control was solarized, we confirmed clear presence of GFP in all the expected samples.

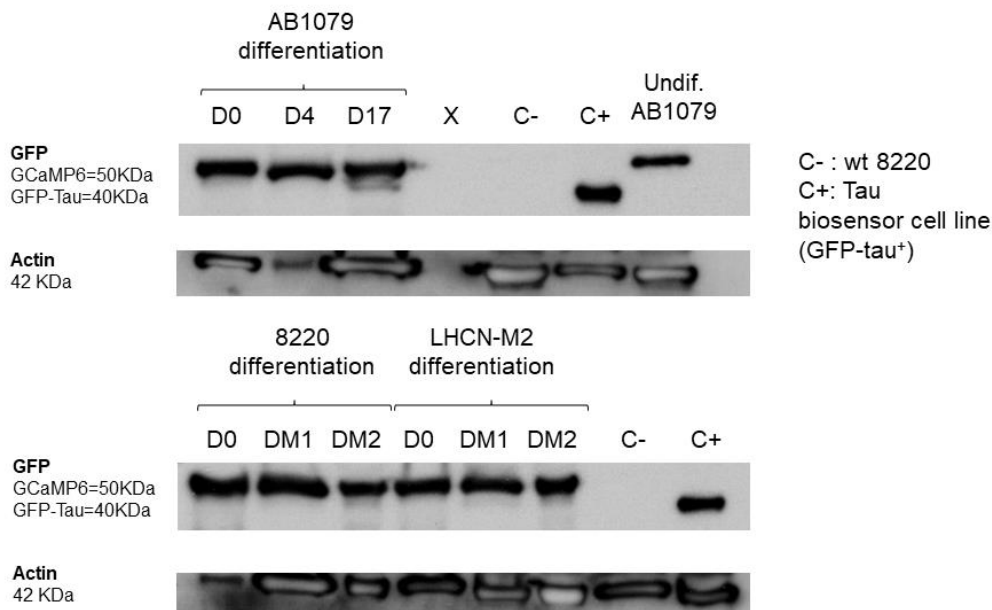


Figure 47. Western blot of GFP expression in GCaMP6⁺ myoblast cell lines at different stages of differentiation. As a negative control, wild-type myoblasts were used. As a positive GFP control, a lysate of tau biosensor cell line expressing a GFP-tau fusion was employed. Actin was used as a loading control.

Next, we evaluated the ability of AB1079 GCaMP6⁺ myoblasts to respond to acetylcholine stimulation. To analyze the calcium waves in the whole construct, we performed recordings at 4x magnification. In these conditions, we determined that the optimal exposure time was 200 ms, as it allowed visualization of a soft fluorescent outline of the muscle bundle in a resting state and an increase in fluorescence upon ACh addition

(**Figure 48**), while still maintaining an appropriate frame rate for extracting calcium traces.

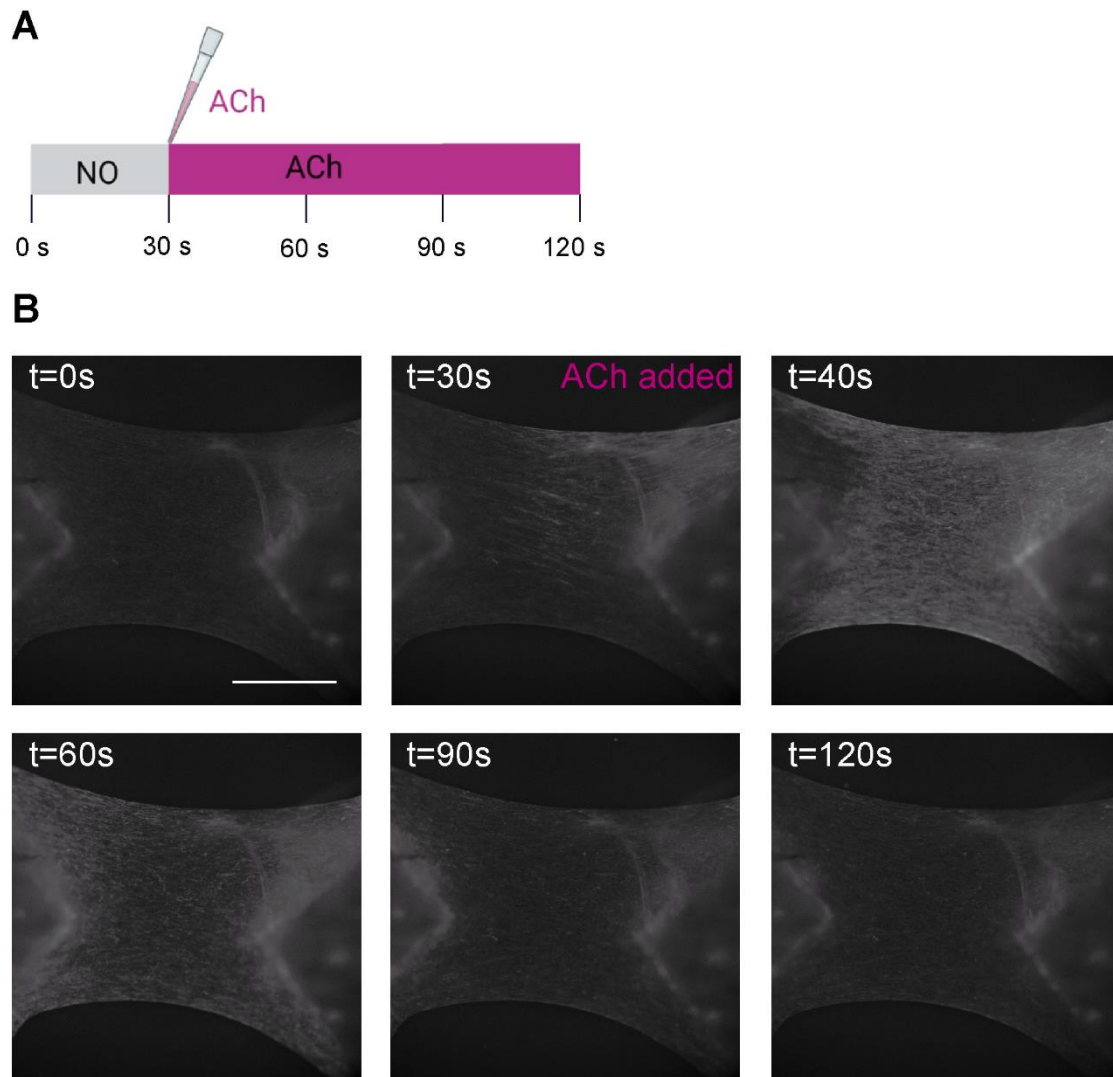


Figure 48. Calcium increase of AB1079 GCaMP6⁺ muscle constructs in response to 100 μ M ACh stimulation. Constructs were seeded in 4-well plate format for this experiment. **A.** Stimulation regimen. **B.** Relevant frames from the calcium transient recording. Scale bar: 1mm.

As observed in **Figure 48**, calcium increase begins immediately after addition of ACh, and reaches its maximum overall fluorescence around 10 seconds later. Calcium waves are propagated across the construct in a gradual fashion. We speculate that this wave effect is partly due to ACh diffusion, and partly due to action potential transmission. After 2 minutes, cytoplasmic calcium returns to a quasi-basal state, with a slightly higher fluorescence than the initial frame. More information regarding data processing of this type of GCaMP6 calcium images will be discussed in the “Modeling myasthenia gravis

in vitro” section, as these myoblasts were mainly used to quantify muscle response to MG serum treatments.

Expression of muscle differentiation markers analyzed by Western Blot

As an additional confirmation that the 3D muscle constructs were fully differentiated after two weeks, we performed Western blot analysis of several muscle differentiation markers at day 0, 7, and 14 of differentiation in AB1079 constructs. As a positive control, we used a rat skeletal muscle lysate obtained from quadriceps muscle tissue. To evaluate sarcomere formation, we used MHC fast and slow isoform antibodies. We also evaluated expression of myogenin, as it is a myogenic factor that should be upregulated in differentiating myoblasts. Finally, we evaluated endplate formation and maturation in terms of AChR and MuSK expression (**Figure 49**).

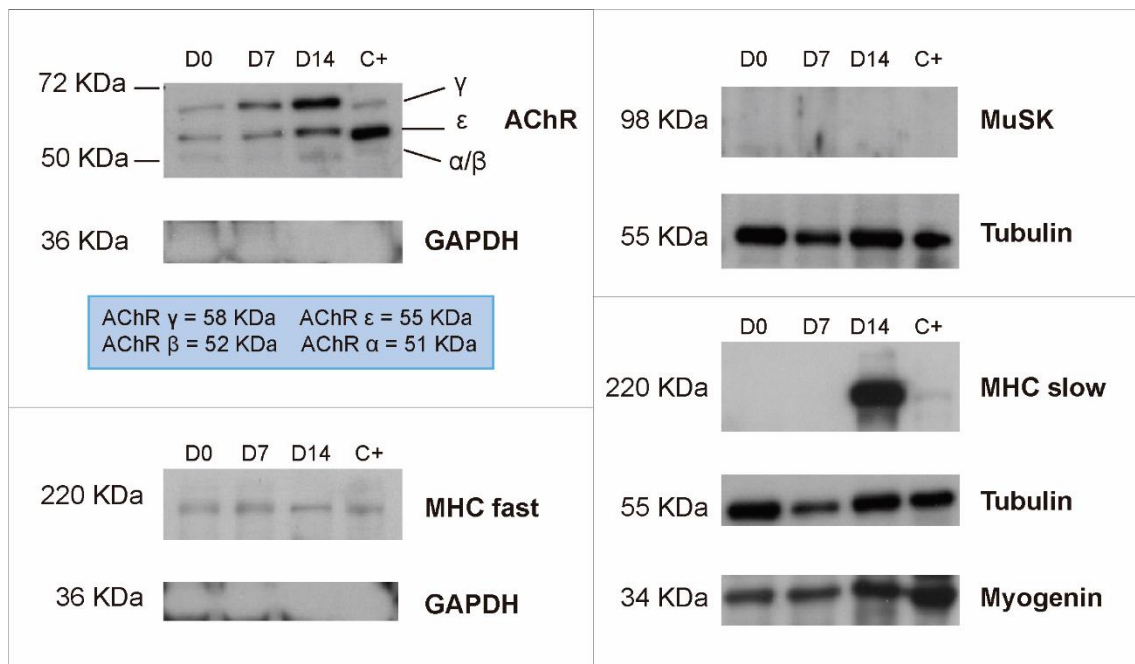


Figure 49. Expression of muscle differentiation markers in AB1079 3D muscle constructs at different timepoints of differentiation. AChR, MuSK, MHC fast isoform, MHC slow isoform, and myogenin are evaluated. GAPDH or Tubulin were used as loading controls.

The first note that must be made is that quantitative information cannot be extracted from blots using GAPDH loading controls, as it was solarized due to excessive concentration. Although the protein concentration was normalized across wells and should be similar in the different replicates of the blot, tubulin loading controls show different patterns in two different blots that were loaded with the same amount of protein; indicating that quantitative information cannot be extrapolated from loading controls pertaining to the other blot replicates.

Regarding myosin heavy chain isoforms, it can be observed that the slow isoform is predominant and is only expressed after 14 days of differentiation. This isoform is also present in the positive control, albeit at a lower concentration. MHC fast isoform shows a more stable expression over time. As the AB1079 cell line is derived from quadriceps muscle, which is predominantly composed of slow twitch fibers, we believe that the high expression of MHC slow isoform is coherent. The fact that its expression is so highly upregulated at Day 14 also supports the claim that cells are fully differentiated at this timepoint and contain sarcomeric structures.

Regarding myogenin expression, the abundance of this factor seems to increase from day 0 to day 7. Tubulin decreases from day 0 to day 7, but still the myogenin band is more intense at day 7. From day 7 to day 14, there does not seem to be an increase in myogenin abundance, as tubulin band intensity increases proportionally. These results are consistent with the upregulation of myogenin during the differentiation process, and its stabilization or downregulation in mature myotubes. The high expression of myogenin in the positive control may be due to ongoing muscle tissue regeneration processes in the harvested muscle tissue.

In terms of endplate formation, it is clear that AChR expression is upregulated as differentiation progresses. The antibody that was used stains all AChR isoforms, and so the different bands correspond to the α , β , ϵ , and γ subunits. The molecular weight of the α and β subunits is very similar, which could result in a single band (the first band observed slightly above 50 KDa). The other two bands in upward sense are consistent with the ϵ and γ subunits, respectively. This observation is interesting because it seems that the ϵ subunit is present in these myoblasts, while the lack of γ -to- ϵ transition is typically an issue faced in *in vitro* modeling of mature endplates. In the positive control, the middle band is more predominant, which is consistent with this band corresponding to the adult ϵ subunit. MuSK presence was not observed in any of the samples (including the positive control), which points at the antibody being the most probable cause, instead of the lack of expression of this protein. In the future, a different antibody should be tested to confirm expression of MuSK by WB.

Modeling myasthenia gravis *in vitro*: Proof-of-concept

Colocalization of anti-AChR antibodies with AChR clusters in 2D cultures

As a first step in evaluating the effect of MG patient serums on muscle function, it was necessary to demonstrate that patient autoantibodies are able to bind AChR clusters *in vitro*. For this, patient serum was used as a primary antibody in immunostaining, at a 1:50 dilution, on cultures of AB1079 myoblasts differentiated in different hydrogels. The spontaneous formation of endplates was induced by the addition of agrin to the culture medium, and staining of AChR clusters was performed using fluorescent BTX.

In **Figure 50**, serum from an AChR MG patient with very high antibody titers, around 900 nM (NHC: 299-19) was used. In Matrigel and VitroGel, AChR clusters are present on the myotubes, and the pattern of autoantibody binding bears a striking resemblance to the endplate localization. In ECM gel, a low number of endplates was achieved, leading to more difficulties in quantifying colocalization. The amount of endplates was highest in VitroGel, albeit with a high variability between fields of view. Colocalization was similar in Matrigel and VitroGel, which was measured to be around 87%.

As a control of autoantibody binding, we also performed stainings with healthy human serum at the same dilution. In the same experiment, we also tested three other MG patient serums: two anti-AChR serums, one with high titers (lower than 299-19), and one with low titers; and an anti-MuSK serum. In this case, cells were cultured with Matrigel overlays. In this experiment, the 299-19 serum with very high anti-AChR IgG titers that had been used in **Figure 50** served as a positive control. Indeed, colocalization was again very evident, as shown by the white arrows. The healthy control serum did not show any colocalization, which confirmed the specificity of the binding in the pathogenic positive control.

Nevertheless, we did not observe any other colocalization events in any of the other tested serums. In the case of the anti-AChR serums, the serum with low titers may have been excessively diluted when applied at a 1:50 dilution for staining. Still, we would have expected binding with the high titer anti-AChR serum but did not observe colocalization even after close inspection of each individual endplate. An unexpected finding in this condition was that the autoantibody binding pattern showed some striated bands, similar

to the ones that would be observed when staining sarcomeres. This led us to hypothesize that this patient may have co-existing anti-striated muscle antibodies that bind sarcomeric proteins. This is common in patients with thymoma, which is a typical comorbidity of anti-AChR MG.

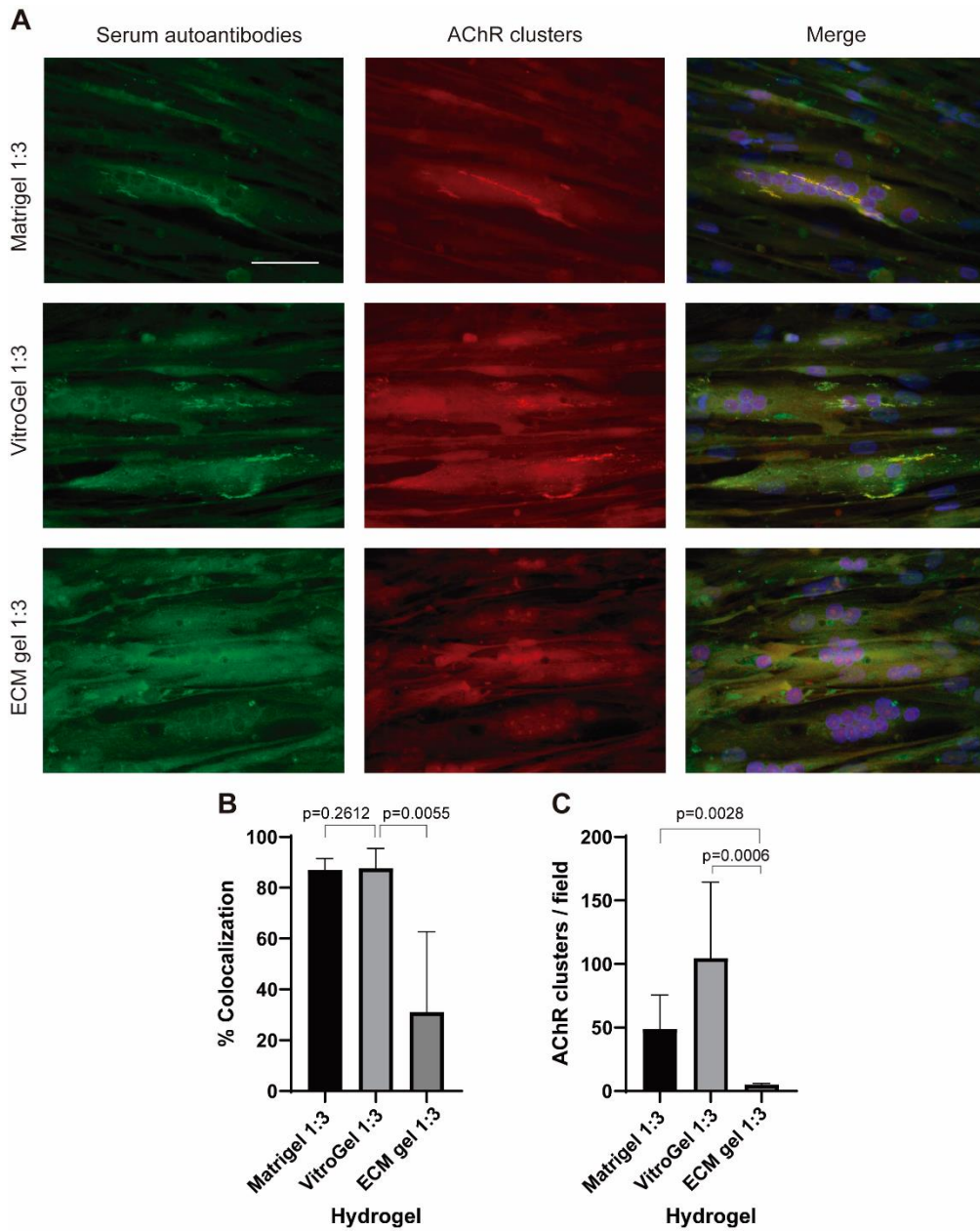


Figure 50. Colocalization of anti-AChR autoantibodies with AChR clusters in AB1079 differentiated in 2D. Different hydrogels overlays are compared in terms of AChR cluster formation and colocalization. **A.** Fluorescence images of autoantibody binding sites (anti-human 488) and AChR clusters (BTX 555). Nuclei stained with Hoechst 34580. **B.** Colocalization of clusters and autoantibody binding sites ($n = 6$ images per hydrogel). **C.** Number of AChR clusters observed per field in each hydrogel. Scale bar: $50\mu\text{m}$.

In the case of anti-MuSK antibodies, we were unsure whether the lack of colocalization was also explained by excessive dilution. However, we later reasoned that it is possible

that MuSK binding would not be observable at the endplate even if it did occur. Even though MuSK is localized at the NMJ or endplate, this protein is merely a signaling mediator that does not form clusters and is therefore much less abundant in relation to AChRs.

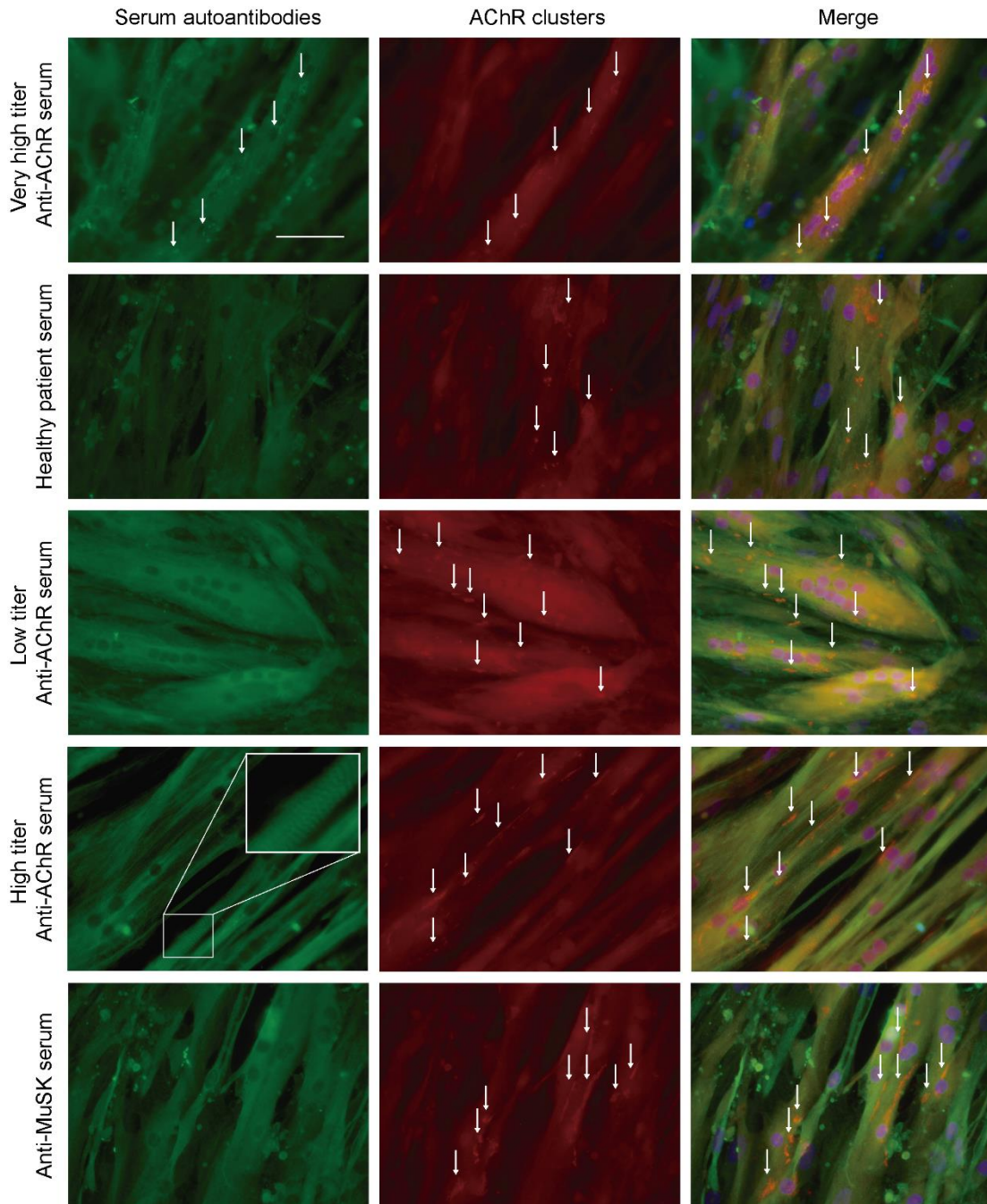


Figure 51. Colocalization of anti-AChR autoantibodies with AChR clusters in AB1079 differentiated in 2D. Different serums are compared in terms of ability to colocalize with endplates (arrows). Endplates stained with BTX-555 and autoantibodies with anti-human 488. Nuclei stained with Hoechst 34580. Scale bar: 50 μ m.

Effect of MG patient serums on muscle function

After developing the 3D anchored muscle construct protocol, we decided to use this model to evaluate the effect of MG serum treatment on muscle function in response to ACh stimulation. At first, we tested the same concentration of serum as was used for staining (1:50) but did not observe any effect on muscle contraction. Therefore, we decided to increase the concentration to a 1:5 dilution, which had also been reported to inhibit muscle contraction in literature (Vila et al., 2019).

For the first experiment that we performed with MG serum treatments, we used muscle constructs seeded in a 35 mm Petri dish format. We quickly realized that the volume of serum needed to achieve 20% of the volume in these plates was very high considering the availability of samples. Therefore, for subsequent experiments, we scaled the constructs down to a 4-well plate format. This reduced the minimum medium volume from 2.5 ml to 0.5 ml, reducing the necessary serum volume from 500 μ l to 100 μ l per construct.

Before reaching this conclusion, in this first experiment, we used the larger format to test the effect of five different conditions: control (no serum), healthy patient serum, AChR MG serum, MuSK serum, and BTX as an AChR blocking control. At this point, we still had not developed the GCaMP6⁺ myoblast cell lines, and so we planned to use fluo-4 to evaluate muscle function. We incubated constructs with the non-decomplemented serum for 48 hours and imaged the calcium response to ACh after treatment for all constructs.

The analysis of fluo-4 images was not possible due to loss of fluorescence when recording many samples on the same day, which we had not anticipated before the experiment design and treatment timepoints. Therefore, we could not perform a reliable calcium analysis after these serum treatments, which is what prompted us to use GCaMP6 to avoid this problem. However, we did perform immunostaining of these muscle constructs after treatment, to visualize autoantibody binding to endplates.

As shown in **Figure 52**, we observed that the presence of AChR clusters was greatly reduced in the anti-AChR treated samples, while it remained similar to the samples treated with healthy patient serum control in anti-MuSK samples. In the only isolated AChR clusters observed in the image, there was colocalization with human autoantibodies, indicating that there was probably an antibody-mediated destruction of AChR clusters. Interestingly, we also observed some colocalization events in the anti-MuSK samples, indicating that endplates must contain MuSK protein colocalized with AChR clusters.

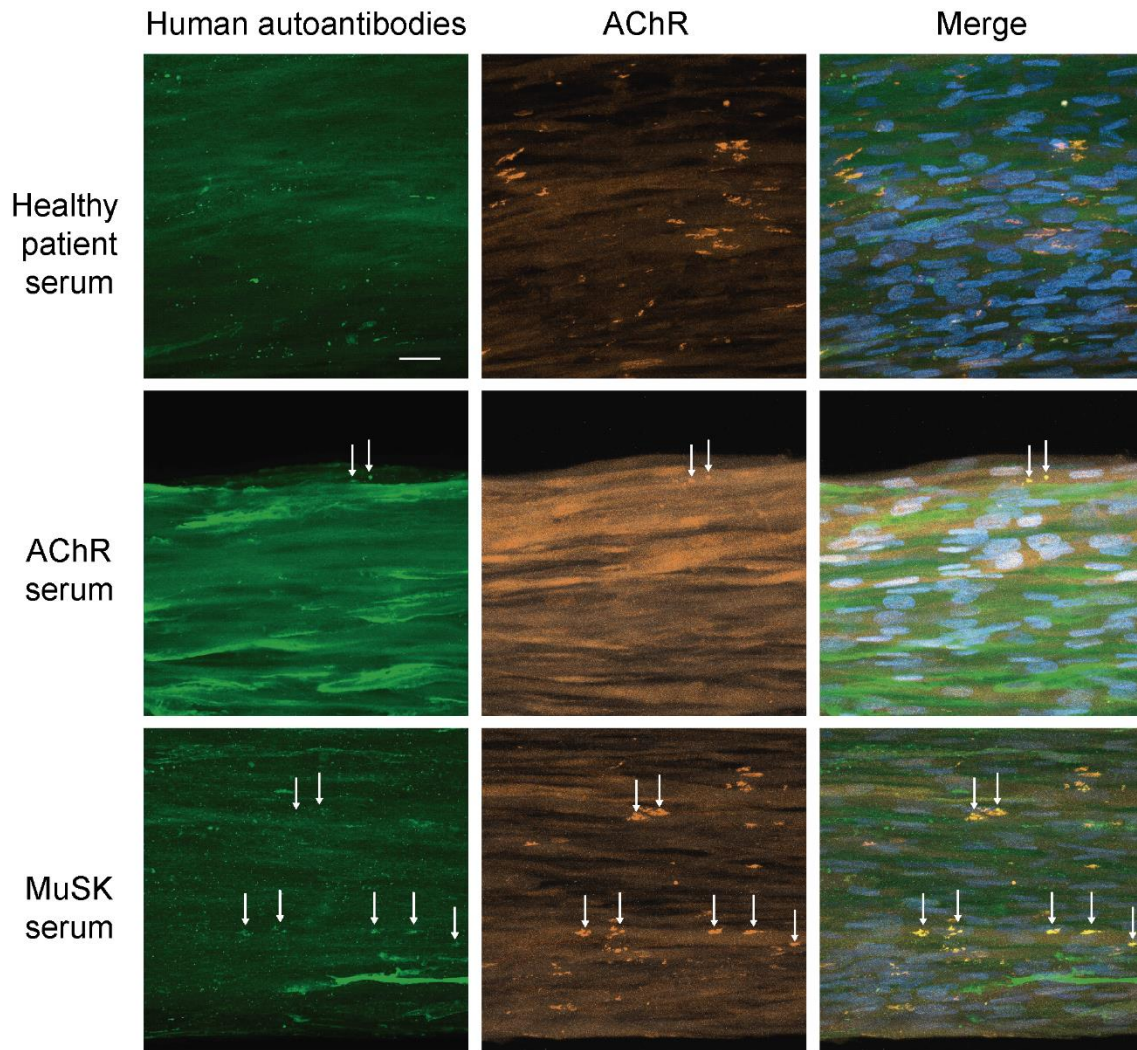


Figure 52. Confocal images of AB1079 3D muscle constructs treated with healthy, MG AChR and MG MuSK at a 1:5 dilution. Endplates stained with BTX-555 and autoantibodies with anti-human 488. Nuclei stained with Hoechst 34580. Maximum intensity projection is shown to represent all of the endplates in the whole construct. Colocalization of antibody binding sites with endplates is marked with arrows. Scale bar: 20 μ m.

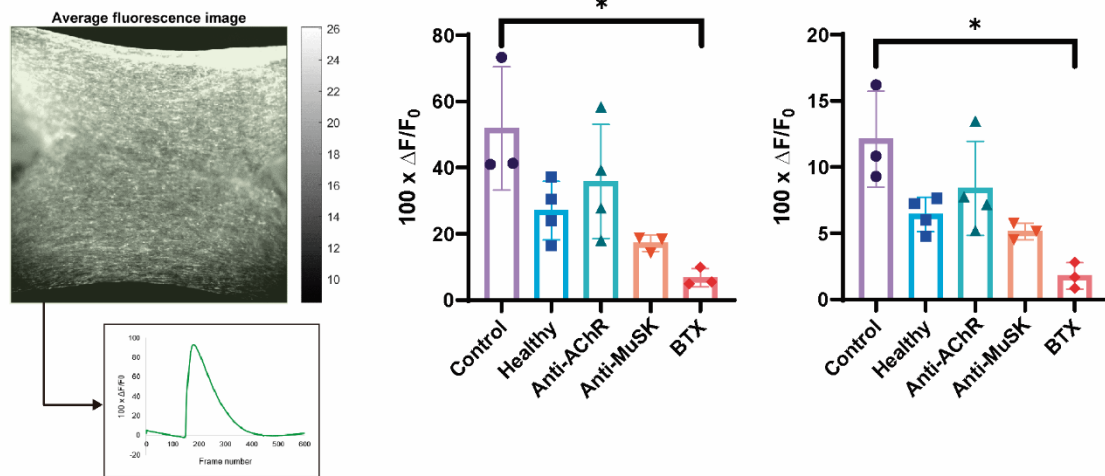
After this experiment, we transitioned to the use of GaMP6⁺ myoblasts to quantify muscle function alterations. We used smaller (4-well format) constructs to reduce the necessary serum volume and evaluated the global calcium transients across the whole muscle construct in response to ACh stimulation. In the first experiment we performed with these conditions, we also did not deplete the serum and added it at a 1:5 dilution as in the previous experiment. We tested the same conditions as mentioned before: control (no serum), healthy patient serum, AChR MG serum, MuSK serum, and BTX.

When processing calcium recordings of GCaMP6⁺ myoblasts, we noticed that calcium transients propagated in a wave that lasted several seconds. In the literature that inspired the use of this GECI (Afshar Bakooshi et al., 2019; Afshar et al., 2020), constructs were comparably smaller and thinner, which probably allowed them to exhibit an almost simultaneous illumination of the whole construct. Therefore, they extracted traces from a single ROI spanning the whole muscle construct. In contrast, our constructs exhibited a wave-like propagation of cytoplasmic calcium across the construct, which began at a different region in each muscle construct. The difference in the origin region of the wave was due to small differences in pipette placement for ACh dispensing.

In order to account for the wave propagation effect, we decided to implement an analysis that separated the field of view into four quadrants, defined as four ROIs. In this way, the maximum $\Delta F/F_0$ of each ROI could be computed separately. If only one ROI were defined, the mean $\Delta F/F_0$ over time might appear globally lower, and changes in muscle function may be obscured. Indeed, when we compared both types of analysis, comparison of muscle function with 1 ROI made it appear as if the only significant difference in $\Delta F/F_0$ was between the control (without serum) and the BTX-treated cells. The same result was seen when comparing maximum $\Delta F/F_0$ and mean $\Delta F/F_0$ (**Figure 53**).

When we applied the 4-ROI analysis, we observed that the BTX $\Delta F/F_0$ was again significantly lower than the control. When the means are compared, there is no significant effect of MG serums, but all conditions are significantly different from BTX. Nevertheless, when maximum fluorescence is compared, the reduction in $\Delta F/F_0$ in the case of the MuSK treatment is considered statistically significant from the control (but not from the healthy patient serum). This is because the $\Delta F/F_0$ of the healthy patient serum-treated samples was unexpectedly lower than that of the control, although the difference between the two was not statistically significant. This led us to use more than one healthy control in subsequent experiments.

1 ROI analysis



4 ROI analysis

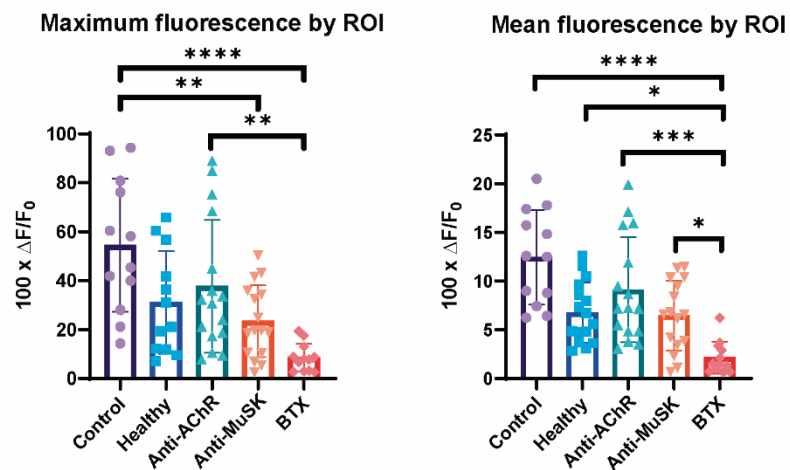
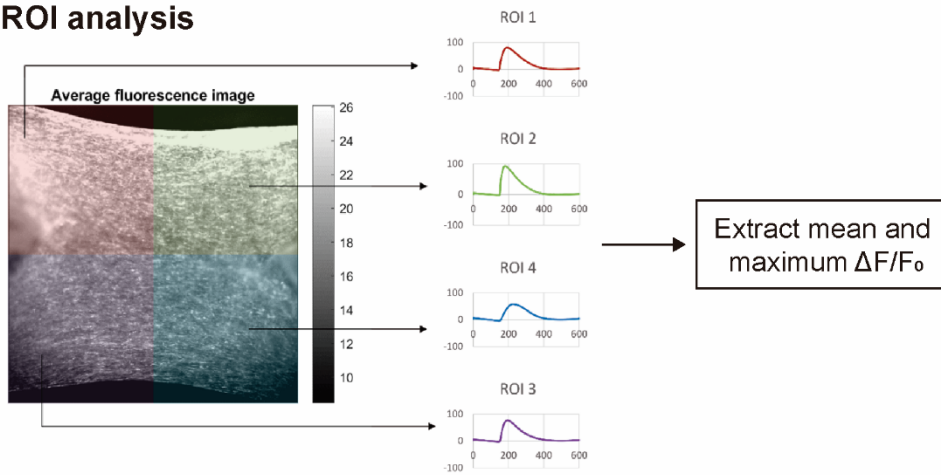


Figure 53. Comparison of calcium analysis strategies with 1 ROI or 4 ROIs to compare functional differences in non-decompensated MG serum-treated constructs generated with GCaMP6⁺ AB1079 cells.

To control the variable of complement activation, we decided to perform an experiment with de-complemented serum. As the patient serum constituted 20% of the medium volume, the effect of complement present in the serum was expected to be non-negligible. Therefore, we heat-inactivated the serum before adding it to the medium and performed treatments and calcium analysis in the same way as before. We observed that the effect of anti-MuSK serum, in this case, was not statistically significant, and the only significant difference was between the control and the BTX condition (**Figure 54**). This result was perplexing in the sense that MuSK autoantibodies generally do not activate complement. However, we are unsure whether other factors present in the serum could be interfering, or if the heat inactivation could have partially denatured the antibodies.

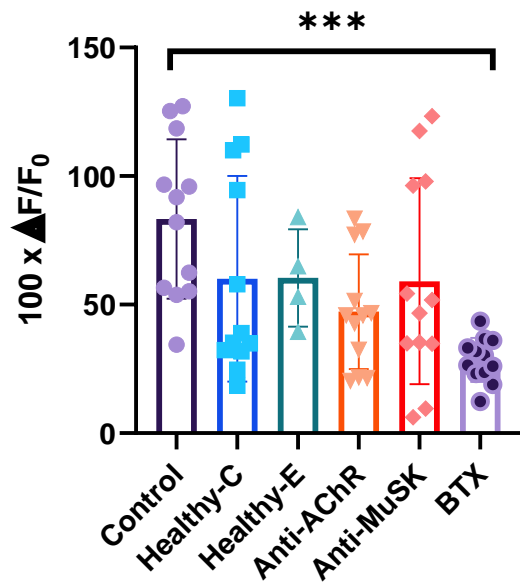


Figure 54. Differences in maximum $\Delta F/F_0$ (from calcium analysis with 4 ROIs) in de-complemented MG serum-treated constructs generated with GCaMP6⁺ AB1079 cells.

As we thought that serum components, and not only complement, could be interfering with the activity of autoantibodies, we decided to use purified IgGs instead of serum. A typical method to purify IgGs is to use an affinity purification system with Protein A or Protein G (Afshar Bakooshli et al., 2019). However, this method requires elution with acidic buffers, which can influence antibody activity in downstream processes. Thus, we used an alternative purification system not based on affinity, which is the Melon™ Gel IgG purification kit from ThermoFisher. This method uses resin columns and an elution buffer with a more neutral pH, to guarantee greater antibody stability. Still, although the column eliminates a large portion of serum contaminants, the resulting product has a

slightly lower purity, as it is based on affinity of unwanted proteins to the resin, and not on specific affinity of IgGs.

First, we received IgGs purified with this system without further concentration, which had been quantified using a nanodrop spectrophotometer. We calculated the necessary volume to obtain a final concentration of 300 nM of IgG in our samples, as this concentration was used in a reference publication (Afshar Bakooshli et al., 2019). After treating constructs with this concentration of IgGs, we observed no significant effects. This led us to question whether the concentration of IgGs reported by the spectrophotometer could be overestimated, considering that the purification system is not entirely specific for IgGs. So, we loaded part of these purified IgGs onto an SDS-PAGE gel and performed Coomassie staining to visualize the typical two-band pattern of IgGs (heavy and light chains). As a positive control, we used a commercial secondary antibody (Figure 55).

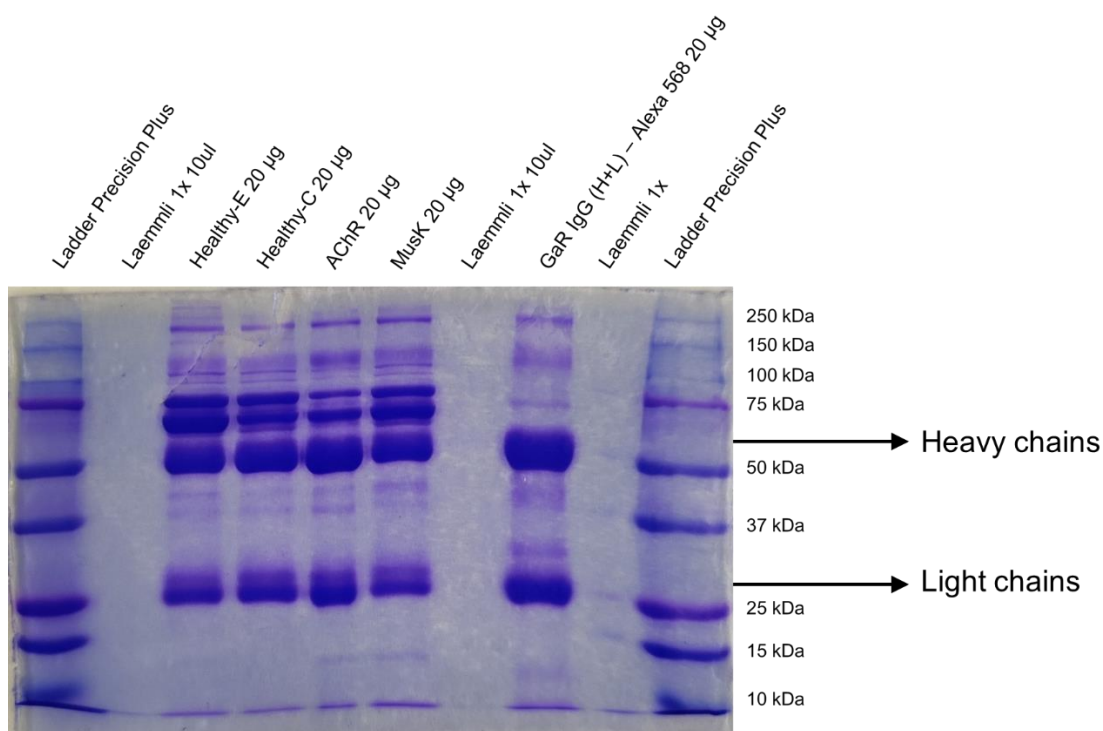


Figure 55. Coomassie staining of Melon™ Gel-purified IgGs loaded on an SDS-PAGE gel. Light and heavy chains can be seen in the positive control (GaR IgG (H+L)). 20 µg of protein were loaded in all cases.

The heavy and light chain bands of IgGs were clearly visible in all samples. Still, approximately half of the protein concentration that was quantified with the nanodrop was probably due to non-IgG proteins. Taking this into account, we decided to use twice the concentration that we had used in the previous experiment (2x) to be closer to the

originally intended 300 nM. Treatments with this IgG concentration were again not statistically different from controls, which is why we decided to also quadruple (4x) the initial concentration. Even at this amount, we did not observe any significant effects (**Figure 56**). In the analyses performed with purified IgGs, we show the muscle response after treatment normalized to the muscle response before treatment (recorded before adding serum), also expressed as the fold change in $\Delta F/F_0$. In this way, variability in basal muscle response among different replicates is taken into account. Results obtained by comparing only the response after treatment were also non-significant.

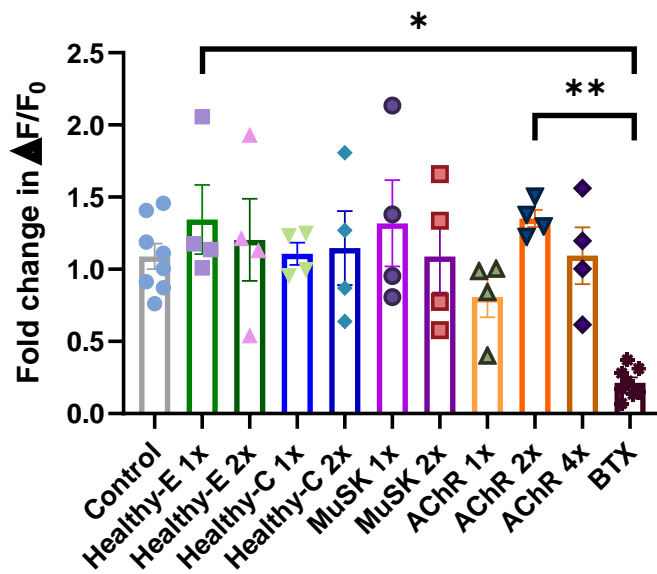


Figure 56. Effect of Melon™ Gel-purified IgGs at 1-4x concentration (estimated to be 150-600 nM) on muscle function of constructs generated with GCaMP6⁺ AB1079 cells.

As we had also had difficulty demonstrating pathogenic effects even when using a fairly high amount of serum (20%), we realized that the concentration of IgGs we were using was equivalent to a very low percentage of unpurified serum. So, we decided to purify more IgGs and then include an additional concentration step with centrifugal filters, as explained in the Methods section. The advantage of this concentration step was that it could increase the original IgG concentration about 25 times (25x), and also allowed a buffer exchange from the purification kit elution buffer to PBS. To compare different AChR patient sera, we purified serum from three different patients (AChR 1, 2, and 3). These were the same serums that were used in **Figure 51** to perform 2D antibody binding analyses.

Despite the much higher concentration, which was equivalent to adding 10% unpurified serum, we still did not see any effect on muscle function. This led us to believe that, at least in the case of AChR MG serum, the lack of complement could be affecting the pathogenicity of the antibodies. In the case of anti-MuSK antibodies, as we only tested serum from one patient, we cannot confirm that the lack of effect is due to low affinity of these antibodies, or whether the primary mechanism of this antibody is to generate ectopic AChR clusters, which cannot be differentiated from the non-innervated AChR clusters that are spontaneously generated in a monoculture model.

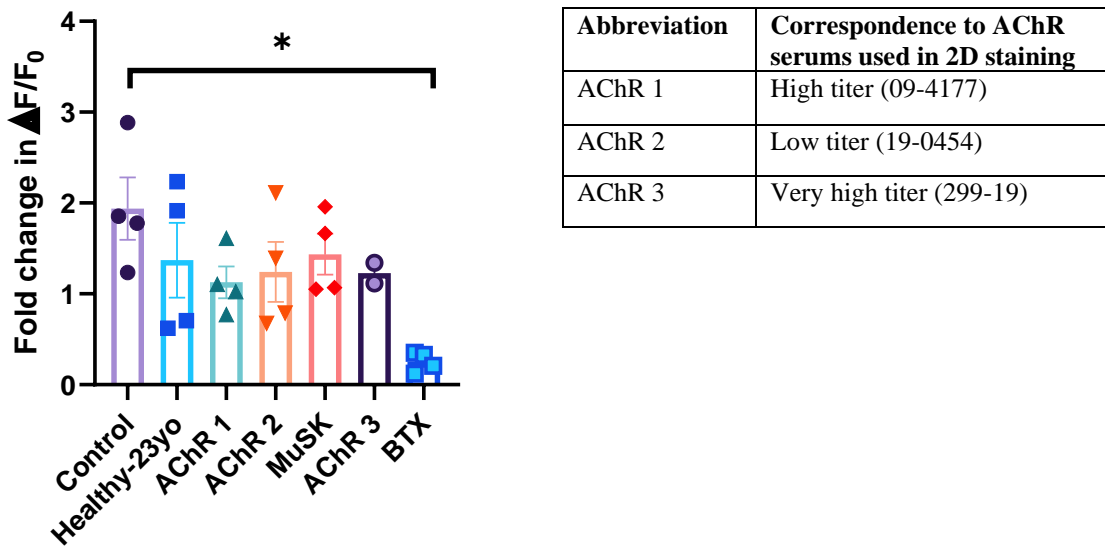


Figure 57. Effect of Melon™ Gel-purified and 25x concentrated IgGs on muscle function of constructs generated with GCaMP6⁺ AB1079 cells. Correspondence of AChR serum numbering to the serums used in 2D stainings shown in the table on the right.

Regarding the effect of these IgGs on endplate presence, we observed that IgGs added at approximately 300 nM (2x concentration) exhibited some colocalization events with endplates on the surface of muscle constructs (**Figure 58**). However, the AChR clusters were not drastically reduced as seen when using non-decomplemented serum. Colocalization was only visible in isolated regions at a more superficial level of the construct (6 μm depth). This could potentially be due to an issue with fluorescent secondary antibody penetration and sensitivity of the imaging. In any case, the presence of remaining AChR clusters pointed at the possibility that complement-mediated destruction could be needed to observe the drastic changes seen in **Figure 52**.

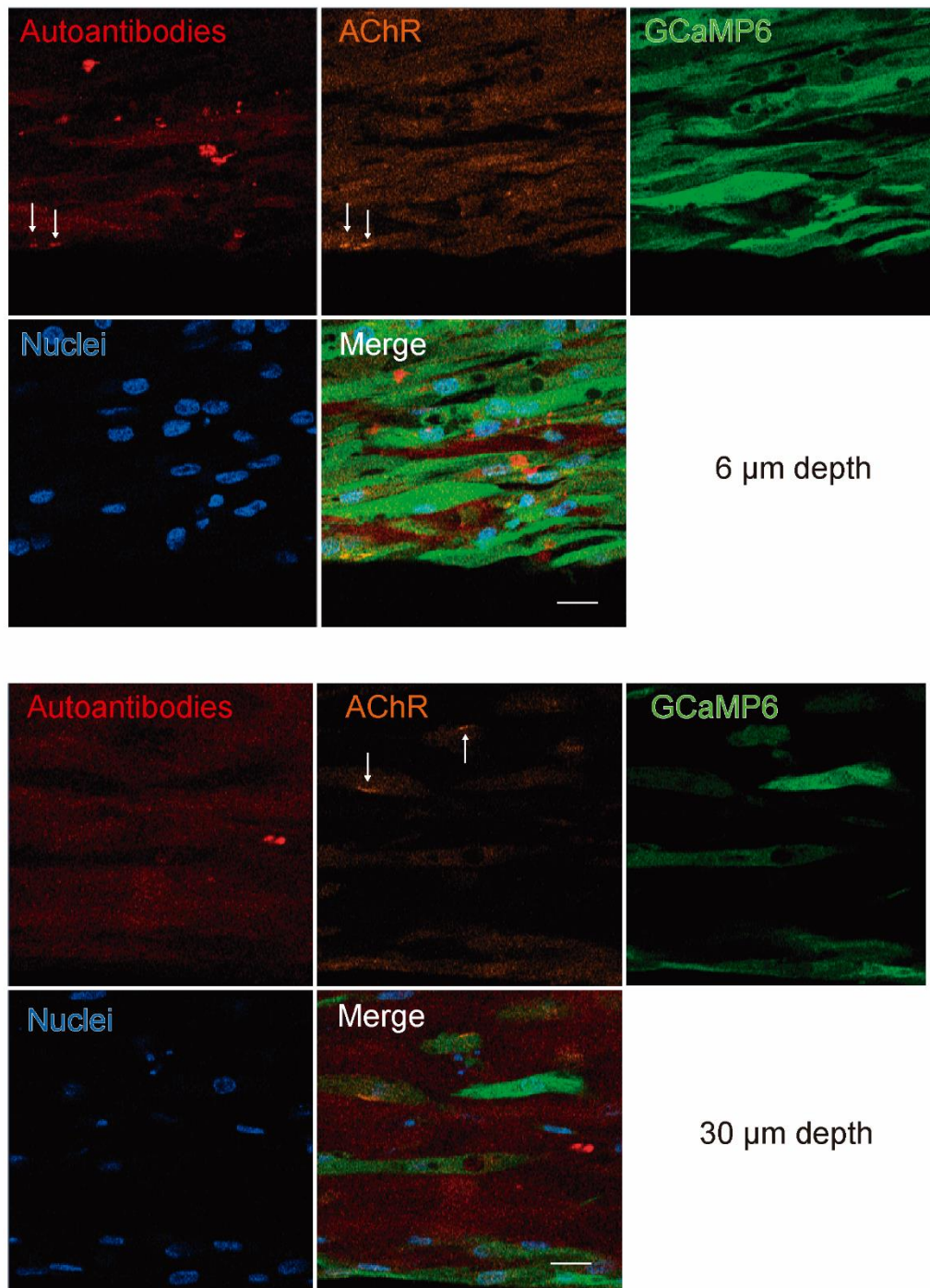


Figure 58. Staining of anti-AChR antibody binding at 2x (~300 nM) concentration in GCaMP6⁺ AB1079 muscle constructs. Examples of frames at different depths are shown to illustrate that colocalization was only seen on superficial layers. Scale bar: 20 μm.

DISCUSSION

Muscle *in vitro* models

Throughout the different platforms that we have tested for muscle differentiation, we have observed that Matrigel-based hydrogel formulations have beneficial effects on muscle differentiation that are maintained across different cell lines. However, alignment of muscle fibers is enhanced by using fibrin-based gels together with mechanical tension, as previously reported (Hinds et al., 2011). Variations of this technique have been effective for cell alignment in both of the 3D models that we tested with human myoblasts. We have demonstrated that 3D culture combined with the use of appropriate scaffolds can generate aligned and mature muscle fibers from immortalized myoblasts, which express differentiation markers and contain contractile sarcomeric structures.

We have also concluded that the use of appropriate anchors in 3D culture, combined with an appropriate scaffold, can provide a much-needed robustness of the generated muscle constructs. In our 3D VELCRO™ anchored model, one of the greatest advantages that we found was the simple setup combined with the complete lack of breakage events across all the experiments we performed. Our only proposal for improvement would be to modify the aspect ratio of the devices to obtain more elongated muscle fibers, as this could further improve alignment and contractile coupling between different myofibers. This was one of the main advantages of the free-floating muscle strips, which were highly elongated and aligned, despite presenting other issues with reproducibility.

Regarding functional analysis, we have tested contraction and calcium analysis for different applications. The use of motion analysis algorithms such as MUSCLEMOTION is more suitable for analyzing patterns of contraction when muscles show twitch contractions, in which the synchronicity and contraction speed can be evaluated over time. Instead, in tetanic contractions observed with ACh stimulation, MUSCLEMOTION data was less informative, as only a single contraction curve is observed, in which contraction speed is high at the beginning and returns to baseline at the tetanus plateau. In this situation, the exact moment of response to the stimulation was more difficult to determine than when applying electrical pulses, as tissue contraction occurred in a gradual manner. The use of calcium imaging is a convenient alternative for quantification of activity when using setups without a system to measure contraction force, as it allows

direct visualization of cell response to the ACh stimulus. In our experience, the use of genetically encoded calcium indicators such as GCaMP6s has proven clearly superior to using calcium dyes in 3D muscle constructs, as they ensure a more homogeneous and long-term expression of the indicator, and do not limit analyses to endpoint experiments.

The methodology of our 3D anchored model could be applied to numerous studies of muscle physiology. Regarding muscular diseases, it could be used to study human diseases such as limb-girdle muscular dystrophy (LGMD) or myasthenia gravis (MG), in which there is little to no motor neuron involvement in pathology. In addition, it could be used as a screening platform to evaluate the effect of drugs or other factors on muscle response to different types of stimulation, as it is amenable to electrical, chemical, and optical stimulation. In addition, with an appropriate source of MN, the system could be adapted to co-culture by using a non-compartmentalized technique similar to the one described in Afshar Bakooshli et al., 2019. Although we were interested in applying this methodology, we considered that the simpler monoculture model was useful for its currently intended purpose of analyzing MG serum effects.

Myasthenia gravis modeling

Current *in vitro* models of MG tend to utilize MN-SKM co-culture models to induce the formation of functional human NMJs. We are aware that our proposed platform does not include co-culture with motor neurons, but we still believe the model could be useful to gain insight on MG. First, the addition of agrin to the medium is a recognized way to mimic MN signaling, as demonstrated by previous evidence (Afshar Bakooshli et al., 2019; Ko et al., 2013). In our cultures, AChR clusters were present throughout the 3D construct and were responsive to ACh stimulation. Second, Western blot of total AChR revealed that the ϵ subunit is present in these cultures, and that it increases over time in culture. This finding had not yet been reported in monoculture of bioengineered muscles, and had only been naturally found in the co-culture model of Afshar Bakooshli et al., 2019 or induced in rhabdomyosarcoma cell lines overexpressing the ϵ subunit (Beeson et al., 1996).

Third, while we acknowledge that the architecture of NMJs is different from that of aneural endplates, we believe that the described mechanisms of autoantibody-mediated NMJ destruction would still be detrimental to muscle function in monoculture conditions.

For example, in reference to anti-AChR autoantibody effects, receptor internalization would probably occur differently than in junctional folds, as AChRs are clustered at the membrane surface and are not necessarily isolated inside deep folds. However, the most probable difference would be that the internalization of AChRs would be accompanied by comorbid internalization of adjacent receptors such as sodium channels, as suggested in Smith et al., 2021. This would still result in a reduced ability to depolarize in response to ACh stimulation, potentially more so than in AChR-only internalization.

In the case of anti-MuSK autoantibodies, we presume that at least one of the described mechanisms of NMJ damage cannot be analyzed in our system. In the case of bivalent binding that dimerizes MuSK receptors, the pathological consequence is the formation of ectopic AChR clusters. In a non-innervated model where AChR clusters are randomly organized, ectopic AChR clusters are no different from the originally present AChR clusters. In fact, it is possible that increased MuSK dimerization could result in an increased density of AChR clusters throughout the construct, which could create a paradoxical increase in muscle function. Alternatively, if there were a constant amount of AChRs at the muscle membrane, there could simply be no difference in ACh sensitivity. To complement AChR functionality data, studies of MuSK phosphorylation after anti-MuSK treatment should be performed.

In our first experiment with non-decomplemented serum and GCaMP6⁺ myoblasts, it was interesting to observe that the anti-MuSK serum treatment had a more pronounced effect than anti-AChR serum. Although *in vivo* MuSK MG is reported to be more severe than AChR MG (Rodolico et al., 2020), we would expect that in an *in vitro*, non-innervated model, the effect of AChR destruction could have a greater impact on endplate functionality than MuSK MG mechanisms of disease. This is especially surprising considering that, when staining endplates in anti-MuSK-treated samples, there did not appear to be a reduction in endplate presence, while a drastic reduction did take place in the anti-AChR-treated samples. In addition, we did not expect the effect of MuSK treatment to be abolished by serum decompensation, but we suspect that the heat inactivation could have altered the serum or antibodies in other uncontrolled ways. Further experiments would be necessary to clarify this data.

From the experiments with purified IgGs, in which we did not observe an effect even at concentrations equivalent to adding 10% serum, we can infer that complement presence

is probably important at least for the pathogenic mechanism of the anti-AChR antibodies. Staining of anti-AChR IgG binding also revealed that there was not a complete loss of AChRs when using these purified IgGs, which is consistent with the hypothesis that complement plays a major role in receptor degradation. In the case of the anti-MuSK antibodies, we believe that it would be beneficial to compare serums from more than one patient, as there can be significant variability in affinities that could affect results. In one publication, it was said that for some MG serums, a purified IgG concentration equivalent to adding 40% serum was needed to observe an effect on muscle function (Vila et al., 2021), meaning that concentration may need to be further increased in future experiments.

In all, we consider that future MG modeling experiments could focus on implementing the following conditions: 1) Use of purified and concentrated IgGs dialyzed to PBS and standardizing concentrations across samples; 2) Preferentially using sera with higher antibody titers or from patients with more severe symptoms, and/or performing a 2D endplate binding analysis before using them for treatments in 3D constructs; 3) Addition of a complement source to evaluate the influence of complement activation on IgG effect, 4) Use of at least 3 different patient serums for each serology, 5) Performing MuSK phosphorylation analyses, and 6) Testing different concentrations of each IgG.

**CHAPTER 2. Development of a 3D scaffold-based
axotomy model and application of optogenetic stimulation to
evaluate its potential in axonal regeneration**

INTRODUCTION

Neuronal regeneration in the central nervous system

Every year, between 250.000 and 500.000 people suffer a spinal cord injury (SCI), according to the World Health Organization. Spinal cord injuries generally occur after traumatic events, but can also be related to certain disease states. Paralysis resulting from these incidents is debilitating and can irreversibly alter the patient's life. Unfortunately, neurons in the central nervous system (CNS) fail to regenerate, and attempts to improve recovery are notoriously unsuccessful. Although a small regenerative potential exists in developmental stages, it is drastically reduced after birth. In contrast, the peripheral nervous system (PNS) has an impressive ability to regenerate, which points at fundamental differences in regulation between these two systems. The factors underlying these differences in regenerative ability are a combination of intrinsic and extrinsic factors (Figure 59).

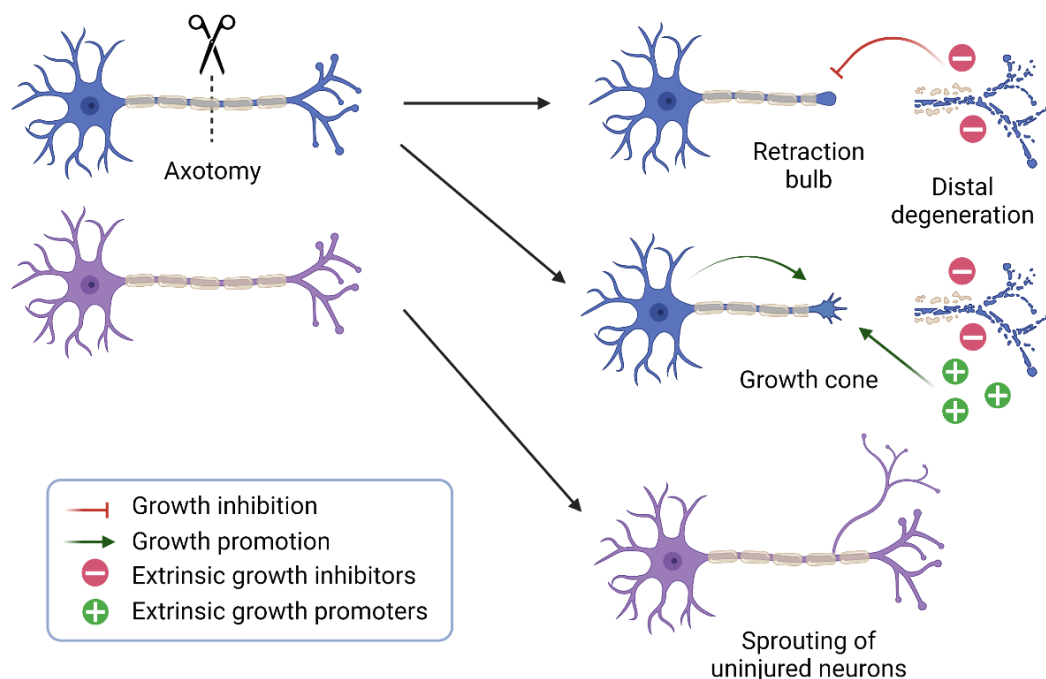


Figure 59. After axotomy, regeneration depends on intrinsic and extrinsic factors, which dictate the formation of a non-regenerating retraction bulb or a regenerating growth cone. Adjacent neurons can also sprout in response to injury, contributing to functional recovery.

After axotomy, the distal portion of the axon degenerates and releases inhibitory factors, which creates an inhibitory environment around the injury site. A neuron with a low intrinsic regenerative ability will fail to regenerate in these conditions, forming a retraction bulb at its severed end. However, if the neuron has a higher intrinsic

regenerative capacity and/or resides in a permissive environment with extrinsic growth promoters, the neuron can form a growth cone that allows it to regenerate. This growth cone has a similar molecular organization as the growth cones present in developing neurons. In parallel, neuronal injury triggers sprouting of adjacent neurons, and the contribution of sprouting to overall recovery of connections can even be predominant over true regeneration (Gordon, 2009; Rosenzweig et al., 2010). Thus, functional recovery is thought to occur as a combination of regeneration and sprouting.

Cellular and molecular events after CNS injury

Events necessary for regeneration of the injured cell

Immediately after a neuronal injury, there is a calcium influx into the cell due to breaching of the membrane. This temporarily changes the osmotic balance of the cell, but also constitutes a pro-regenerative signal, as axons fail to regenerate in a calcium-free environment (Kamber et al., 2009). Calcium signaling also mediates rapid membrane resealing, protein synthesis, and cytoskeletal reorganization to initiate the formation of a growth cone. In the PNS, this local calcium increase also propagates to the soma (Rishal & Fainzilber, 2014), inducing pro-regenerative responses such as nuclear export of histone deacetylase 5 (HDAC5), a regulator of pro-regenerative gene expression (Cho et al., 2013). Nevertheless, this mechanism has not been proven to function equally in CNS injuries; in fact, differences in calcium signaling and HDAC regulation have been reported for spinal cord injuries in a publication from our laboratory group (Hervera et al., 2019).

In non-transecting injuries, such as contusive SCI, mechanopores of various sizes form on the membrane and allow the entry of calcium. These pores are often resealed spontaneously, which permits rapid restoration of ionic homeostasis. Membrane resealing occurs in two steps: firstly, the membrane collapses at the proximal end, and secondly multivesicular complexes accumulate near this area forming a sealing patch. If axons are unable to restore homeostasis, degeneration ensues. Although axons are unable to resealed the membrane at low extracellular calcium concentrations (Spira et al., 2002), axonal degeneration can be rescued by removing calcium from the medium in non-transecting injuries (P. R. Williams et al., 2014). Thus, calcium handling can have contradictory effects at different stages of membrane repair. The calcium-activated protease calpain has

also been reported to be ambiguous in its promotion of regeneration: while its inhibition blocks membrane resealing in mammalian axons (M. J. Howard et al., 1999; Yoo et al., 2003), calpain blocking can also rescue axons from degeneration (P. R. Williams et al., 2014).

After membrane resealing, growth cone formation is initiated. Growth cone assembly is dependent on the origin and age of the neuron, as well as calcium concentration. In vitro studies on mammalian CNS cells have shown their inability to construct a functional growth cone (Kerschensteiner et al., 2005; Lorenzana et al., 2015), in contrast to the robust growth cone formation observed in PNS cells (Ertürk et al., 2007). The main factor that determines these differences is cytoskeletal organization at the injury site. In a functional growth cone, microtubules are organized and can effectively transport mitochondria and anterogradely transported vesicles. At the growing periphery, F-actin forms bundles that drive motility of the axon tip. In turn, retraction bulbs show disorganized microtubules, which cause accumulation of anterogradely transported vesicles and mitochondria. A number of axonal proteins that act as microtubule and/or F-actin stabilizers have been described as key regulators of regeneration, highlighting the pivotal role of the cytoskeleton in this process (Z. He & Jin, 2016) (**Figure 60**).

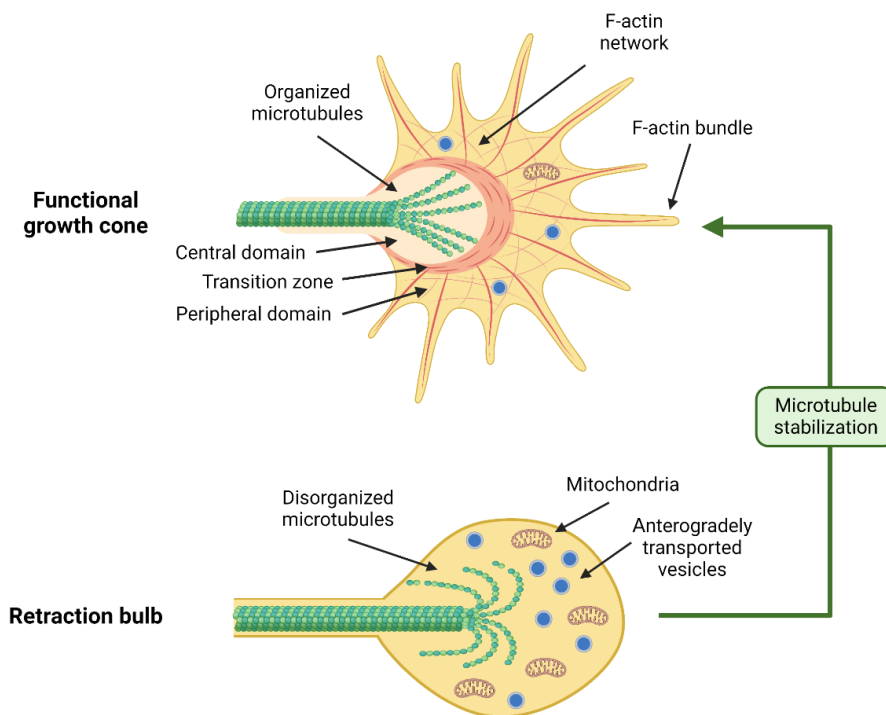


Figure 60. Diagram of the subcellular organization of a functional growth cone or retraction bulb. Microtubule organization and axonal retrograde transport are essential for regenerative success. Microtubule stabilization can rescue refractory neurons and allows them to organize a growth cone.

Pharmacological microtubule stabilization can prevent retraction bulb formation, as shown by several studies (Ertürk et al., 2007; Hellal et al., 2011; Ruschel et al., 2015). Acetylation and tyrosination of tubulin are also implicated in this process. Increases in tyrosinated tubulin and decreases in acetylated tubulin are required to support growth cone formation, but it is only observed in PNS injury and not CNS injury (Cho & Cavalli, 2012). HDAC5 participates in tubulin deacetylation, as shown by the correlation between axonal gradients of HDAC5 and deacetylated tubulin (Cho & Cavalli, 2012). In turn, tubulin tyrosination is mediated by tubulin tyrosine ligase (TTL) (Erck et al., 2005). There are many other regulatory mechanisms involved in growth cone regulation, including epigenetic regulation (Hervera et al., 2019; Puttagunta et al., 2014), which are difficult to summarize in a general introduction.

Even when all the necessary steps for growth cone formation are accomplished, axons still may need to travel long distances to reach their target, depending on the original length of the axon and the location of the injury. During development, axons often grow tethered to their target, but after an injury to the adult CNS, cells must embark on a *de novo* growth course that requires a constant supply of energy and building blocks. Therefore, this requires an anabolic metabolism of the cell for protein synthesis, as well as efficient transport mechanisms along the axon (Z. He & Jin, 2016).

Events in the injury environment: The glial scar

Damage to the CNS results in a glial response, known as reactive gliosis, which leads to the formation of an inhibitory environment known as the glial scar. This process occurs in SCI but is also present in traumatic brain injuries, stroke, and some neurodegenerative diseases (Adams & Gallo, 2018). The glial scar is a dynamic structure that evolves over several days. Even if some injured neurons successfully begin to assemble a growth cone after injury, the progressively inhibitory environment of the glial scar has the ability to cause collapse of these growth cones, ultimately leading to regenerative failure.

The first cells to be recruited to the injury site are macrophages from the bloodstream, together with microglia that migrates from nearby regions of the tissue. This occurs in the first hours of the injury, as a result of blood-brain barrier (BBB) breakdown and leukocyte extravasation (Cregg et al., 2014), resulting in a presence of abundant immune cells at the lesion core. Activated microglia and macrophages secrete matrix metalloproteases that

contribute to vascular permeability that furthers the inflammatory response. The lack of a proper healing process in CNS injuries in contrast to other tissue injuries is partially justified by macrophagic and microglial malfunction, which result in an excessive inflammatory response, as reviewed in Mesquida-Veny et al., 2021.

After 3-5 days, NG2-glia/oligodendrocyte precursor cells (a type of glial cells positive for the NG2 proteoglycan) also migrate to the lesion. This cell type is thought to have a supportive role, attracting and stabilizing injured axons (Dimou & Gallo, 2015). In the end, however, the majority of the structure is composed by astrocytes. This cell type, which has a broad spectrum of functions supporting neuronal physiology, has the ability to become activated and proliferative in response to stress. This activation results in a slow buildup of astrocytes, leading to a presence of an abnormally high density of cells with larger and more complex processes, intertwined and surrounded by ECM. Understandably, this generates a dense barrier for axonal growth, as shown in **Figure 61**. However, apart from their physical impediment to growth, an important reason for the inhibitory nature of reactive astrocytes is that they secrete chondroitin sulfate proteoglycans (CSPGs). CSPGs are the predominant inhibitory factor present in the glial scar (Ohtake & Li, 2015), and can remain at the lesion site for months (Cregg et al., 2014).

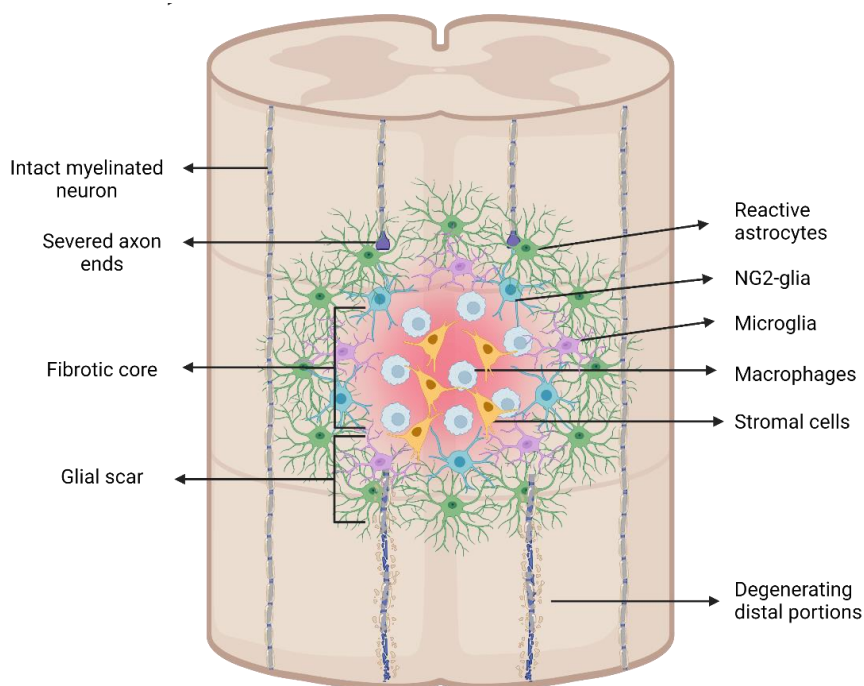


Figure 61. A simplified diagram of the glial scar in a contusive spinal cord injury. At the core of the lesion, stromal cells (yellow) generate a fibrotic core infiltrated with macrophages (blue-gray). Around the core, reactive astrocytes (green), NG2-glia (teal) and microglia (pink) form the glial scar. Distal portions of axons experiment Wallerian degeneration and release cell debris.

In addition to the previously mentioned cell types, a large population of fibroblasts or stromal cells occupy the lesion core, which produce vast amounts of extracellular matrix proteins such as laminin and fibronectin, forming a fibrotic scar. If the injury penetrates the meninges, meningeal fibroblasts also infiltrate the core. This cell type contributes to the inhibitory nature of the scar by secreting axon-repulsive molecules and amplifying astrocyte activation. As the distal portions of axons experience Wallerian degeneration, oligodendrocytes and myelin sheaths also degenerate, releasing myelin debris in the vicinity of the proximal axon stumps. Although myelin debris is slowly cleared by microglia, this process can take weeks, which gives enough time for these molecules to cause growth inhibition to injured axons.

The inflammatory reaction caused by the injury also leads to the production of a reactive oxygen species (ROS). This highly oxidative environment also contributes to growth cone retraction. Nevertheless, ROS also participate in cellular signaling for wound healing, and therefore play a role in axonal healing as well as nerve degeneration (Hervera et al., 2018). Although the glial scar has traditionally been regarded as a barrier for SCI recovery, in recent years it has been shown that the lack of a glial scar (Anderson et al., 2016; Gu et al., 2019) also inhibits recovery. This supports a novel theory that the glial scar plays a dual role in SCI recovery (Yang et al., 2020). The complexity of the glial scar continues to be studied to dissect its interaction with neurons and to direct targeted therapeutic approaches.

***In vitro* axotomy models**

In general, axotomy in cultured neurons has been extensively studied in 2D conditions, but not as much in 3D settings. There are several available methods for axotomizing 2D-cultured cells, which mainly rely on complete transection of axons, instead of the compression injuries that are induced in *in vivo* nerve crush experiments (similar to real-life injuries). Despite this simplification, acute/complete axotomy is one of the simplest and most reliable methods to study response to injury *in vitro* (Varier et al., 2022).

Mechanical tools such as scalpels or needles to transect axons can be used in open configurations such as cells seeded on coverslips (Ohtake et al., 2018; Ziegler et al., 2010). One of the first neuronal injury models, from the inventor of compartmentalized systems for axonal isolation, Robert Campenot, used cold sterile water sprayed through a 23-gauge needle to transect axons (Kimpinski et al., 1997). Laser axotomy has also been

used in *in vitro* (Cengiz et al., 2012) and *in vivo* (Kanamori et al., 2012) models, offering the advantage of precise, rapid, and complete transection. This method is particularly interesting for achieving targeted transection of single axons in cultured neurons (Kunik et al., 2011), or even in live model organisms (Byrne et al., 2011). Nevertheless, this method could be considered less physiological, as typical nerve injuries mostly result from mechanical trauma.

Microfluidic devices for axotomy

Recent models of axotomy use PDMS-based MFDs to create somal and axonal compartments, which isolate axons for transection and regrowth analyses. A typical configuration for axonal isolation uses axon channels of $\leq 10 \times 10 \mu\text{m}$ (width x height) to impede cell bodies from migrating into the channels. Neurons are seeded into a somal compartment, from which axons grow into the microchannels until they reach an axonal compartment. Channels are usually several hundreds of micrometers long (300-900 μm) to ensure isolation in the axonal compartment. An established vendor of this type of MFDs is Xona Microfluidics®, which makes these devices be commonly referred to as Xona devices (left diagram in **Figure 62**).

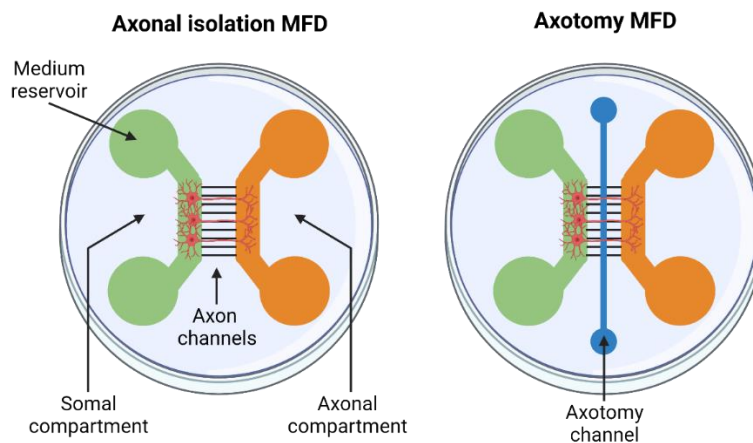


Figure 62. Diagram showing two axonal isolation MFDs. On the left, a traditional two-chamber axonal isolation MFD with an axonal and somal compartment connected by microchannels. On the right, a similar MFD with an axotomy channel for vacuum/air bubble axotomy.

As these MFDs are often closed systems, they do not allow the introduction of sharp tools or lasers. Therefore, axotomy can be achieved by pipetting or vacuum aspiration to create shear forces on the axons. In some cases, the axonal compartment medium is pipetted multiple times or vacuumed to disrupt axons (Ohtake et al., 2018; J.-N. Zhang et al., 2016). Another model, developed and used by our laboratory, uses a microfluidic device

with axonal isolation channels containing an axotomy channel that perpendicularly intersects axonal isolation microchannels (right diagram in **Figure 62**). By the introduction of air bubbles into the axotomy channel, all axons are effectively transected at the same length (Mesquida-Veny et al., 2022; Sala-Jarque et al., 2020; Tong et al., 2014). A comparison of these two methods can be seen in **Figure 63** (reproduced from the review of D. Lee et al., 2023).

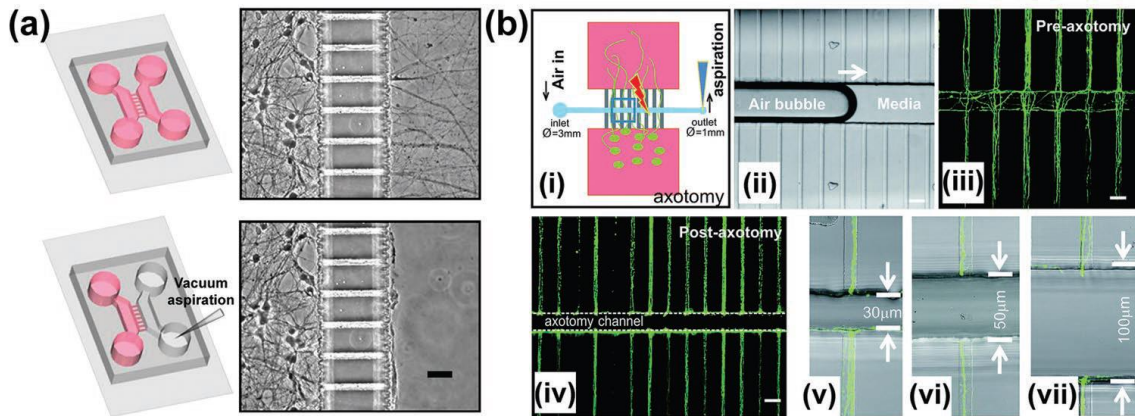


Figure 63. Two methods of axotomizing neurons by pipetting. In (a), axons in the axonal compartment of a non-axotomy MFD are vacuum aspirated. In (b), GFP positive axons are transected by an air bubble (Tong et al., 2015). Reproduced from D. Lee et al., 2023.

Regarding 3D models of axotomy, fewer reports are available in literature. A recent publication uses a microfluidic device that has the option of being open and accessible to axotomy. Axons growing in hydrogels are axotomized by puncturing the hydrogel with a needle (Bang et al., 2022), after which new hydrogel is added in its place. While the design of this MFD is ingenious in the way it allows open and closed configurations, the puncturing method does not allow a clean transection of the axons. The lack of microchannels causes bundled growth of axons, which makes it more difficult to track regrowth of individual injured axons. Nevertheless, the authors do propose an interesting way of tracking regeneration into the new hydrogel, which is the introduction of fluorescent particles in the new gel.

Most recent models including neurons in 3D microfluidic devices are not suited to axotomy, due to the lack of an axotomy channel or an open configuration to allow mechanical transection of hydrogels. Also, some models that include hydrogels do not necessarily culture axons in a 3D environment. For example, in an article by Lotlikar et al., 2022, neural progenitor cells are differentiated inside a “3D matrix” inside axonal isolation MFDs. Despite the 3D claim, the publication only uses a very diluted Matrigel

solution (1:10) in the somal compartment, which is not intended to penetrate into the axonal isolation channels. Although it is possible to introduce hydrogels into MFDs with axon channels, including the axotomy device used in our laboratory (Tong et al., 2014), its correct penetration into small microchannels is difficult to achieve. In addition, complete axotomy by the use of air bubbles is less reliable than when using liquid media.

Sources of cells for *in vitro* neuronal models

The primary obstacle for developing *in vitro* models of neural tissue is the non-proliferative nature of neuronal cells. This makes the generation of neuronal cell lines a technical impossibility. Therefore, there are two main approaches to neuronal tissue modeling, which are the use of primary neuron cultures (from murine or rat origin, most commonly), or the use of stem cells and direct reprogramming approaches.

Murine cultures have the advantage of being highly characterized, having been used in *in vitro* models since the beginning of neuroscience research. Indeed, our research group has also predominantly used primary cultures for around three decades. The main strengths of this cell source is that physiological properties of primary neurons are very similar to *in vivo* neurons. Traditional primary cultures have been performed mostly on 2D substrates, and although 3D models using primary neurons have been perfected in the past few years (J. Zhang et al., 2022), they were already explored as early as the 90s (Placzek et al., 1990).

Several neural stem cell lines are used in *in vitro* models. Rodent cell lines include C17.2 (Lundqvist et al., 2013), NS-1, and NE-4C; and common human stem cell lines include neuroblastoma cell lines such as SH-SY5Y (Hoffmann et al., 2022) and Neuro2A (Tremblay et al., 2008), and encephalic fetal immortalized stem cells such as hNS1 (Villa et al., 2000). The main attractive feature of neural stem cell lines is the simplicity of their maintenance and differentiation protocols, combined with the possibility to obtain human-derived neurons. Neural stem cell lines present some limitations, as the origin of the cell line can dictate the properties of the resulting cells, and their physiological properties are not always parallel to *in vivo* neurons.

As an alternative that allows more precise differentiation into specific neuronal lineages, iPSCs (Galiakberova & Dashinimaev, 2020) and embryonic stem cells (ESCs) (Gaspard et al., 2009) are used in many neuronal differentiation protocols and several *in vitro*

models (Marshall et al., 2023; Matamoros-Angles et al., 2018). These cells have been shown to be a promising source of functionally mature neurons with specific phenotypes, due to the vast array of possibilities opened by genetic modification methods and the possibility to design patient-specific models. However, the high complexity of these protocols creates a considerable technical barrier, which may be undesirable when patient-specific phenotypes or particular cell lineages are not a priority. Still, iPSC-derived neurons do not fully recapitulate the properties observed in primary cells (Berry et al., 2018).

To improve the maturation and physiology of neuronal models, neural organoids have become a promising field, with multiple applications in disease modeling (Sala-Jarque et al., 2022). Organoids can form layered structures organized in a similar fashion as brain regions, which adds physiological relevance to these models (Shou et al., 2020). As well as brain organoid, spinal cord organoids have also been developed with the appropriate spinal cord patterning mechanisms (Iyer & Ashton, 2022).

With all this in mind, the main constraint for axotomy models is the ability of the chosen cells to extend long, isolated axonal processes that are amenable to axotomy. Not all methods guarantee this outcome, as certain neural stem cells have been developed mainly for network analysis, electrophysiological studies, or cell therapy purposes. Neural organoids are also often grown in flotation, without the intention of obtaining axonal growth outside of the confines of the organoid. Therefore, the specific choice of cells must be tailored to the specific needs of the study.

Scaffolds for neuronal tissue modeling

The brain extracellular matrix is mainly composed of glycosaminoglycans such as hyaluronan, proteoglycans (i.e. neurocan, brevican, versican and aggrecan), glycoproteins such as laminin and tenascin, and a lower amount of fibrous proteins (i.e. collagen IV, fibronectin, and vitronectin) (Lam et al., 2019). Neural ECM is comparatively softer than most mammalian tissues, with brain tissue stiffness being in an average range of 1 kPa (Weickenmeier et al., 2016). With this in mind, hydrogels for neuronal culture must present a balance of appropriate biological and mechanical properties to allow *in vitro* survival and development of this fragile cell type.

Matrigel is a common choice for neural cell culture due to its biomimetic composition, as its main components are laminin (~60%), collagen IV (~30%), entactin (~8%) and the heparan sulfate proteoglycan perlecan (~2–3%) (Aisenbrey & Murphy, 2020). It also contains a variety of growth factors which promote neuronal growth and differentiation. Due to these properties, Matrigel has been incorporated into numerous *in vitro* models of neuronal tissue, both as a 3D scaffold (Bang et al., 2022; Tong et al., 2014; Wevers et al., 2016) and as a coating (Qian & Saltzman, 2004).

In our laboratory group, collagen type I has been used for many years as a suitable scaffold for analyzing growth and behavior of neuronal cells of primary origin (Borrell et al., 1999; Gil & Del Río, 2012, 2019). This collagen is extracted from rat tails and diluted in an acidic MEM medium, which is gentler for neuronal cells than the acetic acid solution used in commercial collagen products. Although collagen type I is not one of the main components of natural brain ECM, its high biocompatibility, mechanical properties, and ease of extraction make it a widely used choice for neuronal cell culture, and also one of the first published scaffolds for this purpose (Placzek et al., 1990).

The group of Dr. Jordi Soriano (a collaborator from the Physics department at the University of Barcelona) routinely uses PEG-fibrin hydrogels (Koroleva et al., 2016) for primary neuron cultures. The main advantage of these gels is their high transparency, which makes them amenable to microscopic imaging. In addition, the mechanical properties and porous microstructure of these gels can be tuned by modifying the ratios of its precursor ingredients. Another option which has a high transparency and also mimics the brain ECM are hyaluronic acid-based gels. As hyaluronic acid (HA) does not contain binding motifs, they are often formulated as hybrid gels with other protein components (Addington et al., 2017) or modified to contain binding domains (Seidlits et al., 2019). These gels are also amenable for use in regenerative medicine approaches (G. Jensen et al., 2020).

Many other synthetic hydrogels are being developed for neural cell culture, with tunable biological and mechanical properties. One example that is being currently applied in our research institute are gels based on methacrylated gelatin (GelMA) and alginate with or without HA, which can be applied to bioprinting through UV crosslinking of the methacrylate chains (Cadena et al., 2021; Pereira et al., 2023). Low cell viability after bioprinting is still an unresolved issue, due to a combination of neuronal cells' low

resistance to shear stress, UV crosslinking agents, and the need to print isolated cells instead of neural aggregates (i.e., neurospheres or explants, which are more suited to growth in hydrogels than dissociated cells).

Strategies for treating CNS injuries

As pro-regenerative factors encompass both intrinsic and extrinsic regulators, therapeutic mechanisms can also be targeted at increasing intrinsic regenerative capacity or at improving the permissiveness of the extracellular environment. Combinatorial therapies have also been explored, to create synergistic effects of different growth promotion mechanisms (Lu et al., 2004; Lu & Tuszynski, 2008).

In the category of extrinsic regulators, a first example could be the use of externally supplied neurotrophic factors that promote neuronal growth (Lu & Tuszynski, 2008). Another option that has been considered is the use of stem cell implantation to promote regeneration, with some success, although the development of cell-based therapies is still in more initial phases due to its complexity (Bonosi et al., 2022; Shin et al., 2018). Another example is the degradation of inhibitory factors, As CSPGs are the main inhibitory molecule in the glial scar, enzymatic digestion of CSPG with locally applied chondroitinase ABC has been applied *in vivo* to reduce scar inhibition (Bradbury et al., 2002). Notwithstanding, several drawbacks discourage the use of this bacterial enzyme as a treatment in humans (Ohtake & Li, 2015). An alternative to this enzyme was proposed last year, which is a human CSPG-degrading enzyme that can be incorporated into a hydrogel with sustained release properties (Park et al., 2022). Finally, another strategy is the use of bioactive scaffolds such as hydrogels or peptides that can guide neuronal regeneration or reduce glial scar formation. A recent example of significant clinical impact are the scaffolds used by Álvarez et al., 2021, which have been tested *in vivo* with impressive results.

In terms of pharmacological intervention, the main barrier for treating the CNS is the highly selective permeability of the blood-brain barrier (BBB). For this purpose, cell-penetrating peptides (CPPs) have been developed, which are able to cross the BBB and deliver cargo to neuronal cells. In addition, some CPPs may have an intrinsic therapeutic activity. In a collaborating group, a library of CPPs, based on synthetic cis- γ -Amino-L-proline-derived peptides, was generated (Farrera-Sinfreu et al., 2005). The library was tested on cerebellar granule cells, and preliminary results indicated that some of them

promoted axonal regeneration. Circumstantial technical issues with the purification of the peptides in the collaborating laboratory prevented us from testing these CPPs in cortical axons, but it would be interesting to examine their effects in future studies.

Next, we will devote the following subsection to therapies based on neuronal stimulation, also known as activity-based therapies. It has been proposed that maintaining neuronal activity can be beneficial for regeneration, and we have therefore explored the potential of optogenetic stimulation to improve regrowth after injury in this thesis.

Activity-based therapies

As explained previously, the transient osmotic imbalance resulting from an axonal injury constitutes a pro-regenerative signal. Therefore, maintaining neuronal activity could be a strategy to amplify the duration of this type of signaling. In addition, electrical stimulation can promote growth of non-injured neurons, increasing overall repair of synaptic connections. This is why electrical stimulation protocols have been applied as a therapy for nerve injury patients for many years, with limited success. However, this therapy is still more effective in peripheral nerve injuries than in SCI, and the mechanisms that explain its benefits are still not entirely clear.

One way in which electrical stimulation can improve regeneration is through its enhancement of neurotrophic factor release after injury. After axotomy, neurons naturally upregulate expression of neurotrophins. This upregulation is normally not immediate, as it begins after 7 days (Gordon, 2009). However, this process may be accelerated by electrical stimulation, as demonstrated in peripheral nerve repair (Al-Majed et al., 2000; English et al., 2006).

As well as increasing neurotrophin release, stimulation can also increase regeneration-associated gene (RAG) expression (Sharma et al., 2010). This has mostly been demonstrated in the PNS (Al-Majed et al., 2004). In our group, RAGs were not found to be upregulated in optically stimulated mouse cortical neurons, as analyzed by RT-PCR (Mesquida-Veny et al., 2022). This result was obtained despite having proof that neurons were becoming activated in response to the optical stimulus (*c-fos*, a marker of neuronal activity (Bullitt, 1990) was shown to be upregulated after stimulation). This could mean that the activation of intrinsic mechanisms of regeneration may not occur in the same manner in CNS neurons as it does for the PNS.

Cyclic adenosine monophosphate (cAMP), which plays numerous roles in regenerative signaling (Zhou et al., 2022), also increases after electrical stimulation. The use of rolipram, a cAMP-degrading enzyme inhibitor, was shown to improve regeneration in cervical SCI (Kajana & Goshgarian, 2009), and several other methods to increase cAMP have been used to promote regeneration. However, it has been shown that using electrical stimulation as a strategy to increase cAMP was not sufficient to induce regeneration of injured neurons in a rat model of SCI. Instead, functional improvements were due to an increase in sprouting from collaterals above the injury site (Batty et al., 2020). Other studies have also shown that stimulation of neurons improves regeneration through lateral sprouting and plasticity (Carmel et al., 2010, 2013, 2014; Engesser-Cesar et al., 2007; Goldshmit et al., 2008; Sánchez-Ventura et al., 2021).

Optogenetic stimulation

As highlighted in the general introduction, optogenetic stimulation can overcome some of the drawbacks of electrical stimulation, which has made it an attractive alternative for studies involving CNS regeneration (Ahmad et al., 2015). Although these techniques are limited in their clinical application due to the need to use light for internal tissues, they could provide valuable insights on the role of activity in promoting regeneration, as well as delineating appropriate targets for stimulation in patients (Hogan et al., 2020). Some recent publications have reported benefits of optogenetic stimulation in *in vivo* models of SCI (Deng et al., 2021), although in some cases this was still due to lateral sprouting (Petersen et al., 2022). Another different but complementary result is that optogenetic stimulation has been shown to enhance neuronal outgrowth in *in vitro* platforms (Hyung et al., 2019).

In our laboratory, cortical neurons cultured in 2D and optically stimulated after axotomy have shown that activity can promote regeneration in a permissive environment. However, from the results of this study, it seemed that optogenetic stimulation could not override the effect of an inhibitory environment (Mesquida-Veny et al., 2021). Therefore, we sought to use optogenetic stimulation in axotomized neurons in 3D *in vitro* models to complement these results.

OBJECTIVES

The objectives for this chapter stem from two fundamental pillars aimed at enhancing the *in vitro* models of axotomy and regeneration used in our laboratory. Our first goal was to use human neurons to increase the clinical relevance of the model, as primary mouse or rat neurons were the main neuronal source for our studies. Therefore, we decided to test different approaches using stem cell lines and direct reprogramming of human cells to address this need. The second objective was to develop 3D culture systems that would more accurately model the mechanical aspect of neuronal regeneration inside an extracellular matrix, as all the *in vitro* axotomy studies in the group had been performed in 2D culture.

Our final goal was to use the developed 3D platforms to study the effect of optogenetic stimulation on neuronal regrowth after axotomy. Therefore, the first constraint was that the model should sustain a robust outgrowth of long axons amenable to axotomy. In addition, these platforms should enable the modeling of a permissive or inhibitory environment for regeneration. This would serve to complement results on the regeneration of optically stimulated cortical neuron results obtained in 2D permissive and inhibitory environments (Mesquida-Veny et al., 2021).

Thus, the specific objectives for this chapter were:

1. Optimization of culture and differentiation protocols of neural stem cell lines and comparison of their axonal outgrowth in different hydrogel compositions.
2. Setup of a 3D axotomy platform using mouse cortical explants.
 - 2.1. Optimization of hydrogel composition for cortical explant culture.
 - 2.2. Development of a suitable axotomy method for hydrogel transection and regrowth analysis.
 - 2.3. Study of the effect of optogenetic stimulation on regrowth of ChR2⁺ neurons after axotomy, both in permissive and inhibitory environments.

MATERIALS AND METHODS

Cell lines: maintenance and differentiation protocols

C17.2-eGFP cell line

C17.2-eGFP is a murine neural stem cell line derived from cerebellum, expressing eGFP. This cell line is maintained in T75 flasks cultured in a humidified 37°C incubator with 5% CO₂. The maintenance medium is composed of DMEM (41966-029 Life Technologies) supplemented with 10% FBS (10500-064, Life Technologies), 5% NHS (26050088, ThermoFisher), 1% Glutamine 200 mM (25030-024 Life Technologies) and 1% P/S (15140-122, Life Technologies). Cells were passaged at a 1:50-1:100 dilution twice per week. Differentiation medium was composed of DMEM/F12 (11320033, ThermoFisher) supplemented with 1% glutamine 200 mM, 1% P/S, 1% N2 supplement (17502048, ThermoFisher) and 10 ng/ml of nerve growth factor (NGF, N0513, Sigma Aldrich) and brain-derived neurotrophic factor (BDNF, 450-02, Peprotech). Differentiation medium was added for 7 days and changed every 2-3 days. Cells were differentiated both in 2D and in 3D. For the former case, we used poly-D-lysine coated glass coverslips of 12 mm Ø in 24-well plates. In the latter case, aggregates were formed by the hanging drop technique as explained in the next section.

Hanging drop C17.2-eGFP aggregates

In some cases, aggregates of C17.2-eGFP cells were formed using the hanging drop technique, prepared using a protocol similar to the one in (Foty, 2011). Briefly, cells were counted and resuspended in complete C17.2-eGFP maintenance medium containing 0.5% methylcellulose, and droplets were formed on the lid of a large Petri dish. Different sizes of aggregates were made by adding 1000, 5000 or 10.000 cells per drop. These numbers were decided based on a reference that used 5000 cells per aggregate in another aggregation technique (L.-G. Zhang et al., 2014). The lid was inverted quickly and placed on top of the dish containing a layer of PBS to create a humidifying chamber. The next day, aggregates were harvested and seeded in hydrogels using the hydrogel sandwich technique.

Collagen aggregates of C17.2-eGFP cells

To generate collagen aggregates of C17.2-eGFP cells, we used the protocol illustrated in Figure 2 of Gil & Del Río, 2012. Briefly, seeded cells on 35 mm Ø Petri dishes, and used

each confluent dish to obtain a cell pellet by trypsinization. We resuspended each pellet in 150 μ l of collagen mixture (prepared as explained in the Hydrogel preparation section). Then, the cell-collagen mixture was pipetted onto a new Petri dish, forming a thick strip. Gelification was allowed to proceed in the incubator for 15 minutes, after which maintenance medium was added on top of the strip. Strips with medium could be kept in the incubator for one night or used immediately to obtain aggregates. The strip was detached from the plate using two metal spatulas, and transferred to a tissue chopper (McIlwain). The strip was cut into 300 x 300 μ m cubes by orienting the blade in two perpendicular directions. The cubes were transferred to a new plate with cell culture medium and seeded into hydrogels using the hydrogel sandwich technique.

hNS1 cell line

hNS1, formerly also known as hNSC.100, is a human neural stem cell line derived from diencephalic and telencephalic regions of 10-10.5 w aborted human Caucasian embryo. This cell line was obtained from Dr. Alberto Martínez Serrano (Universidad Autónoma de Madrid). In the absence of specific coatings, this cell line grows in suspension, forming neurospheres. Thus, neurospheres were kept in T-25 flasks with 10 ml maintenance medium in a humidified 37°C incubator with 5% CO₂. The cell maintenance medium consists of a mixture of equal parts DMEM high glucose (11960-044, Life Technologies) and Ham's F-12 Nutrient Mix (11765-054 Life Technologies), with 1% bovine serum albumin (BSA) (A7906, Sigma Aldrich) and 1% P/S. This medium was supplemented with the mitogens EGF (315-09, Peprotech) and hFGFb (100-18B, Peprotech), both at a final concentration of 0.02 μ g/ml; as well as N2 supplement at a final concentration of 1.25%.

Neurospheres were mechanically dissociated when they reached a size larger than 300-400 μ m in diameter, which was 1-3 times a week. Maintenance medium was replaced every 5 days or after every dissociation. Neurosphere size was measured using a microscope micrometer and was also monitored by checking for hypoxia in the center of the neurosphere (darker in color, see **Figure 64**). For mechanical dissociation, neurospheres were collected in a falcon tube by pipetting, and centrifuged at 800 rpm for 5 minutes. The medium was removed leaving around 0.5 ml at the bottom containing the neurospheres. 2 ml of dissecting solution were added, which was composed of HBSS (14175-053, Life technologies) with 0.1 M HEPES, 1% P/S, and 6 g/L glucose (G8769,

Sigma Aldrich). Then, neurospheres were mechanically dissociated by repeatedly pipetting with a 200 μ l filter tip until individual neurospheres were not visible to the naked eye. Then, this suspension was centrifuged again at 800 rpm for 10 min, and the neurosphere pellet was resuspended in new maintenance medium. Neurospheres were passaged at a 1:2-1:4 dilution in new T-25 flasks. When neurosphere size was not homogeneous, small neurospheres were separated from large spheres by sedimenting the large neurospheres in a falcon tube for 2-3 minutes and separating non-sedimented aggregates in the supernatant. Then, only the remaining neurospheres were dissociated as explained.

Differentiation was achieved by removal of the mitogens in the medium (EGF and hFGFb), and addition of 0.5% FBS to promote glial survival. In some cases, FBS was not added to prevent glial overgrowth. Differentiation in 2D was performed by seeding neurospheres onto glass coverslips coated with poly-L-ornithine (P4957, Sigma Aldrich) and laminin (L2020, Sigma Aldrich). 3D differentiation was performed by using the hydrogel sandwich technique.

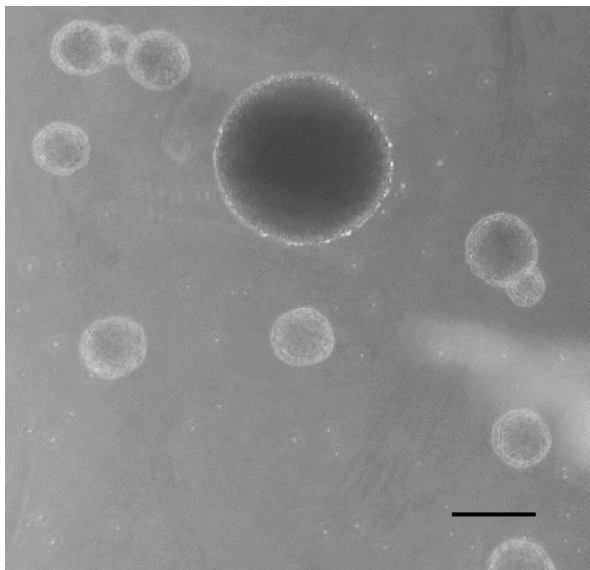


Figure 64. Example of a large neurosphere with hypoxia (>400 μ m \varnothing) among smaller neurospheres (~150 μ m \varnothing). Scale bar: 200 μ m.

Hydrogel sandwich technique

Hydrogel preparation

Collagen gels

Collagen solution and its respective dilutions were prepared in the lab as described in Gil & Del Río, 2012. This protocol is based on the extraction of type I collagen from rat tails using acetic acid, followed by a dialysis into a diluted cell culture medium, MEM 0.1X (11012044, ThermoFisher). The naturally acidic pH of this solution prevents collagen gelation, but avoids the use of acetic acid that is commonly found in commercial collagen solutions. To prepare dilutions of the collagen stock, additional MEM 0.1X was added. To prepare collagen gels, we used the proportions in **Table 12**. Gelation was allowed to proceed for 10-15 minutes in the incubator. If using undiluted collagen, gelation could be performed at room temperature.

Table 12. Collagen gel preparation. Volume of each component was adjusted according to each batch of collagen and its gelation properties.

Component	Order of addition	Volume
MEM 10X	1	40 μ l
NaHCO ₃ 7.5%	2	8-10 μ l
Collagen stock solution	3	300-320 μ l

PEG-fibrin gels

The preparation of PEG-fibrin gels is based on the methods in Koroleva et al., 2016 . A stock solution of fibrinogen (F8630, Sigma Aldrich) was prepared at 25 mg/ml according to the manufacturer's instructions and frozen at -20°C in 1 ml aliquots. Thrombin stock solution was also prepared at 100 U/ml according to the manufacturer's instructions and kept at -20°C. On the day of preparation of the gel, thrombin solution was diluted to a use concentration of 5 U/ml in PBS. In parallel, a solution of PEG-NHS (O,O'-Bis[2-(N-Succinimidyl-succinylamino)ethyl]polyethylene glycol) (713783, Sigma Aldrich) was prepared by dissolving 3 mg of PEG-NHS in 500 μ l of PBS and sterile-filtering. 121 μ l of this PEG-NHS solution were added to a defrosted 1 ml aliquot of fibrinogen stock solution to achieve a 5:1 molar ratio. This mixture was left in the incubator for 2 hours to obtain PEGylated fibrinogen. Then, this solution was mixed at a 2:1:1 ratio of (cell

medium):(PEGylated fibrinogen):thrombin use solution) and quickly pipetted to form the desired gel structure. Gelation was allowed to proceed in the incubator for 15 minutes.

Seeding technique

Hydrogel bases were prepared in advance, depending on the gelation time of each hydrogel. 20 μ L of hydrogel were used to form a circle in the center of a 4-well culture dish. Then, cell aggregates or explants were seeded on top of the hydrogel base using a P2 pipette tip, to transfer the minimum amount of liquid to the hydrogel. This step was carried out under a dissection microscope. After placing the aggregate or explant on the hydrogel, it was covered with 15-20 μ L of hydrogel (top). To re-center the cells, tungsten needles were used to push them into place. Then, the plate was moved to the incubator to solidify the hydrogel, after which the medium was added carefully, drop by drop, to prevent detachment of the hydrogel portions.

Embryonic cortical neuron cultures

Ethical statement

Animals were kept in the animal facility of the Faculty of Pharmacy at the University of Barcelona under controlled environmental conditions and were provided with food and drink ad libitum. Animal care and experimental protocols were performed in compliance with the Ethics Committee on Animal Experimentation (CEEA) of the University of Barcelona. All housing, breeding, and procedures were performed under the guidelines and protocols OB47/19, C-007, 276/16, and 47/20 of CEEA.

Dissection and culture of primary cortical neurons

Primary cortical cultures were prepared from embryonic day 16.5 (E16.5) embryos of wild-type OF1 mice (Charles River Laboratories, France). Pregnant females were euthanized by isoflurane overdose followed by pneumothorax. Then, embryos were extracted and transferred to ice-cold sterile 0.1 M PBS containing 6.5 mg/mL glucose (108337, Merck Millipore) for dissection. Brains were extracted and meninges were removed, after which cerebral cortices were isolated. Olfactory bulb and entorhinal cortex were removed with a scalpel, and the resulting fragments were transferred to trypsin solution and digested for 15 min at 37°C with mixing every 3 minutes. Trypsin was inactivated by addition of NHS (26050088, ThermoFisher) at a 1:3 ratio to the trypsin

solution. Then, cells were centrifuged and mechanically dissociated in a solution of PBS-Glucose containing 0.025% DNase (4536282001, Roche). After this step, cells were counted at a 1:100 dilution using a hemocytometer and seeded on poly-D-lysine-coated coverslips (P6407, Sigma Aldrich). Cells were seeded using complete Neurobasal medium supplemented with 5% NHS. Neurobasal medium (21103049, Invitrogen) was prepared with 6.5 mg/mL glucose (G8769, Sigma Aldrich), 0.087% NaHCO₃, 1X B27, 1% GlutaMAX, and 1% P/S. For the first three days after seeding, cells were kept in medium containing NHS to promote glial survival, and then it was removed for the rest of the culture. Medium was changed every 2-3 days and cells were kept in a humidified 37°C incubator with 5% CO₂.

Cortical explant dissection

Dissection was performed in the same way as described for dissociated neurons, until the cortex isolation step. Cortices were cut diagonally, parallel to the fimbria as shown in **Figure 65**. Then, the caudal portion was placed on a tissue chopper at a 45° angle from the blade, as shown in Figure 3 of J. A. del R o & Soriano, 2010. 500  m slices were cut and transferred to PBS-Glucose. Slices in which the cortex could be clearly distinguished were used to manually generate explants with a scalpel, aided by a hypodermic needle to separate the tissue pieces from the scalpel. Explant size was roughly 300-500  m in diameter, which ensured that they could be aspirated by a P2 pipette for seeding procedures. After cutting, explants were transferred to complete Neurobasal medium and left on ice for 15 minutes. Then, explants were kept in the incubator in new complete Neurobasal medium (with 5% NHS) O/N for viral infections or were directly seeded into hydrogel sandwiches. Viruses used for infection of cortical explants were the following: LV-EF1 -hChR2(H134R)-EYFP-WPRE (LV-ChR2), AAV9-hSyn-hChR2(H134R)-EYFP (AAV-ChR2), and AAV9.Syn.NES-jRCaMP1b.WPRE.SV40 (AAV-RCaMP). All viruses were used at a 1:500 dilution. After seeding, medium without NHS was used thereafter.

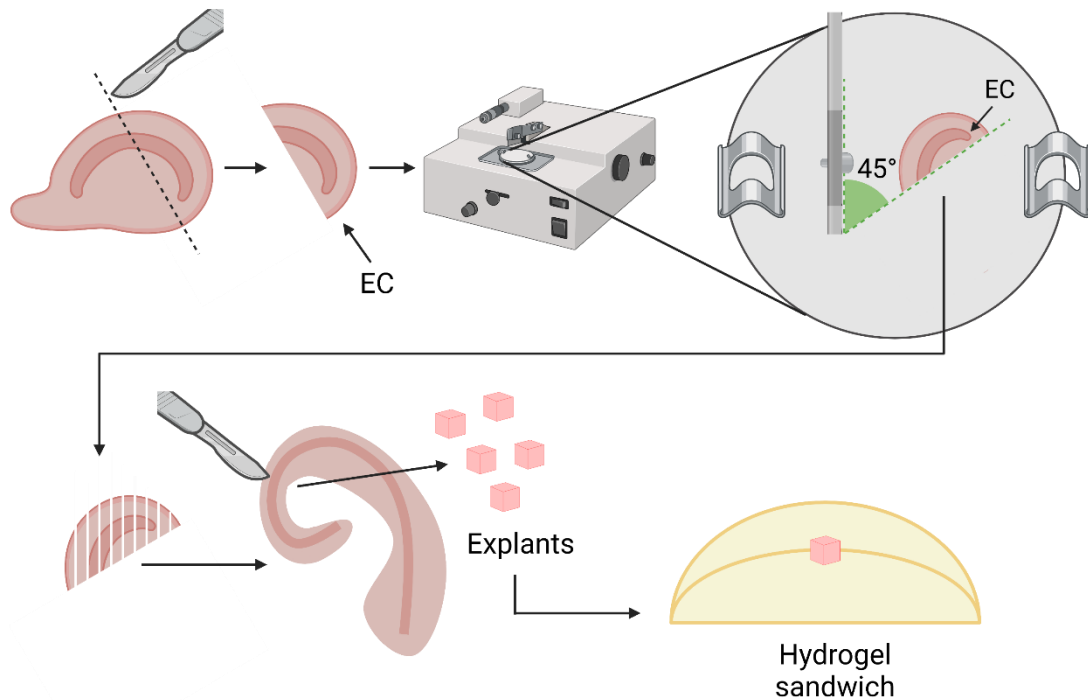


Figure 65. Manual preparation of mouse embryonic cortical explants using 500 μm cortical slices obtained with a tissue chopper.

Axotomy of cortical explants

If gels were to be axotomized, they were seeded on top of poly-D-lysine coated glass 12 mm \O coverslips. The poly-D-lysine coating enhanced attachment of the collagen gel to the glass surface, and the glass coverslip acted as a surface tension barrier to contain new hydrogel added onto a previously wet surface (**Figure 66**).

Axotomy of cortical explants in collagen gel sandwiches was performed with a straight surgical scalpel blade (#9, Schwann-Morton). This model was chosen as it allowed introduction of the blade into cell culture wells of a 4-well plate, while allowing a clean cutting motion perpendicular to the gel. The size and location of the explant was carefully observed under a dissection microscope, and one side of the gel was cut at a distance approximately equal to 1-1.5 times the explant diameter, to ensure that axons were cut at an intermediate distance from the soma and the tip of the axon. Before cutting the gel, the medium was removed as thoroughly as possible to facilitate cutting. In most cases, the axotomized gel portion could not be completely removed due to the difficulty in cutting a fragile gel on top of a glass surface. The cut portion was pushed aside to allow regrowth into the adjacent region refilled with new gel.

After cutting, the coverslip was taken with fine tweezers and placed in a new, dry, cell culture dish of choice. If cells were to be optically stimulated, a glass bottom MatTek 35 mm Ø dish was used for each coverslip. Then, new collagen solution was prepared. Concentrated collagen was used instead of 3:1 collagen, as it facilitated gelification of the gel around the extra medium still present around the old gel. 50 µl of new collagen were added on top of the gel and coverslip and were allowed to gelify for 15 minutes in the culture incubator. Finally, pre-warmed Neurobasal medium was carefully added to the plates.

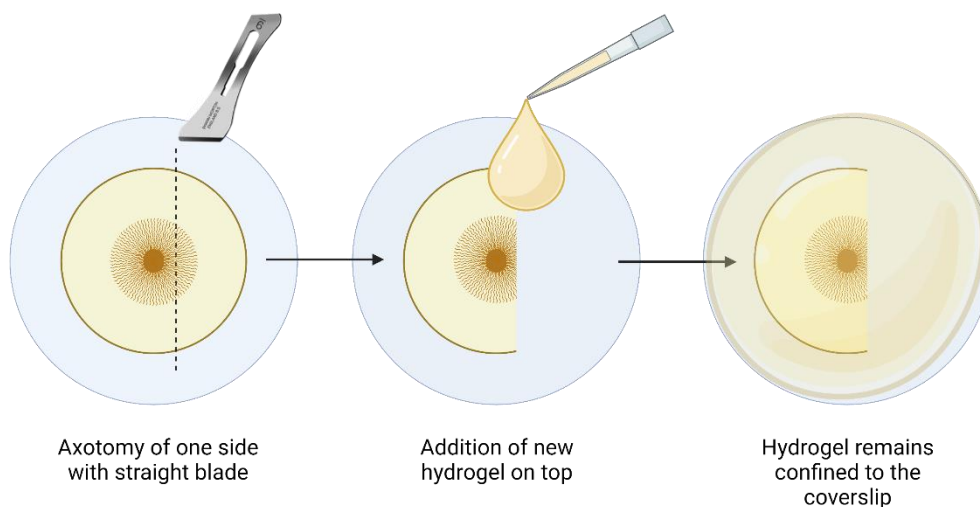


Figure 66. Axotomy of cortical explants in collagen gels using a straight blade and glass coverslips. The coverslip aids in creating a barrier for the new hydrogel drop when it is placed on a wet surface (previously containing cell culture medium).

CSPG treatments

In some cases, we added 20 µg/ml CSPG to the new gel added after axotomy, to simulate astrocyte secretion of CSPG. Before adding collagen to the gel mixture, CSPG was added to the MEM 10X and NaHCO₃. This concentration was chosen based on the fact that glial scar extracts have been reported to contain concentrations in the order of 1 µg CSPG/mg of tissue (Park et al., 2022). No literature has used CSPG in 3D *in vitro* models with hydrogels, and it has only been used in coatings at around 20 µg/ml in the coating solution.

Quantification of regrowth after axotomy and statistical analysis

To quantify regrowth after axotomy, we used TUJ1 peroxidase/DAB staining to label the full length of regrown axons. In these images, we defined three areas to quantify with ImageJ: the control side (not axotomized), the regrowth area (on the axotomized side),

and the explant area. Areas were drawn freehand with ImageJ. Ratios of these areas were calculated to serve as regrowth indicators, as explained in the corresponding subsection of the Results section (see **Figure 75**).

For each condition, we analyzed 6 images ($n=6$). Statistical analysis was performed in GraphPad Prism. Due to the small sample sizes, a non-parametric Kruskal-Wallis test was chosen, to account for the potential non-normality of the data. We compared the medians of all groups by enabling the option of Multiple Comparisons between all columns. A confidence interval of 95% was chosen, ($p<0.05$ was considered significant).

Calcium imaging and analysis

Spontaneous activity of RCaMP⁺ cortical explants

For calcium imaging in jRCaMP1b⁺ explants, we used an inverted IX71 microscope (Olympus) equipped with a Hamamatsu ORCA Flash 4.0 camera and an LED light source (CoolLED pE-300white, Delta Optics). Images were acquired with Olympus cellSensTM software (Olympus Corporation) and saved as 16-bit “.tiff” files. Videos were recorded at 10 fps (100ms/frame), and 512x512 px resolution.

Calcium transients in jRCaMP1b⁺ explants were analyzed using Netcal for Matlab (Orlandi et al., 2017). In explants where individual cells were not visible, circular ROIs were defined on several regions of the explant to represent the increases in fluorescence at different locations. Fast mode was enabled for the preprocessing step, and traces were smoothed after extraction. Trace data was obtained as $100x\Delta F/F_0$.

Induced activity in optically stimulated ChR2⁺/ RCaMP⁺ 2D cortical neurons

For imaging calcium transients in 2D ChR2-eYFP⁺ and jRCaMP1b⁺ cortical neurons and analyzing their response to blue light stimulation, we used the Dragonfly 505 confocal microscope due to the possibility to apply two laser wavelengths at the same time, while only acquiring the emitted light from the calcium indicator.

We imaged cells at 11 DIV, which had been infected at 4 DIV with AAV. We used a 20X water immersion objective and placed coverslips with neurons on glass bottom Petri dishes. Cells were maintained in a microscope incubator (37°C, 5% CO₂) during recording. First, we imaged a chosen area of cells using only a green laser (561 nm) and

acquired emitted light using a red light filter (617 nm), to observe spontaneous activity. We programmed a time lapse acquisition of 1200 frames, at a frame rate of 10 fps (2 minutes of recording). Exposure time was 25 ms for the green laser, which was set to 10% power. Resolution was set to 1024 x 1024 px and 16 bits.

Then, to stimulate cells with blue light, we recorded the same area of cells, but also turned on the blue (488 nm) laser during recording. Only the emitted red light was acquired with the 617 nm filter, to observe the induced activity. Lasers were set to 10% power, and exposure time was set to 25 ms for the 561 nm laser and 5 ms for the 488 nm laser, to reduce the total acquisition time. Linear range of fluorescence was confirmed to determine the appropriate exposure settings in both cases. After recording the second video, a snapshot was taken using the same settings as used for the video, but with only one timepoint. The emitted green light was also acquired in this case using a green light filter (530 nm). This picture would serve as a representation of the expression of jRCaMP1b and ChR2-eYFP in the chosen area of cells. Recordings were saved in .ims format and later converted to .avi with ImageJ.

Analysis was performed using ImageJ, with the same protocol as was used for muscle constructs loaded with fluo-4 AM in Chapter 1. Briefly, elliptical ROIs were defined with the ellipse tool on cell bodies that became activated in the recording with blue light stimulation. The mean gray value for each frame was extracted using the Measure option, and the average background fluorescence was extracted from an average intensity projection of the recording. Using this background value (F_0), the $\Delta F/F_0$ was calculated for each ROI and timepoint. $\Delta F/F_0$ before and after stimulation was compared for each ROI and represented using GraphPad Prism 8.4.3.

Optical stimulation of cortical explants

As mentioned in the axotomy methodology, when ChR2⁺ explants were to be optically stimulated, we placed each gel in a glass bottom 35 mm Ø MatTek dish, since our optical stimulation system was adapted to 6-well or 35 mm Ø Petri dish formats. Optical stimulation was performed 6 hours after axotomy, to allow sufficient time for membrane resealing, as noted in (Mesquida-Veny et al., 2022). The stimulation protocol consisted in 1 hour of stimulation at 20 Hz frequency, using 5 ms ON / 45 ms OFF pulses organized in trains of 1 s ON / 1s OFF. A 470 nm emission LED array (LuxeonRebel™) under the control of a Driver LED (FemtoBuck, SparkFun) of 600 mA and a pulse generator,

PulsePal (OpenEphys) was used to deliver blue light to neuronal cultures. During experiments, temperature changes inside the optogenetic platform were monitored by an Arduino-UNO™ microcontroller using a temperature probe DS18B20 with PWM relay output (CEBEK I-86, Spain) connected to a 12 V cooling fan. The cooling fan switched on with temperature increases >0.5 °C from 37 °C. The LED array was placed onto aluminum heat sink plates below the culture dishes in the optogenetic platform at a distance of 2 cm to ensure that the complete area of the well plate was illuminated. In these conditions, the external stimulation voltage unit drives 12 V and 600 mA for each Quad LED module, with an average light intensity of approximately 20–25 mW/cm² measured at the culture dish containing the devices with a Newport 1919 optical power meter (Newport Photonics, USA).

Immunostaining

Antibodies used for neural differentiation stainings are shown in **Table 13** and **Table 14**.

Table 13. Primary antibodies used in neural immunostainings.

Primary antibody	Origin	Dilution	Reference
Anti-TUJ1	Mouse	1:1000 (fluorescent staining) or 1:5000 (DAB staining)	801201, Biolegend
Anti-GFAP	Rabbit	1:500	Z0334, Dako
Anti-Olig2	Rabbit	1:500	AB9610, Millipore
Anti-MAP2	Rabbit	1:200	M3696, Sigma Aldrich
Anti-acetylated tubulin	Mouse	1:500	T6793, Sigma Aldrich

Table 14. Secondary antibodies used for neural immunostainings.

Secondary antibody	Origin	Dilution	Reference
Anti-mouse 488	Goat	1:500	A11029, Invitrogen
Anti-rabbit 488	Donkey	1:500	A21206, Invitrogen
Anti-mouse 568	Goat	1:500	A11031, Invitrogen
Anti-rabbit 568	Goat	1:500	A11011, Invitrogen
Anti-mouse biotinylated	Horse	1:200	BA-2000, Vector Laboratories

2D immunostaining

2D immunostaining was performed using the same protocol as described in Chapter 1.

3D immunostaining of cells in hydrogels

The staining protocol for cells in hydrogel sandwiches was similar to the one explained in Chapter 1 for 3D construct stainings. Fixation was performed for 30-60 minutes at RT or 4°C depending on the hydrogel (Matrigel or ECM Gel at RT to avoid depolymerization). After fixation, hydrogel sandwiches were washed and detached from the bottom of the plate using a fine paintbrush. From that moment, all steps were performed with gels in flotation. Blocking and antibody solutions were prepared with 10% or 5% NHS instead of FBS, and primary antibody incubation was performed for 2-3 O/N at 4°C. Hydrogels were mounted using a fine paintbrush to transfer them to a microscope slide, and excess buffer was dried off with filter paper. Mowiol® 4-88 (475904, Calbiochem) was added on top of the constructs and slides were sealed with 24x50 mm coverslips modified with nail polish drops on the corners to create space for the construct height (**Figure 22**). Slides were allowed to harden for at least 48 hours before imaging. Fluorescently stained neurospheres or explants were imaged using an inverted IX71 microscope equipped with a Hamamatsu ORCA Flash 4.0 camera, or by confocal microscopy using a Zeiss LSCM-800 confocal microscope or a Dragonfly 505 confocal microscope. Confocal images were reconstructed and analyzed using ImageJ and Bitplane Imaris™ v7.4 software.

Peroxidase staining with DAB

Peroxidase staining with DAB (3,3'-Diaminobenzidine) was used to visualize axons in hydrogels, mainly by using TUJ1 primary antibody (801201, BioLegend) derived from mouse (1:4000-1:5000 dilution). The staining protocol was performed as explained for a 3D immunostaining, up until the secondary antibody incubation step. Instead of using fluorescent antibody, horse anti-mouse HRP antibody was added at a 1:200 dilution in antibody buffer. Then, three 10-minute washes were performed using PBS-Triton 0.5% and gels were incubated overnight in a solution of streptavidin biotinylated HRP (GERPN1051, Sigma Aldrich) diluted 1:400 in antibody buffer. The next day, 3x10 minute washes were performed with PBS-Triton 0.5%, followed by 3x5 minute washes in PBS and 3x5 minute washes in Tris-HCl 0.1 M pH=7.6. Then, 0.03% DAB solution

was prepared in Tris-HCl 0.1 M pH=7.6. This solution was added to the gels together with 0.01% hydrogen peroxide to develop the signal. The oxidation process was monitored using a tabletop brightfield microscope and the reaction was stopped by washing with Tris-HCl 0.1 M pH=7.6 three times. Then, gels were mounted as previously explained.

RESULTS

Our first objective at the beginning of the thesis was to find a suitable method to derive neurons from a stem cell line or from direct reprogramming of human cells. As will be explained, we tested two neural stem cell lines, the mouse cerebellum stem cell line C17.2 (we used a GFP-expressing variant) and the human neural stem cell line hNS1. We also used these cells in different hydrogel cultures to determine the optimal hydrogel for neuronal differentiation and neurite outgrowth.

C17.2-eGFP differentiation

With this cell line, before culturing in 3D, we first confirmed its differentiation capabilities in traditional 2D culture. We used poly-D-lysine-coated coverslips and performed the standard differentiation protocol of 7 days. To confirm differentiation, we stained for a series of neural markers. For neurons, we used Neuron-specific class III beta-tubulin (TUJ1), which stains microtubules of newly formed neurons, and microtubule-associated protein 2 (MAP2), associated with dendrites of more mature neurons. For glia, we used glial fibrillary acidic protein (GFAP), and for oligodendrocytes we used oligodendrocyte transcription factor 2 (Olig2). Considering the cell line expressed GFP, we performed all stainings in red with a nuclear counterstain.

The results, shown in **Figure 67**, confirmed appropriate differentiation of the cells. Most cells were neuronal according to TUJ1 and MAP2 staining. Some glial cells were present, and a low or null amount of oligodendrocytes were generated with this protocol. GFP fluorescence was visible after fixation without staining.

Culture of C17.2-eGFP aggregates in hydrogels

Next, we cultured these cells in hydrogels. We compared four different compositions, which were Matrigel, Collagen, ECM gel, and VitroGel. In order to obtain a radial projection of axons from a neuronal sphere, we also tested two different methods of obtaining cell aggregates (**Figure 68**). The first was to embed a high density of cells inside collagen gels, which were then cut into small cubes and seeded in hydrogel sandwiches. The second was to use the hanging drop technique, in which we varied the number of cells per drop to modulate the size of the aggregate. We based the numbers on a publication that used 5000 C17.2 cells/aggregate (L.-G. Zhang et al., 2014).

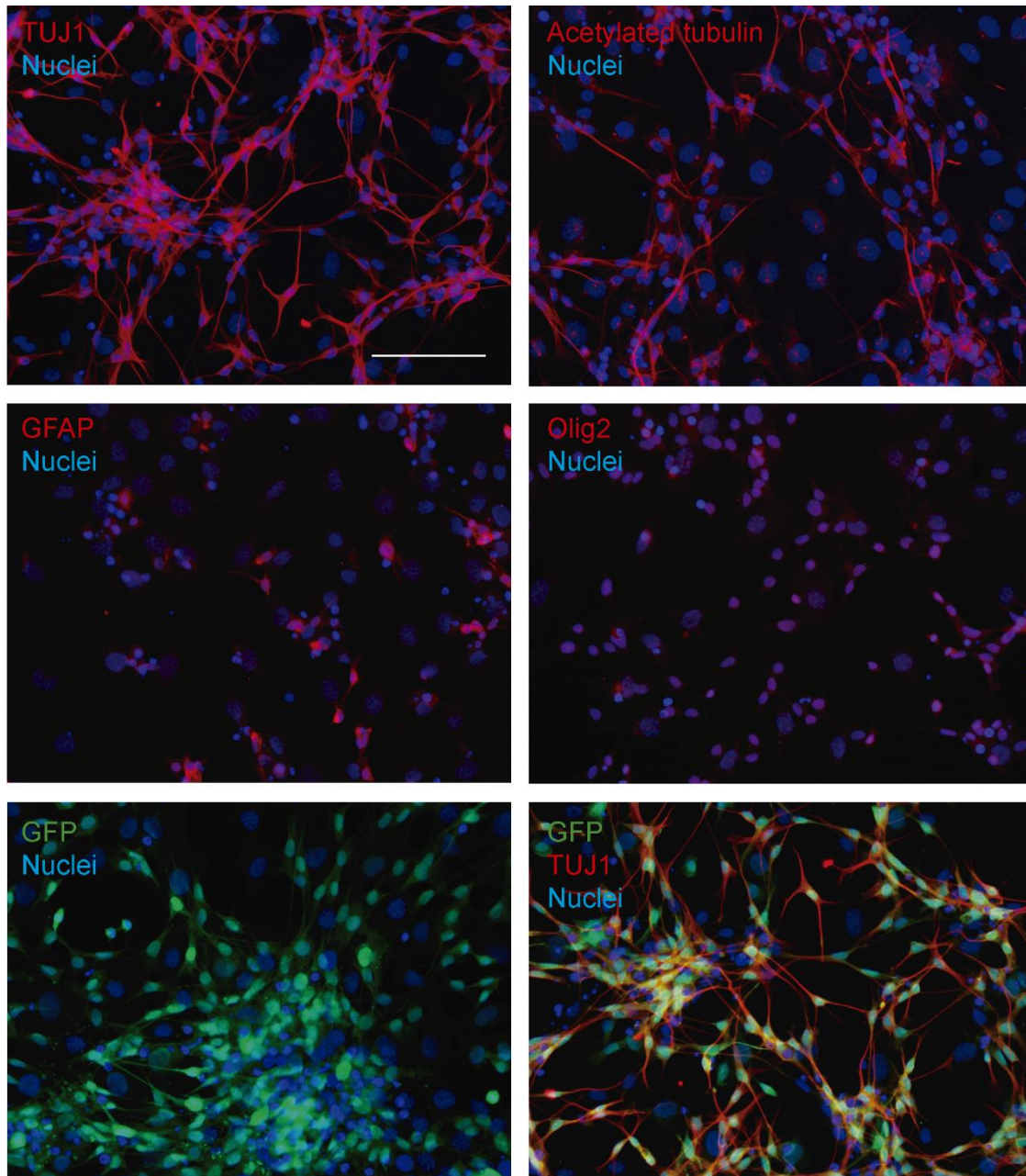


Figure 67. Immunostaining of differentiation markers in C17.2-eGFP cells differentiated in 2D for 7 days. We used the neuronal markers TUJ1 and Acetylated tubulin, the glial marker GFAP and the oligodendrocyte marker Olig2. Nuclei were stained with Hoechst 34580. Endogenous GFP fluorescence is shown without additional GFP antibody staining. Scale bar: 100 μ m.

Regarding the aggregation methods, as shown in **Figure 68A**, the collagen aggregates were considerably less dense than the hanging drop aggregates (seen by GFP fluorescence), as the latter are based on direct cell-cell contacts. In the case of hanging drop aggregates, the smaller ones composed of 1000 cells did not behave as a neurosphere, as there was excessive cell migration compared to the amount of cells that stayed contained in the aggregate. In contrast, the largest aggregates showed some hypoxia in the center, meaning that the cell number was excessive at this density.

Regarding hydrogel composition, in **Figure 68B** we show a comparison of neurite outgrowth and cell migration after the first 3 days in culture using the medium-sized hanging drop aggregates, which seemed to behave as neurospheres with minimal hypoxia. Matrigel promoted excessive migration from the aggregate, but this was the only hydrogel in which we observed a neuronal morphology of cells after 7 days. Collagen gels supported cell growth but did not show clear neurite outgrowth. ECM gel was considerably less effective for promoting cell growth and neurite extension, while cells cultured in VitroGel (without binding motifs) had a rounded morphology and did not migrate or extend neurites at all.

Due to these results, we performed immunostaining of aggregates cultured in Matrigel, as shown in **Figure 68C**. In some cases, we seeded 5 aggregates per gel instead of a single aggregate per gel, to examine the ability of neurites to interact between aggregates. In both cases, we observed TUJ1-positive axons which extended past the neurosphere region, albeit with a considerable amount of migration of cell bodies from the sphere. The axons were not considered long or isolated enough from the aggregate to be able to perform axotomy, as the average length was around 100 μm and the longest was 300-400 μm . Interestingly, aggregates cultured together had a tendency to generate connections, with cell attraction occurring from the initial days in culture. In any case, with these results, we did not find a suitable condition that would allow us to perform axotomy studies. In addition, these cells were not derived from brain tissue (they were derived from cerebellum) and are of murine origin, which prompted us to test a human neural stem cell line.

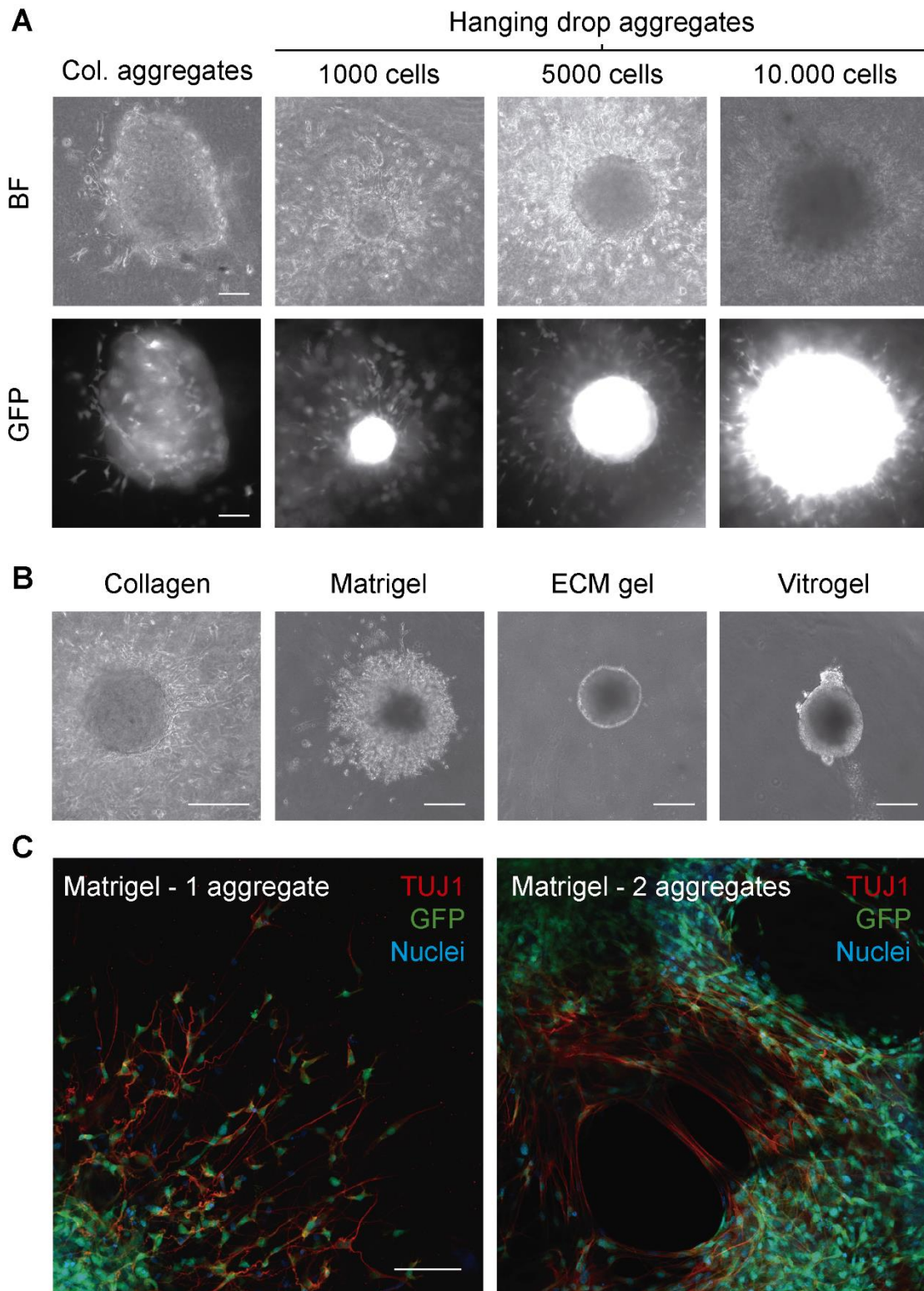


Figure 68. Aggregates of C17.2-eGFP cells cultured in hydrogels. **A.** Comparison of different aggregate formation techniques, collagen aggregates or hanging drop aggregates with different numbers of cells per drop. Brightfield (BF) or GFP images are shown for the same aggregate. **B.** Comparison of migration and neurite extension of hanging drop aggregates of 5000 cells/drop in different hydrogels after the first 3 days of differentiation. **C.** Confocal images of hanging drop aggregates of 5000 cells/drop differentiated in Matrigel for 7 days. TUJ1 was stained as a neuronal marker and is shown together with endogenous GFP. Nuclei stained with Hoechst 34580. Note that when 2 or more aggregates are cultured together, connections form between them. Scale bars: **A.** 100 μ m. **B.** 200 μ m. **C.** 100 μ m.

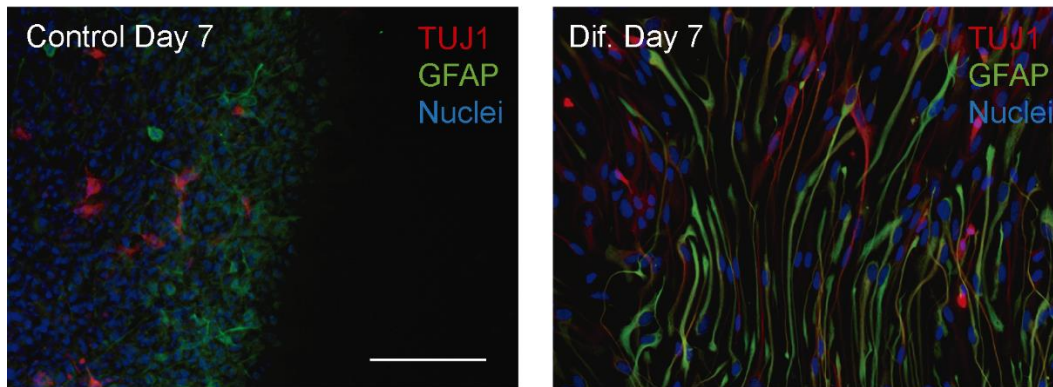
hNS1 differentiation

The first experiments we performed with the hNS1 cell line had the objective of demonstrating their ability to differentiate into mixed cultures of neurons and glia. We evaluated this in 2D cultures on poly-L-ornithine/laminin-coated coverslips and in collagen hydrogel sandwich cultures by differentiating the cells for 7 days and staining for the glial marker GFAP and the neuronal marker TUJ1. The publication describing the properties of this cell line (Villa et al., 2000) reported a proportion of around 10% TUJ1-positive cells, with the majority of cells staining positive for GFAP. However, these results were after 12 days of differentiation, while we performed a shorter differentiation of 7 days. We shortened the differentiation time to be able to detect a larger proportion of neuronal cells, as the proportion of glia increases over time and dilutes the neuronal population.

In our experience (**Figure 69**), 2D cultures showed a similar proportion of both cell types, with around 60% glia and 40% neurons, based on TUJ1 and GFAP expression. It must be noted that some cells showed double staining for GFAP and TUJ, which can be the case for neural progenitors, meaning that these cultures were not entirely differentiated at 7 days. The undifferentiated control neurospheres showed some degree of differentiation, which was potentially caused by the neurogenic effect of hypoxia at the center of neurospheres of excessive size (Dey et al., 2023). In any case, the abundance of cells expressing differentiation markers was clearly lower than in differentiated cultures. Cell morphology was also considerably more neural-like in differentiated cultures.

In 3D culture in collagen gels, we obtained a similar differentiation pattern in terms of proportions, but we also observed a particular organization of the cells within the neurosphere. Glial cells tended to be located at the edges of the neurosphere, encapsulating the neural cells. This effect likely prevented axons from being projected outside of the neurospheres. This was seen both in larger and smaller neurospheres, meaning that the organization of glia around the edges was apparently not dependent on neurosphere size.

A. 2D culture



B. 3D culture (collagen)

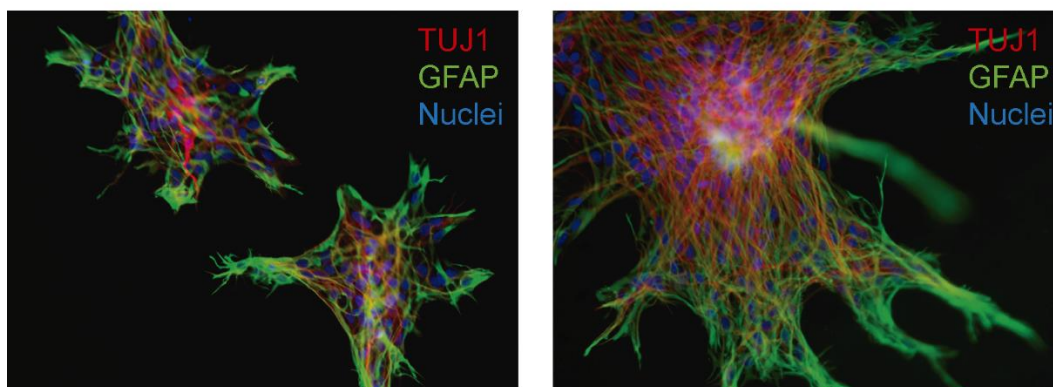


Figure 69. Expression of neuronal (TUJ1) and glial (GFAP) markers in hNS1 cells differentiated for 7 days. In 2D cultures, neurospheres were seeded on poly-L-ornithine/laminin-coated coverslips. A control neurosphere kept in maintenance medium is shown. In 3D cultures, neurospheres were seeded in collagen gels. Nuclei stained with Hoechst 34580. Scale bar: 100 μ m.

From these immunostaining images, we gathered that it was possible that the axonal projections were too thin to be visualized clearly by fluorescence microscopy. Therefore, we decided to perform peroxidase stainings with DAB (3,3'-Diaminobenzidine), which have a higher sensitivity than fluorescent stainings for neurite visualization. In this case, we compared differentiation in Matrigel and collagen hydrogels. The latter hydrogel was also tested at different dilutions, as the stiffness of the collagen can influence neurite extension (Gunn et al., 2005). Soft hydrogels are generally more conducive to axon growth, although there exists a lower threshold of Young's modulus at which neurite extension decreases, primarily because of inadequate cell attachment and traction support.

In our initial experiments, we compared undiluted Collagen and Matrigel, to determine which gel was more suitable for differentiation and neurite extension. In the initial days in culture, we observed more migration and cell growth in Matrigel than in Collagen. This migration was clear after one week of differentiation, as TUJ1 peroxidase stainings

showed that cell bodies were not contained inside the neurosphere. In the case of collagen gels, there was less migration than in Matrigel, but it was clear that axons were contained inside the borders of the spread-out neurosphere. This can be observed in **Figure 70**. The lack of isolated axonal projections was similar to that observed in fluorescent stainings, indicating that the differentiation protocol or hydrogel composition may need to be adjusted to improve this.

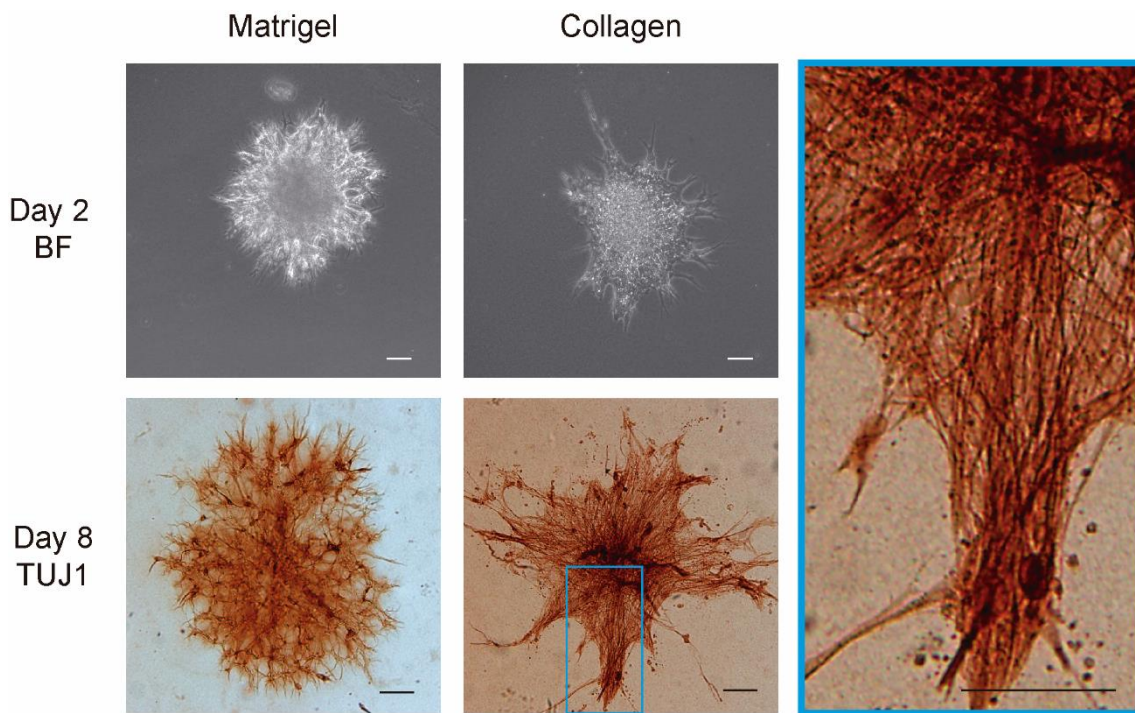


Figure 70. Growth of hNS1 cells in different hydrogel compositions, Matrigel or Collagen. Brightfield images are shown from the first days in culture to evaluate neurite extension and overall morphology of neurospheres. At Day 8, cells were fixed and stained with TUJ1 antibody using peroxidase/DAB staining. A magnified portion of the lower middle image is shown on the right, to highlight the presence of axonal projections inside the neurosphere borders. Scale bar: 100 μm .

As the differentiation protocol used 0.5% FBS to promote glial survival, and the glial border seemed to be what was preventing axons from exiting the neurosphere, we decided to remove the FBS in some cases to see if this could reduce the encapsulation effect. In addition, we tested two dilutions of the collagen gel, as the stiffness of the gel could influence the axons' ability to extend into the matrix (**Figure 71**). Despite a discrete improvement in the more diluted collagen (1:1) in the condition without FBS, in which we observed some longer axons of around 300-400 μm , there was still a very low amount of isolated axonal projections. In addition, this length was still insufficient to be able to perform axotomy studies. Due to the lack of success in using neural stem cells to generate axotomizable axons, we decided to use primary cultures as a source of neurons in future

experiments. Despite their non-human origin and the use of experimental animals, which we strived to avoid; primary culture is a reliable source of CNS neurons with long axonal projections and a fully functional phenotype.

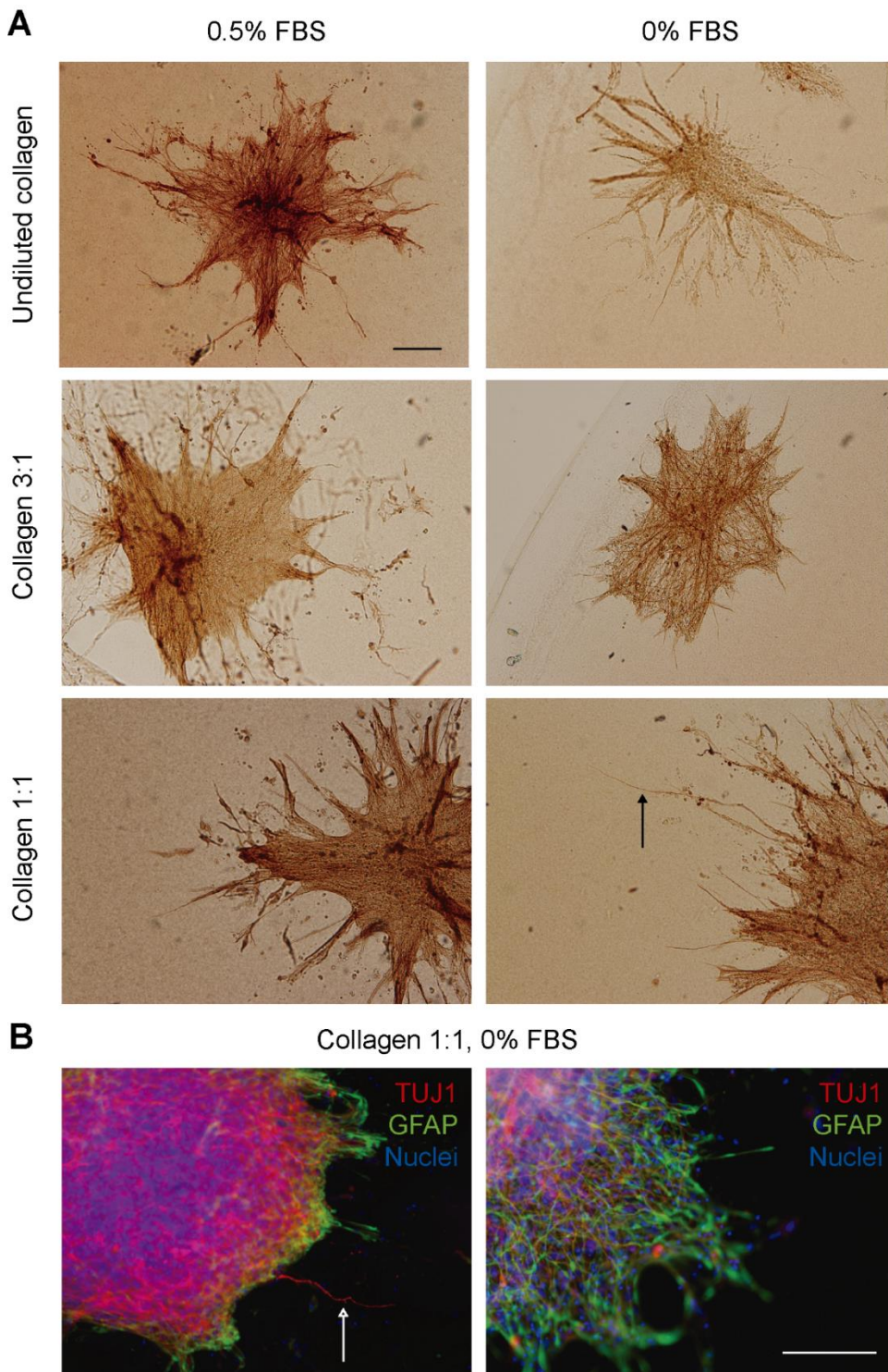


Figure 71. Comparison of different collagen dilutions and addition or removal of FBS in hNS1 neurosphere cultures differentiated for 12 days. **A.** Comparison of TUJ1-positive axons by peroxidase staining. **B.** Fluorescent stainings of TUJ1 and GFAP in Collagen 1:1 dilution without FBS. Scale bars in **A** and **B**: 100 μ m.

Primary cortical explant cultures

Optimization of hydrogel composition and culture timepoints

Primary cortical explants had been previously used in our laboratory, and cultured in collagen (3:1 dilution) and Matrigel gels. As a first step, we corroborated that the explants behaved as expected in the aforementioned hydrogels, as a way to ensure reproducibility of the dissection technique and culture conditions between different researchers. We also used PEG-fibrin hydrogels as an additional condition. Explants were cultured for different periods: 7 days in vitro (DIV), 11 DIV, or 14 DIV, to evaluate their survival and axon length at each timepoint. We performed peroxidase stainings with TUJ1 antibody to visualize the full length of axons with more sensitivity (**Figure 72**).

Although in the figure we show representative images of explants that were embedded correctly into gels, we quickly realized that the manipulation of PEG-fibrin hydrogels for the sandwich technique was not ideal. The hydrophobic nature of the PEG-containing gel made it more prone to detachment of the sandwich portions. Also, the small amount of liquid transferred together with the explant during seeding did not mix with the hydrogel solution during polymerization. This resulted in a low efficiency of encapsulation and the presence of liquid “bubbles” inside the hydrogel constructs.

In addition to this, we observed that survival in the PEG-fibrin hydrogels was lower than in all the other conditions, with axons starting to degenerate as early as 7 DIV. This time window would not be enough to perform axotomy and regrowth experiments, considering that neurons dissected at this embryonic stage reach a mature phenotype around 7 DIV. In the case of Matrigel, survival was the highest of all hydrogels, with axons persisting in higher amounts until 14 DIV. Nevertheless, there was considerable migration which resulted in a loss of the explant (cell soma was not contained in the explant center, as observed by the fainter TUJ1 staining of the explant over time). In collagen gels, there was some axonal survival up to 14 DIV, although it would be advisable not to maintain cultures past 11 DIV to avoid excessive degeneration. There was also less migration, as expected based on previous results from the laboratory and in our previous experience with neural stem cells. Regarding axon length, in all hydrogels we obtained axons with an average length of over 1 mm, which is more than enough to perform axotomy. The

longest axons were obtained in Matrigel (up to 2 mm), followed by Collagen (around 1.5 mm) and PEG-fibrinogen (around 1 mm).

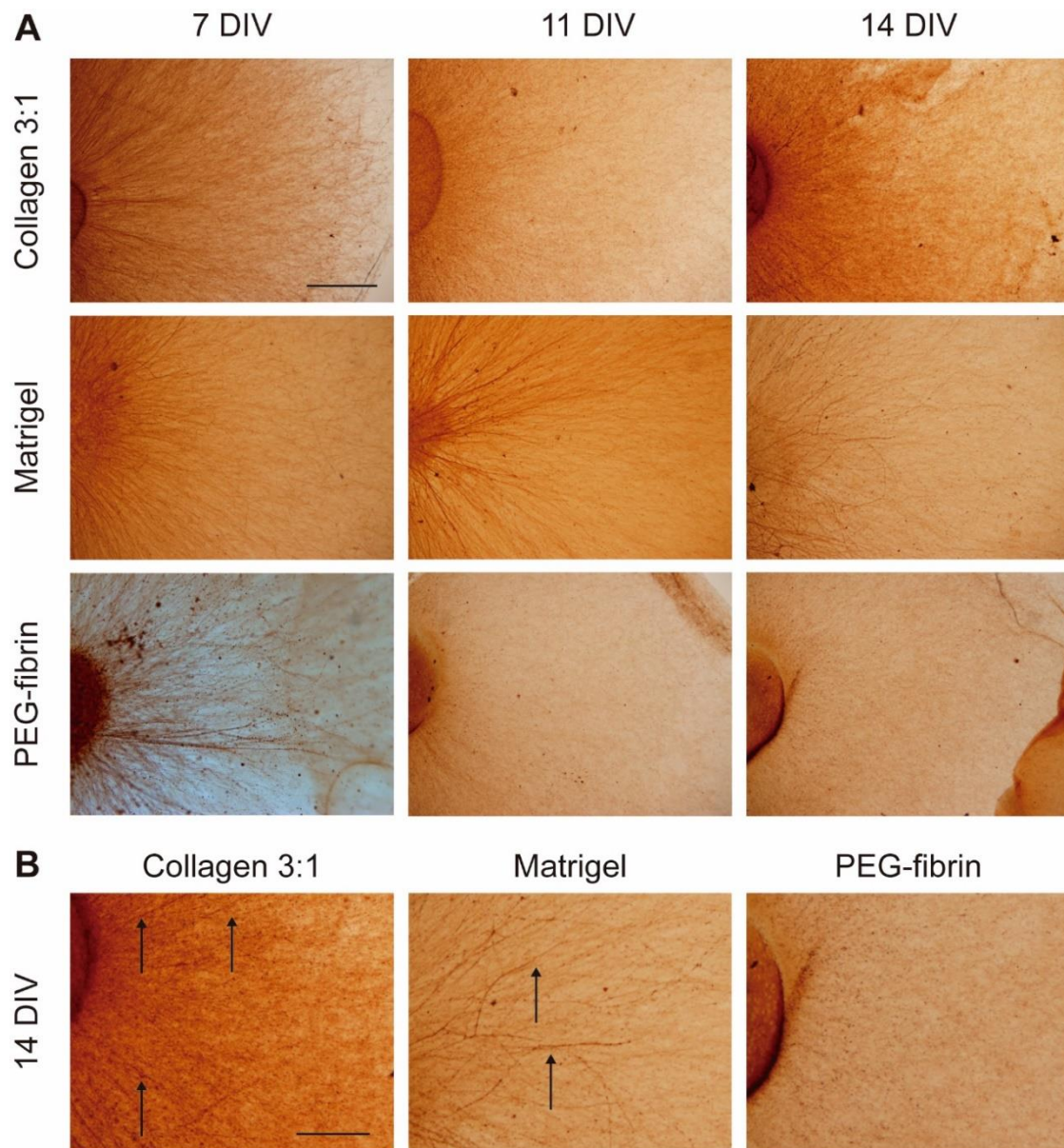


Figure 72. Axonal outgrowth and survival of cortical explants in Collagen 3:1, Matrigel, or PEG-fibrin hydrogels at different timepoints. Axons were stained with TUJ1 antibody by peroxidase staining with DAB. **A.** Comparison of the different timepoints at a lower magnification. **B.** Close-up of axons at 14 DIV in each hydrogel. Arrows indicate visible axons. Scale bars: **A.** 500 μ m, **B.** 250 μ m.

With these results, we decided to use Collagen 3:1 gels for further experiments. To ensure maturity of the cells while avoiding cell death, we performed axotomy at 7-8DIV and fixed the cells at 11 DIV to evaluate regrowth.

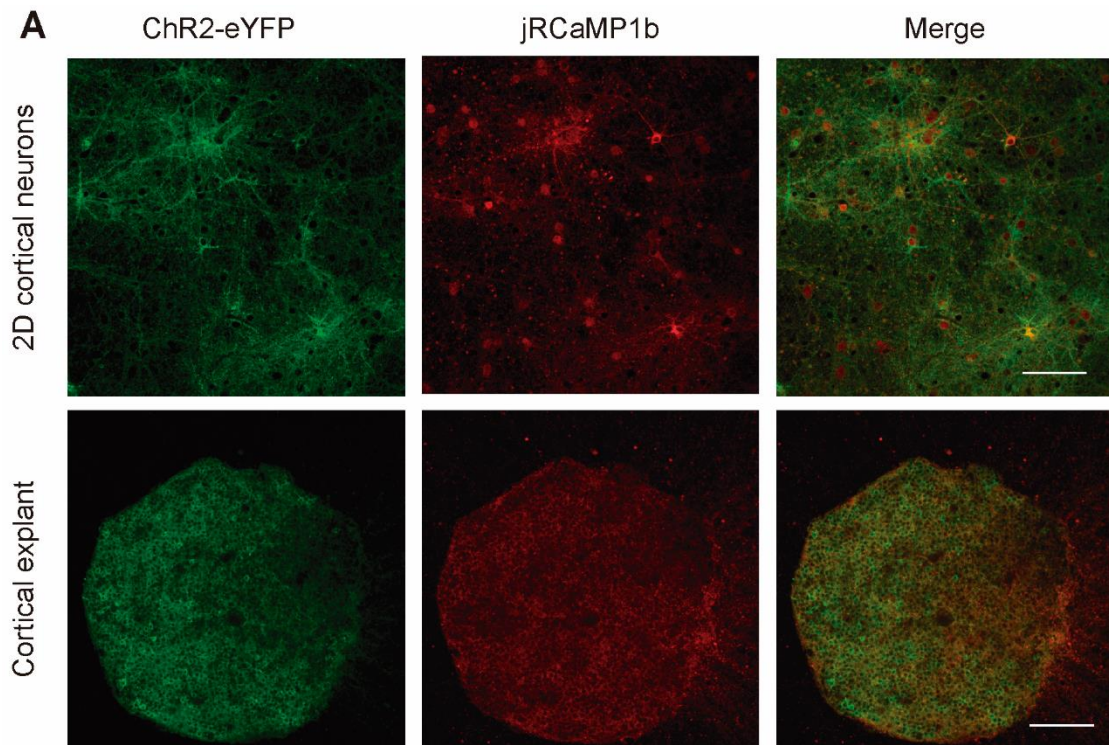
Infection of explants with ChR2 and RCaMP viral vectors

After determination of the appropriate hydrogel and timepoints for axotomy, we also needed to find the appropriate conditions for infection of explants with ChR2 vectors, in

order to make the neurons optically stimuable. Normally, infection of primary neurons is carried out a few days after seeding, to prevent cell death. However, as we were seeding explants into hydrogels, it would have been difficult for the virus to penetrate the hydrogel matrix if added into the medium. Therefore, we decided to perform overnight infections of explants on the day of the dissection. Apart from using the ChR2 virus, we wanted to perform co-infections with jRCaMP1b, for which we had an AAV vector expressing this GECI under a synapsin promoter.

Initially, we thought that lentiviral infection would be more efficient at this stage, but we did not have a neuron-specific lentiviral vector for ChR2. Infection with this virus was possible using the overnight infection method, but when we tested a coinfection with jRCaMP1b AAV, neurons expressing ChR2 and jRCaMP1b did not colocalize. Also, glial cells could express ChR2, which was not desirable for our experiments. However, as we had tested the co-infection and the AAV seemed to work well, we decided to perform co-infections with AAV for ChR2 and jRCaMP1b, which both expressed the transgene under the synapsin promoter. Cortical explants coinfecting with these AAV showed expression of both transgenes as early as 4 DIV, with a peak of expression around 6 DIV. As a control, cortical neurons cultured in 2D were also co-infected with these viruses at 4 DIV, and we observed expression at 8 DIV with a maximum at 11 DIV.

In explants infected with the RCaMP AAV, we observed spontaneous activity of the explants at 6 DIV. In some cases, the activity was propagated along the explant as a periodic wave. In the example shown in **Figure 73B**, the outer region of the explant showed calcium increases in a clockwise fashion, indicating electrical coupling of the neurons in the explant. To analyze activity, we defined 9 ROIs at different regions of the outer part, as well as a ROI in the center, and analyzed the calcium transients using Netcal. It must be noted that these ROIs are not defined on single cells, as focusing on individual cells with our inverted microscope was not possible due to the 3D morphology of the explant. Therefore, ROIs represent similarly spaced regions of the explant, to obtain an overall view of activity in the explant. Periodic calcium release was observed when analyzing the traces of each ROI in **Figure 73D**. Although at this stage the activity cannot be defined as spikes, which only appear in more mature *in vitro* cultures, these results indicate that explants are healthy and active at 6DIV. Therefore, performing axotomy and optical stimulation at 7-8 DIV is appropriate in terms of timing.



Spontaneous activity at 6 DIV

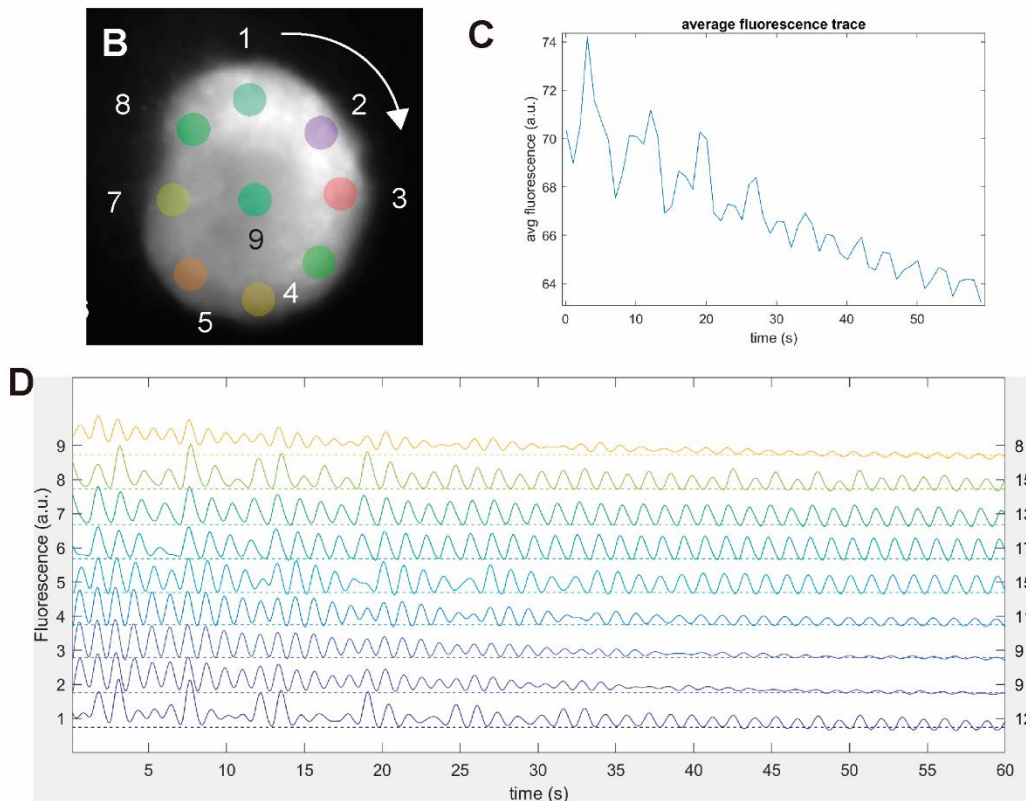


Figure 73. Expression of ChR2 and RCaMP in cortical neurons and explants infected with AAC. **A.** Expression of ChR2-eYFP and jRCaMP1b in 2D cortical neurons or explants co-infected with AAV at 4DIV or 0DIV, respectively. **B.** Example of an explant infected with RCaMP-AAV showing clockwise calcium waves (arrow) at 6DIV. 9 ROIs were defined on the explant. **C.** Average fluorescence trace of the recording in **B.** **D.** Smoothed traces of each ROI in **B.** Scale bar in **A.**: 100 μ m.

Demonstration of neuronal activation after optical stimulation using ChR2⁺/RCaMP⁺ neurons

The objective behind co-infecting cells with ChR2 and RCaMP vectors was to be able to demonstrate that neuronal activity increased after optical stimulation. However, our main obstacle was to find the appropriate microscopy setup. For this experiment, we needed to be able to stimulate these double-positive cells with blue light while also illuminating them with green light (to excite RCaMP). Then, the emitted light needed to be filtered with a red light filter to record RCaMP fluorescence. Although we purchased specific dichroic mirrors and had an LED setup capable of illuminating samples with different wavelengths simultaneously, we observed non-specific increases in fluorescence when the blue light was turned on, meaning there was probably some degree of crossing of green light through the red light filter, or a light diffraction effect that resulted in non-specific red light emission.

Therefore, we used an alternative setup, which was the high-speed Dragonfly 505 confocal microscope. The spinning disk setup of this equipment allows rapid time-lapse scans, which would allow us to record activity at an appropriate frame rate (around 10 fps). In addition, the confocal microscope can be programmed to use two lasers simultaneously, which meant that we could use both a green light laser and a blue light laser during recording. As explained in the methods section, we acquired time-lapse recordings of double-positive cortical neurons in three steps. First, we recorded spontaneous activity with only the green light laser and red light filter. Next, we recorded another time-lapse with blue light laser stimulation, while maintaining all the settings from the previous video. Finally, we took a snapshot of ChR2 and RCaMP expression in the selected area to confirm colocalization of both proteins in the same cell. This sequence is shown in **Figure 74A**. The overall fluorescence in the stimulated recording was higher than in the case of the non-stimulated recording. More firing events and active cells were visually identified in the stimulated recordings when viewing them at high speed. In addition, a high degree of colocalization of ChR2 and RCaMP can be observed in the snapshot, confirming that these activated cells were optically stimuable.

After recording, we used ImageJ to define ROIs on cells that became active after blue light stimulation and extract their fluorescence information over time. An example of these ROIs is also shown in **Figure 74A** on the left and middle images, where the same

ROIs were analyzed for both recordings of the same area. In **Figure 74B**, four examples of ROIs in which $\Delta F/F_0$ increased after stimulation are shown.

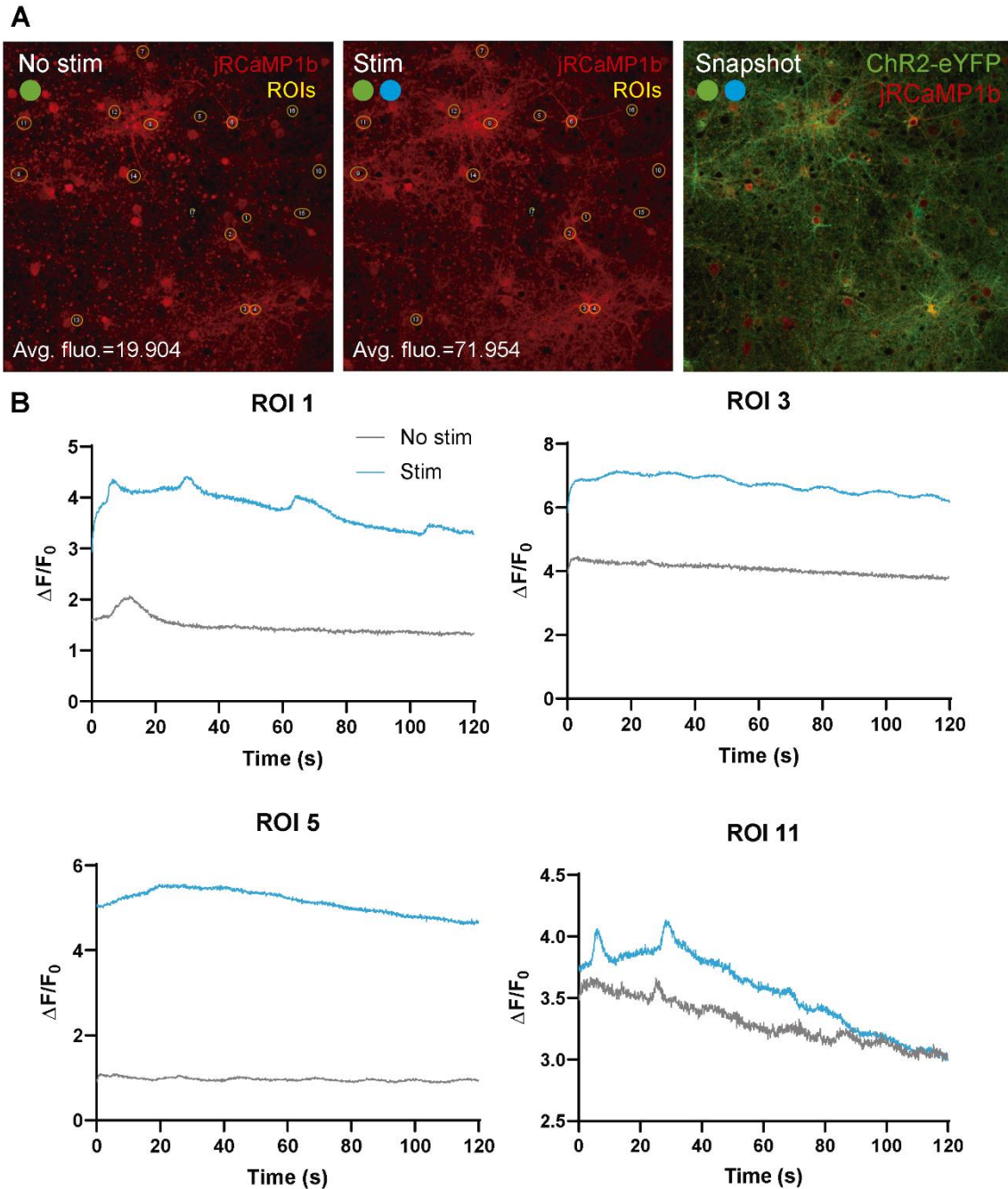


Figure 74. Activation of ChR2-eYFP+/jRCaMP1b+ neurons in response to blue light stimulation. **A.** Average intensity projection of non-stimulated and stimulated recordings (green and blue lasers are shown with dots). Average fluorescence of each recording is shown below each image. ROIs are shown as yellow ellipses. On the right, a snapshot of the localization of both proteins is shown. **B.** Four examples of ROIs that showed an increase in $\Delta F/F_0$ after stimulation are shown.

The main caveat of this experiment is that the blue light laser of the spinning disk confocal microscope cannot be programmed in square pulses, and the constant stimulation is likely not ideal to induce calcium spikes. This is why we chose a simpler analysis of individual

traces of different ROIs with ImageJ, instead of using a spike inference algorithm and analyzing traces obtained with Netcal. In fact, when we tried to analyze the effect of stimulation on spikes using Netcal, fewer spikes were observed in the stimulated recording compared to the number of spontaneous spikes. This is consistent with the idea that a constant stimulation depolarizes neurons excessively, and does not allow them to fire periodically, as would occur in the case of spontaneous activity or activity induced with square pulse stimulation. Still, the individual ROIs shown in **Figure 74** clearly show an increase in calcium transients over the recording, meaning that optical stimulation causes calcium release in these cells.

Although we also attempted this calcium recording protocol in cortical explants embedded in collagen, we experienced issues with the recording, as the laser power needed to penetrate into the 3D construct was much higher, leading to significant bleaching during recording. Therefore, we used cortical neurons cultured in 2D (same origin as the explants) infected with the same AAV vectors to perform this experiment.

Analysis of the effect of optical stimulation on axonal regrowth after injury in permissive and inhibitory conditions

Once we had confirmed the appropriate culture timepoints and verified that the infection protocol was efficient, we performed axotomy experiments in different conditions. As mentioned before, we infected explants on the day of dissection with ChR2 AAV, and cultured them in collagen 3:1 gels until 7-8 DIV. On that day, we performed axotomy of one side of the explant using a scalpel, and added new hydrogel to replace the one removed after axotomy. In some cases, we added 20 $\mu\text{g/ml}$ CSPG to the collagen mixture to simulate the inhibitory environment of the glial scar. After axotomy, we allowed 6 hours without additional manipulation for membrane resealing and stabilization of axon stumps. After these 6 hours, we applied optical stimulation in half of the explants of each condition (with or without CSPG).

To quantify regrowth after axotomy, we stained axons at 11 DIV with TUJ1 peroxidase staining. In the TUJ1 staining images, we defined two areas to quantify on the two different sides of the explant, the non-axotomized side (control) and the axotomized side (regrowth). We also defined the area of the explant as an additional value to consider, as it could influence overall axon growth (**Figure 75A**). We quantified the regrowth area and control area for all conditions, and compared the overall regrowth area (**Figure 75B**)

as well as the ratio of regrowth area to control area (**Figure 75C**). In both cases, regrowth was significantly lower in the stimulated samples without CSPG, meaning that stimulation was detrimental to regrowth. CSPG treatment did not show significant differences with the permissive substrate control, which could be due to insufficient CSPG concentration or the loss of CSPG gradient over time in culture.

To check if optical stimulation or CSPG treatment affected non-axotomized axonal area, we also normalized the control area to the explant area and compared it across conditions (**Figure 75D**). The control area was also significantly lower in stimulated samples without CSPG, meaning that stimulation is detrimental to control axon growth in addition to axon regrowth. Control areas and explant areas were not significantly different from each other, as shown in **Figure 75E-F**. However, it is possible that the trend in explant areas could influence this result, as the means are somewhat higher in the stimulated samples compared to the non-stimulated samples.

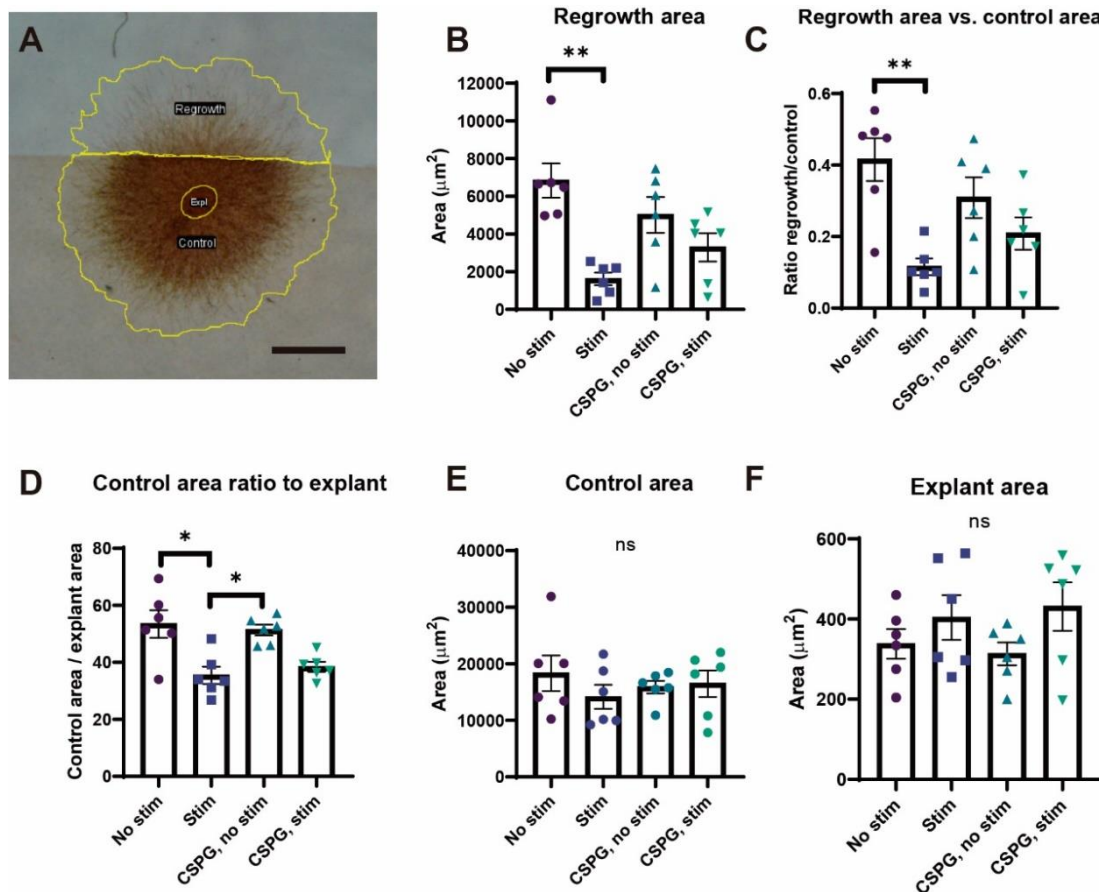


Figure 75. Axonal regrowth after axotomy in permissive and inhibitory conditions, with or without receiving optical stimulation 6 hours after axotomy. **A.** Definition of control and regrowth areas in an axotomized explant stained for TUJ1 with peroxidase staining. **B.** Regrowth area for each condition. **C.** Regrowth area normalized to control area. **D.** Control area normalized to explant area. **E.** Control area. **F.** Explant area. For all conditions, 6 explants were used for quantification (n=6).

DISCUSSION

In this chapter, we had the objective of developing a 3D axotomy platform to enable the study of different strategies to improve axonal regeneration. Ideally, we would have preferred to use a non-primary source of cells, but none of the protocols that we tested were suitable for obtaining isolated axons for axotomy. To make the platform more clinically relevant, it would be better to use a human source of cells, but we did not find a way to differentiate the hNS1 cell line in 3D conditions while also obtaining isolated axons for axotomy.

Arguably, there are other sources such as iPSCs or other neural progenitor cell lines that might have been suitable for this purpose, but many of these protocols require a longer time of differentiation. Ultimately, using these more complex protocols would have increased the total time required for each experiment, and would have limited our ability to test iterations of the 3D platform. Due to this fact, we finally decided to use cortical explants as a reliable source of long and isolated axons, which were routinely 1-2 mm long when using collagen gels.

A common observation with stem cells (C17.2 and hNS1) and cortical explants was that collagen hydrogels promoted retention of cell bodies inside cell aggregates, as compared to Matrigel which is known to induce cell migration. The increased soma-axon separation achieved with this gel was our main reason to choose it as the optimal gel for the axotomy platform, together with the fact that it supported culture of explants for at least 11 days *in vitro*. PEG-fibrin gels, despite possessing a high transparency and inducing less cell migration, were difficult to manipulate due to their hydrophobicity (reducing explant encapsulation reproducibility) and did not support the longer-term culture needed for axotomy experiments.

In order to study the effect of optical stimulation on axonal regeneration, we first needed to demonstrate three main concepts: 1) the ability to infect cortical explants with ChR2-eYFP, 2) the presence of spontaneous activity in the infected cortical explants around the time of axotomy, and 3) the activation of explants in response to optical stimulation. Concerning the first question, our main issue was determining an appropriate protocol for infection of embryonic explants that were to be cultured in hydrogels. We found that these explants survived overnight infection on the day of dissection, and that they were efficiently infected or co-infected with ChR2 and/or RCaMP AAV vectors. Once we had

demonstrated this, we also proved the existence of spontaneous activity in RCaMP+ explants at 6DIV, which is right before the day on which axotomy and optical stimulation was planned.

Finally, in isolated cortical neurons coinfecting with both proteins, we also demonstrated an increase in calcium following stimulation with blue light. Normally, optical stimulation uses trains of square pulses applied at a low frequency (20 Hz) in trains of 1 s ON / 1 s OFF to allow repolarization of neurons. This results in synchronic calcium spikes in response to the stimulation. Despite the fact that our stimulation protocol was performed using confocal lasers, which do not allow square pulse stimulation in pulse trains, we did observe an increase in calcium release in some cells. In addition, the overall fluorescence of the recording was higher, indicating that the majority of cells in frame became depolarized. In this case, we did not expect an increase in spikes, due to the constant stimulation provided by the blue laser.

In our axotomy experiments with embryonic cortical explants, we must consider that neurons derived from embryonic tissue have a naturally higher intrinsic ability to regenerate than adult neurons. Although at 7DIV the neurons are already at a postnatal stage (approximately 3 days postnatal), some regenerative ability is likely maintained at this early stage. The advantage of this is that it facilitates the study of factors that affect regeneration. If the regeneration capacity of the neurons in our model were null even in a permissive environment, it would not be possible to distinguish the effect of an inhibitory environment, and potentially useful treatments might not be identified. However, the difference with real injuries in adult patients must be acknowledged, and results should be interpreted with this consideration in mind.

Regarding axotomy experiments in permissive and inhibitory conditions, we believe that the conditions of these experiments still require some adaptations to avoid unwanted effects of uncontrolled variables. In the case of optical stimulation, we had the previous reference that cortical neurons were responsive to optical stimulation when applied 6 hours after axotomy, while it was detrimental to survival when applied 30 minutes after axotomy (Mesquida-Veny et al., 2022). We would have assumed that this time was sufficient to allow membrane resealing, to prevent calcium toxicity upon depolarization of cells by optical stimulation. However, it seems that this time was still insufficient to stabilize the injured axons before stimulation in 3D conditions. It is possible that

differences in the interaction of cells with the extracellular matrix could affect the rate at which membrane resealing is achieved, or that the cytoskeletal organization of budding growth cones occurs in a different manner in these conditions.

Another unexpected result was that the CSPG concentration we added to some gels after axotomy (20 $\mu\text{g/ml}$) was not significantly detrimental to axonal regrowth. We had seen that, in extracts of spinal cord glial scar tissue, around 1 μg CSPG/mg of tissue were quantified by glycosaminoglycan assay in a recent publication (Park et al., 2022). Also, a common coating concentration for 2D cultures treated with CSPG is 20 $\mu\text{g/ml}$. Using these values as a reference, we chose the selected concentration to add in hydrogels. To our knowledge, no other publications have used CSPG in this way in 3D *in vitro* axotomy models. Our theory as to why there was no significant effect is that the gradient may have been lost by diffusion over the three days that were allowed for regrowth. However, CSPGs have a high molecular weight, which makes them less prone to diffusion. Therefore, higher concentrations could be tested to confirm this hypothesis, or CSPG could be added to the culture medium at the same concentration to prevent dilution.

An additional consideration regarding the regrowth results is that the quantification of regrowth areas does not factor in the density of axons in the selected area. In some cases, a much higher density of axons is present in the same area. The main issue with quantifying axon density in our images, in which axons were stained with TUJ1 by peroxidase/DAB staining, is that staining intensity does not linearly correlate to abundance of the stained protein. Therefore, an alternative method of imaging axons should be used to analyze axon density. One option would be to use fluorescence, for which intensity quantifications are possible. Calcein staining could be a suitable option, considering that these neurons are already infected with a ChR2-eYFP construct, and the combined green fluorescence emission would be strong even in thin axonal processes.

Finally, we would also propose the use of high-magnification time-lapse recordings to track individual regrowing axons after axotomy. In this case, fluorescence could also be useful to visualize axonal processes, which are not clearly distinguished in semi-opaque collagen gels by brightfield imaging. This method would allow the discrimination of regeneration and lateral growth, which for the moment, our system is unable to differentiate. However, with the appropriate adaptations, our model could be used to complement the data obtained in 2D cultures. Our initial results point at differences in the

response to optical stimulation in 3D cultures, which highlights the importance of comparing these two culture modalities.

CHAPTER 3. Potential of optical modulation of neuronal activity to enhance axon regeneration after axotomy in entorhino-hippocampal organotypic slice co-cultures

INTRODUCTION

Organotypic slice cultures as relevant *in vitro* models of neural tissue

Perinatal brain slice cultures offer unique advantages over other 2D or 3D *in vitro* methods, since they mimic numerous *in vivo* aspects due to the presence of most of the cell types observed *in vivo* (Gahwiler, 1988; Gahwiler, Capogna, Debanne, McKinney, & Thompson, 1997; Holopainen, 2005). For most purposes, slices obtained from early postnatal brain and cultured for long periods, termed organotypic slice cultures (OSC), largely preserve a high degree of cellular differentiation and tissue organization (e.g., laminar organization and synaptic target specificity) during culture (see below). OSCs have been prepared from several brain regions, including hippocampus, neocortex, allocortex, striatum, spinal cord, hypothalamus or cerebellum (Behan, Kroker, & Bolz, 1991; Del Turco & Deller, 2007; Gahwiler, 1981a; Hildebrandt-Einfeldt et al., 2021; Hurtado de Mendoza, Balana, Slesinger, & Verma, 2011; Kim, Kim, Park, Lee, & Namkoong, 2013; D. Li, Field, Starega, Li, & Raisman, 1993; Lonchamp, Dupont, Beekenkamp, Poulain, & Bossu, 2006; Ostergaard, 1993; Sofroniew, Dreifuss, & Gahwiler, 1988; Stoppini, Buchs, & Muller, 1991; Zimmer & Gahwiler, 1984).

Relevantly, the use of OSCs obviates the need for extensive animal surgery and expensive laboratory equipment (e.g., Humpel, 2015). Thus, their use in basic and applied research has been applied over the years and more recently due to the 3R strategy of animal research (Del Turco & Deller, 2007; Gahwiler et al., 1997; Kim et al., 2013; Lossi & Merighi, 2018). In fact, OSCs have shown intrinsic relevance also shared by other approaches based on the use of induced pluripotent stem cells (iPSC) such as 3D organoids (Kim, Jang, Sankpal, Patel, & Patel, 2023; Y. Li, Zeng, Wu, & Luo, 2023; Zhang, O'Laughlin, Song, & Ming, 2022). As a main advantage, a number of neuropathological events (genetic, traumatic or infective) that affect specific brain regions have been easily reproduced in OSCs (Adamchik, Frantseva, Weisspapir, Carlen, & Perez Velazquez, 2000; Bali, Nagy, & Kovacs, 2007; Croft, Futch, Moore, & Golde, 2019; Diekmann, Nitsch, & Ohm, 1994; Falsig et al., 2008; Laake, Haug, Wieloch, & Ottersen, 1999; Lamoureux et al., 2022; Mayer, Fischer, Schneider, Heimrich, & Schwemmler, 2005; McCarthy et al., 2021; Perez-Gomez & Tasker, 2014; Routbort, Bausch, & McNamara, 1999; Stoppini et al., 2000), allowing them to be currently used

as model of neurodegeneration (e.g., Alzheimer's (Farrell, Mumford, & Wiseman, 2022; S. Jang et al., 2018; Kamikubo et al., 2022) or Parkinson's (Elfarrash et al., 2019) diseases).

Organotypic slice culture methodologies

Several methods and modifications have been developed for long-term culture of brain slices, from the pioneer “roller tube” technique of Gahwiler (Gahwiler, 1981b) to the interphase method of Muller and coworkers (del Rio & Soriano, 2010; Gahwiler et al., 1997; Stoppini et al., 1991), or current methods using adult-derived brain tissue (e.g., (Humpel, 2019; Lee et al., 2020; Schommer, Schrag, Nackenoff, Marwarha, & Ghribi, 2017). Pioneer OSCs (Gahwiler, 1981b) have proved tedious to prepare with high cytoarchitectonic variability due to thinning of slices. Furthermore, hydrogel-embedded cultures show intense glial reactivity, which largely conditioned functional studies and optical *in situ* analysis (del Rio, Heimrich, Soriano, Schwegler, & Frotscher, 1991; del Rio & Soriano, 2010).

The membrane interface culture method (MICM) developed by Muller and coworkers facilitates access to the culture, for applications ranging from optical to pharmacological studies (see (Gahwiler et al., 1997; Humpel, 2015; Stoppini et al., 1991) for review). The standard of the MICM is to maintain slices on a semiporous polytetrafluoroethylene (PTFE) membrane (0.4 μm \emptyset pore; MillicellTM, Millipore), at 35-37° C temperature in the interface between the medium and the humidified atmosphere of the 5% CO₂ incubator. In this method, the medium reaches cultures through the porous membrane *via* capillarity.

This culture technique and its current modification allow the culture of nerve cells, from neurons to glial cells, that are highly differentiated in terms of their morphological and physiological characteristics (see (Caeser & Aertsen, 1991; Caeser, Bonhoeffer, & Bolz, 1989; Zimmer & Gahwiler, 1984) for classic studies). Moreover, the presence of glial cells is believed to provide a microenvironment that facilitates differentiation of neurons. In this respect, glial (mainly astroglial) cells proliferate in the culture and a border of laterally migrating reactive astrocytes surrounds the MCIM (Caeser & Aertsen, 1991; del Rio et al., 1991; del Rio & Soriano, 2010). Scarred astroglial cells in MICM cultures are also located at the bottom of the slice. This is important, since the culture medium is applied below the membrane, and this dense glial scar hinders the penetration of putative

drug treatments and, in some studies, additional functional analysis (Drexler, Hentschke, Antkowiak, & Grasshoff, 2010; Pena, 2010).

Organotypic slice cultures recapitulate key aspects of brain anatomy and regeneration after axotomy

In anatomical terms, the hippocampus and the dentate gyrus are discrete brain regions with a unique laminar organization of cell layers and afferent connections (Paxinos, Franklin, & Franklin, 2001). The entorhino-hippocampal connection (EHC), also termed the perforant pathway, is the main afferent connection to the hippocampus. The perforant pathway derives from neuronal cells located in the upper layers of the entorhinal cortex (mainly layer II-III), which terminate in the stratum lacunosum-moleculare (SLM) of the hippocampus proper and the outer two-thirds of the molecular layers of the dentate gyrus (Andersen, 2007; Seifert, 1983). The EHC has been analyzed in detail, and various cellular and molecular factors mediating its development have been determined (see (Skutella & Nitsch, 2001) for review).

Moreover, as seen in pioneer studies by G. Raisman (D. Li, Field, Yoshioka, & Raisman, 1994), P.L. Woodhams (Woodhams & Atkinson, 1996; Woodhams, Atkinson, & Raisman, 1993) and M. Frotscher (Frotscher & Heimrich, 1993; Heimrich & Frotscher, 1993), reviewed in (Del Turco & Deller, 2007; Hildebrandt-Einfeldt et al., 2021), entorhino-hippocampal (EH) co-cultures possess some key features that make them particularly interesting in studies of axonal regeneration: i) the EHC is reproduced easily *in vitro* in MCIM cultures (see above references); ii) the EHC *in vitro* showed a laminar specificity similar to that found *in vivo* (e.g., (Del Rio et al., 1997; Gaiarsa & Heimrich, 1995; Kluge, Hailer, Horvath, Bechmann, & Nitsch, 1998; Skutella & Nitsch, 2001)); iii) the EHC is myelinated both *in vitro* in MCIM similarly to *in vivo* (e.g. (Del Rio et al., 1996; Mingorance et al., 2006; Savaskan et al., 1999)); and iv) most of the cellular and molecular barriers to axon regeneration (e.g, myelin or chondroitin sulphate proteoglycans) are present and overexpressed by different cell types after the axotomy of the perforant pathway *in vitro* similar to *in vivo* (e.g., (del Rio & Soriano, 2010; Mingorance et al., 2006; Seira et al., 2010)). Thus, due to the target-specific termination of the EC axons, it is possible to study their growth or remodelling and to quantify the number of reinnervating axons after axotomy *in vitro* (e.g., (Kluge et al., 1998)).

Indeed, this platform has been used to demonstrate age-related decline as a function of the regenerative ability of EH axons, as it occurs *in vivo* during postnatal development (del Rio et al., 1991; del Rio, Sole, Borrell, Martinez, & Soriano, 2002; Prang, Del Turco, & Kapfhammer, 2001; Savaskan et al., 1999; Woodhams & Atkinson, 1996; Woodhams et al., 1993). The ability of young hippocampal tissue to support the regrowth of lesioned E18-P1 entorhinal axons in culture has been examined in detail for many years by using heterochronic co-cultures (e.g., (del Rio et al., 1991; del Rio et al., 2002; Prang et al., 2001; Woodhams & Atkinson, 1996; Woodhams et al., 1993)). This tissue appears to be permissive for regeneration and results in an axonal projection to the hippocampal tissue, terminating in the appropriate targets (del Rio et al., 1991; del Rio et al., 2002; Prang et al., 2001; Woodhams & Atkinson, 1996; Woodhams et al., 1993).

However, it has also been established that there is a limited ability to modify the regenerative connections made from the postnatal entorhinal cortex (EC) by juxtaposition of different hippocampal target fields due to the apparent early specification of entorhinal projection neurons (Frotscher & Heimrich, 1995; Frotscher, Heimrich, & Deller, 1997; Super, Martinez, Del Rio, & Soriano, 1998). In addition, most of these cues disappeared progressively from the hippocampal tissue during the first 10 days in culture (Del Rio et al., 1996; del Rio et al., 2002). Thus, because of this limited capacity for regeneration following lesion within the perforant pathway, the period at 6-10 DIV provides an optimal basis for screening agents and modifications that might enhance axon regeneration.

Importantly, in heterochronic cocultures, the addition of a full young hippocampus might modify the developed glial scar (see (del Rio et al., 2002)). Furthermore, not only does the inhibitory environment play a role in the absence of regeneration in OSCs, but it is also well known that lesioned CNS neurons showed a limited intrinsic regenerative capacity in adult CNS stages, which also contributes to the failure of axon regeneration after axotomy (e.g., (Curcio & Bradke, 2018)). In OSCs, the projecting EC neurons survive after axotomy at 15 days *in vitro* (DIV) but are unable to regrow (del Rio et al., 2002; Sole, Fontana, Gavin, Soriano, & del Rio, 2004). Thus, in the last years there have been several studies approaching different aspects of projecting neuron physiology aimed at triggering intrinsic regrowth ability (He & Jin, 2016; Mar, Bonni, & Sousa, 2014). In this direction, neuronal activity modulation has been explored. In the spinal cord, electrical stimulation has been shown to enhance regeneration of sensory axons after peripheral nerve or dorsal column injury; and sprouting of cortical axons into contralateral spinal

cord grey matter after axotomy (e.g., see (Mesquida-Veny, Martinez-Torres, Del Rio, & Hervera, 2022) for details).

OBJECTIVES

Taking into account the aforementioned considerations and properties of OSCs, in this chapter, we will focus our attention on OSCs containing EC and hippocampus to explore axonal development and regeneration of CNS neurons after axotomy, and whether this regeneration can be modulated by neuronal activity using projecting EC neurons as model. Using cell-directed optogenetics (ChR2), calcium imaging (GECIs) and axonal tracing techniques (Biocytin), axonal development and regeneration will be monitored in MCIM cultures, where some of the molecular and cellular mechanisms responsible for its absence after adult CNS lesions are described (del Rio et al., 2002; Mingorance et al., 2004; Mingorance, Fontana, Soriano, & Del Rio, 2005; Mingorance et al., 2006; Sole et al., 2004).

Our objectives for this chapter were the following:

1. To generate optically stimuable OSCs with ChR2⁺ ECs, and to demonstrate their stimulation-induced activation by calcium imaging.
2. To determine whether the specific activation of EC neurons might modify the natural development of the EHC.
3. To determine whether the specific activation of EC neurons might modify regeneration after axotomy in two different scenarios:
 - a. In permissive conditions (axotomy at 7 DIV)
 - b. In inhibitory conditions (axotomy at 14 DIV)

METHODS

Entorhino-hippocampal culture (EHC) experiments

Co-cultures were prepared from P0–P1 CD1 newborn mice (Charles River, Lyon, France). After brain removal, single horizontal sections (300–350 μm thick) containing both the EC and the hippocampus were obtained using a tissue chopper (McIlwain) and maintained in ice cold slice preparation media (75% minimal essential medium, 25% HBSS, 2 mM glutamine and 0.044% NaHCO_3 ; pH 7.3). Slices were further dissected under dark-field binocular control to isolate the hippocampus and the EC. In dissected slices, the subiculum was preserved with the hippocampal slice. After dissection, the dissected EC (n=45) were incubated overnight under gentle agitation with AAV9-Syn-ChR2 virus (diluted 1:500 v/v). In some cases, some EC were double-infected with AAV9-Syn-ChR2 and AAV9-Syn-JRCaMP1b. The dissected hippocampal slices were seeded onto MillicellTM transwells and incubated with culture medium (50% minimal essential medium, 25% horse serum, 25% HBSS) containing 2 mM glutamine and 0.044% NaHCO_3 ; pH 7.3.

The next day, the infected and non-infected ECs were rinsed in incubation medium and the EHC were established by transferring the EC slices to the cultured hippocampus and reoriented using fine tungsten needles. Co-cultures were fed with 1.2 ml of culture medium. The membrane cultures were maintained in a humidified incubator at 37°C in 5% CO_2 . This day was considered 0 DIV. The medium was changed after 24 h and subsequently every 48 h until the tissue was examined. Two groups of EHC cultures were established for optogenetic stimulation experiments. A first group of 18 EHCs were used to investigate effect of optical stimulation on axonal growth and development of EH connections. Half of these EHC were stimulated with blue (470 nm) light (n=9, AAV9-ChR2 infected), while the other half (n=9, AAV9-ChR2 infected) were not stimulated. In a second group, the EH connection was axotomized at 7 DIV (n=9, AAV9-ChR2 infected) and 14 DIV (n=9, AAV9-ChR2 infected) by cutting the co-cultures from the rhinal fissure to the ventricular side along the entire EH interface with a thin tungsten needle (del Rio et al., 2002). This second group was also stimulated with blue light following the protocol described in the following section. The first group was stimulated

The first group was processed after 7 DIV (4 days of light treatment). The second group was processed after 7 days post-light treatment.

All experiments were performed under the guidelines and protocols of the Ethical Committee for Animal Experimentation (CEEA) of the University of Barcelona, and the protocol for the use of animals in this study was reviewed and approved by the CEEA of the University of Barcelona (CEEA approval #276/16 and #141/15).

***In vitro* optogenetic stimulation of EC projecting neurons**

EHC containing the infected ECs with AAV9-Syn-ChR2 were used for *in vitro* optogenetic stimulation experiments. A 470 nm emission LED array (LuxeonRebel™) under the control of a Driver LED (FemtoBuck, SparkFun) of 600mA and a pulse generator PulsePlus (Prizmatix) was used to deliver blue light to neuronal cultures (Sala-Jarque et al., 2020). During experiments, temperature changes inside the optogenetic platform were monitored by an Arduino-UNO™ microcontroller using a temperature probe DS18B20 with PWM relay output (CEBEK I-86, Spain) connected to a 12 V cooling fan. The cooling fan switched on with temperature increases >0.5 °C from 37 °C. The LED array was placed onto aluminum heat sink plates below the culture dishes in the optogenetic platform at a distance of 2 cm to ensure that the complete area of the well plate was illuminated. The optogenetic stimulation protocol consisted of cycles of illumination at 20 Hz of frequency with 5 ms – 45 ms pulses, in 1 s ON- 1 s OFF periods. In these conditions, the external stimulation voltage unit drives 12 V and 600 mA for each Quad LED module, with an average light intensity of approximately 20–25 mW/cm² measured at the culture dish containing the devices with a Newport 1919 optical power meter (Newport Photonics). The stimulation was applied 72 h after the establishment of the EHCs (see above). For axotomized EHC slices, the stimulation time-point after the axotomy was 24 h after axotomy and performed twice a day for 5 or 7 days as indicated above.

Calcium imaging in AAV9-Syn-ChR2 and AAV9-Syn-jRCaMP1b double-infected EC neurons

Some double-infected EH co-cultures were analyzed for Ca²⁺ transients in an Olympus IX61 microscope equipped with an Fluoview-II (5 MPx) camera and CellP software

(Olympus). The microscope used a X-Cyte illumination system (Xenon halide lamp of 100W working at a 50% regime). Slices were illuminated at 15 DIV using *ad hoc* designed filter sets by using a 20 X water immersion objective with an NA of 0.50, infinity corrected (UM Plan FL, Olympus). Pictures (512 x 512 pixels) were obtained every 200 ms, allowing the capture of Ca²⁺ changes revealed by jRCaMP1b, as spontaneous neuronal activity. In addition, double immunofluorescence images were obtained to demonstrate that stimulated EC neurons expressed both ChR2 and jRCaMP1b. First, basal spontaneous activity was recorded during 5-10 s. After this time, the slice was illuminated for 30 s with a 470 nm diode laser collimated beam of 0.4 mm diameter and 100 mW at 90° relative to the optical axis (**Figure 79**). The xyz position of the laser beam was controlled using a 3-axis micromanipulator (Nashirigue, Japan) to target the EC, and the changes induced by the illumination were recorded for additional 40 sec. Time lapse videos (multi *.tif files) were processed in FijiTM, and denoised using AydinTM v.0-1-13 <https://doi.org/10.5281/zenodo.5654826>, with the self-supervised auto-tuned Classic-Butterworth algorithm, and motion corrected and ROIs selected by using EzCalcium (Cantu et al., 2020). Selected ROIs were analyzed using custom-made MatlabTM macros (Analyca) based on the MatlabTM macros developed by Prof. Thomas C. Südhof's lab (Sun & Südhof, 2021) for GECI fluorescence changes and a clustered cross-correlation analysis was applied using NeuroCaTM software (M. J. Jang & Nam, 2015). Computation was performed on an iMac computer (macOS Big Sur 11.6, 3.2 GHz i7, 6 nuclei and 32 GB) running Python 3.9-12, Conda 23.5.2; Napari 0.4.12 and Matlab 2022b update 3 (9.13.0.2126072).

EHC labeling with biocytin

After 7–10 days of treatment, a small crystal of biocytin (Sigma Aldrich) was injected in the entorhinal slice to label the entorhinal-hippocampal projections (EHP). The following day, co-cultures were fixed with paraformaldehyde and 50 µm thick sections were obtained using a vibratome. Sections were incubated overnight with an avidin-biotin peroxidase complex (ABC-eliteTM, diluted 1:100; Vector Laboratories) and peroxidase activity was visualized using a nickel-enhanced diaminobenzidine (DAB) reaction. Some cultures were double processed for biocytin detection and calretinin (a marker of Cajal-Retzius cells) as previously described (del Rio et al., 2002). Only cultures displaying equivalent biocytin labeling in the entorhinal cortex were considered.

Immunohistochemical procedures

For immunocytochemistry, vibratome sections (50 μm thick) were permeabilized with DMSO and blocked with normal serum containing Fab IgG fragments (Jackson Immunocytochemical Laboratories). Free-floating sections were incubated for two days with either anti-GFAP (diluted 1:2000), anti-NG2 (diluted 1:1000, Chemicon International), or anti-MAG2 (diluted 1:200, Sigma Aldrich) primary antibodies and the ABC Kit (Vector Laboratories). Controls, including omission of the primary antibody or its substitution by normal serum, prevented immunostaining. In some cases, EH co-cultures infected with AAV-Syn-ChR2, were fixed and sectioned in the vibratome as above and mounted in MowiolTM.

EHC treatments

Taking advantage of the early generation of Cajal-Retzius (CR) cells with respect to granule cells and pyramidal neurons and of their layer-specific distribution, we ablated CR cells by local application of domoic acid, an α -amino-3-hydroxy-5-methylisoxazole-4-propionic/kainate (AMPA/KA) receptor agonist (Del Rio et al., 1997). After two days, 95% of the CR cells were removed from the hippocampal slice that received the EC slice (Del Rio et al., 1997). In a second set of experiments, EHC were prepared and were axotomized at 10 DIV. After rinsing, a small piece of P0 hippocampus containing the stratum lacunosum moleculare and the molecular layer of the dentate gyrus (*slm/ml*) was transplanted in the lesion site (del Rio et al., 2002). After 7 additional DIV, cultures were traced with biocytin and double processed for biocytin tracing and calretinin as described above.

RESULTS

Analysis of the regenerative properties of lesioned entorhino-hippocampal projections in organotypic slice cultures

OSCs of the EHCs were prepared as indicated in **Figure 76A**. After 7-10 DIV, Biocytin-traced EHC displayed EC axons crossing the subicular region and innervating the *stratum lacunosum moleculare (slm)* of the hippocampus proper and the molecular layer (ml) of the dentate gyrus in a lamina-specific manner (**Figure 76B**). Indeed, double-labeled cultures with Biocytin and Calretinin showed that EC axons specifically innervate regions populated with hippocampal Cajal-Retzius cells (**Figure 76C-D**) as indicated in other studies (e.g. (Del Rio et al., 1997; J. B. Deng, Yu, & Li, 2006; J. B. Deng, Yu, Wu, & Li, 2007)). Next, in a second set of experiments, EHC were axotomized at 7 or 14 DIV. At 12 days after lesion (DAL), they were traced with Biocytin and processed for light or electron microscopy (**Figure 76E-H**).

Developed sections demonstrated the decline in the number of EHC that showed EC axon regeneration in the hippocampus and the dentate gyrus when axotomy was performed at 14 DIV (**Figure 76E-F**). In fact, none of the EHC lesioned at 14 DIV showed EC axons in the hippocampus (**Figure 76F**). In contrast, EHC lesioned at 7 DIV showed regenerating EC axons in the natural target regions. In electron microscopy images, Biocytin-labeled axon terminals were observed to contact with dendrites of pyramidal and granule cells (**Figure 76G-H**). In conclusion, our results demonstrate that layer-specific regeneration of lesioned EC neurons is absent after 2 weeks *in vitro*.

Increased glial scar generation after EHC lesion *in vitro*

The EHC axotomy *in vitro* was followed by a robust glial reaction, as observed by immunocytochemistry (**Figure 77**). Slight cavitation (<25–30 μm) occurred during the first 5–7 days after lesion (DAL), with abundant reactive astroglia (GFAP-positive; **Figure 77B and D**), amoeboid microglia (not shown) and NG2-positive oligodendrocyte progenitors on both sides of the transection (**Figure 77C and E**). After > 10 DAL, the cavity was filled with a dense network of glial cells and processes (see **Figure 77E**). Overexpression of the myelin-associated glycoprotein (MAG) in small-size proliferating oligodendrocytes after lesion was also observed in lesioned OSC at 15 DIV.

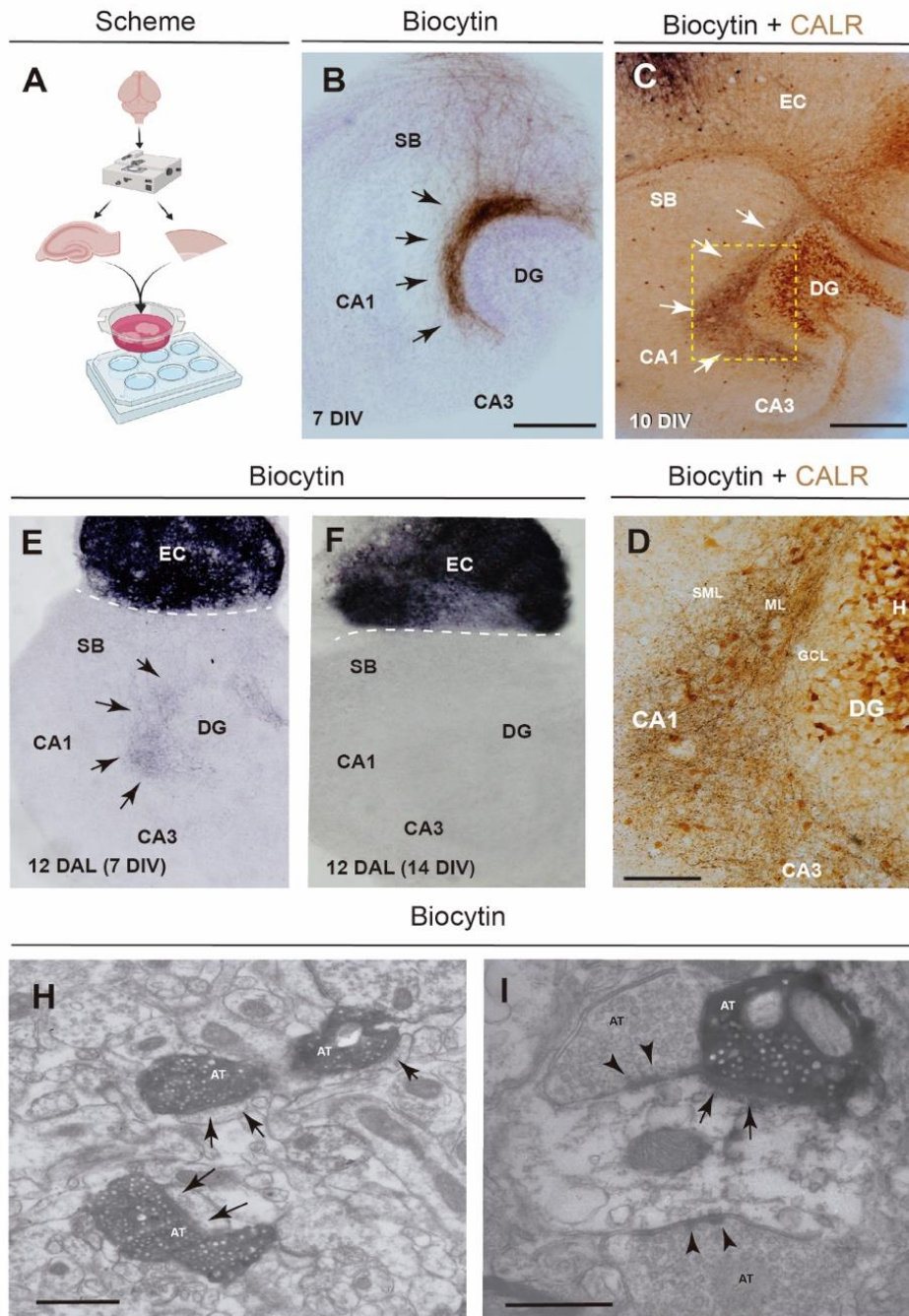


Figure 76. Decline of axon regeneration of EC axons in aged EHC. **A)** Scheme illustrating the procedure of the EHC preparation (see Material and Methods for details) **B.** Vibratome section of a EHC of 7 DIV labeled with Biocytin in the EC. Labeled Axons (arrows) innervate the hippocampus in a layer-specific manner. **C-D.** Vibratome section of a double-labeled EHC (Biocytin (black) and Calretinin (brown)) of 10 DIV. The boxed region in **C** can be seen in **D.** **E-F.** Low magnification of Biocytin traced EHC 12 days after axotomy (DAL) at 7 **E** and 14 DIV **F.** Notice the regeneration of the EHC after axotomy at 7 DIV (arrows in **E**) and the absence of regeneration after a lesion at 14 DIV. **H-I.** Examples of electron microscopy photomicrographs illustrating the presence of Biocytin labeled axon terminal in the slm/ml of EHC lesioned at 7 DIV and analyzed 12 DAL. Arrows point to asymmetric synapses on unidentified dendrites. Arrowheads in **I** point to symmetric contacts onto a dendrite that also showed a symmetric contact from a regenerating EC axon labeled with Biocytin. Scale bars: **B** = 200 μ m pertains to **E-F**; **C** = 200 μ m; **D** = 100 μ m. **H-I** = 1 μ m. Abbreviations: DG: dentate gyrus; CA1-2: Hippocampal regions; SB: Subiculum; EC: Entorhinal cortex; GCL: granule cell layer; ML: molecular layer; SLM. *stratum lacunosum moleculare*; H: Hilus; AT: Axon terminal.

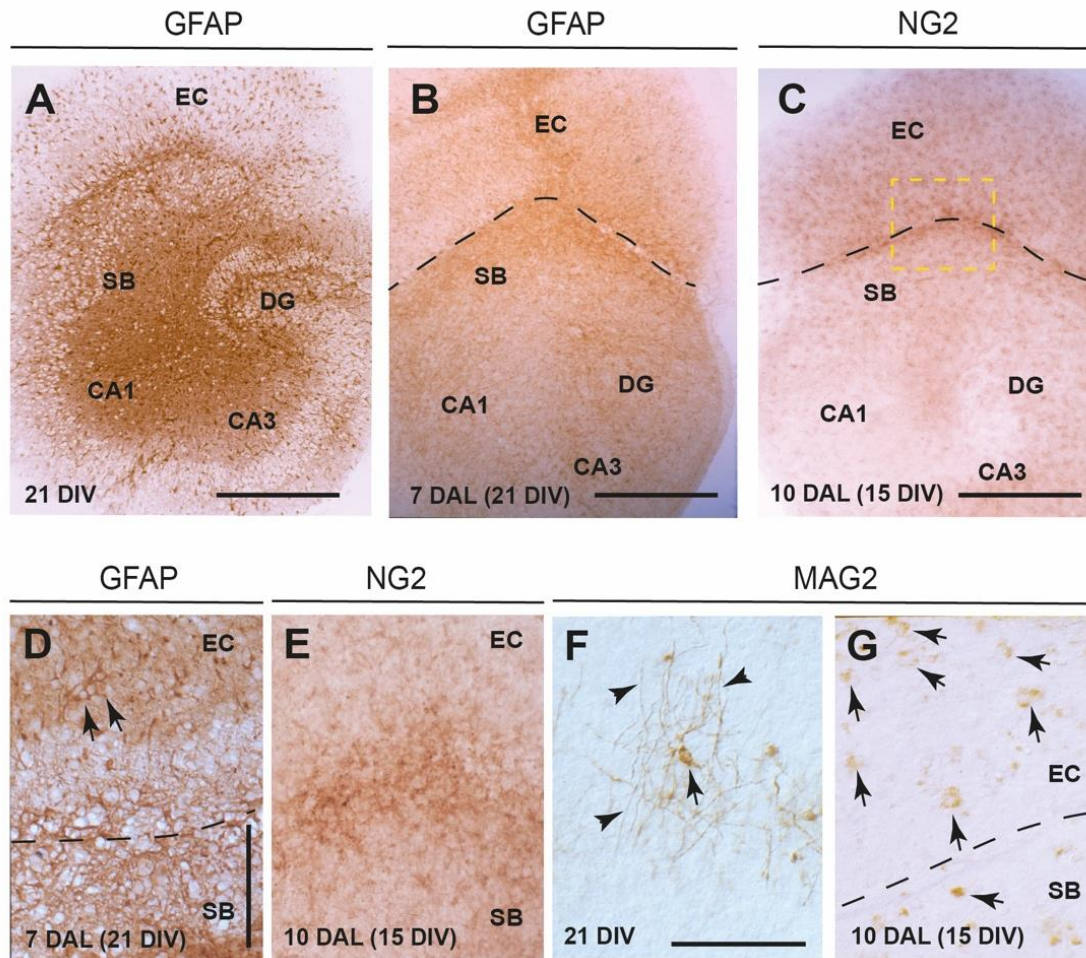


Figure 77. Glial proliferation after EHC axotomy in vitro. **A.** Low power photomicrograph illustrating the distribution of the GFAP-positive astrocytes in a OSC after 21 DIV. The distribution of GFAP-positive cells is similar to those reported in vivo (e.g., del Rio et al., 1991). **B-C.** Changes in GFAP (**B**) and NG2-immunostaining (**C**) after EHC axotomy at 21 DIV **B** and 15 DIV **C**. The dashed line shows the axotomy trajectory, and the boxed area in **C** is shown in **E**. Numerous reactive cells are located close to the axotomy transection (arrows in **D**). As indicated, a cavitation can be seen during the first week after lesion **D**, which is occupied by reactive cells **E**. **F-G.** Example of the morphological changes in the MAG-positive cells after EHC axotomy. In non-lesioned cultures MAG positive cells (arrow in **F**) are mainly located in the white matter displaying long expansions (arrowheads in **F**) as chandelier-like processes. After axotomy in **G**, these features are no longer observed, and a numerous number of small proliferating cells (arrows) with MAG-positive labelling in the soma can be observed in both sides of the lesion. Scale bars: A-C: 200 mm; D and F: 100 mm pertains to E and G respectively. Abbreviations as in **Figure 76**.

Target ablation of EC axons by domoic acid impairs axon development of the EHP, but target transplantation is unable to overcome the absence of EHP regeneration after axotomy in aged OSCs

In a third set of experiments, we aimed to explore whether changes in the target regions of the hippocampus could affect the regenerative potential of lesioned EC. Thus, as a control, we treated hippocampal slices with domoic acid to reduce the number of Cajal-Retzius (CR) cells in the hippocampus following the protocols published in (Del Rio et al., 1997; Super, Del Rio, Martinez, Perez-Sust, & Soriano, 2000) (**Figure 78A**). 10 DAL the EHC was traced with biocytin and the EHC were double processed for calretinin and Biocytin (**Figure 78B**). Results demonstrated that the absence of the Cajal-Retzius cells impair the establishment of the EHC. In contrast, subicular cells were able to innervate the entorhinal cortex being retrogradely labeled with Biocytin (**Figure 78B**). This situation was similar to those observed in OSCs axotomized at 15 DIV analyzed at 10 DAL (**Figure 78C**).

Next, we aimed to explore whether the ectopic transplantation of the postnatal *slm/ml* was robust enough to recapitulate the EC axon regrowth after lesion (**Figure 78D**). Thus, EHC lesioned at 10 DIV were transplanted with P0-dissected *slm/ml* (**Figure 78D-F**). 7 DAL, OSC were processed for Biocytin labeling and calretinin immunostaining. Results showed the survival of Cajal-Retzius cells in the transplanted *slm/ml* (**Figure 78E-F**). However, although some small bundles of EC axons were observed at the frontier, most lesioned EC axons were unable to enter in the transplanted target region as well in the remaining hippocampus. In contrast, some Cajal-Retzius cells (arrow in **Figure 78F**) were retrogradely labeled with Biocytin, suggesting their capability to innervate the lesioned EC as suggested during development (Anstotz et al., 2016; Frotscher, Seress, Abraham, & Heimrich, 2001). This suggests that the presence of the appropriate target is not robust enough to induce the regeneration of lesioned EC axons, and that other intrinsic factors might impair the expected regeneration.

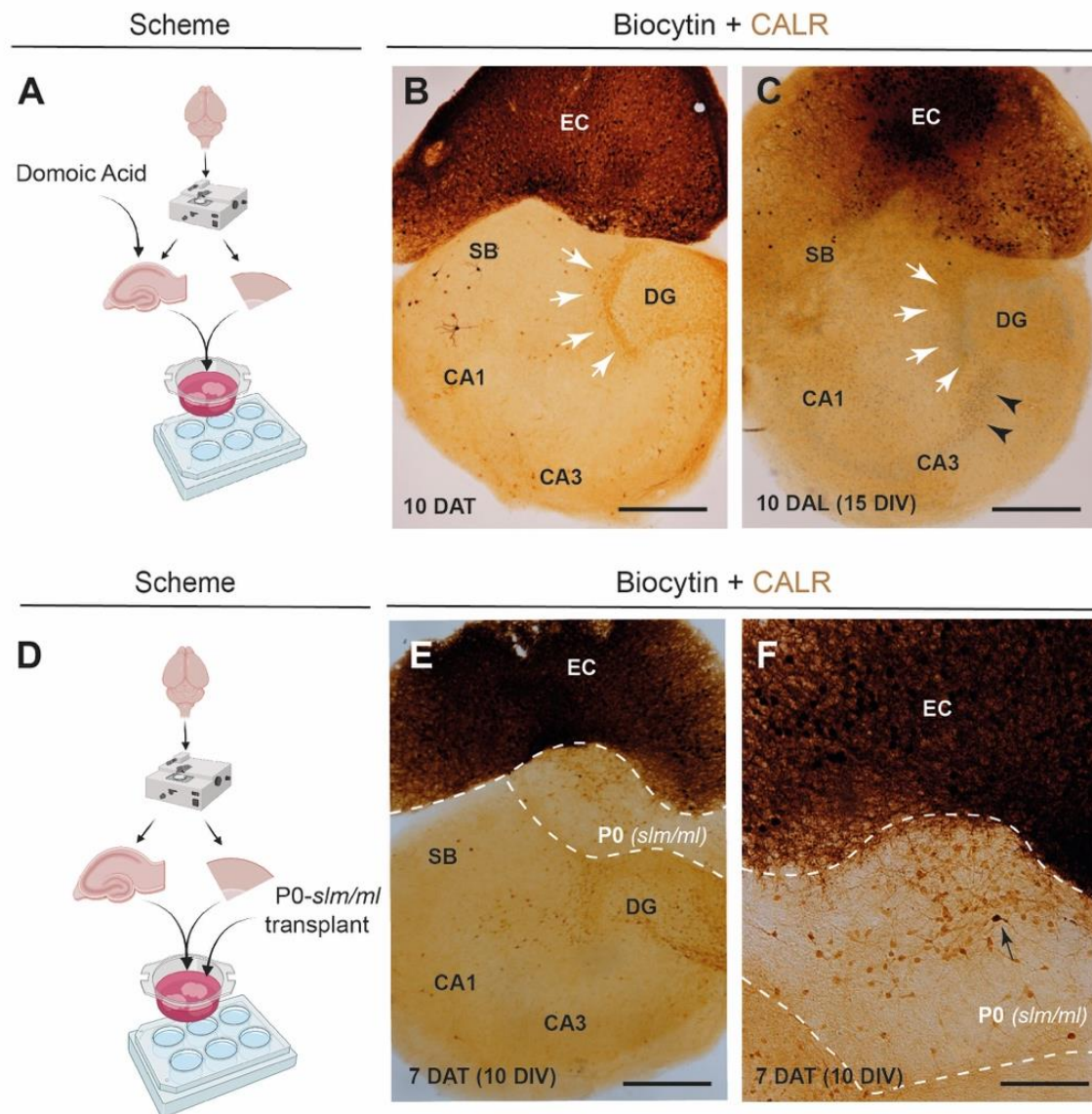


Figure 78. *In vitro* manipulation of the EHC reveals EC intrinsic factors that negatively influenced axon regeneration in aged OSCs. **A.** Scheme illustrating the treatment of the OSCs with domoic acid (see Material and Methods for details). **B.** Photomicrograph of a vibratome section of an OSC treated with domoic acid after 10 DAL. Notice both the absence of EC axons in the hippocampus and the absence of Cajal-Retzius cells (arrows) after domoic acid treatment of the hippocampus slice. **C.** Example of an OSC of the EHC at 10 DAL of the EC axons at 15 DIV. As also illustrated in Figure 1, EC axons are unable to innervate the hippocampus (arrows). In addition, numerous proliferating cells can be observed in the deafferented region of the CA1-3 (arrowheads). **D.** Scheme illustrating the transplantation procedure after EC axotomy. **E-F** Low **E** and high-power **F** photomicrograph illustrating vibratome sections of two examples of transplanted EHCs with slm/ml from P0 hippocampus after Biocytin tracing and Calretinin immunostaining 7 DAL at 10 DIV. The dashed line indicates the axotomy trajectory and delineated the transplanted region. Notice the survival of the transplanted Cajal-Retzius cells in the slm/ml, the presence of residual Cajal-Retzius cells in the lesioned hippocampus and the presence of a retrogradely labeled Cajal-Retzius cell (arrow). In addition, notice the absence of EC axons in the transplanted target and the hippocampal slice. Scale bars: B, C and E: 200 μm; F: 100 μm. Abbreviations as in **Figure 76**.

Development of an optogenetic stimulation setup of the EC neurons in EHCs

Cell-specific neural stimulation has been used in several paradigms (see General introduction). In our laboratory, optogenetic stimulation has been applied in several culture platforms ((Mesquida-Veny et al., 2022; Sala-Jarque et al., 2020; Wells-Cembrano et al., 2022). More relevantly, our data in 2D DRG cultures point at the observation that neuronal or chemogenetic stimulation of lesioned DRG only induce axon regeneration when neurons are cultured on permissive in contrast to inhibitory (CSPG-containing) substrates. CSPG, among other inhibitory molecules, is largely present after EHC axotomy in OSCs (Mingorance et al., 2006).

Thus, we aimed to explore whether the specific activation of EC neurons might modify the natural development of the EHC and its regeneration after axotomy. However, in order to perform these experiments, we needed to demonstrate that the optogenetic activation of the EC takes place in our OSCs. Therefore, we built a specific setup in our Olympus BX61 microscope to demonstrate the effectiveness of the optical treatment (**Figure 79**). To allow simultaneous optical stimulation and calcium imaging, the EC slices were double-infected the same day of dissection with two AAVs encoding ChR2-eGFP and jRCaMP1b (see Materials and Methods for details), both under the synapsin promoter. Examples of double-labeled EC neurons can be seen in Figure 6B-E.

In the setup, a diode laser of 470 nm and 100 mW was placed perpendicular to the optical plane to illuminate the OSCs. In addition, the activity measured as Ca^{2+} changes was monitored using the appropriate filter sets that blocked light wavelength lower than 618 nm (**Figure 79A**). In these conditions, we recorded short videos of 80 s to determine whether the illumination with the diode laser induced an increase in the intracellular Ca^{2+} of jRCaMP1b-transfected ECs. In **Figure 79B** we show a frame of a representative jRCaMP1b video.

As the observation implies the immersion of our objective in the media, the putative non-rigid movements in our sample were corrected by using EzCalciumTM and the ROIs were selected by CNMF-E algorithms of the software (**Figure 79C**). In addition, time lapse videos were processed by using AydinTM to reduce the noise of the recording. After this, selected ROIs were analyzed using Analyca (**Figure 79D**) and NeuroCaTM (**Figure 79E**).

As observed, after the illumination between 5 and 40 s, a transient increase in the Ca^{2+} on jRCaMP1b EC cells was observed. However, the clustered correlation activity was low (0.757) (**Figure 79E**), indicating that these cells were sparsely interconnected in the EC slice. Thus, with these experiments, we demonstrated that our treatment could activate EC neurons expressing Chr2. A raster plot of the activity observed in the example recording can be seen in **Figure 81E**.

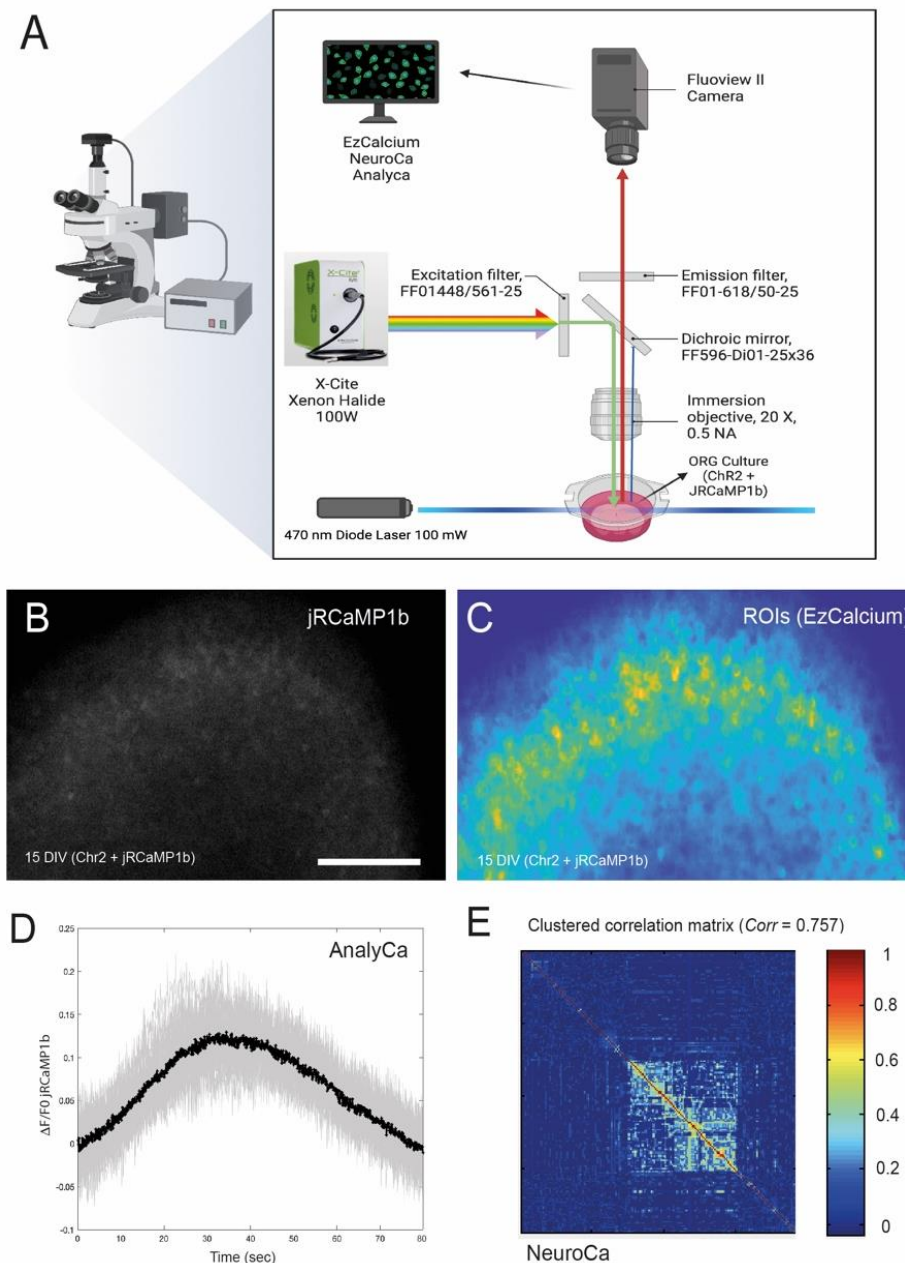


Figure 79. Optogenetic stimulation platform for OSCs double-infected with Chr2 and jRCaMP1b. **A.** Scheme of the optical stimulation and calcium imaging setup (see detailed explanations above). **B.** Example frame of a representative jRCaMP1b time lapse recording. **C.** ROI selection in the recording shown in **B**. **D.** $\Delta F/F_0$ graph obtained with AnalyCa software, showing an increase in calcium after the stimulation applied between 5 and 40 s. **E.** Clustered correlation matrix obtained in NeuroCa software.

Optogenetic stimulation of developing EHP largely impairs their development in OSC

Considering that our stimulation protocol was able to enhance EC neuron activity, we aimed first to determine whether this increased activity could change the lamina-specific innervation of EC into the hippocampus (**Figure 80**). In a first set of experiments, we determined that, with the AAV infection protocol, only EC projecting neurons expressing ChR2 were stimulated. Whole mount imaging demonstrated that treated EC axons innervating the hippocampus express ChR2 during OSCs development (see **Figure 81A**) in an example imaged at 15 DIV.

Next, we stimulated a group of EHC infected with AAV encoding ChR2 in the EC during the first 7 DIV. In **Figure 80**, some examples of Biocytin-labeled EHC can be seen. In non-stimulated OSCs, the development and the layer-specific development of the EHP is maintained (**Figure 80A**). However, in stimulated cultures, we observed that although EC axons were able to innervate the hippocampus, a large number of EC axons showed misrouted trajectories innervating regions other than the *slm/ml* (**Figure 80B-E**). This indicates that the stimulation protocol induces an aberrant growth of projecting EC neurons in our OSCs.

Optogenetic stimulation of axotomized EHP does not enhance axon regeneration in aged EHC

In a final set of experiments, we aimed to explore whether the stimulation of lesioned EC neurons could enhance their regenerative ability. As indicated above, we first ensured that only projecting EC axons would be target of our stimulation protocol. For this, infected OSCs were imaged by fluorescence microscopy, and results demonstrated that only the EHP was eGFP-positive, indicating that projecting EC neurons express ChR2 and its reporter protein eGFP (**Figure 81A**). This was corroborated at the cellular level (**Figure 81B-D**), where numerous ChR2-expressing cells were also JRCaMP1b positive, as the synthesis of both proteins is driven by the same synapsin promoter.

Next, we performed axotomy of several OSCs at 14 DIV, and performed the stimulation protocol (**Figure 81F-I**). Unfortunately, fluorescent observation (**Figure 81H**) and Biocytin tracing (**Figure 81F-H and I**) rendered similar negative results, with no EC

axons innervating the hippocampal slice. In a parallel experiment, we analyzed whether the stimulation might affect the establishment of the glial scar observed in **Figure 77**. Results indicated that the stimulation process does not affect the generation of the glial scar, which might impair EC axon regeneration (not shown).

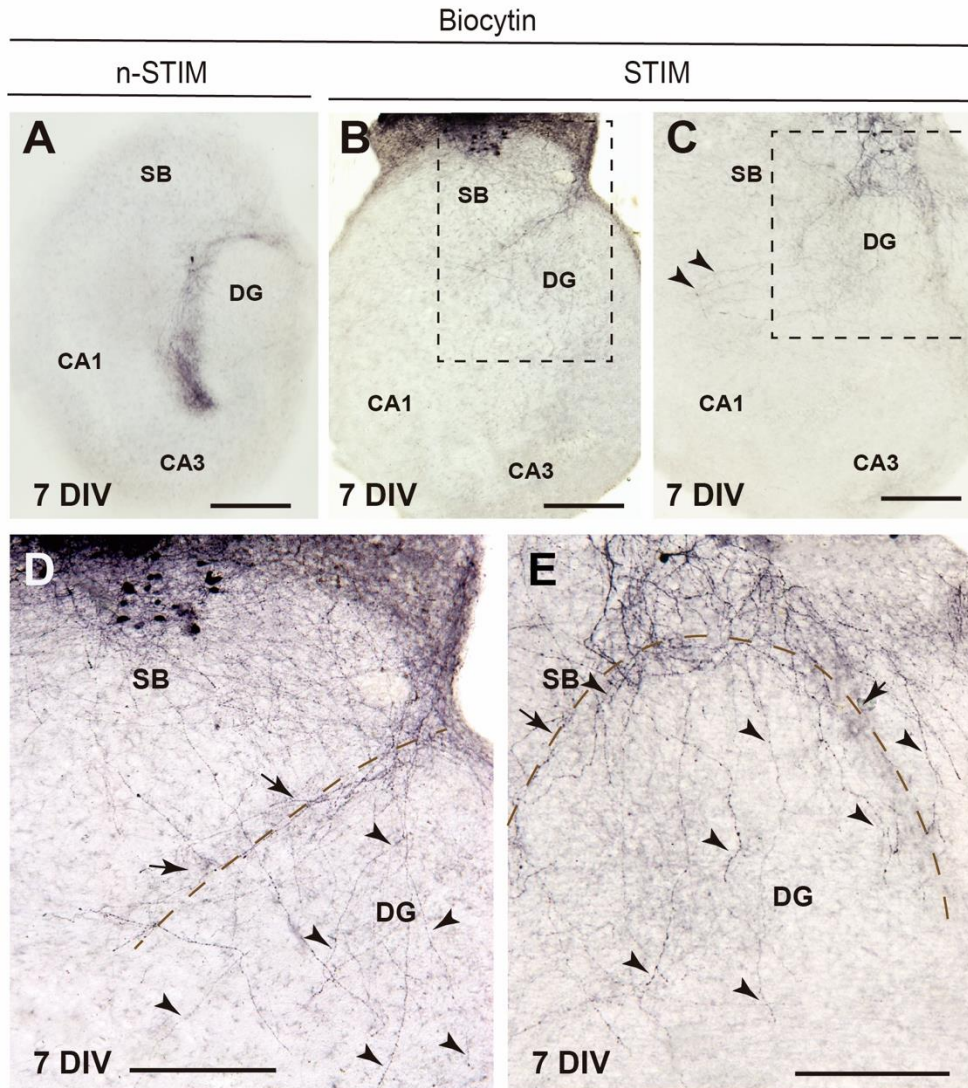


Figure 80. The optogenetic stimulation of developing EHC in OSCs impairs target derived signals on growing EC axons leading to misrouted axon innervation. **A.** Vibratome section of a non-stimulated EHC illustrating the “natural” development of the EHP in vitro. Comparison of this picture with the one shown in **B** shows differences in axonal growth trajectories. **B-C.** Examples Biocytin traced EHC at 7DIV after the stimulation of EC neurons (see Materials and Methods for details). Numerous axons reached the hippocampus, showing aberrant trajectories. The dashed Box in **B** and **C** is magnified in **D-E** respectively. **D-E.** At high magnification, EC-labeled axons (arrowheads in **D** and **E**) reached the hippocampal fissure (dashed line) crossing the subiculum, but crossed granule cell layer reaching the hilus and the CA1 and CA3 regions. Scale bars: A-C: 200 μm ; D-E: 100 μm . Abbreviations as in **Figure 76**.

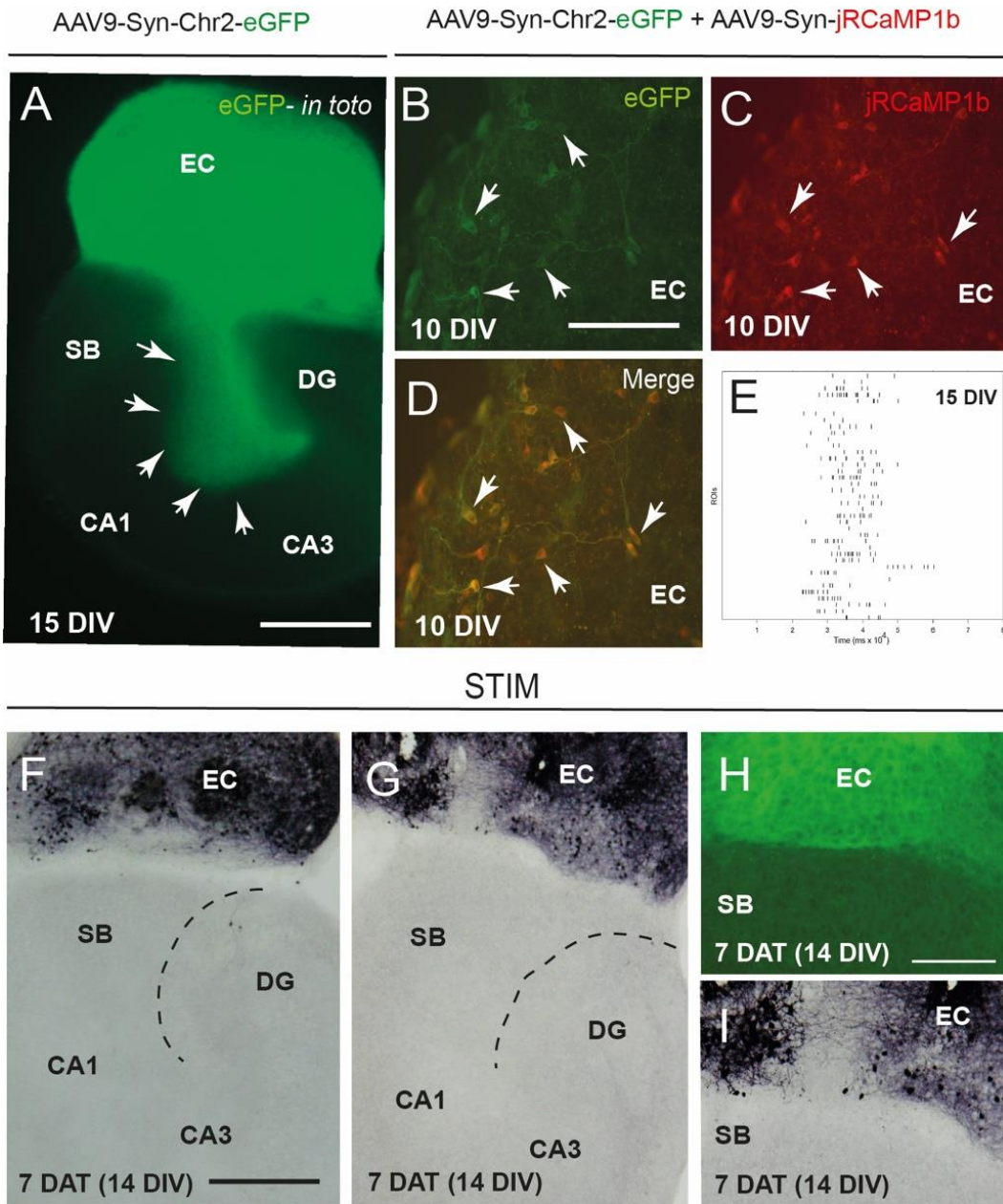


Figure 81. Failure of the optogenetic stimulation of axotomized EHC in promoting axon regeneration in OSCs. **A.** Whole mount fluorescence photomicrograph of an OSC infected in the EC with AAV expressing Chr2-eGFP. Notice that the expression of Chr2 does not impair the correct development and target specific development of the EHP (arrows). **B-C.** High power photomicrograph of a double-infected EC with AAV expressing Chr2-eGFP (**B**) and jRCaMP1b (**C**). **E** Raster plot of the activity of several ROIs (Y axes) along time (X axes). Each dot indicates the maximum increase in the fluorescence per ROI at a particular time point after the illumination with the diode laser of 470 nm (from 5 to 40 sec). **F-I.** Medium (**F-G**) and high magnification photomicrographs illustrating the absence of EC axonal regeneration after the stimulation procedure, analyzed by Biocytin (**F-G** and **I**) or eGFP fluorescence (**H**). Scale Bars: A: 200 μ m; B: 100 μ m pertains to C-D; F: 200 μ m pertains to G; H: 100 μ m pertains to I. Abbreviations: DAT=days after treatment; the rest of abbreviations are as in **Figure 76**.

Decreased expression of axonal growth-related genes under enhanced activity of EC neurons

Due to the fact that our experiments point to a dysregulation of the pathfinding properties of developing EC axons and the absence of EHP regeneration after lesion, we aimed to explore whether the stimulation protocol of the EC neurons altered the expression of genes involved in axonal growth. Thus, levels of *GAP43*, *CAP23*, *BDNF*, *NGF* and *SP11A* were analyzed in axotomized EHC after stimulation, and their expression was compared to non-stimulated cultures using *GADPH* as control. Although the number of analyzed cultures was low, results indicate some trends in downregulation of gene expression between stimulated vs non-stimulated EC neurons (**Figure 82**). These results reinforce the notion that, although we cannot completely rule out that glial scar-derived inhibitory molecules might be involved, the applied stimulation protocol is not robust enough to induce positive changes in gene expression to enhance axon regeneration in EHC after axotomy. In fact, our data points to the conclusion that the forced stimulation of EC activity is detrimental for regeneration and, most probably to development of the EHC *in vitro*.

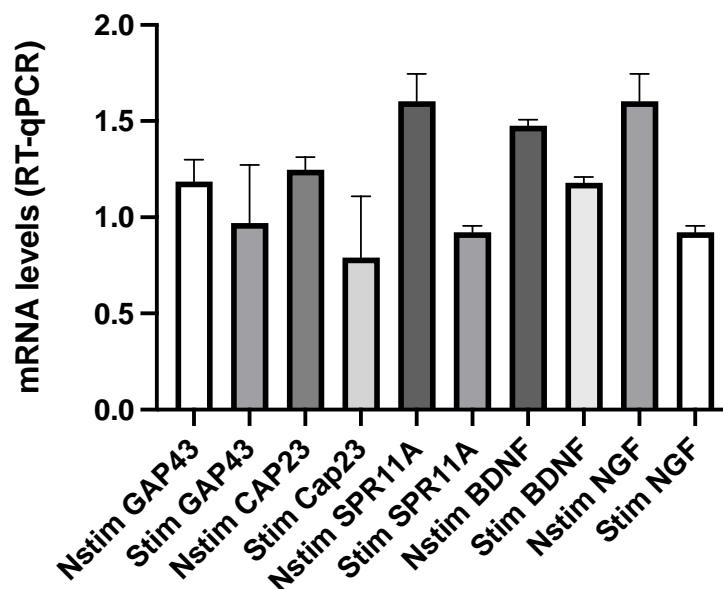


Figure 82. Expression of regeneration-associated genes is decreased after stimulation, as analyzed by RT-qPCR. Abbreviations: Nstim = Non-stimulated; Stim=stimulated.

DISCUSSION

Axonal wiring in vertebrates is controlled by genetic cascades as well as by intrinsic activity-dependent development and refinement of connections (Curcio & Bradke, 2018). Activity-dependent development has been described, among other cases, in the optic tectum (Kita, Scott, & Goodhill, 2015), motor neurons (Kastanenka & Landmesser, 2013; Plazas, Nicol, & Spitzer, 2013) or midline callosal axons (Gao, Stevenson, Douglass, Barrios, & Bonkowsky, 2018). For several years, it has been considered that spontaneous activity is important in refining neural projections once axons have reached their targets, but early pathfinding events have been thought to be activity-independent. In other words, the general consensus in the field has been that early events such as axon growth towards the target depend on a complex series of molecular signals, but are independent of neural activity (Katz & Shatz, 1996; Sengpiel & Kind, 2002). Thus, a physiological balance must be established to modulate both axonal growth and target recognition.

In a pioneer study during spinal cord development, stimulated motor axons correctly executed the binary dorsal-ventral pathfinding decision, but failed to make the subsequent pool-specific decision to target the appropriate muscles (Kastanenka & Landmesser, 2013). In addition, decreasing the frequency of spontaneous bursting episodes results in dorsal-ventral pathfinding errors for motor projections (see (Hanson, Milner, & Landmesser, 2008) for review). The EHP is one of the best-studied pathfinding models and is fundamental to the establishment of archicortex connectivity in the nervous system. However, it is not known whether EHP development requires intrinsic activity in axons, and which factors control this activity. Further, a mechanism linking neuronal activity and gene expression has not been identified for axon pathfinding.

In our experiments, the increase of the endogenous spontaneous activity in developing EC neurons impaired target recognition in the developing hippocampus. This is of relevance, since it reinforces previously published studies indicating that changes in neuronal activity might affect axonal pathfinding in the optical and motor systems (see (Cang et al., 2005; Chandrasekaran, Plas, Gonzalez, & Crair, 2005; Huberman, Speer, & Chapman, 2006; McLaughlin, Torborg, Feller, & O'Leary, 2003) for additional references).

Although more experiments must be performed, in our current results we observed that several genes involved in axon growth and regeneration (e.g., GAP43, among others) was decreased in stimulated axotomized cultures. Although the role of GAP43 in developing axons has been largely studied (see (Zang, Chaudhari, & Bashaw, 2021) for review), a recent study indicates that the decrease of GAP43 in the hippocampus impairs target specificity and function of mossy fibers (Maroto et al., 2023). Similarly, some years ago, the role of neural activity as a consolidator of hippocampal inhibitory circuits in the hippocampus was described (Marty, Wehrle, & Sotelo, 2000). Thus, neuronal activity regulates the density of inhibitory synapses formed by postnatal hippocampal interneurons, and BDNF could mediate part of this regulation. This regulation of the density of inhibitory synapses could represent a feedback mechanism aimed at maintaining an appropriate level of activity in the developing hippocampal networks, including the EHP (Marty et al., 2000).

Similar defects during cortical development and axonal wiring have been described for deficits in BDNF (Aguado et al., 2003; Yamamoto & Hanamura, 2005) or NGF (Chang, Hsu, Lin, Lu, & Chen, 2013). In fact, some regeneration-associated genes are dependent on neurotrophin expression (e.g., (Klocker, Jung, Stuermer, & Bahr, 2001), see Ebadi et al., 1997 for review. This is also relevant since some of these neurotrophins (e.g., NGF) can act on growing or regenerating neurons (e.g., (Lefebvre et al., 1992)), but also can be released anterogradely in order to enhance correct target recognition and synaptic function (Guo, Yeh, Cuzon Carlson, Johnson-Venkatesh, & Yeh, 2012).

Taking this into account, we can consider that the gene expression decrease induced by the stimulation protocol largely impaired pathfinding and target recognition of EC axons during regeneration, and most probably during development. We consider that this is of relevance since our previous results (Mesquida-Veny et al., 2022) also point in this direction. Additionally, and from a regenerative strategy point of view, sprouting of spared axons, instead of injured ones, is also responsible for recovery after increase neuronal activity by exercise and/or electrical stimulation (see (Mesquida-Veny, Del Rio, & Hervera, 2021) for review). In agreement to this, success of these approaches is only significant in incomplete injuries with a significant number of spared axons. Incomplete injuries might also help to explain why in our model (complete lesion of the EHP) we did not observe recovery after optogenetic stimulation, while others did on lesioned spinal cord (e.g., (W. W. Deng et al., 2021)), as different injuries (incomplete lesion) were used.

Moreover, complete injuries also present larger glial scars (as observed in EHC *in vitro*, and therefore greater accumulation of growth-inhibitory molecules (Mingorance et al., 2004; Mingorance et al., 2005; Mingorance et al., 2006). Furthermore, the expression of the receptors for most of these molecules is maintained in the projecting EC neurons after axotomy (Agudo et al., 2005; Montolio et al., 2009), increasing the negative effects that the stimulation protocol cannot overcome. In parallel, our stimulation strategy does not affect the generation of the glial scar in axotomized EHP. This raised the question of whether modulating both glial scar formation, as demonstrated by (Goritz et al., 2011) and neuronal activity to trigger the axotomized projecting neurons from an apparent resting stage (e.g., as Purkinje cells (Dusart, Morel, Wehrle, & Sotelo, 1999) to a pro-regenerative stage could render better results; taking into account that EC neurons do not disappear after axotomy (Peterson, Lucidi-Phillipi, Murphy, Ray, & Gage, 1996; Sole et al., 2004)

GENERAL DISCUSSION

In this work, we have developed two new 3D *in vitro* model setups, one human muscle 3D model and one primary culture-derived 3D axotomy model. Both models have been validated as appropriate tools for our research objectives, and have begun to be tested as platforms for evaluating disease conditions or treatments. In addition, we have used an existing organotypic slice culture model to evaluate the effect of optical stimulation as a potential regulator of axonal regeneration and development.

We believe that the models that have been developed and presented in this work can be useful for future use as *in vitro* platforms. On the one hand, we have strived to use 3D culture in appropriate tissue architecture configurations, which constitutes an improvement to previous models used in our laboratory. On the other hand, we have implemented two complementary optical techniques, namely calcium imaging and optogenetic stimulation, in all three chapters of the thesis. This makes our models amenable to precise and non-invasive manipulation and analysis.

The 3D anchored muscle culture platform that was developed in Chapter 1 demonstrated a high robustness and simplicity for establishing aligned and contractile cultures of human immortalized myoblasts. Contractile activity and response to chemical and optical stimulation (in ChR2⁺ cultures) were observed, as well as expression of relevant differentiation markers. Two different analyses of muscle function are proposed, making the model highly versatile. The model was also able to partially recapitulate some events of myasthenia gravis in preliminary experiments, although further research is needed to extract valuable conclusions on disease mechanisms using this platform. 2D culture with hydrogel overlays can also be a useful model to investigate certain molecular events by immunostaining, due to the increased clarity of microscopic imaging. Thus, this platform can be used as a complementary tool in studies of myasthenia gravis or other muscular diseases. Contractile activity and functional, differentiated myotubes were also obtained in this system, despite presenting a more limited alignment. These models constituted the first applications of human myoblasts in our research group (Sala-Jarque et al., 2020), which can provide an improvement in clinical relevance.

Regarding the establishment of a 3D axotomy platform, our results highlight the fact that not all neuronal cell sources are morphologically appropriate for performing axotomy studies. Despite the ability to obtain mature neurons from stem cell differentiation,

primary culture is still far superior in terms of its ability to extend isolated axonal processes. In our 3D cultures of cortical explants, we achieved sufficient cell survival over the period needed to evaluate axotomy, and also demonstrated the possibility of successfully modifying explants to express optogenetic and calcium imaging tools, thus permitting optical stimulation and evaluation of neuronal activity. Co-infection with ChR2 and jRCaMP1b allowed us to demonstrate the successful activation of neurons after optical stimulation, which had only been previously evaluated in our laboratory using c-fos staining, which can also be upregulated by other non-specific variables (Bullitt, 1990).

In both studies involving optogenetic stimulation as a strategy to promote axonal regeneration (Chapters 2 and 3), we observed that maintaining neuronal activity is not a sufficient condition for regeneration in CNS neurons, and may even be detrimental to regeneration. In 3D explant cultures, optogenetic stimulation timing could be a relevant factor affecting these results, which should be analyzed in further detail in subsequent experiments. In organotypic slice culture, optical stimulation treatment was unable to improve regenerative ability of neurons in the inhibitory environment of OSCs axotomized at 14 DIV. These results are in line with previous studies from the group, in which positive effects of optical stimulation could not overcome an inhibitory environment (Mesquida-Veny et al., 2022). The complete transections used in our experiments could also contribute to the lack of beneficial effects of stimulation, as lateral sprouting has been reported as an important contributor to activity-based therapy success.

Thus, these conclusions reinforce the idea that although neuronal activity can be an important regulator of intrinsic regenerative ability, synergistic therapies may be needed for successfully overcoming the unfavorable milieu of CNS injuries. Another interesting conclusion of OSC optogenetic experiments was that an increase in neuronal activity can cause axonal misrouting of projecting EC axons. This coincides with the recent paradigm shift related to the activity dependence of pathfinding mechanisms in axonal development. This effect could also impact regeneration outcomes, as demonstrated by the lack of regeneration and decreased expression of RAGs in stimulated OSCs.

In all, we consider that the methodologies developed in this thesis will be useful for continuing our ongoing lines of research. Our preliminary results on the mechanisms of neuromuscular disease or axonal regeneration have pointed at future paths of our research on these topics, which will be useful for guiding the design of new investigations.

CONCLUSIONS

Considering the aforementioned results, we hereby conclude:

1. We have developed a 3D anchored *in vitro* platform for the culture of aligned, differentiated, and contractile human muscle, which responds to electrical, chemical, and optical stimulation. Muscle function in this model been analyzed by contraction using motion analysis algorithms or by calcium imaging.
2. Myasthenia gravis patient serums have shown colocalization with endplates in 2D and 3D human myocyte cultures, and AChR-mediated endplate destruction has been recapitulated in our 3D platform.
3. Functional effects of MG patient serums *in vitro* were shown to be dependent on autoantibody titer and complement presence. Treatment with anti-MuSK MG serum caused a significant reduction in muscle function compared to control.
4. Stem cell-derived neurons cultured as neurospheres in 3D matrices were not suitable for axotomy studies, due to their lack of isolated axonal projections.
5. Embryonic cortical explants cultured in collagen gels constitute a reliable source of extensive and isolated axonal projections for 3D *in vitro* axotomy. Cells remain viable for up to 14 DIV and axotomy can be successfully performed at 7 DIV.
6. Embryonic cortical explants and entorhinal cortex slices can be efficiently infected and co-infected with ChR2 and jRCaMP1b using adenoviral vectors. Neurons in both models show spontaneous and optically induced activity by calcium imaging.
7. Optical stimulation was shown to be detrimental to axonal regeneration in CNS neurons, with coherent results observed both in axotomized cortical explant neurons and organotypic slice cultures.
8. Increased neuronal activity can result in axonal misrouting in developing entorhinal cortex projections, which could also impair regeneration.

REFERENCES

- Abdel-Raouf, K. M. A., Rezgui, R., Stefanini, C., Teo, J. C. M., & Christoforou, N. (2021). Transdifferentiation of Human Fibroblasts into Skeletal Muscle Cells: Optimization and Assembly into Engineered Tissue Constructs through Biological Ligands. *Biology*, 10(6), 539. <https://doi.org/10.3390/biology10060539>
- Adamantidis, A., Arber, S., Bains, J. S., Bamberg, E., Bonci, A., Buzsáki, G., Cardin, J. A., Costa, R. M., Dan, Y., Goda, Y., Graybiel, A. M., Häusser, M., Hegemann, P., Huguenard, J. R., Insel, T. R., Janak, P. H., Johnston, D., Josselyn, S. A., Koch, C., ... Wilson, R. I. (2015). Optogenetics: 10 years after ChR2 in neurons—views from the community. *Nature Neuroscience*, 18(9), Article 9. <https://doi.org/10.1038/nn.4106>
- Adamchik, Y., Frantseva, M. V., Weisspapir, M., Carlen, P. L., & Perez Velazquez, J. L. (2000). Methods to induce primary and secondary traumatic damage in organotypic hippocampal slice cultures. *Brain Res Brain Res Protoc*, 5(2), 153-158. doi:10.1016/s1385-299x(00)00007-6
- Adams, K. L., & Gallo, V. (2018). The diversity and disparity of the glial scar. *Nature Neuroscience*, 21(1), Article 1. <https://doi.org/10.1038/s41593-017-0033-9>
- Addgene: Optogenetics Guide. (2023, mayo 31). <https://www.addgene.org/guides/optogenetics/>
- Addington, C. P., Dharmawaj, S., Heffernan, J. M., Sirianni, R. W., & Stabenfeldt, S. E. (2017). Hyaluronic acid-laminin hydrogels increase neural stem cell transplant retention and migratory response to SDF-1 α . *Matrix Biology: Journal of the International Society for Matrix Biology*, 60-61, 206-216. <https://doi.org/10.1016/j.matbio.2016.09.007>
- Afshar Bakooshli, M., Lippmann, E. S., Mulcahy, B., Iyer, N., Nguyen, C. T., Tung, K., Stewart, B. A., van den Dorpel, H., Fuehrmann, T., Shoichet, M., Bigot, A., Pegoraro, E., Ahn, H., Ginsberg, H., Zhen, M., Ashton, R. S., & Gilbert, P. M. (2019). A 3D culture model of innervated human skeletal muscle enables studies of the adult neuromuscular junction. *ELife*, 8, e44530. <https://doi.org/10.7554/eLife.44530>
- Afshar Saber, W., Gasparoli, F. M., Dirks, M. G., Gunn-Moore, F. J., & Antkowiak, M. (2018). All-Optical Assay to Study Biological Neural Networks. *Frontiers in Neuroscience*, 12, 451. <https://doi.org/10.3389/fnins.2018.00451>
- Afshar, M. E., Abraha, H. Y., Bakooshli, M. A., Davoudi, S., Thavandiran, N., Tung, K., Ahn, H., Ginsberg, H. J., Zandstra, P. W., & Gilbert, P. M. (2020). A 96-well culture platform enables longitudinal analyses of engineered human skeletal muscle microtissue strength. *Scientific Reports*, 10(1), 6918. <https://doi.org/10.1038/s41598-020-62837-8>
- Aguado, F., Carmona, M. A., Pozas, E., Aguilo, A., Martinez-Guijarro, F. J., Alcantara, S., ... Soriano, E. (2003). BDNF regulates spontaneous correlated activity at early developmental stages by increasing synaptogenesis and expression of the K⁺/Cl⁻ co-transporter KCC2. *Development*, 130(7), 1267-1280. doi:10.1242/dev.00351
- Agudo, M., Robinson, M., Cafferty, W., Bradbury, E. J., Kilkenny, C., Hunt, S. P., & McMahon, S. B. (2005). Regulation of neuropilin 1 by spinal cord injury in adult rats. *Mol Cell Neurosci*, 28(3), 475-484. doi:10.1016/j.mcn.2004.10.008
- Ahmad, A., Ashraf, S., & Komai, S. (2015). Optogenetics Applications for Treating Spinal Cord Injury. *Asian Spine Journal*, 9(2), 299-305. <https://doi.org/10.4184/asj.2015.9.2.299>
- Airan, R. D., Thompson, K. R., Fenno, L. E., Bernstein, H., & Deisseroth, K. (2009). Temporally precise in vivo control of intracellular signalling. *Nature*, 458(7241), 1025-1029. <https://doi.org/10.1038/nature07926>
- Aisenbrey, E. A., & Murphy, W. L. (2020). Synthetic alternatives to Matrigel. *Nature reviews. Materials*, 5(7), 539-551. <https://doi.org/10.1038/s41578-020-0199-8>
- Ajalik, R. E., Alenchery, R. G., Cognetti, J. S., Zhang, V. Z., McGrath, J. L., Miller, B. L., & Awad, H. A. (2022). Human Organ-on-a-Chip Microphysiological Systems to Model Musculoskeletal Pathologies and Accelerate Therapeutic Discovery. *Frontiers in Bioengineering and Biotechnology*, 10, 846230. <https://doi.org/10.3389/fbioe.2022.846230>
- Akerboom, J., Carreras Calderón, N., Tian, L., Wabnig, S., Prigge, M., Tolö, J., Gordus, A., Orger, M., Severi, K., Macklin, J., Patel, R., Pulver, S., Wardill, T., Fischer, E., Schöler, C., Chen, T.-W., Sarkisyan, K., Marvin, J., Bargmann, C., ... Looger, L. (2013). Genetically encoded calcium indicators for multi-color neural activity imaging and combination with optogenetics. *Frontiers in Molecular Neuroscience*, 6. <https://www.frontiersin.org/articles/10.3389/fnmol.2013.00002>
- Al-Majed, A. A., Brushart, T. M., & Gordon, T. (2000). Electrical stimulation accelerates and increases expression of BDNF and trkB mRNA in regenerating rat femoral motoneurons. *The European Journal of Neuroscience*, 12(12), 4381-4390.

- Al-Majed, A. A., Tam, S. L., & Gordon, T. (2004). Electrical stimulation accelerates and enhances expression of regeneration-associated genes in regenerating rat femoral motoneurons. *Cellular and Molecular Neurobiology*, 24(3), 379-402. <https://doi.org/10.1023/b:cemn.0000022770.66463.f7>
- Alberts, B., Johnson, A., & Lewis, J. (2008). *Molecular Biology of the Cell* (5.a ed., 1-1). Garland Science.
- Almeida, C. F., Frair, E. C., Huang, N., Neinast, R., McBride, K. L., Weiss, R. B., Flanigan, K. M., & Wein, N. (2021). Direct Reprogramming of Human Fibroblasts into Myoblasts to Investigate Therapies for Neuromuscular Disorders. *Journal of Visualized Experiments: JoVE*, 170. <https://doi.org/10.3791/61991>
- Álvarez, Z., Kolberg-Edelbrock, A. N., Sasselli, I. R., Ortega, J. A., Qiu, R., Syrgiannis, Z., Mirau, P. A., Chen, F., Chin, S. M., Weigand, S., Kiskinis, E., & Stupp, S. I. (2021). Bioactive scaffolds with enhanced supramolecular motion promote recovery from spinal cord injury. *Science*, 374(6569), 848-856. <https://doi.org/10.1126/science.abh3602>
- Andersen, P. (2007). *The hippocampus book*. Oxford ; New York: Oxford University Press.
- Anderson, M. A., Burda, J. E., Ren, Y., Ao, Y., O'Shea, T. M., Kawaguchi, R., Coppola, G., Khakh, B. S., Deming, T. J., & Sofroniew, M. V. (2016). Astrocyte scar formation aids central nervous system axon regeneration. *Nature*, 532(7598), 195-200. <https://doi.org/10.1038/nature17623>
- Anstötz, M., Huang, H., Marchionni, I., Haumann, I., Maccaferri, G., & Lubke, J. H. (2016). Developmental Profile, Morphology, and Synaptic Connectivity of Cajal-Retzius Cells in the Postnatal Mouse Hippocampus. *Cereb Cortex*, 26(2), 855-872. doi:10.1093/cercor/bhv271
- Bali, B., Nagy, Z., & Kovacs, K. J. (2007). Oxygen-glucose deprivation-induced changes in organotypic cultures of the rat hippocampus. *Ideggyogy Sz*, 60(3-4), 140-143.
- Bang, S., Lee, S., Hwang, K. S., Kim, J., Choi, N., & Kim, H. N. (2022). Three-Dimensional Axotomy and Regeneration on Open-Access Microfluidic Platform. *IEEE Transactions on Nanobioscience*, 21(3), 395-404. <https://doi.org/10.1109/TNB.2021.3136869>
- Banghart, M., Borges, K., Isacoff, E., Trauner, D., & Kramer, R. H. (2004). Light-activated ion channels for remote control of neuronal firing. *Nature Neuroscience*, 7(12), Article 12. <https://doi.org/10.1038/nm1356>
- Batty, N. J., Torres-Espín, A., Vavrek, R., Raposo, P., & Fouad, K. (2020). Single-session cortical electrical stimulation enhances the efficacy of rehabilitative motor training after spinal cord injury in rats. *Experimental Neurology*, 324, 113136. <https://doi.org/10.1016/j.expneurol.2019.113136>
- Beeson, D., Amar, M., Bermudez, I., Vincent, A., & Newsom-Davis, J. (1996). Stable functional expression of the adult subtype of human muscle acetylcholine receptor following transfection of the human rhabdomyosarcoma cell line TE671 with cDNA encoding the epsilon subunit. *Neuroscience Letters*, 207(1), 57-60. [https://doi.org/10.1016/0304-3940\(96\)12488-5](https://doi.org/10.1016/0304-3940(96)12488-5)
- Behan, M., Kroker, A., & Bolz, J. (1991). Cortical barrelfields in organotypic slice cultures from rat somatosensory cortex. *Neurosci Lett*, 133(2), 191-194.
- Berry, B. J., Smith, A. S. T., Young, J. E., & Mack, D. L. (2018). Advances and Current Challenges Associated with the Use of Human Induced Pluripotent Stem Cells in Modeling Neurodegenerative Disease. *Cells Tissues Organs*, 205(5-6), 331-349. <https://doi.org/10.1159/000493018>
- Blanco-Fernandez, B., Rey-Vinolas, S., Bağcı, G., Rubi-Sans, G., Otero, J., Navajas, D., Perez-Amodio, S., & Engel, E. (2022). Bioprinting Decellularized Breast Tissue for the Development of Three-Dimensional Breast Cancer Models. *ACS Applied Materials & Interfaces*, 14(26), 29467-29482. <https://doi.org/10.1021/acsami.2c00920>
- Bonosi, L., Silven, M. P., Biancardino, A. A., Sciortino, A., Giammalva, G. R., Scerrati, A., Sturiale, C. L., Albanese, A., Tumbiolo, S., Visocchi, M., Iacopino, D. G., & Maugeri, R. (2022). Stem Cell Strategies in Promoting Neuronal Regeneration after Spinal Cord Injury: A Systematic Review. *International Journal of Molecular Sciences*, 23(21), Article 21. <https://doi.org/10.3390/ijms232112996>
- Borrell, V., Ruiz, M., Del Río, J. A., & Soriano, E. (1999). Development of commissural connections in the hippocampus of reeler mice: Evidence of an inhibitory influence of Cajal-Retzius cells. *Experimental Neurology*, 156(2), 268-282. <https://doi.org/10.1006/exnr.1999.7022>
- Boyden, E. S., Zhang, F., Bamberg, E., Nagel, G., & Deisseroth, K. (2005). Millisecond-timescale, genetically targeted optical control of neural activity. *Nature Neuroscience*, 8(9), 1263-1268. <https://doi.org/10.1038/nm1525>
- Bradbury, E. J., Moon, L. D. F., Popat, R. J., King, V. R., Bennett, G. S., Patel, P. N., Fawcett, J. W., & McMahon, S. B. (2002). Chondroitinase ABC promotes functional recovery after spinal cord injury. *Nature*, 416(6881), 636-640. <https://doi.org/10.1038/416636a>
- Bruge, C., Geoffroy, M., Benabides, M., Pellier, E., Gicquel, E., Dhiab, J., Hoch, L., Richard, I., & Nissan, X. (2022). Skeletal Muscle Cells Derived from Induced Pluripotent Stem Cells: A Platform for

- Limb Girdle Muscular Dystrophies. *Biomedicines*, 10(6), Article 6. <https://doi.org/10.3390/biomedicines10061428>
- Bubuioc, A.-M., Kudebayeva, A., Turuspekova, S., Lisnic, V., & Leone, M. A. (2021). The epidemiology of myasthenia gravis. *Journal of Medicine and Life*, 14(1), 7-16. <https://doi.org/10.25122/jml-2020-0145>
- Bullitt, E. (1990). Expression of c-fos-like protein as a marker for neuronal activity following noxious stimulation in the rat. *The Journal of Comparative Neurology*, 296(4), 517-530. <https://doi.org/10.1002/cne.902960402>
- Burges, J., Wray, D. W., Pizzighella, S., Hall, Z., & Vincent, A. (1990). A myasthenia gravis plasma immunoglobulin reduces miniature endplate potentials at human endplates in vitro. *Muscle & Nerve*, 13(5), 407-413. <https://doi.org/10.1002/mus.880130507>
- Byrne, A. B., Edwards, T. J., & Hammarlund, M. (2011). In vivo Laser Axotomy in *C. elegans*. *Journal of Visualized Experiments : JoVE*, 51, 2707. <https://doi.org/10.3791/2707>
- Cadena, M., Ning, L., King, A., Hwang, B., Jin, L., Serpooshan, V., & Sloan, S. A. (2021). Three Dimensional Bioprinting of Neural Tissues. *Advanced healthcare materials*, 10(15), e2001600. <https://doi.org/10.1002/adhm.202001600>
- Caeser, M., & Aertsen, A. (1991). Morphological organization of rat hippocampal slice cultures. *J Comp Neurol*, 307(1), 87-106.
- Caeser, M., Bonhoeffer, T., & Bolz, J. (1989). Cellular organization and development of slice cultures from rat visual cortex. *Exp Brain Res*, 77(2), 234-244.
- Cai, Y., Han, L., Zhu, D., Peng, J., Li, J., Ding, J., Luo, J., Hong, R., Wang, K., Wan, W., Xie, C., Zhou, X., Zhang, Y., Hao, Y., & Guan, Y. (2021). A Stable Cell Line Expressing Clustered AChR: A Novel Cell-Based Assay for Anti-AChR Antibody Detection in Myasthenia Gravis. *Frontiers in Immunology*, 12. <https://www.frontiersin.org/articles/10.3389/fimmu.2021.666046>
- Cang, J., Renteria, R. C., Kaneko, M., Liu, X., Copenhagen, D. R., & Stryker, M. P. (2005). Development of precise maps in visual cortex requires patterned spontaneous activity in the retina. *Neuron*, 48(5), 797-809. doi:10.1016/j.neuron.2005.09.015
- Cantu, D. A., Wang, B., Gongwer, M. W., He, C. X., Goel, A., Suresh, A., . . . Portera-Cailliau, C. (2020). EZcalcium: Open-Source Toolbox for Analysis of Calcium Imaging Data. *Front Neural Circuits*, 14, 25. doi:10.3389/fncir.2020.00025
- Carmel, J. B., Berrol, L. J., Brus-Ramer, M., & Martin, J. H. (2010). Chronic electrical stimulation of the intact corticospinal system after unilateral injury restores skilled locomotor control and promotes spinal axon outgrowth. *The Journal of Neuroscience: The Official Journal of the Society for Neuroscience*, 30(32), 10918-10926. <https://doi.org/10.1523/JNEUROSCI.1435-10.2010>
- Carmel, J. B., Kimura, H., & Martin, J. H. (2014). Electrical stimulation of motor cortex in the uninjured hemisphere after chronic unilateral injury promotes recovery of skilled locomotion through ipsilateral control. *The Journal of Neuroscience: The Official Journal of the Society for Neuroscience*, 34(2), 462-466. <https://doi.org/10.1523/JNEUROSCI.3315-13.2014>
- Carmel, J. B., Kimura, H., Berrol, L. J., & Martin, J. H. (2013). Motor cortex electrical stimulation promotes axon outgrowth to brain stem and spinal targets that control the forelimb impaired by unilateral corticospinal injury. *The European Journal of Neuroscience*, 37(7), 1090-1102. <https://doi.org/10.1111/ejn.12119>
- Carraro, E., Rossi, L., Maghin, E., Canton, M., & Piccoli, M. (2022). 3D in vitro Models of Pathological Skeletal Muscle: Which Cells and Scaffolds to Elect? *Frontiers in Bioengineering and Biotechnology*, 10, 941623. <https://doi.org/10.3389/fbioe.2022.941623>
- Castillo Bautista, C. M., & Sternecker, J. (2023). Progress and challenges in directing the differentiation of human iPSCs into spinal motor neurons. *Frontiers in Cell and Developmental Biology*, 10. <https://www.frontiersin.org/articles/10.3389/fcell.2022.1089970>
- Cengiz, N., Öztürk, G., Erdoğan, E., Him, A., & Oğuz, E. K. (2012). Consequences of Neurite Transection In Vitro. *Journal of Neurotrauma*, 29(15), 2465-2474. <https://doi.org/10.1089/neu.2009.0947>
- Cetin, H., Beeson, D., Vincent, A., & Webster, R. (2020). The Structure, Function, and Physiology of the Fetal and Adult Acetylcholine Receptor in Muscle. *Frontiers in Molecular Neuroscience*, 13. <https://www.frontiersin.org/articles/10.3389/fnmol.2020.581097>
- Chandrasekaran, A. R., Plas, D. T., Gonzalez, E., & Crair, M. C. (2005). Evidence for an instructive role of retinal activity in retinotopic map refinement in the superior colliculus of the mouse. *J Neurosci*, 25(29), 6929-6938. doi:10.1523/JNEUROSCI.1470-05.2005
- Chang, Y. J., Hsu, C. M., Lin, C. H., Lu, M. S., & Chen, L. (2013). Electrical stimulation promotes nerve growth factor-induced neurite outgrowth and signaling. *Biochim Biophys Acta*, 1830(8), 4130-4136. doi:10.1016/j.bbagen.2013.04.007

- Cho, Y., & Cavalli, V. (2012). HDAC5 is a novel injury-regulated tubulin deacetylase controlling axon regeneration. *The EMBO Journal*, 31(14), 3063-3078. <https://doi.org/10.1038/emboj.2012.160>
- Cho, Y., Sloutsky, R., Naegle, K. M., & Cavalli, V. (2013). Injury-induced HDAC5 nuclear export is essential for axon regeneration. *Cell*, 155(4), 894-908. <https://doi.org/10.1016/j.cell.2013.10.004>
- Clifford, K. M., Hobson-Webb, L. D., Benatar, M., Burns, T. M., Barnett, C., Silvestri, N. J., Howard, J. F., Visser, A., Crum, B. A., Nowak, R., Beekman, R., Kumar, A., Ruzhansky, K., Chen, I.-H. A., Pulley, M. T., Laboy, S. M., Fellman, M. A., Howard, D. B., Kolb, N. A., ... Hehir, M. K. (2019). Thymectomy may not be associated with clinical improvement in MuSK myasthenia gravis. *Muscle & Nerve*, 59(4), 404-410. <https://doi.org/10.1002/mus.26404>
- Cregg, J., DePaul, M., Filous, A., Lang, B., Tran, A., & Silver, J. (2014). Functional Regeneration Beyond the Glial Scar. *Experimental neurology*, 253. <https://doi.org/10.1016/j.expneurol.2013.12.024>
- Croft, C. L., Futch, H. S., Moore, B. D., & Golde, T. E. (2019). Organotypic brain slice cultures to model neurodegenerative proteinopathies. *Molecular Neurodegeneration*, 14(1), 45. <https://doi.org/10.1186/s13024-019-0346-0>
- Curcio, M., & Bradke, F. (2018). Axon Regeneration in the Central Nervous System: Facing the Challenges from the Inside. *Annu Rev Cell Dev Biol*, 34, 495-521. doi:10.1146/annurev-cellbio-100617-062508
- Dalva, M. B., & Katz, L. C. (1994). Rearrangements of synaptic connections in visual cortex revealed by laser photostimulation. *Science (New York, N.Y.)*, 265(5169), 255-258. <https://doi.org/10.1126/science.7912852>
- Dana, H., Mohar, B., Sun, Y., Narayan, S., Gordus, A., Hasseman, J. P., Tsegaye, G., Holt, G. T., Hu, A., Walpita, D., Patel, R., Macklin, J. J., Bargmann, C. I., Ahrens, M. B., Schreiter, E. R., Jayaraman, V., Looger, L. L., Svoboda, K., & Kim, D. S. (2016). Sensitive red protein calcium indicators for imaging neural activity. *eLife*, 5, e12727. <https://doi.org/10.7554/eLife.12727>
- Das, M., Rumsey, J. W., Bhargava, N., Stancescu, M., & Hickman, J. J. (2010). A Defined Long-Term In Vitro Tissue Engineered Model of Neuromuscular Junctions. *Biomaterials*, 31(18), 4880-4888. <https://doi.org/10.1016/j.biomaterials.2010.02.055>
- De Chiara, F., Ferret-Miñana, A., Fernández-Costa, J. M., Senni, A., Jalan, R., & Ramón-Azcón, J. (2022). Fatty Hepatocytes Induce Skeletal Muscle Atrophy In Vitro: A New 3D Platform to Study the Protective Effect of Albumin in Non-Alcoholic Fatty Liver. *Biomedicines*, 10(5), 958. <https://doi.org/10.3390/biomedicines10050958>
- Deisseroth, K., Feng, G., Majewska, A. K., Miesenböck, G., Ting, A., & Schnitzer, M. J. (2006). Next-generation optical technologies for illuminating genetically targeted brain circuits. *The Journal of Neuroscience: The Official Journal of the Society for Neuroscience*, 26(41), 10380-10386. <https://doi.org/10.1523/JNEUROSCI.3863-06.2006>
- Del Río, J. A., & Soriano, E. (2010). Regenerating cortical connections in a dish: The entorhino-hippocampal organotypic slice co-culture as tool for pharmacological screening of molecules promoting axon regeneration. *Nature Protocols*, 5(2), Article 2. <https://doi.org/10.1038/nprot.2009.202>
- Del Rio, J. A., Heimrich, B., Borrell, V., Forster, E., Drakew, A., Alcantara, S., ... Soriano, E. (1997). A role for Cajal-Retzius cells and reelin in the development of hippocampal connections. *Nature*, 385(6611), 70-74. doi:10.1038/385070a0
- Del Rio, J. A., Heimrich, B., Soriano, E., Schwegler, H., & Frotscher, M. (1991). Proliferation and differentiation of glial fibrillary acidic protein-immunoreactive glial cells in organotypic slice cultures of rat hippocampus. *Neuroscience*, 43(2-3), 335-347. doi:10.1016/0306-4522(91)90298-3
- Del Rio, J. A., Heimrich, B., Super, H., Borrell, V., Frotscher, M., & Soriano, E. (1996). Differential survival of Cajal-Retzius cells in organotypic cultures of hippocampus and neocortex. *J Neurosci*, 16(21), 6896-6907. doi:10.1523/JNEUROSCI.16-21-06896.1996
- Del Río, J. A., Solé, M., Borrell, V., Martínez, A., & Soriano, E. (2002). Involvement of Cajal-Retzius cells in robust and layer-specific regeneration of the entorhino-hippocampal pathways. *European Journal of Neuroscience*, 15(12), 1881-1890. <https://doi.org/10.1046/j.1460-9568.2002.02027.x>
- Del Turco, D., & Deller, T. (2007). Organotypic entorhino-hippocampal slice cultures--a tool to study the molecular and cellular regulation of axonal regeneration and collateral sprouting in vitro. *Methods Mol Biol*, 399, 55-66. doi:10.1007/978-1-59745-504-6_5
- Deng, J. B., Yu, D. M., & Li, M. S. (2006). Formation of the entorhino-hippocampal pathway: a tracing study in vitro and in vivo. *Neurosci Bull*, 22(6), 305-314.
- Deng, J. B., Yu, D. M., Wu, P., & Li, M. S. (2007). The tracing study of developing entorhino-hippocampal pathway. *Int J Dev Neurosci*, 25(4), 251-258. doi:10.1016/j.ijdevneu.2007.03.002

- Deng, W., Wu, G., Min, L., Feng, Z., Chen, H., Tan, M., Sui, J., Liu, H., & Hou, J. (2021). Optogenetic Neuronal Stimulation Promotes Functional Recovery After Spinal Cord Injury. *Frontiers in Neuroscience*, 15. <https://www.frontiersin.org/articles/10.3389/fnins.2021.640255>
- Dey, D., Shrivastava, V., Joshi, D., Singal, C. M. S., Tyagi, S., Bhat, M. A., Jaiswal, P., Sharma, J. B., Palanichamy, J. K., Sinha, S., Seth, P., & Sen, S. (2023). Hypoxia Induces Early Neurogenesis in Human Fetal Neural Stem Cells by Activating the WNT Pathway. *Molecular Neurobiology*, 60(5), 2910-2921. <https://doi.org/10.1007/s12035-023-03248-4>
- Deymeer, F. (2020). History of Myasthenia Gravis Revisited. *Archives of Neuropsychiatry*, 58(2), 154-162. <https://doi.org/10.29399/npa.27315>
- Diekmann, S., Nitsch, R., & Ohm, T. G. (1994). The organotypic entorhinal-hippocampal complex slice culture of adolescent rats. A model to study transcellular changes in a circuit particularly vulnerable in neurodegenerative disorders. *J Neural Transm Suppl*, 44, 61-71. doi:10.1007/978-3-7091-9350-1_5
- Dimou, L., & Gallo, V. (2015). NG2-glia and their functions in the central nervous system. *Glia*, 63(8), 1429-1451. <https://doi.org/10.1002/glia.22859>
- Ditterich, J., Mazurek, M. E., & Shadlen, M. N. (2003). Microstimulation of visual cortex affects the speed of perceptual decisions. *Nature Neuroscience*, 6(8), Article 8. <https://doi.org/10.1038/nn1094>
- Dresser, L., Wlodarski, R., Rezania, K., & Soliven, B. (2021). Myasthenia Gravis: Epidemiology, Pathophysiology and Clinical Manifestations. *Journal of Clinical Medicine*, 10(11), 2235. <https://doi.org/10.3390/jcm10112235>
- Drexler, B., Hentschke, H., Antkowiak, B., & Grasshoff, C. (2010). Organotypic cultures as tools for testing neuroactive drugs - link between in-vitro and in-vivo experiments. *Curr Med Chem*, 17(36), 4538-4550. doi:10.2174/092986710794183042
- Du, Z.-W., Chen, H., Liu, H., Lu, J., Qian, K., Huang, C. T.-Ling., Zhong, X., Fan, F., & Zhang, S.-C. (2015). Generation and Expansion of highly-pure Motor Neuron Progenitors from Human Pluripotent Stem Cells. *Nature communications*, 6, 6626. <https://doi.org/10.1038/ncomms7626>
- Dusart, I., Morel, M. P., Wehrle, R., & Sotelo, C. (1999). Late axonal sprouting of injured Purkinje cells and its temporal correlation with permissive changes in the glial scar. *J Comp Neurol*, 408(3), 399-418.
- Ebadi, M., Bashir, R. M., Heidrick, M. L., Hamada, F. M., Refaey, H. E., Hamed, A., . . . Lassi, N. K. (1997). Neurotrophins and their receptors in nerve injury and repair. *Neurochem Int*, 30(4-5), 347-374. doi:10.1016/s0197-0186(96)00071-x
- Elfarrash, S., Jensen, N. M., Ferreira, N., Betzer, C., Thevathasan, J. V., Diekmann, R., . . . Jensen, P. H. (2019). Organotypic slice culture model demonstrates inter-neuronal spreading of alpha-synuclein aggregates. *Acta Neuropathol Commun*, 7(1), 213. doi:10.1186/s40478-019-0865-5
- Engel, A. G., Lambert, E. H., & Howard, F. M. (1977). Immune complexes (IgG and C3) at the motor end-plate in myasthenia gravis: Ultrastructural and light microscopic localization and electrophysiologic correlations. *Mayo Clinic Proceedings*, 52(5), 267-280.
- Engesser-Cesar, C., Ichiyama, R. M., Nefas, A. L., Hill, M. A., Edgerton, V. R., Cotman, C. W., & Anderson, A. J. (2007). Wheel running following spinal cord injury improves locomotor recovery and stimulates serotonergic fiber growth. *The European Journal of Neuroscience*, 25(7), 1931-1939. <https://doi.org/10.1111/j.1460-9568.2007.05469.x>
- Engler, A. J., Sen, S., Sweeney, H. L., & Discher, D. E. (2006). Matrix Elasticity Directs Stem Cell Lineage Specification. *Cell*, 126(4), 677-689. <https://doi.org/10.1016/j.cell.2006.06.044>
- English, A., Schwartz, G., Meador, W., Sabatier, M., & Mulligan, A. (2006). Electrical Stimulation Promotes Peripheral Axon Regeneration By Enhanced Neuronal Neurotrophin Signaling. *Developmental neurobiology*, 67, 158-172. <https://doi.org/10.1002/dneu.20339>
- Erck, C., Peris, L., Andrieux, A., Meissirel, C., Gruber, A. D., Vernet, M., Schweitzer, A., Saoudi, Y., Pointu, H., Bosc, C., Salin, P. A., Job, D., & Wehland, J. (2005). A vital role of tubulin-tyrosinase for neuronal organization. *Proceedings of the National Academy of Sciences of the United States of America*, 102(22), 7853-7858. <https://doi.org/10.1073/pnas.0409626102>
- Ertürk, A., Hellal, F., Enes, J., & Bradke, F. (2007). Disorganized microtubules underlie the formation of retraction bulbs and the failure of axonal regeneration. *The Journal of Neuroscience: The Official Journal of the Society for Neuroscience*, 27(34), 9169-9180. <https://doi.org/10.1523/JNEUROSCI.0612-07.2007>
- Falsig, J., Julius, C., Margalith, I., Schwarz, P., Heppner, F. L., & Aguzzi, A. (2008). A versatile prion replication assay in organotypic brain slices. *Nat Neurosci*, 11(1), 109-117.
- Farmakidis, C., Pasnoor, M., Dimachkie, M. M., & Barohn, R. J. (2018). Treatment of Myasthenia Gravis. *Neurologic clinics*, 36(2), 311-337. <https://doi.org/10.1016/j.ncl.2018.01.011>

- Farrell, C., Mumford, P., & Wiseman, F. K. (2022). Rodent Modeling of Alzheimer's Disease in Down Syndrome: In vivo and ex vivo Approaches. *Front Neurosci*, 16, 909669. doi:10.3389/fnins.2022.909669
- Farrera-Sinfreu, J., Giralt, E., Castel, S., Albericio, F., & Royo, M. (2005). Cell-Penetrating cis- γ -Amino-L-Proline-Derived Peptides. *Journal of the American Chemical Society*, 127(26), 9459-9468. https://doi.org/10.1021/ja051648k
- Fenno, L., Yizhar, O., & Deisseroth, K. (2011). The Development and Application of Optogenetics. *Annual review of neuroscience*, 34, 389-412. https://doi.org/10.1146/annurev-neuro-061010-113817
- Ferdowsian, H. R., & Beck, N. (2011). Ethical and Scientific Considerations Regarding Animal Testing and Research. *PLOS ONE*, 6(9), e24059. https://doi.org/10.1371/journal.pone.0024059
- Fernández-Garibay, X., Gómez-Florit, M., Domingues, R. M. A., Gomes, M. E., Fernández-Costa, J. M., & Ramón-Azcón, J. (2022). Xeno-free bioengineered human skeletal muscle tissue using human platelet lysate-based hydrogels. *Biofabrication*, 14(4). https://doi.org/10.1088/1758-5090/ac8dc8
- Fernández-Garibay, X., Ortega, M., Herreros, E., Comelles, J., Martínez, E., Artero, R., Fernández Costa, J. M., & Ramón-Azcón, J. (2021). Bioengineered in vitro 3D model of myotonic dystrophy type 1 human skeletal muscle. *Biofabrication*, 13. https://doi.org/10.1088/1758-5090/abf6ae
- Fernández-Costa, J. M., Ortega, M. A., Rodríguez-Comas, J., Lopez-Muñoz, G., Yeste, J., Mangas-Florencio, L., Fernández-González, M., Martín-Lasierra, E., Tejedera-Villafranca, A., & Ramon-Azcon, J. (2023). Training-on-a-Chip: A Multi-Organ Device to Study the Effect of Muscle Exercise on Insulin Secretion in Vitro. *Advanced Materials Technologies*, 8(7), 2200873. https://doi.org/10.1002/admt.202200873
- Fleming, J. W., Capel, A. J., Rimington, R. P., Wheeler, P., Leonard, A. N., Bishop, N. C., Davies, O. G., & Lewis, M. P. (2020). Bioengineered human skeletal muscle capable of functional regeneration. *BMC Biology*, 18(1), 145. https://doi.org/10.1186/s12915-020-00884-3
- Foty, R. (2011). A Simple Hanging Drop Cell Culture Protocol for Generation of 3D Spheroids. *Journal of Visualized Experiments : JoVE*, 51, 2720. https://doi.org/10.3791/2720
- Frotscher, M., & Heimrich, B. (1993). Formation of layer-specific fiber projections to the hippocampus in vitro. *Proc Natl Acad Sci U S A*, 90(21), 10400-10403. doi:10.1073/pnas.90.21.10400
- Frotscher, M., & Heimrich, B. (1995). Lamina-specific synaptic connections of hippocampal neurons in vitro. *J Neurobiol*, 26(3), 350-359. doi:10.1002/neu.480260307
- Frotscher, M., Heimrich, B., & Deller, T. (1997). Sprouting in the hippocampus is layer-specific. *Trends Neurosci*, 20(5), 218-223. doi:10.1016/s0166-2236(96)01018-1
- Frotscher, M., Seress, L., Abraham, H., & Heimrich, B. (2001). Early generated Cajal-Retzius cells have different functions in cortical development. *Symp Soc Exp Biol*(53), 43-49.
- Gahwiler, B. H. (1981a). Morphological differentiation of nerve cells in thin organotypic cultures derived from rat hippocampus and cerebellum. *Proc R Soc Lond B Biol Sci*, 211(1184), 287-290. doi:10.1098/rspb.1981.0007
- Gahwiler, B. H. (1981b). Organotypic monolayer cultures of nervous tissue. *J Neurosci Methods*, 4(4), 329-342. doi:10.1016/0165-0270(81)90003-0
- Gahwiler, B. H. (1988). Organotypic cultures of neural tissue. *Trends Neurosci*, 11(11), 484-489.
- Gahwiler, B. H., Capogna, M., Debanne, D., McKinney, R. A., & Thompson, S. M. (1997). Organotypic slice cultures: a technique has come of age. *Trends Neurosci*, 20(10), 471-477. doi:10.1016/s0166-2236(97)01122-3
- Gaiarsa, J. L., & Heimrich, B. (1995). Restoration of mossy fiber projection in slice co-cultures of dislocated dentate gyrus and degranulated hippocampus. *Brain Res Dev Brain Res*, 86(1-2), 250-258. doi:10.1016/0165-3806(95)00034-b
- Galiakberova, A. A., & Dashinimaev, E. B. (2020). Neural Stem Cells and Methods for Their Generation From Induced Pluripotent Stem Cells in vitro. *Frontiers in Cell and Developmental Biology*, 8. https://www.frontiersin.org/articles/10.3389/fcell.2020.00815
- Gao, J., Stevenson, T. J., Douglass, A. D., Barrios, J. P., & Bonkowsky, J. L. (2018). The Midline Axon Crossing Decision Is Regulated through an Activity-Dependent Mechanism by the NMDA Receptor. *eNeuro*, 5(2). doi:10.1523/ENEURO.0389-17.2018
- García-Lizarriar, A., Fernández-Garibay, X., Velasco-Mallorquí, F., Castaño, A. G., Samitier, J., & Ramon-Azcon, J. (2018). Composite Biomaterials as Long-Lasting Scaffolds for 3D Bioprinting of Highly Aligned Muscle Tissue. *Macromolecular Bioscience*, 18(10), e1800167. https://doi.org/10.1002/mabi.201800167
- Gaspard, N., Bouschet, T., Herpoel, A., Naeije, G., van den Ameele, J., & Vanderhaeghen, P. (2009). Generation of cortical neurons from mouse embryonic stem cells. *Nature protocols*, 4, 1454-1463. https://doi.org/10.1038/nprot.2009.157

- Gil, V., & Del Río, J. A. (2012). Analysis of axonal growth and cell migration in 3D hydrogel cultures of embryonic mouse CNS tissue. *Nature Protocols*, 7(2), 268-280. <https://doi.org/10.1038/nprot.2011.445>
- Gil, V., & Del Río, J. A. (2019). Generation of 3-D Collagen-based Hydrogels to Analyze Axonal Growth and Behavior During Nervous System Development. *Journal of Visualized Experiments: JoVE*, 148. <https://doi.org/10.3791/59481>
- Gilhus, N. E., Tzartos, S., Evoli, A., Palace, J., Burns, T. M., & Verschuuren, J. J. G. M. (2019). Myasthenia gravis. *Nature Reviews Disease Primers*, 5(1), Article 1. <https://doi.org/10.1038/s41572-019-0079-y>
- Goldshmit, Y., Lythgo, N., Galea, M. P., & Turnley, A. M. (2008). Treadmill training after spinal cord hemisection in mice promotes axonal sprouting and synapse formation and improves motor recovery. *Journal of Neurotrauma*, 25(5), 449-465. <https://doi.org/10.1089/neu.2007.0392>
- Gomez, C. M., & Richman, D. P. (1983). Anti-acetylcholine receptor antibodies directed against the alpha-bungarotoxin binding site induce a unique form of experimental myasthenia. *Proceedings of the National Academy of Sciences of the United States of America*, 80(13), 4089-4093. <https://doi.org/10.1073/pnas.80.13.4089>
- Gong, M., Bi, Y., Jiang, W., Zhang, Y., Chen, L., Hou, N., Liu, Y., Wei, X., Chen, J., & Li, T. (2011). Immortalized mesenchymal stem cells: An alternative to primary mesenchymal stem cells in neuronal differentiation and neuroregeneration associated studies. *Journal of Biomedical Science*, 18(1), 87. <https://doi.org/10.1186/1423-0127-18-87>
- Gordon, T. (2009). The role of neurotrophic factors in nerve regeneration. *Neurosurgical Focus*, 26(2), E3. <https://doi.org/10.3171/FOC.2009.26.2.E3>
- Goritz, C., Dias, D. O., Tomilin, N., Barbacid, M., Shupliakov, O., & Frisen, J. (2011). A pericyte origin of spinal cord scar tissue. *Science*, 333(6039), 238-242. doi:10.1126/science.1203165
- Grefte, S., Vullingsh, S., Kuijpers-Jagtman, A. M., Torensma, R., & Von den Hoff, J. W. (2012). Matrigel, but not collagen I, maintains the differentiation capacity of muscle derived cells in vitro. *Biomedical Materials (Bristol, England)*, 7(5), 055004. <https://doi.org/10.1088/1748-6041/7/5/055004>
- Gryniewicz, G., Poenie, M., & Tsien, R. Y. (1985). A new generation of Ca²⁺ indicators with greatly improved fluorescence properties. *The Journal of Biological Chemistry*, 260(6), 3440-3450.
- Gu, Y., Cheng, X., Huang, X., Yuan, Y., Qin, S., Tan, Z., Wang, D., Hu, X., He, C., & Su, Z. (2019). Conditional ablation of reactive astrocytes to dissect their roles in spinal cord injury and repair. *Brain, Behavior, and Immunity*, 80, 394-405. <https://doi.org/10.1016/j.bbi.2019.04.016>
- Guix, M., Mestre, R., Patiño, T., De Corato, M., Fuentes, J., Zarpellon, G., & Sánchez, S. (2021). Biohybrid soft robots with self-stimulating skeletons. *Science Robotics*, 6(53), eabe7577. <https://doi.org/10.1126/scirobotics.abe7577>
- Gungor-Ozkerim, P. S., Inci, I., Zhang, Y. S., Khademhosseini, A., & Dokmeci, M. R. (2018). Bioprinting for 3D bioprinting: An overview. *Biomaterials Science*, 6(5), 915-946. <https://doi.org/10.1039/C7BM00765E>
- Gunn, J. W., Turner, S. D., & Mann, B. K. (2005). Adhesive and mechanical properties of hydrogels influence neurite extension. *Journal of Biomedical Materials Research*, 72A(1), 91-97. <https://doi.org/10.1002/jbm.a.30203>
- Guo, L., Yeh, M. L., Cuzon Carlson, V. C., Johnson-Venkatesh, E. M., & Yeh, H. H. (2012). Nerve growth factor in the hippocamposeptal system: evidence for activity-dependent anterograde delivery and modulation of synaptic activity. *J Neurosci*, 32(22), 7701-7710. doi:10.1523/JNEUROSCI.0028-12.2012
- Han, X., Chow, B. Y., Zhou, H., Klapoetke, N. C., Chuong, A., Rajimehr, R., Yang, A., Baratta, M. V., Winkle, J., Desimone, R., & Boyden, E. S. (2011). A high-light sensitivity optical neural silencer: Development and application to optogenetic control of non-human primate cortex. *Frontiers in Systems Neuroscience*, 5, 18. <https://doi.org/10.3389/fnsys.2011.00018>
- Hanson, M. G., Milner, L. D., & Landmesser, L. T. (2008). Spontaneous rhythmic activity in early chick spinal cord influences distinct motor axon pathfinding decisions. *Brain Res Rev*, 57(1), 77-85. doi:10.1016/j.brainresrev.2007.06.021
- Happe, C. L., Tenerelli, K. P., Gromova, A. K., Kolb, F., & Engler, A. J. (2017). Mechanically patterned neuromuscular junctions-in-a-dish have improved functional maturation. *Molecular Biology of the Cell*, 28(14), 1950-1958. <https://doi.org/10.1091/mbc.e17-01-0046>
- Harrison, R. G., Greenman, M. J., Mall, F. P., & Jackson, C. M. (1907). Observations of the living developing nerve fiber. *The Anatomical Record*, 1(5), 116-128. <https://doi.org/10.1002/ar.1090010503>

- Hasselbach, W. (1964). ATP-DRIVEN ACTIVE TRANSPORT OF CALCIUM IN THE MEMBRANES OF THE SARCOPLASMIC RETICULUM. *Proceedings of the Royal Society of London. Series B, Biological Sciences*, 160, 501-504. <https://doi.org/10.1098/rspb.1964.0064>
- Hatanaka, Y., Hemmi, S., Morgan, M. B., Scheufele, M. L., Claussen, G. C., Wolfe, G. I., & Oh, S. J. (2005). Nonresponsiveness to anticholinesterase agents in patients with MuSK-antibody-positive MG. *Neurology*, 65(9), 1508-1509. <https://doi.org/10.1212/01.wnl.0000183145.91579.74>
- He, S., Nakada, D., & Morrison, S. J. (2009). Mechanisms of stem cell self-renewal. *Annual Review of Cell and Developmental Biology*, 25, 377-406. <https://doi.org/10.1146/annurev.cellbio.042308.113248>
- He, Z., & Jin, Y. (2016). Intrinsic Control of Axon Regeneration. *Neuron*, 90(3), 437-451. <https://doi.org/10.1016/j.neuron.2016.04.022>
- Heimrich, B., & Frotscher, M. (1993). Slice cultures as a model to study entorhinal-hippocampal interaction. *Hippocampus*, 3 Spec No, 11-17.
- Hellal, F., Hurtado, A., Ruschel, J., Flynn, K. C., Laskowski, C. J., Umlauf, M., Kapitein, L. C., Strikis, D., Lemmon, V., Bixby, J., Hoogenraad, C. C., & Bradke, F. (2011). Microtubule stabilization reduces scarring and causes axon regeneration after spinal cord injury. *Science (New York, N.Y.)*, 331(6019), 928-931. <https://doi.org/10.1126/science.1201148>
- Hernández-Hernández, J. M., García-González, E. G., Brun, C. E., & Rudnicki, M. A. (2017). The myogenic regulatory factors, determinants of muscle development, cell identity and regeneration. *Seminars in Cell & Developmental Biology*, 72, 10-18. <https://doi.org/10.1016/j.semcdb.2017.11.010>
- Hervera, A., De Virgiliis, F., Palmisano, I., Zhou, L., Tantardini, E., Kong, G., Hutson, T., Danzi, M. C., Perry, R. B.-T., Santos, C. X. C., Kapustin, A. N., Fleck, R. A., Del Río, J. A., Carroll, T., Lemmon, V., Bixby, J. L., Shah, A. M., Fainzilber, M., & Di Giovanni, S. (2018). Reactive oxygen species regulate axonal regeneration through the release of exosomal NADPH oxidase 2 complexes into injured axons. *Nature Cell Biology*, 20(3), 307-319. <https://doi.org/10.1038/s41556-018-0039-x>
- Hervera, A., Zhou, L., Palmisano, I., McLachlan, E., Kong, G., Hutson, T. H., Danzi, M. C., Lemmon, V. P., Bixby, J. L., Matamoros-Angles, A., Forsberg, K., De Virgiliis, F., Matheos, D. P., Kwapis, J., Wood, M. A., Puttagunta, R., del Río, J. A., & Di Giovanni, S. (2019). PP4-dependent HDAC3 dephosphorylation discriminates between axonal regeneration and regenerative failure. *The EMBO Journal*, 38(13), e101032. <https://doi.org/10.15252/embj.2018101032>
- Higuchi, O., Hamuro, J., Motomura, M., & Yamanashi, Y. (2011). Autoantibodies to low-density lipoprotein receptor-related protein 4 in myasthenia gravis. *Annals of Neurology*, 69(2), 418-422. <https://doi.org/10.1002/ana.22312>
- Hildebrandt-Einfeldt, L., Yap, K., Paul, M. H., Stoffer, C., Zahn, N., Drakew, A., . . . Deller, T. (2021). Crossed Entorhino-Dentate Projections Form and Terminate With Correct Layer-Specificity in Organotypic Slice Cultures of the Mouse Hippocampus. *Front Neuroanat*, 15, 637036. doi:10.3389/fnana.2021.637036
- Hinds, S., Bian, W., Dennis, R. G., & Bursac, N. (2011). The role of extracellular matrix composition in structure and function of bioengineered skeletal muscle. *Biomaterials*, 32(14), 3575-3583. <https://doi.org/10.1016/j.biomaterials.2011.01.062>
- Hoch, W., McConville, J., Helms, S., Newsom-Davis, J., Melms, A., & Vincent, A. (2001). Auto-antibodies to the receptor tyrosine kinase MuSK in patients with myasthenia gravis without acetylcholine receptor antibodies. *Nature Medicine*, 7(3), 365-368. <https://doi.org/10.1038/85520>
- Hochbaum, D. R., Zhao, Y., Farhi, S. L., Klapoetke, N., Werley, C. A., Kapoor, V., Zou, P., Kralj, J. M., Maclaurin, D., Smedemark-Margulies, N., Saulnier, J. L., Boulting, G. L., Straub, C., Cho, Y. K., Melkonian, M., Wong, G. K.-S., Harrison, D. J., Murthy, V. N., Sabatini, B. L., . . . Cohen, A. E. (2014). All-optical electrophysiology in mammalian neurons using engineered microbial rhodopsins. *Nature Methods*, 11(8), Article 8. <https://doi.org/10.1038/nmeth.3000>
- Hoffmann, L. F., Martins, A., Majolo, F., Contini, V., Laufer, S., & Goettert, M. I. (2022). Neural regeneration research model to be explored: SH-SY5Y human neuroblastoma cells. *Neural Regeneration Research*, 18(6), 1265-1266. <https://doi.org/10.4103/1673-5374.358621>
- Hogan, M. K., Hamilton, G. F., & Horner, P. J. (2020). Neural Stimulation and Molecular Mechanisms of Plasticity and Regeneration: A Review. *Frontiers in Cellular Neuroscience*, 14, 271. <https://doi.org/10.3389/fncel.2020.00271>
- Holopainen, I. E. (2005). Organotypic hippocampal slice cultures: a model system to study basic cellular and molecular mechanisms of neuronal cell death, neuroprotection, and synaptic plasticity. *Neurochem Res*, 30(12), 1521-1528. doi:10.1007/s11064-005-8829-5

- Hosseini, V., Ahadian, S., Ostrovidov, S., Camci-Unal, G., Chen, S., Kaji, H., Ramalingam, M., & Khademhosseini, A. (2012). Engineered Contractile Skeletal Muscle Tissue on a Microgrooved Methacrylated Gelatin Substrate. *Tissue Engineering. Part A*, 18(23-24), 2453-2465. <https://doi.org/10.1089/ten.tea.2012.0181>
- Howard, F. M., Lennon, V. A., Finley, J., Matsumoto, J., & Elveback, L. R. (1987). Clinical correlations of antibodies that bind, block, or modulate human acetylcholine receptors in myasthenia gravis. *Annals of the New York Academy of Sciences*, 505, 526-538. <https://doi.org/10.1111/j.1749-6632.1987.tb51321.x>
- Howard, J. F., Barohn, R. J., Cutter, G. R., Freimer, M., Juel, V. C., Mozaffar, T., Mellion, M. L., Benatar, M. G., Farrugia, M. E., Wang, J. J., Malhotra, S. S., Kissel, J. T., & MG Study Group. (2013). A randomized, double-blind, placebo-controlled phase II study of eculizumab in patients with refractory generalized myasthenia gravis. *Muscle & Nerve*, 48(1), 76-84. <https://doi.org/10.1002/mus.23839>
- Howard, J. F., Brill, V., Vu, T., Karam, C., Peric, S., Margania, T., Murai, H., Bilinska, M., Shakarishvili, R., Smilowski, M., Guglietta, A., Ulrichs, P., Vangeneugden, T., Utsugisawa, K., Verschuuren, J., Mantegazza, R., Bleecker, J. L. D., Koning, K. D., Mey, K. D., ... Frishberg, B. (2021). Safety, efficacy, and tolerability of efgartigimod in patients with generalised myasthenia gravis (ADAPT): A multicentre, randomised, placebo-controlled, phase 3 trial. *The Lancet Neurology*, 20(7), 526-536. [https://doi.org/10.1016/S1474-4422\(21\)00159-9](https://doi.org/10.1016/S1474-4422(21)00159-9)
- Howard, M. J., David, G., & Barrett, J. N. (1999). Resealing of transected myelinated mammalian axons in vivo: Evidence for involvement of calpain. *Neuroscience*, 93(2), 807-815. [https://doi.org/10.1016/S0306-4522\(99\)00195-5](https://doi.org/10.1016/S0306-4522(99)00195-5)
- Hu, B.-Y., Weick, J. P., Yu, J., Ma, L.-X., Zhang, X.-Q., Thomson, J. A., & Zhang, S.-C. (2010). Neural differentiation of human induced pluripotent stem cells follows developmental principles but with variable potency. *Proceedings of the National Academy of Sciences of the United States of America*, 107(9), 4335-4340. <https://doi.org/10.1073/pnas.0910012107>
- Huberman, A. D., Speer, C. M., & Chapman, B. (2006). Spontaneous retinal activity mediates development of ocular dominance columns and binocular receptive fields in v1. *Neuron*, 52(2), 247-254. doi:10.1016/j.neuron.2006.07.028
- Huijbers, M. G., Vergoossen, D. L., Fillié-Grijpma, Y. E., Es, I. E. van, Koning, M. T., Slot, L. M., Veelken, H., Plomp, J. J., Maarel, S. M. van der, & Verschuuren, J. J. (2019). MuSK myasthenia gravis monoclonal antibodies: Valency dictates pathogenicity. *Neurology - Neuroimmunology Neuroinflammation*, 6(3). <https://doi.org/10.1212/NXI.0000000000000547>
- Huijbers, M. G., Zhang, W., Klooster, R., Niks, E. H., Friese, M. B., Straasheijm, K. R., Thijssen, P. E., Vrolijk, H., Plomp, J. J., Vogels, P., Losen, M., Van der Maarel, S. M., Burden, S. J., & Verschuuren, J. J. (2013). MuSK IgG4 autoantibodies cause myasthenia gravis by inhibiting binding between MuSK and Lrp4. *Proceedings of the National Academy of Sciences of the United States of America*, 110(51), 20783-20788. <https://doi.org/10.1073/pnas.1313944110>
- Humpel, C. (2015). Organotypic brain slice cultures: A review. *Neuroscience*, 305, 86-98. <https://doi.org/10.1016/j.neuroscience.2015.07.086>
- Humpel, C. (2019). Organotypic Brain Slices of ADULT Transgenic Mice: A Tool to Study Alzheimer's Disease. *Curr Alzheimer Res*, 16(2), 172-181. doi:10.2174/1567205016666181212153138
- Hurtado de Mendoza, T., Balana, B., Slesinger, P. A., & Verma, I. M. (2011). Organotypic cerebellar cultures: apoptotic challenges and detection. *J Vis Exp*(51). doi:10.3791/2564
- Huxley, A. F., & Niedergerke, R. (1954). Structural changes in muscle during contraction; interference microscopy of living muscle fibres. *Nature*, 173(4412), 971-973. <https://doi.org/10.1038/173971a0>
- Huxley, H., & Hanson, J. (1954). Changes in the Cross-Striations of Muscle during Contraction and Stretch and their Structural Interpretation. *Nature*, 173(4412), Article 4412. <https://doi.org/10.1038/173973a0>
- Hyung, S., Lee, S.-R., Kim, Y. J., Bang, S., Tahk, D., Park, J.-C., Suh, J.-K. F., & Jeon, N. L. (2019). Optogenetic neuronal stimulation promotes axon outgrowth and myelination of motor neurons in a three-dimensional motor neuron-Schwann cell coculture model on a microfluidic biochip. *Biotechnology and Bioengineering*, 116(10), 2425-2438. <https://doi.org/10.1002/bit.27083>
- Iberite, F., Gruppioni, E., & Ricotti, L. (2022). Skeletal muscle differentiation of human iPSCs meets bioengineering strategies: Perspectives and challenges. *Npj Regenerative Medicine*, 7(1), Article 1. <https://doi.org/10.1038/s41536-022-00216-9>
- In vitro models | Home. (2022). <https://www.springer.com/journal/44164/>

- Ito, A., Yamamoto, Y., Sato, M., Ikeda, K., Yamamoto, M., Fujita, H., Nagamori, E., Kawabe, Y., & Kamiyama, M. (2014). Induction of functional tissue-engineered skeletal muscle constructs by defined electrical stimulation. *Scientific Reports*, 4, 4781. <https://doi.org/10.1038/srep04781>
- Iuliano, A., Wal, E., Ruijmbek, C., Groen, S., Pijnappel, W., de Greef, J., & Saggiomo, V. (2020). Coupling 3D Printing and Novel Replica Molding for In House Fabrication of Skeletal Muscle Tissue Engineering Devices. *Advanced Materials Technologies*, 5, 2000344. <https://doi.org/10.1002/admt.202000344>
- Iyer, N. R., & Ashton, R. S. (2022). Bioengineering the human spinal cord. *Frontiers in Cell and Developmental Biology*, 10. <https://www.frontiersin.org/articles/10.3389/fcell.2022.942742>
- Jalal, S., Dastidar, S., & Tedesco, F. S. (2021). Advanced models of human skeletal muscle differentiation, development and disease: Three-dimensional cultures, organoids and beyond. *Current Opinion in Cell Biology*, 73, 92-104. <https://doi.org/10.1016/j.ceb.2021.06.004>
- Jang, M. J., & Nam, Y. (2015). NeuroCa: integrated framework for systematic analysis of spatiotemporal neuronal activity patterns from large-scale optical recording data. *Neurophotonics*, 2(3), 035003. doi:10.1117/1.NPh.2.3.035003
- Jang, S., Kim, H., Kim, H. J., Lee, S. K., Kim, E. W., Namkoong, K., & Kim, E. (2018). Long-Term Culture of Organotypic Hippocampal Slice from Old 3xTg-AD Mouse: An ex vivo Model of Alzheimer's Disease. *Psychiatry Investig*, 15(2), 205-213. doi:10.30773/pi.2017.04.02
- Jensen, C., & Teng, Y. (2020). Is It Time to Start Transitioning From 2D to 3D Cell Culture? *Frontiers in Molecular Biosciences*, 7. <https://www.frontiersin.org/articles/10.3389/fmolb.2020.00033>
- Jensen, G., Holloway, J. L., & Stabenfeldt, S. E. (2020). Hyaluronic Acid Biomaterials for Central Nervous System Regenerative Medicine. *Cells*, 9(9), 2113. <https://doi.org/10.3390/cells9092113>
- Jobsis, P. D., Rothstein, E. C., & Balaban, R. S. (2007). Limited Utility of Acetoxymethyl (AM) Based Intracellular Delivery Systems, in vivo: Interference by Extracellular Esterases. *Journal of microscopy*, 226(Pt 1), 74-81. <https://doi.org/10.1111/j.1365-2818.2007.01755.x>
- Kajana, S., & Goshgarian, H. G. (2009). Systemic administration of rolipram increases medullary and spinal cAMP and activates a latent respiratory motor pathway after high cervical spinal cord injury. *The Journal of Spinal Cord Medicine*, 32(2), 175-182. <https://doi.org/10.1080/10790268.2009.11760769>
- Kajzar, A., Cesa, C. M., Kirchgessner, N., Hoffmann, B., & Merkel, R. (2008). Toward physiological conditions for cell analyses: Forces of heart muscle cells suspended between elastic micropillars. *Biophysical Journal*, 94(5), 1854-1866. <https://doi.org/10.1529/biophysj.107.115766>
- Kalamida, D., Poulas, K., Avramopoulou, V., Fostieri, E., Lagoumintzis, G., Lazaridis, K., Sideri, A., Zouridakis, M., & Tzartos, S. J. (2007). Muscle and neuronal nicotinic acetylcholine receptors. Structure, function and pathogenicity. *The FEBS Journal*, 274(15), 3799-3845. <https://doi.org/10.1111/j.1742-4658.2007.05935.x>
- Kamber, D., Erez, H., & Spira, M. E. (2009). Local calcium-dependent mechanisms determine whether a cut axonal end assembles a retarded endbulb or competent growth cone. *Experimental Neurology*, 219(1), 112-125. <https://doi.org/10.1016/j.expneurol.2009.05.004>
- Kamikubo, Y., Jin, H., Zhou, Y., Niisato, K., Hashimoto, Y., Takasugi, N., & Sakurai, T. (2022). Ex vivo analysis platforms for monitoring amyloid precursor protein cleavage. *Front Mol Neurosci*, 15, 1068990. doi:10.3389/fnmol.2022.1068990
- Kanamori, A., Catrinescu, M.-M., Belisle, J. M., Costantino, S., & Levin, L. A. (2012). Retrograde and Wallerian Axonal Degeneration Occur Synchronously after Retinal Ganglion Cell Axotomy. *The American Journal of Pathology*, 181(1), 62-73. <https://doi.org/10.1016/j.ajpath.2012.03.030>
- Kandel, E. R., Schwartz, J. H., Jessell, T. M., Siegelbaum, S. A., & Hudspeth, A. J. (2013). *Principles of Neural Science* (5.a ed.). Mc Graw Hill.
- Kandel, E. R., Spencer, W. A., & Brinley, F. J. (1961). Electrophysiology of hippocampal neurons. I. Sequential invasion and synaptic organization. *Journal of Neurophysiology*, 24, 225-242. <https://doi.org/10.1152/jn.1961.24.3.225>
- Kao, I., & Drachman, D. B. (1977). Myasthenic immunoglobulin accelerates acetylcholine receptor degradation. *Science (New York, N.Y.)*, 196(4289), 527-529. <https://doi.org/10.1126/science.850793>
- Karlin, A. (1993). Structure of nicotinic acetylcholine receptors. *Current Opinion in Neurobiology*, 3(3), 299-309. [https://doi.org/10.1016/0959-4388\(93\)90121-E](https://doi.org/10.1016/0959-4388(93)90121-E)
- Kastanenka, K. V., & Landmesser, L. T. (2013). Optogenetic-mediated increases in in vivo spontaneous activity disrupt pool-specific but not dorsal-ventral motoneuron pathfinding. *Proc Natl Acad Sci U S A*, 110(43), 17528-17533. doi:10.1073/pnas.1316457110
- Katz, L. C., & Shatz, C. J. (1996). Synaptic activity and the construction of cortical circuits. *Science*, 274(5290), 1133-1138. doi:10.1126/science.274.5290.1133

- Kerschensteiner, M., Schwab, M. E., Lichtman, J. W., & Misgeld, T. (2005). In vivo imaging of axonal degeneration and regeneration in the injured spinal cord. *Nature Medicine*, 11(5), 572-577. <https://doi.org/10.1038/nm1229>
- Kim, H., Jang, E. J., Sankpal, N. V., Patel, M., & Patel, R. (2023). Recent Development of Brain Organoids for Biomedical Application. *Macromol Biosci*, 23(3), e2200346. doi:10.1002/mabi.202200346
- Kim, H., Kim, E., Park, M., Lee, E., & Namkoong, K. (2013). Organotypic hippocampal slice culture from the adult mouse brain: a versatile tool for translational neuropsychopharmacology. *Prog Neuropsychopharmacol Biol Psychiatry*, 41, 36-43. doi:10.1016/j.pnpbp.2012.11.004
- Kim, H., Osaki, T., Kamm, R. D., & Asada, H. H. (2022). Multiscale engineered human skeletal muscles with perfusable vasculature and microvascular network recapitulating the fluid compartments. *Biofabrication*, 15(1). <https://doi.org/10.1088/1758-5090/ac933d>
- Kimpinski, K., Campenot, R. B., & Mearow, K. (1997). Effects of the neurotrophins nerve growth factor, neurotrophin-3, and brain-derived neurotrophic factor (BDNF) on neurite growth from adult sensory neurons in compartmented cultures. *Journal of Neurobiology*, 33(4), 395-410. [https://doi.org/10.1002/\(SICI\)1097-4695\(199710\)33:4<395::AID-NEU5>3.0.CO;2-5](https://doi.org/10.1002/(SICI)1097-4695(199710)33:4<395::AID-NEU5>3.0.CO;2-5)
- Kita, E. M., Scott, E. K., & Goodhill, G. J. (2015). The influence of activity on axon pathfinding in the optic tectum. *Dev Neurobiol*, 75(6), 608-620. doi:10.1002/dneu.22262
- Klockner, N., Jung, M., Stuermer, C. A., & Bahr, M. (2001). BDNF increases the number of axotomized rat retinal ganglion cells expressing GAP-43, L1, and TAG-1 mRNA--a supportive role for nitric oxide? *Neurobiol Dis*, 8(1), 103-113. doi:10.1006/nbdi.2000.0329
- Kluge, A., Hailer, N. P., Horvath, T. L., Bechmann, I., & Nitsch, R. (1998). Tracing of the entorhinal-hippocampal pathway in vitro. *Hippocampus*, 8(1), 57-68. doi:10.1002/(SICI)1098-1063(1998)8:1<57::AID-HIPO6>3.0.CO;2-4
- Ko, I. K., Lee, B.-K., Lee, S. J., Andersson, K.-E., Atala, A., & Yoo, J. J. (2013). The effect of in vitro formation of acetylcholine receptor (AChR) clusters in engineered muscle fibers on subsequent innervation of constructs in vivo. *Biomaterials*, 34(13), 3246-3255. <https://doi.org/10.1016/j.biomaterials.2013.01.029>
- Koneczny, I., & Herbst, R. (2019). Myasthenia Gravis: Pathogenic Effects of Autoantibodies on Neuromuscular Architecture. *Cells*, 8(7), Article 7. <https://doi.org/10.3390/cells8070671>
- Koneczny, I., Cossins, J., Waters, P., Beeson, D., & Vincent, A. (2013). MuSK Myasthenia Gravis IgG4 Disrupts the Interaction of LRP4 with MuSK but Both IgG4 and IgG1-3 Can Disperse Preformed Agrin-Independent AChR Clusters. *PLOS ONE*, 8(11), e80695. <https://doi.org/10.1371/journal.pone.0080695>
- Kordas, G., Lagoumintzis, G., Sideris, S., Poulas, K., & Tzartos, S. J. (2014). Direct proof of the in vivo pathogenic role of the AChR autoantibodies from myasthenia gravis patients. *PLoS One*, 9(9), e108327. <https://doi.org/10.1371/journal.pone.0108327>
- Koroleva, A., Deiwick, A., Nguyen, A., Narayan, R., Shpichka, A., Kufelt, O., Kiyan, R., Bagratashvili, V., Timashev, P., Scheper, T., & Chichkov, B. (2016). Hydrogel-based microfluidics for vascular tissue engineering. *BioNanoMaterials*, 17(1-2), 19-32. <https://doi.org/10.1515/bnm-2015-0026>
- Kudoh, A., Satoh, H., Hirai, H., Watanabe, T., & Shimabukuro, M. (2018). Preliminary Evidence for Adipocytokine Signals in Skeletal Muscle Glucose Uptake. *Frontiers in Endocrinology*, 9, 295. <https://doi.org/10.3389/fendo.2018.00295>
- Kunik, D., Dion, C., Ozaki, T., Levin, L. A., & Costantino, S. (2011). Laser-Based Single-Axon Transection for High-Content Axon Injury and Regeneration Studies. *PLoS ONE*, 6(11), e26832. <https://doi.org/10.1371/journal.pone.0026832>
- Laake, J. H., Haug, F. M., Wieloch, T., & Ottersen, O. P. (1999). A simple in vitro model of ischemia based on hippocampal slice cultures and propidium iodide fluorescence. *Brain Res Brain Res Protoc*, 4(2), 173-184.
- Lam, D., Enright, H. A., Cadena, J., Peters, S. K. G., Sales, A. P., Osburn, J. J., Soscia, D. A., Kulp, K. S., Wheeler, E. K., & Fischer, N. O. (2019). Tissue-specific extracellular matrix accelerates the formation of neural networks and communities in a neuron-glia co-culture on a multi-electrode array. *Scientific Reports*, 9(1), Article 1. <https://doi.org/10.1038/s41598-019-40128-1>
- Lamoureux, L., Sajesh, B., Slota, J. A., Medina, S. J., Mayor, M., Frost, K. L., . . . Booth, S. A. (2022). Non-Productive Infection of Glial Cells with SARS-CoV-2 in Hamster Organotypic Cerebellar Slice Cultures. *Viruses*, 14(6). doi:10.3390/v14061218
- Langelaan, M. L. P., Boonen, K. J. M., Rosaria-Chak, K. Y., van der Schaft, D. W. J., Post, M. J., & Baaijens, F. P. T. (2011). Advanced maturation by electrical stimulation: Differences in response between C2C12 and primary muscle progenitor cells. *Journal of Tissue Engineering and Regenerative Medicine*, 5(7), 529-539. <https://doi.org/10.1002/term.345>

- Latenser, S., Keller, H., Leupin, O., Rausch, M., Graf-Hausner, U., & Rimann, M. (2018). A Novel Microplate 3D Bioprinting Platform for the Engineering of Muscle and Tendon Tissues. *Slas Technology*, 23(6), 599-613. <https://doi.org/10.1177/2472630318776594>
- Lazaridis, K., & Tzartos, S. J. (2020). Autoantibody Specificities in Myasthenia Gravis; Implications for Improved Diagnostics and Therapeutics. *Frontiers in Immunology*, 11. <https://www.frontiersin.org/articles/10.3389/fimmu.2020.00212>
- Lee, C. W., Zhang, H., Geng, L., & Peng, H. B. (2014). Crosslinking-induced endocytosis of acetylcholine receptors by quantum dots. *PloS One*, 9(2), e90187. <https://doi.org/10.1371/journal.pone.0090187>
- Lee, D., Yang, K., & Xie, J. (2023). Advances in Nerve Injury Models on a Chip. *Advanced Biology*, n/a(n/a), 2200227. <https://doi.org/10.1002/adbi.202200227>
- Lee, K., Park, T. I., Heppner, P., Schweder, P., Mee, E. W., Draganow, M., & Montgomery, J. M. (2020). Human in vitro systems for examining synaptic function and plasticity in the brain. *J Neurophysiol*, 123(3), 945-965. doi:10.1152/jn.00411.2019
- Lefebvre, P. P., Van de Water, T. R., Staecker, H., Weber, T., Galinovic-Schwartz, V., Moonen, G., & Ruben, R. J. (1992). Nerve growth factor stimulates neurite regeneration but not survival of adult auditory neurons in vitro. *Acta Otolaryngol*, 112(2), 288-293. doi:10.1080/00016489.1992.11665420
- Leite, M. I., Jacob, S., Viegas, S., Cossins, J., Clover, L., Morgan, B. P., Beeson, D., Willcox, N., & Vincent, A. (2008). IgG1 antibodies to acetylcholine receptors in 'seronegative' myasthenia gravis†. *Brain*, 131(7), 1940-1952. <https://doi.org/10.1093/brain/awn092>
- Leng, Y., Li, X., Zheng, F., Liu, H., Wang, C., Wang, X., Liao, Y., Liu, J., Meng, K., Yu, J., Zhang, J., Wang, B., Tan, Y., Liu, M., Jia, X., Li, D., Li, Y., Gu, Z., & Fan, Y. (2022). Advances in In vitro Models of Neuromuscular Junction: Focusing on Organ-on-a-chip, Organoids and Biohybrid Robotics. *Advanced Materials*, n/a(n/a), 2211059. <https://doi.org/10.1002/adma.202211059>
- Li, D., Field, P. M., Starega, U., Li, Y., & Raisman, G. (1993). Entorhinal axons project to dentate gyrus in organotypic slice co-culture. *Neuroscience*, 52(4), 799-813. doi:10.1016/0306-4522(93)90530-s
- Li, D., Field, P. M., Yoshioka, N., & Raisman, G. (1994). Axons regenerate with correct specificity in horizontal slice culture of the postnatal rat entorhino-hippocampal system. *Eur J Neurosci*, 6(6), 1026-1037.
- Li, Y., Zeng, P. M., Wu, J., & Luo, Z. G. (2023). Advances and Applications of Brain Organoids. *Neurosci Bull*. doi:10.1007/s12264-023-01065-2
- Lima, S. Q., & Miesenböck, G. (2005). Remote Control of Behavior through Genetically Targeted Photostimulation of Neurons. *Cell*, 121(1), 141-152. <https://doi.org/10.1016/j.cell.2005.02.004>
- Lindstrom, J. M., Seybold, M. E., Lennon, V. A., Whittingham, S., & Duane, D. D. (1976). Antibody to acetylcholine receptor in myasthenia gravis. Prevalence, clinical correlates, and diagnostic value. *Neurology*, 26(11), 1054-1059. <https://doi.org/10.1212/wnl.26.11.1054>
- Loewa, A., Feng, J. J., & Hedtrich, S. (2023). Human disease models in drug development. *Nature Reviews Bioengineering*, 1-15. <https://doi.org/10.1038/s44222-023-00063-3>
- Lonchamp, E., Dupont, J. L., Beekenkamp, H., Poulain, B., & Bossu, J. L. (2006). The mouse cerebellar cortex in organotypic slice cultures: an in vitro model to analyze the consequences of mutations and pathologies on neuronal survival, development, and function. *Crit Rev Neurobiol*, 18(1-2), 179-186. doi:10.1615/critrevneurobiol.v18.i1-2.180
- Lorenzana, A. O., Lee, J. K., Mui, M., Chang, A., & Zheng, B. (2015). A surviving intact branch stabilizes remaining axon architecture after injury as revealed by in vivo imaging in the mouse spinal cord. *Neuron*, 86(4), 947-954. <https://doi.org/10.1016/j.neuron.2015.03.061>
- Lossi, L., & Merighi, A. (2018). The Use of ex Vivo Rodent Platforms in Neuroscience Translational Research With Attention to the 3Rs Philosophy. *Front Vet Sci*, 5, 164. doi:10.3389/fvets.2018.00164
- Lotlikar, M. S., Tarantino, M. B., Jorfi, M., Kovacs, D. M., Tanzi, R. E., & Bhattacharyya, R. (2022). Microfluidic separation of axonal and somal compartments of neural progenitor cells differentiated in a 3D matrix. *STAR Protocols*, 3(1), 101028. <https://doi.org/10.1016/j.xpro.2021.101028>
- Lu, P., & Tuszynski, M. H. (2008). Growth Factors and Combinatorial Therapies for CNS Regeneration. *Experimental neurology*, 209(2), 313-320. <https://doi.org/10.1016/j.expneurol.2007.08.004>
- Lu, P., Yang, H., Jones, L. L., Filbin, M. T., & Tuszynski, M. H. (2004). Combinatorial therapy with neurotrophins and cAMP promotes axonal regeneration beyond sites of spinal cord injury. *The Journal of Neuroscience: The Official Journal of the Society for Neuroscience*, 24(28), 6402-6409. <https://doi.org/10.1523/JNEUROSCI.1492-04.2004>

- Luckman, S. P., Skeie, G. O., Helgeland, G., & Gilhus, N. E. (2006). Effects of myasthenia gravis patient sera on human myoblast cultures. *Acta Neurologica Scandinavica. Supplementum*, 183, 28-32. <https://doi.org/10.1111/j.1600-0404.2006.00611.x>
- Luis, N. M., & Schnorrer, F. (2021). Mechanobiology of muscle and myofibril morphogenesis. *Cells & Development*, 168, 203760. <https://doi.org/10.1016/j.cdev.2021.203760>
- Lundqvist, J., EL Andaloussi-Lilja, J., Svensson, C., Gustafsson Dorfh, H., & Forsby, A. (2013). Optimisation of culture conditions for differentiation of C17.2 neural stem cells to be used for in vitro toxicity tests. *Toxicology in Vitro*, 27(5), 1565-1569. <https://doi.org/10.1016/j.tiv.2012.04.020>
- Macpherson, P. C. D., Suhr, S. T., & Goldman, D. (2004). Activity-dependent gene regulation in conditionally-immortalized muscle precursor cell lines. *Journal of Cellular Biochemistry*, 91(4), 821-839. <https://doi.org/10.1002/jcb.10784>
- Madden, L., Juhas, M., Kraus, W. E., Truskey, G. A., & Bursac, N. (2015). Bioengineered human myobundles mimic clinical responses of skeletal muscle to drugs. *ELife*, 4, e04885. <https://doi.org/10.7554/eLife.04885>
- Madduma-Bandarage, U. S. K., & Madihally, S. V. (2021). Synthetic hydrogels: Synthesis, novel trends, and applications. *Journal of Applied Polymer Science*, 138(19), 50376. <https://doi.org/10.1002/app.50376>
- Maffioletti, S. M., Sarcar, S., Henderson, A. B. H., Mannhardt, I., Pinton, L., Moyle, L. A., Steele-Stallard, H., Cappellari, O., Wells, K. E., Ferrari, G., Mitchell, J. S., Tyzack, G. E., Kotiadis, V. N., Khedr, M., Ragazzi, M., Wang, W., Duchen, M. R., Patani, R., Zammit, P. S., ... Tedesco, F. S. (2018). Three-Dimensional Human iPSC-Derived Artificial Skeletal Muscles Model Muscular Dystrophies and Enable Multilineage Tissue Engineering. *Cell Reports*, 23(3), 899-908. <https://doi.org/10.1016/j.celrep.2018.03.091>
- Mamchaoui, K., Trollet, C., Bigot, A., Negroni, E., Chaouch, S., Wolff, A., Kandalla, P. K., Marie, S., Di Santo, J., St Guily, J. L., Muntoni, F., Kim, J., Philippi, S., Spuler, S., Levy, N., Blumen, S. C., Voit, T., Wright, W. E., Aamiri, A., ... Mouly, V. (2011). Immortalized pathological human myoblasts: Towards a universal tool for the study of neuromuscular disorders. *Skeletal Muscle*, 1, 34. <https://doi.org/10.1186/2044-5040-1-34>
- Mantegazza, R., & Antozzi, C. (2018). When myasthenia gravis is deemed refractory: Clinical signposts and treatment strategies. *Therapeutic Advances in Neurological Disorders*, 11, 1756285617749134. <https://doi.org/10.1177/1756285617749134>
- Mao, Q., Acharya, A., Rodríguez-de-laRosa, A., Marchiano, F., Dehapiot, B., Al Tanoury, Z., Rao, J., Díaz-Cuadros, M., Mansur, A., Wagner, E., Chardes, C., Gupta, V., Lenne, P.-F., Habermann, B. H., Theodoly, O., Pourquié, O., & Schnorrer, F. (2022). Tension-driven multi-scale self-organisation in human iPSC-derived muscle fibers. *eLife*, 11, e76649. <https://doi.org/10.7554/eLife.76649>
- Mar, F. M., Bonni, A., & Sousa, M. M. (2014). Cell intrinsic control of axon regeneration. *EMBO Rep*, 15(3), 254-263. doi:10.1002/embr.201337723
- Maroto, I. B., Costas-Insua, C., Berthoux, C., Moreno, E., Ruiz-Calvo, A., Montero-Fernandez, C., . . . Guzman, M. (2023). Control of a hippocampal recurrent excitatory circuit by cannabinoid receptor-interacting protein Gap43. *Nat Commun*, 14(1), 2303. doi:10.1038/s41467-023-38026-2
- Marshall, K. L., Rajbhandari, L., Venkatesan, A., Maragakis, N. J., & Farah, M. H. (2023). Enhanced axonal regeneration of ALS patient iPSC-derived motor neurons harboring SOD1A4V mutation. *Scientific Reports*, 13(1), Article 1. <https://doi.org/10.1038/s41598-023-31720-7>
- Marty, S., Wehrle, R., & Sotelo, C. (2000). Neuronal activity and brain-derived neurotrophic factor regulate the density of inhibitory synapses in organotypic slice cultures of postnatal hippocampus. *J Neurosci*, 20(21), 8087-8095. doi:10.1523/JNEUROSCI.20-21-08087.2000
- Matamoros-Angles, A., Gayosso, L. M., Richaud-Patin, Y., di Domenico, A., Vergara, C., Hervera, A., Sousa, A., Fernández-Borges, N., Consiglio, A., Gavín, R., López de Maturana, R., Ferrer, I., López de Munain, A., Raya, Á., Castilla, J., Sánchez-Pernaute, R., & del Río, J. A. (2018). IPS Cell Cultures from a Gerstmann-Sträussler-Scheinker Patient with the Y218N PRNP Mutation Recapitulate tau Pathology. *Molecular Neurobiology*, 55(4), 3033-3048. <https://doi.org/10.1007/s12035-017-0506-6>
- Mauro, A. (1961). Satellite cell of skeletal muscle fibers. *The Journal of Biophysical and Biochemical Cytology*, 9(2), 493-495. <https://doi.org/10.1083/jcb.9.2.493>
- Mayer, D., Fischer, H., Schneider, U., Heimrich, B., & Schwemmle, M. (2005). Borna disease virus replication in organotypic hippocampal slice cultures from rats results in selective damage of dentate granule cells. *J Virol*, 79(18), 11716-11723. doi:10.1128/JVI.79.18.11716-11723.2005

- McCarthy, J. M., Virdee, J., Brown, J., Ursu, D., Ahmed, Z., Cavallini, A., & Nuthall, H. N. (2021). Development of P301S tau seeded organotypic hippocampal slice cultures to study potential therapeutics. *Sci Rep*, 11(1), 10309. doi:10.1038/s41598-021-89230-3
- McLaughlin, T., Torborg, C. L., Feller, M. B., & O'Leary, D. D. (2003). Retinotopic map refinement requires spontaneous retinal waves during a brief critical period of development. *Neuron*, 40(6), 1147-1160. doi:10.1016/s0896-6273(03)00790-6
- Mesquida-Veny, F., Del Río, J. A., & Hervera, A. (2021). Macrophagic and microglial complexity after neuronal injury. *Progress in Neurobiology*, 200, 101970. <https://doi.org/10.1016/j.pneurobio.2020.101970>
- Mesquida-Veny, F., Martínez-Torres, S., Del Río, J. A., & Hervera, A. (2022). Genetic control of neuronal activity enhances axonal growth only on permissive substrates. *Molecular Medicine*, 28(1), 97. <https://doi.org/10.1186/s10020-022-00524-2>
- Mestre, R., García, N., Patiño, T., Guix, M., Fuentes, J., Valerio-Santiago, M., Almiñana, N., & Sánchez, S. (2021). 3D-bioengineered model of human skeletal muscle tissue with phenotypic features of aging for drug testing purposes. *Biofabrication*, 13(4). <https://doi.org/10.1088/1758-5090/ac165b>
- Mingorance, A., Fontana, X., Sole, M., Burgaya, F., Urena, J. M., Teng, F. Y., . . . del Rio, J. A. (2004). Regulation of Nogo and Nogo receptor during the development of the entorhino-hippocampal pathway and after adult hippocampal lesions. *Mol Cell Neurosci*, 26(1), 34-49. doi:10.1016/j.mcn.2004.01.001
- Mingorance, A., Fontana, X., Soriano, E., & Del Rio, J. A. (2005). Overexpression of myelin-associated glycoprotein after axotomy of the perforant pathway. *Mol Cell Neurosci*, 29(3), 471-483. doi:10.1016/j.mcn.2005.03.016
- Mingorance, A., Sole, M., Muneton, V., Martinez, A., Nieto-Sampedro, M., Soriano, E., & del Rio, J. A. (2006). Regeneration of lesioned entorhino-hippocampal axons in vitro by combined degradation of inhibitory proteoglycans and blockade of Nogo-66/NgR signaling. *Faseb J*, 20(3), 491-493.
- Minta, A., Kao, J. P., & Tsien, R. Y. (1989). Fluorescent indicators for cytosolic calcium based on rhodamine and fluorescein chromophores. *The Journal of Biological Chemistry*, 264(14), 8171-8178.
- Miyawaki, A., Llopis, J., Heim, R., McCaffery, J. M., Adams, J. A., Ikura, M., & Tsien, R. Y. (1997). Fluorescent indicators for Ca²⁺ based on green fluorescent proteins and calmodulin. *Nature*, 388(6645), Article 6645. <https://doi.org/10.1038/42264>
- Montolio, M., Messeguer, J., Masip, I., Guijarro, P., Gavin, R., Antonio Del Rio, J., . . . Soriano, E. (2009). A semaphorin 3A inhibitor blocks axonal chemorepulsion and enhances axon regeneration. *Chem Biol*, 16(7), 691-701. doi:10.1016/j.chembiol.2009.05.006
- Moysidou, C.-M., Barberio, C., & Owens, R. M. (2021). Advances in Engineering Human Tissue Models. *Frontiers in Bioengineering and Biotechnology*, 8. <https://www.frontiersin.org/articles/10.3389/fbioe.2020.620962>
- Myasthenia Gravis—Symptoms, Causes, Treatment | National Organization for Rare Disorders. (2023, junio). <https://rarediseases.org/rare-diseases/myasthenia-gravis/>
- Nagel, G., Szellas, T., Huhn, W., Kateriya, S., Adeishvili, N., Berthold, P., Ollig, D., Hegemann, P., & Bamberg, E. (2003). Channelrhodopsin-2, a directly light-gated cation-selective membrane channel. *Proceedings of the National Academy of Sciences*, 100(24), 13940-13945. <https://doi.org/10.1073/pnas.1936192100>
- Nakai, J., Ohkura, M., & Imoto, K. (2001). A high signal-to-noise Ca(2+) probe composed of a single green fluorescent protein. *Nature Biotechnology*, 19(2), 137-141. <https://doi.org/10.1038/84397>
- Oh, J., Lee, C., & Kaang, B.-K. (2019). Imaging and analysis of genetically encoded calcium indicators linking neural circuits and behaviors. *The Korean Journal of Physiology & Pharmacology: Official Journal of the Korean Physiological Society and the Korean Society of Pharmacology*, 23(4), 237-249. <https://doi.org/10.4196/kjpp.2019.23.4.237>
- Ohtake, Y., & Li, S. (2015). Molecular mechanisms of scar-sourced axon growth inhibitors. *Brain research*, 1619, 22-35. <https://doi.org/10.1016/j.brainres.2014.08.064>
- Ohtake, Y., Matsuhisa, K., Kaneko, M., Kanemoto, S., Asada, R., Imaizumi, K., & Saito, A. (2018). Axonal Activation of the Unfolded Protein Response Promotes Axonal Regeneration Following Peripheral Nerve Injury. *Neuroscience*, 375, 34-48. <https://doi.org/10.1016/j.neuroscience.2018.02.003>
- Orkin, R. W., Gehron, P., McGoodwin, E. B., Martin, G. R., Valentine, T., & Swarm, R. (1977). A murine tumor producing a matrix of basement membrane. *The Journal of Experimental Medicine*, 145(1), 204-220. <https://doi.org/10.1084/jem.145.1.204>
- Orlandi, J. G., Fernández-García, S., Comella-Bolla, A., Masana, M., Barriga, G. G.-D., Yaghoubi, M., Kipp, A., Canals, J. M., Colicos, M. A., Davidsen, J., Alberch, J., & Soriano, J. (2017). NETCAL:

- An interactive platform for large-scale, NETWORK and population dynamics analysis of CALcium imaging recordings [Software]. Zenodo. <https://doi.org/10.5281/zenodo.1119026>
- Osaki, T., Sivathanu, V., & Kamm, R. D. (2018). Crosstalk between developing vasculature and optogenetically engineered skeletal muscle improves muscle contraction and angiogenesis. *Biomaterials*, 156, 65-76. <https://doi.org/10.1016/j.biomaterials.2017.11.041>
- Osaki, T., Uzel, S. G. M., & Kamm, R. D. (2018). Microphysiological 3D model of amyotrophic lateral sclerosis (ALS) from human iPSC-derived muscle cells and optogenetic motor neurons. *Science Advances*, 4(10), eaat5847. <https://doi.org/10.1126/sciadv.aat5847>
- Osaki, T., Uzel, S. G. M., & Kamm, R. D. (2020). On-chip 3D neuromuscular model for drug screening and precision medicine in neuromuscular disease. *Nature Protocols*, 15(2), 421-449. <https://doi.org/10.1038/s41596-019-0248-1>
- Ostergaard, K. (1993). Organotypic slice cultures of the rat striatum--I. A histochemical and immunocytochemical study of acetylcholinesterase, choline acetyltransferase, glutamate decarboxylase and GABA. *Neuroscience*, 53(3), 679-693.
- Park, H. H., Kim, Y.-M., Anh Hong, L. T., Kim, H. S., Kim, S. H., Jin, X., Hwang, D. H., Kwon, M. J., Song, S.-C., & Kim, B. G. (2022). Dual-functional hydrogel system for spinal cord regeneration with sustained release of arylsulfatase B alleviates fibrotic microenvironment and promotes axonal regeneration. *Biomaterials*, 284, 121526. <https://doi.org/10.1016/j.biomaterials.2022.121526>
- Patrick, J., & Lindstrom, J. (1973). Autoimmune response to acetylcholine receptor. *Science (New York, N.Y.)*, 180(4088), 871-872. <https://doi.org/10.1126/science.180.4088.871>
- Paxinos, G., Franklin, K. B. J., & Franklin, K. B. J. (2001). *The mouse brain in stereotaxic coordinates* (2nd ed.). San Diego: Academic Press.
- Pena, F. (2010). Organotypic cultures as tool to test long-term effects of chemicals on the nervous system. *Curr Med Chem*, 17(10), 987-1001. doi:10.2174/092986710790820679
- Pereira, I., Lopez-Martinez, M. J., Villasante, A., Introna, C., Tornero, D., Canals, J. M., & Samitier, J. (2023). Hyaluronic acid-based bioink improves the differentiation and network formation of neural progenitor cells. *Frontiers in Bioengineering and Biotechnology*, 11, 1110547. <https://doi.org/10.3389/fbioe.2023.1110547>
- Perez-Gomez, A., & Tasker, R. A. (2014). Enhanced mossy fiber sprouting and synapse formation in organotypic hippocampal cultures following transient domoic acid excitotoxicity. *Neurotox Res*, 25(4), 402-410. doi:10.1007/s12640-013-9450-z
- Petersen, E. D., Sharkey, E. D., Pal, A., Shafau, L. O., Zenchak-Petersen, J., Peña, A. J., Aggarwal, A., Prakash, M., & Hochgeschwender, U. (2022). Restoring Function After Severe Spinal Cord Injury Through BioLuminescent-OptoGenetics. *Frontiers in Neurology*, 12. <https://www.frontiersin.org/articles/10.3389/fneur.2021.792643>
- Peterson, D. A., Lucidi-Phillipi, C. A., Murphy, D. P., Ray, J., & Gage, F. H. (1996). Fibroblast growth factor-2 protects entorhinal layer II glutamatergic neurons from axotomy-induced death. *J Neurosci*, 16(3), 886-898. doi:10.1523/JNEUROSCI.16-03-00886.1996
- Pettit, D. L., Helms, M. C., Lee, P., Augustine, G. J., & Hall, W. C. (1999). Local Excitatory Circuits in the Intermediate Gray Layer of the Superior Colliculus. *Journal of Neurophysiology*, 81(3), 1424-1427. <https://doi.org/10.1152/jn.1999.81.3.1424>
- Pevzner, A., Schoser, B., Peters, K., Cosma, N.-C., Karakatsani, A., Schalke, B., Melms, A., & Kröger, S. (2012). Anti-LRP4 autoantibodies in AChR- and MuSK-antibody-negative myasthenia gravis. *Journal of Neurology*, 259(3), 427-435. <https://doi.org/10.1007/s00415-011-6194-7>
- Pinton, L., Khedr, M., Lionello, V. M., Sarcar, S., Maffioletti, S. M., Dastidar, S., Negroni, E., Choi, S., Khokhar, N., Bigot, A., Counsell, J. R., Bernardo, A. S., Zammit, P. S., & Tedesco, F. S. (2023). 3D human induced pluripotent stem cell-derived bioengineered skeletal muscles for tissue, disease and therapy modeling. *Nature Protocols*, 18(4), 1337-1376. <https://doi.org/10.1038/s41596-022-00790-8>
- Placzek, M., Tessier-Lavigne, M., Jessell, T., & Dodd, J. (1990). Orientation of commissural axons in vitro in response to a floor plate-derived chemoattractant. *Development (Cambridge, England)*, 110(1), 19-30. <https://doi.org/10.1242/dev.110.1.19>
- Plazas, P. V., Nicol, X., & Spitzer, N. C. (2013). Activity-dependent competition regulates motor neuron axon pathfinding via PlexinA3. *Proc Natl Acad Sci U S A*, 110(4), 1524-1529. doi:10.1073/pnas.1213048110
- Powell, C. A., Smiley, B. L., Mills, J., & Vandenberg, H. H. (2002). Mechanical stimulation improves tissue-engineered human skeletal muscle. *American Journal of Physiology. Cell Physiology*, 283(5), C1557-1565. <https://doi.org/10.1152/ajpcell.00595.2001>

- Prang, P., Del Turco, D., & Kapfhammer, J. P. (2001). Regeneration of entorhinal fibers in mouse slice cultures is age dependent and can be stimulated by NT-4, GDNF, and modulators of G-proteins and protein kinase C. *Exp Neurol*, 169(1), 135-147.
- Puttagunta, R., Tedeschi, A., Sória, M. G., Hervera, A., Lindner, R., Rathore, K. I., Gaub, P., Joshi, Y., Nguyen, T., Schmandke, A., Laskowski, C. J., Boutillier, A.-L., Bradke, F., & Di Giovanni, S. (2014). PCAF-dependent epigenetic changes promote axonal regeneration in the central nervous system. *Nature Communications*, 5, 3527. <https://doi.org/10.1038/ncomms4527>
- Qian, L., & Saltzman, W. M. (2004). Improving the expansion and neuronal differentiation of mesenchymal stem cells through culture surface modification. *Biomaterials*, 25(7-8), 1331-1337. <https://doi.org/10.1016/j.biomaterials.2003.08.013>
- Raffa, P., Easler, M., & Urciuolo, A. (2021). Three-dimensional in vitro models of neuromuscular tissue. *Neural Regeneration Research*, 17(4), 759-766. <https://doi.org/10.4103/1673-5374.322447>
- Rajabian, N., Shahini, A., Asmani, M., Vydiam, K., Choudhury, D., Nguyen, T., Ikhapoh, I., Zhao, R., Lei, P., & Andreadis, S. T. (2021). Bioengineered Skeletal Muscle as a Model of Muscle Aging and Regeneration. *Tissue Engineering. Part A*, 27(1-2), 74-86. <https://doi.org/10.1089/ten.tea.2020.0005>
- Renault, R., Sukenik, N., Descroix, S., Malaquin, L., Viovy, J.-L., Peyrin, J.-M., Bottani, S., Monceau, P., Moses, E., & Vignes, M. (2015). Combining Microfluidics, Optogenetics and Calcium Imaging to Study Neuronal Communication In Vitro. *PLoS ONE*, 10. <https://doi.org/10.1371/journal.pone.0120680>
- Ringer, S., & Buxton, D. W. (1887). Concerning the Action of Calcium, Potassium, and Sodium Salts upon the Eel's Heart and upon the Skeletal Muscles of the Frog. *The Journal of Physiology*, 8(1), 15-19.
- Río, J., & Ferrer, I. (2020). Potential of Microfluidics and Lab-on-Chip Platforms to Improve Understanding of “prion-like” Protein Assembly and Behavior. *Frontiers in Bioengineering and Biotechnology*, 8, 570692. <https://doi.org/10.3389/fbioe.2020.570692>
- Rishal, I., & Fainzilber, M. (2014). Axon-soma communication in neuronal injury. *Nature Reviews. Neuroscience*, 15(1), 32-42. <https://doi.org/10.1038/nrn3609>
- Rodolico, C., Bonanno, C., Toscano, A., & Vita, G. (2020). MuSK-Associated Myasthenia Gravis: Clinical Features and Management. *Frontiers in Neurology*, 11, 660. <https://doi.org/10.3389/fneur.2020.00660>
- Rose, N. R., & Bona, C. (1993). Defining criteria for autoimmune diseases (Witebsky's postulates revisited). *Immunology Today*, 14(9), 426-430. [https://doi.org/10.1016/0167-5699\(93\)90244-F](https://doi.org/10.1016/0167-5699(93)90244-F)
- Rose, N., Estrada Chavez, B., Sonam, S., Nguyen, T., Grecni, G., Bigot, A., Muchir, A., Ladoux, B., Cadot, B., Le Grand, F., & Trichet, L. (2023). Bioengineering a miniaturized in vitro 3D myotube contraction monitoring chip to model muscular dystrophies. *Biomaterials*, 293, 121935. <https://doi.org/10.1016/j.biomaterials.2022.121935>
- Rosenzweig, E. S., Courtine, G., Jindrich, D. L., Brock, J. H., Ferguson, A. R., Strand, S. C., Nout, Y. S., Roy, R. R., Miller, D. M., Beattie, M. S., Havton, L. A., Bresnahan, J. C., Edgerton, V. R., & Tuszynski, M. H. (2010). Extensive spontaneous plasticity of corticospinal projections after primate spinal cord injury. *Nature Neuroscience*, 13(12), 1505-1510. <https://doi.org/10.1038/nn.2691>
- Routbort, M. J., Bausch, S. B., & McNamara, J. O. (1999). Seizures, cell death, and mossy fiber sprouting in kainic acid-treated organotypic hippocampal cultures. *Neuroscience*, 94(3), 755-765. [doi:10.1016/s0306-4522\(99\)00358-9](https://doi.org/10.1016/s0306-4522(99)00358-9)
- Ruschel, J., Hellal, F., Flynn, K. C., Dupraz, S., Elliott, D. A., Tedeschi, A., Bates, M., Sliwinski, C., Brook, G., Dobrindt, K., Peitz, M., Brüstle, O., Norenberg, M. D., Blesch, A., Weidner, N., Bunge, M. B., Bixby, J. L., & Bradke, F. (2015). Axonal regeneration. Systemic administration of ephriline B promotes axon regeneration after spinal cord injury. *Science (New York, N.Y.)*, 348(6232), 347-352. <https://doi.org/10.1126/science.aaa2958>
- Russell, W. M. S., & Burch, R. L. (1959). The principles of humane experimental technique. *The Principles of Humane Experimental Technique*. <https://www.cabdirect.org/cabdirect/abstract/19592204037>
- Sala-Jarque, J., Mesquida-Veny, F., Badiola-Mateos, M., Samitier, J., Hervera, A., & del Río, J. A. (2020). Neuromuscular Activity Induces Paracrine Signaling and Triggers Axonal Regrowth after Injury in Microfluidic Lab-On-Chip Devices. *Cells*, 9(2), Article 2. <https://doi.org/10.3390/cells9020302>
- Sala-Jarque, J., Zimkowska, K., Ávila, J., Ferrer, I., & del Río, J. A. (2022). Towards a Mechanistic Model of Tau-Mediated Pathology in Tauopathies: What Can We Learn from Cell-Based In Vitro Assays? *International Journal of Molecular Sciences*, 23(19), 11527. <https://doi.org/10.3390/ijms231911527>

- Sala, L., Van Meer, B., Tertoolen, L., Bakkers, J., Bellin, M., Davis, R., Denning, C., Dieben, M., Eschenhagen, T., Giacomelli, E., Grandela, C., Hansen, A., Holman, E., Jongbloed, M., Kamel, S., Koopman, C., Lachaud, Q., Mannhardt, I., Mol, M., & Mummery, C. (2017). MUSCLEMOTION: A versatile open software tool to quantify cardiomyocyte and cardiac muscle contraction in vitro and in vivo. *Circulation Research*, 122, CIRCRESAHA.117.312067. <https://doi.org/10.1161/CIRCRESAHA.117.312067>
- Salzman, C. D., Britten, K. H., & Newsome, W. T. (1990). Cortical microstimulation influences perceptual judgements of motion direction. *Nature*, 346(6280), Article 6280. <https://doi.org/10.1038/346174a0>
- Sánchez-Ventura, J., Giménez-Llort, L., Penas, C., & Udina, E. (2021). Voluntary wheel running preserves lumbar perineuronal nets, enhances motor functions and prevents hyperreflexia after spinal cord injury. *Experimental Neurology*, 336, 113533. <https://doi.org/10.1016/j.expneurol.2020.113533>
- Savaskan, N. E., Plaschke, M., Ninnemann, O., Spillmann, A. A., Schwab, M. E., Nitsch, R., & Skutella, T. (1999). Myelin does not influence the choice behaviour of entorhinal axons but strongly inhibits their outgrowth length in vitro. *Eur J Neurosci*, 11(1), 316-326. doi:10.1046/j.1460-9568.1999.00430.x
- Schmidt, M., Schüler, S., Hüttner, S., Von Eyss, B., & Maltzahn, J. (2019). Adult stem cells at work: Regenerating skeletal muscle. *Cellular and Molecular Life Sciences*, 76. <https://doi.org/10.1007/s00018-019-03093-6>
- Schneider-Gold, C., & Gilhus, N. E. (2021). Advances and challenges in the treatment of myasthenia gravis. *Therapeutic Advances in Neurological Disorders*, 14, 17562864211065406. <https://doi.org/10.1177/17562864211065406>
- Schommer, J., Schrag, M., Nackenoff, A., Marwarha, G., & Ghribi, O. (2017). Method for organotypic tissue culture in the aged animal. *MethodsX*, 4, 166-171. doi:10.1016/j.mex.2017.03.003
- Seale, P., Sabourin, L. A., Girgis-Gabardo, A., Mansouri, A., Gruss, P., & Rudnicki, M. A. (2000). Pax7 Is Required for the Specification of Myogenic Satellite Cells. *Cell*, 102(6), 777-786. [https://doi.org/10.1016/S0092-8674\(00\)00066-0](https://doi.org/10.1016/S0092-8674(00)00066-0)
- Seidlits, S. K., Liang, J., Bierman, R. D., Sohrabi, A., Karam, J., Holley, S. M., Cepeda, C., & Walthers, C. M. (2019). Peptide-modified, hyaluronic acid-based hydrogels as a 3D culture platform for neural stem/progenitor cell engineering. *Journal of biomedical materials research. Part A*, 107(4), 704-718. <https://doi.org/10.1002/jbm.a.36603>
- Seifert, W. (1983). *Neurobiology of the hippocampus*. London ; New York: Academic Press.
- Seira, O., Gavin, R., Gil, V., Llorens, F., Rangel, A., Soriano, E., & del Rio, J. A. (2010). Neurites regrowth of cortical neurons by GSK3beta inhibition independently of Nogo receptor 1. *J Neurochem*, 113(6), 1644-1658. doi:10.1111/j.1471-4159.2010.06726.x
- Sengpiel, F., & Kind, P. C. (2002). The role of activity in development of the visual system. *Curr Biol*, 12(23), R818-826. doi:10.1016/s0960-9822(02)01318-0
- Shahin-Shamsabadi, A., & Selvaganapathy, P. R. (2020). A 3D Self-Assembled In Vitro Model to Simulate Direct and Indirect Interactions between Adipocytes and Skeletal Muscle Cells. *Advanced Biosystems*, 4(6), 2000034. <https://doi.org/10.1002/adbi.202000034>
- Sharma, N., Marzo, S. J., Jones, K. J., & Foeking, E. M. (2010). Electrical stimulation and testosterone differentially enhance expression of regeneration-associated genes. *Experimental Neurology*, 223(1), 183-191. <https://doi.org/10.1016/j.expneurol.2009.04.031>
- Shay, J. W., Wright, W. E., & Werbin, H. (1991). Defining the molecular mechanisms of human cell immortalization. *Biochimica Et Biophysica Acta*, 1072(1), 1-7. [https://doi.org/10.1016/0304-419x\(91\)90003-4](https://doi.org/10.1016/0304-419x(91)90003-4)
- Shea, K. L., Xiang, W., LaPorta, V. S., Licht, J. D., Keller, C., Basson, M. A., & Brack, A. S. (2010). Sprouty1 regulates reversible quiescence of a self-renewing adult muscle stem cell pool during regeneration. *Cell Stem Cell*, 6(2), 117-129. <https://doi.org/10.1016/j.stem.2009.12.015>
- Shepherd, G. M. G., Pologruto, T. A., & Svoboda, K. (2003). Circuit Analysis of Experience-Dependent Plasticity in the Developing Rat Barrel Cortex. *Neuron*, 38(2), 277-289. [https://doi.org/10.1016/S0896-6273\(03\)00152-1](https://doi.org/10.1016/S0896-6273(03)00152-1)
- Shieh, C.-C., Petrini, M. F., Dwyer, T. M., & Farley, J. M. (1995). Calcium Mobilization and Muscle Contraction Induced by Acetylcholine in Swine Trachealis. *Journal of Biomedical Science*, 2(3), 272-282. <https://doi.org/10.1007/BF02253388>
- Shima, A., Morimoto, Y., Sweeney, H. L., & Takeuchi, S. (2018). Three-dimensional contractile muscle tissue consisting of human skeletal myocyte cell line. *Experimental Cell Research*, 370(1), 168-173. <https://doi.org/10.1016/j.yexcr.2018.06.015>
- Shin, J. E., Jung, K., Kim, M., Hwang, K., Lee, H., Kim, I.-S., Lee, B. H., Lee, I.-S., & Park, K. I. (2018). Brain and spinal cord injury repair by implantation of human neural progenitor cells seeded onto

- polymer scaffolds. *Experimental & Molecular Medicine*, 50(4), Article 4. <https://doi.org/10.1038/s12276-018-0054-9>
- Shou, Y., Liang, F., Xu, S., & Li, X. (2020). The Application of Brain Organoids: From Neuronal Development to Neurological Diseases. *Frontiers in Cell and Developmental Biology*, 8. <https://www.frontiersin.org/articles/10.3389/fcell.2020.579659>
- Skutella, T., & Nitsch, R. (2001). New molecules for hippocampal development. *Trends Neurosci*, 24(2), 107-113. doi:10.1016/s0166-2236(00)01717-3
- Smith, I. C., Adam, H., & Herzog, W. (2020). A brief contraction has complex effects on summation of twitch pairs in human adductor pollicis. *Experimental Physiology*, 105(4), 676-689. <https://doi.org/10.1113/EP088401>
- Smith, V. M., Nguyen, H., Rumsey, J. W., Long, C. J., Shuler, M. L., & Hickman, J. J. (2021). A Functional Human-on-a-Chip Autoimmune Disease Model of Myasthenia Gravis for Development of Therapeutics. *Frontiers in Cell and Developmental Biology*, 9, 745897. <https://doi.org/10.3389/fcell.2021.745897>
- Sofroniew, M. V., Drefuss, J. J., & Gahwiler, B. H. (1988). Slice cultures of rat hypothalamus examined by immunohistochemical staining for neurohypophyseal peptides and GFAP. *Brain Res Bull*, 20(6), 669-674.
- Solé, M., Fontana, X., Gavín, R., Soriano, E., & del Río, J. A. (2004). Bcl-2 overexpression does not promote axonal regeneration of the entorhino-hippocampal connections in vitro after axotomy. *Brain Research*, 1020(1-2), 204-209. <https://doi.org/10.1016/j.brainres.2004.05.107>
- Spira, M. E., Oren, R., Dormann, A., Ilouz, N., & Lev, S. (2002). Calcium, Protease Activation, and Cytoskeleton Remodeling Underlie Growth Cone Formation and Neuronal Regeneration. *Cellular and Molecular Neurobiology*.
- Steinbeck, J. A., Jaiswal, M. K., Calder, E. L., Kishinevsky, S., Weishaupt, A., Toyka, K. V., Goldstein, P. A., & Studer, L. (2016). Functional connectivity under optogenetic control allows modeling of human neuromuscular disease. *Cell stem cell*, 18(1), 134-143. <https://doi.org/10.1016/j.stem.2015.10.002>
- Stoppini, L., Buchs, P. A., & Muller, D. (1991). A simple method for organotypic cultures of nervous tissue. *J Neurosci Methods*, 37(2), 173-182. doi:10.1016/0165-0270(91)90128-m
- Stoppini, L., Buchs, P. A., Brun, R., Muller, D., Dupont, S., Parisi, L., & Seebeck, T. (2000). Infection of organotypic slice cultures from rat central nervous tissue with *Trypanosoma brucei brucei*. *Int J Med Microbiol*, 290(1), 105-113. doi:10.1016/S1438-4221(00)80113-7
- Sun, Z., & Sudhof, T. C. (2021). A simple Ca(2+)-imaging approach to neural network analyses in cultured neurons. *J Neurosci Methods*, 349, 109041. doi:10.1016/j.jneumeth.2020.109041
- Super, H., Del Rio, J. A., Martinez, A., Perez-Sust, P., & Soriano, E. (2000). Disruption of neuronal migration and radial glia in the developing cerebral cortex following ablation of Cajal-Retzius cells. *Cereb Cortex*, 10(6), 602-613. doi:10.1093/cercor/10.6.602
- Super, H., Martinez, A., Del Rio, J. A., & Soriano, E. (1998). Involvement of distinct pioneer neurons in the formation of layer-specific connections in the hippocampus. *J Neurosci*, 18(12), 4616-4626. doi:10.1523/JNEUROSCI.18-12-04616.1998
- Takahashi, K., & Yamanaka, S. (2006). Induction of pluripotent stem cells from mouse embryonic and adult fibroblast cultures by defined factors. *Cell*, 126(4), 663-676. <https://doi.org/10.1016/j.cell.2006.07.024>
- Tan, P., He, L., Huang, Y., & Zhou, Y. (2022). Optophysiology: Illuminating cell physiology with optogenetics. *Physiological Reviews*, 102(3), 1263-1325. <https://doi.org/10.1152/physrev.00021.2021>
- Tong, Z., Seira, O., Casas, C., Reginensi, D., Homs-Corbera, A., Samitier, J., & Del Río, J. A. (2014). Engineering a functional neuro-muscular junction model in a chip. *RSC Adv.*, 4(97), 54788-54797. <https://doi.org/10.1039/C4RA10219C>
- Toral-Ojeda, I., Aldanondo, G., Lasa-Elgarresta, J., Lasa-Fernandez, H., Vesga-Castro, C., Mouly, V., Munain, A. L. D., & Vallejo-Illarramendi, A. (2018). A Novel Functional In Vitro Model that Recapitulates Human Muscle Disorders. En K. Sakuma (Ed.), *Muscle Cell and Tissue—Current Status of Research Field*. InTech. <https://doi.org/10.5772/intechopen.75903>
- Trailovic, S. M., Rajkovic, M., Marjanovic, D. S., Neveu, C., & Charvet, C. L. (2021). Action of Carvacrol on *Parascaris* sp. And Antagonistic Effect on Nicotinic Acetylcholine Receptors. *Pharmaceuticals* (Basel, Switzerland), 14(6), 505. <https://doi.org/10.3390/ph14060505>
- Tremblay, R., Sikorska, M., Sandhu, J., Lanthier, P., Ribocco-Lutkiewicz, M., & Bani-Yaghoob, M. (2008). Differentiation of N2a cells into dopamine neurons.
- Truffault, F., de Montpreville, V., Eymard, B., Sharshar, T., Le Panse, R., & Berrih-Aknin, S. (2017). Thymic Germinal Centers and Corticosteroids in Myasthenia Gravis: An Immunopathological

- Study in 1035 Cases and a Critical Review. *Clinical Reviews in Allergy & Immunology*, 52(1), 108-124. <https://doi.org/10.1007/s12016-016-8558-3>
- Unwin, N. (1993). Nicotinic acetylcholine receptor at 9 A resolution. *Journal of Molecular Biology*, 229(4), 1101-1124. <https://doi.org/10.1006/jmbi.1993.1107>
- Van Der Schaft, D. W. J., Van Spreeuwel, A. C. C., Boonen, K. J. M., Langelaan, M. L. P., Bouten, C. V. C., & Baaijens, F. P. T. (2013). Engineering Skeletal Muscle Tissues from Murine Myoblast Progenitor Cells and Application of Electrical Stimulation. *Journal of Visualized Experiments*, 73, 4267. <https://doi.org/10.3791/4267>
- Vandenburgh, H., Shansky, J., Benesch-Lee, F., Barbata, V., Reid, J., Thorrez, L., Valentini, R., & Crawford, G. (2008). Drug-screening platform based on the contractility of tissue-engineered muscle. *Muscle & Nerve*, 37(4), 438-447. <https://doi.org/10.1002/mus.20931>
- Varier, P., Raju, G., Madhusudan, P., Jerard, C., & Shankarappa, S. A. (2022). A Brief Review of In Vitro Models for Injury and Regeneration in the Peripheral Nervous System. *International Journal of Molecular Sciences*, 23(2), 816. <https://doi.org/10.3390/ijms23020816>
- Vianney, J.-M., Miller, D. A., & Spitsbergen, J. M. (2014). Effects of acetylcholine and electrical stimulation on glial cell line-derived neurotrophic factor production in skeletal muscle cells. *Brain Research*, 1588, 47-54. <https://doi.org/10.1016/j.brainres.2014.09.024>
- Vila, O. F., Chavez, M., Ma, S. P., Yeager, K., Zhuludeva, L. V., Colón-Mercado, J. M., Qu, Y., Nash, T. R., Lai, C., Feliciano, C. M., Carter, M., Kamm, R. D., Judge, L. M., Conklin, B. R., Ward, M. E., McDevitt, T. C., & Vunjak-Novakovic, G. (2021). Bioengineered optogenetic model of human neuromuscular junction. *Biomaterials*, 276, 121033. <https://doi.org/10.1016/j.biomaterials.2021.121033>
- Vila, O. F., Uzel, S. G. M., Ma, S. P., Williams, D., Pak, J., Kamm, R. D., & Vunjak-Novakovic, G. (2019). Quantification of human neuromuscular function through optogenetics. *Theranostics*, 9(5), 1232-1246. <https://doi.org/10.7150/thno.25735>
- Villa, A., Snyder, E. Y., Vescovi, A., & Martínez-Serrano, A. (2000). Establishment and properties of a growth factor-dependent, perpetual neural stem cell line from the human CNS. *Experimental Neurology*, 161(1), 67-84. <https://doi.org/10.1006/exnr.1999.7237>
- Volpato, V., Smith, J., Sandor, C., Ried, J. S., Baud, A., Handel, A., Newey, S. E., Wessely, F., Attar, M., Whiteley, E., Chintawar, S., Verheyen, A., Barta, T., Lako, M., Armstrong, L., Muschet, C., Artati, A., Cusulin, C., Christensen, K., ... Lakics, V. (2018). Reproducibility of Molecular Phenotypes after Long-Term Differentiation to Human iPSC-Derived Neurons: A Multi-Site Omics Study. *Stem Cell Reports*, 11(4), 897-911. <https://doi.org/10.1016/j.stemcr.2018.08.013>
- Wang, Q., Shui, B., Kotlikoff, M. I., & Sondermann, H. (2008). Structural Basis for Calcium Sensing by GCaMP2. *Structure*, 16(12), 1817-1827. <https://doi.org/10.1016/j.str.2008.10.008>
- Ward, E. S., Zhou, J., Ghetie, V., & Ober, R. J. (2003). Evidence to support the cellular mechanism involved in serum IgG homeostasis in humans. *International Immunology*, 15(2), 187-195. <https://doi.org/10.1093/intimm/dxg018>
- Weickenmeier, J., de Rooij, R., Budday, S., Steinmann, P., Ovaert, T., & Kuhl, E. (2016). Brain stiffness increases with myelin content. *Acta Biomaterialia*, 42. <https://doi.org/10.1016/j.actbio.2016.07.040>
- Weitkunat, M., Kaya-Çopur, A., Grill, S. W., & Schnorrer, F. (2014). Tension and Force-Resistant Attachment Are Essential for Myofibrillogenesis in Drosophila Flight Muscle. *Current Biology*, 24(7), 705-716. <https://doi.org/10.1016/j.cub.2014.02.032>
- Wells-Cembrano, K., Sala-Jarque, J., & Rio, J. A. del. (2022). Development of a simple and versatile in vitro method for production, stimulation, and analysis of bioengineered muscle. *PLOS ONE*, 17(8), e0272610. <https://doi.org/10.1371/journal.pone.0272610>
- Weng, J., Wang, Y., Li, M., Zhang, D., & Jiang, B. (2018). GSK3β inhibitor promotes myelination and mitigates muscle atrophy after peripheral nerve injury. *Neural Regeneration Research*, 13. <https://doi.org/10.4103/1673-5374.226403>
- Wevers, N., Vught, R., Wilschut, K., Nicolas, A., Chiang, C., Lanz, H., Trietsch, S., Joore, J., & Vulto, P. (2016). High-throughput compound evaluation on 3D networks of neurons and glia in a microfluidic platform. *Scientific Reports*, 6, 38856. <https://doi.org/10.1038/srep38856>
- Williams, J. A. (1981). Electrical correlates of secretion in endocrine and exocrine cells. *Federation Proceedings*, 40(2), 128-134.
- Williams, P. R., Marincu, B.-N., Sorbara, C. D., Mahler, C. F., Schumacher, A.-M., Griesbeck, O., Kerschensteiner, M., & Misgeld, T. (2014). A recoverable state of axon injury persists for hours after spinal cord contusion in vivo. *Nature Communications*, 5(1), 5683. <https://doi.org/10.1038/ncomms6683>

- Witebsky, E., Rose, N. R., Terplan, K., Paine, J. R., & Egan, R. W. (1957). Chronic thyroiditis and autoimmunization. *Journal of the American Medical Association*, 164(13), 1439-1447. <https://doi.org/10.1001/jama.1957.02980130015004>
- Wolfe, G. I., Kaminski, H. J., Aban, I. B., Minisman, G., Kuo, H.-C., Marx, A., Ströbel, P., Mazia, C., Oger, J., Cea, J. G., Heckmann, J. M., Evoli, A., Nix, W., Cifaloni, E., Antonini, G., Witoonpanich, R., King, J. O., Beydoun, S. R., Chalk, C. H., ... Cutter, G. R. (2016). Randomized Trial of Thymectomy in Myasthenia Gravis. *New England Journal of Medicine*, 375(6), 511-522. <https://doi.org/10.1056/NEJMoa1602489>
- Woodhams, P. L., & Atkinson, D. J. (1996). Regeneration of entorhino-dentate projections in organotypic slice cultures: mode of axonal regrowth and effects of growth factors. *Exp Neurol*, 140(1), 68-78. doi:10.1006/exnr.1996.0116
- Woodhams, P. L., Atkinson, D. J., & Raisman, G. (1993). Rapid decline in the ability of entorhinal axons to innervate the dentate gyrus with increasing time in organotypic co-culture. *Eur J Neurosci*, 5(12), 1596-1609. doi:10.1111/j.1460-9568.1993.tb00229.x
- Yamamoto, N., & Hanamura, K. (2005). Formation of the thalamocortical projection regulated differentially by BDNF- and NT-3-mediated signaling. *Rev Neurosci*, 16(3), 223-231. doi:10.1515/revneuro.2005.16.3.223
- Yang, T., Dai, Y., Chen, G., & Cui, S. (2020). Dissecting the Dual Role of the Glial Scar and Scar-Forming Astrocytes in Spinal Cord Injury. *Frontiers in Cellular Neuroscience*, 14, 78. <https://doi.org/10.3389/fncel.2020.00078>
- Yazdanpanah, Z., Johnston, J. D., Cooper, D. M. L., & Chen, X. (2022). 3D Bioprinted Scaffolds for Bone Tissue Engineering: State-Of-The-Art and Emerging Technologies. *Frontiers in Bioengineering and Biotechnology*, 10, 824156. <https://doi.org/10.3389/fbioe.2022.824156>
- Yoo, S., Nguyen, M. P., Fukuda, M., Bittner, G. D., & Fishman, H. M. (2003). Plasmalemmal sealing of transected mammalian neurites is a gradual process mediated by Ca(2+)-regulated proteins. *Journal of Neuroscience Research*, 74(4), 541-551. <https://doi.org/10.1002/jnr.10771>
- Yoshimura, Y., Dantzer, J. L. M., & Callaway, E. M. (2005). Excitatory cortical neurons form fine-scale functional networks. *Nature*, 433(7028), Article 7028. <https://doi.org/10.1038/nature03252>
- Yoshioka, K., Ito, A., Horie, M., Ikeda, K., Kataoka, S., Sato, K., Yoshigai, T., Sakurai, H., Hotta, A., Kawabe, Y., & Kamihira, M. (2021). Contractile Activity of Myotubes Derived from Human Induced Pluripotent Stem Cells: A Model of Duchenne Muscular Dystrophy. *Cells*, 10(10), 2556. <https://doi.org/10.3390/cells10102556>
- Zammit, P. S. (2017). Function of the myogenic regulatory factors Myf5, MyoD, Myogenin and MRF4 in skeletal muscle, satellite cells and regenerative myogenesis. *Seminars in Cell & Developmental Biology*, 72, 19-32. <https://doi.org/10.1016/j.semcdb.2017.11.011>
- Zang, Y., Chaudhari, K., & Bashaw, G. J. (2021). New insights into the molecular mechanisms of axon guidance receptor regulation and signaling. *Curr Top Dev Biol*, 142, 147-196. doi:10.1016/bs.ctdb.2020.11.008
- Zemelman, B. V., Lee, G. A., Ng, M., & Miesenböck, G. (2002). Selective Photostimulation of Genetically ChARGed Neurons. *Neuron*, 33(1), 15-22. [https://doi.org/10.1016/S0896-6273\(01\)00574-8](https://doi.org/10.1016/S0896-6273(01)00574-8)
- Zemelman, B. V., Nesnas, N., Lee, G. A., & Miesenböck, G. (2003). Photochemical gating of heterologous ion channels: Remote control over genetically designated populations of neurons. *Proceedings of the National Academy of Sciences*, 100(3), 1352-1357. <https://doi.org/10.1073/pnas.242738899>
- Zeng, J., Xu, X., Chen, X., Liang, Q., Bian, X., Yang, L., & Jing, X. (2003). Biodegradable electrospun fibers for drug delivery. *Journal of Controlled Release*, 92(3), 227-231. [https://doi.org/10.1016/S0168-3659\(03\)00372-9](https://doi.org/10.1016/S0168-3659(03)00372-9)
- Zhang, F., Vierock, J., Yizhar, O., Fenno, L. E., Tsunoda, S., Kianianmomeni, A., Prigge, M., Berndt, A., Cushman, J., Polle, J., Magnuson, J., Hegemann, P., & Deisseroth, K. (2011). The Microbial Opsin Family of Optogenetic Tools. *Cell*, 147(7), 1446-1457. <https://doi.org/10.1016/j.cell.2011.12.004>
- Zhang, F., Wang, L.-P., Brauner, M., Liewald, J. F., Kay, K., Watzke, N., Wood, P. G., Bamberg, E., Nagel, G., Gottschalk, A., & Deisseroth, K. (2007). Multimodal fast optical interrogation of neural circuitry. *Nature*, 446(7136), 633-639. <https://doi.org/10.1038/nature05744>
- Zhang, H., Fang, H., Liu, D., Zhang, Y., Adu-Amankwaah, J., Yuan, J., Tan, R., & Zhu, J. (2022). Applications and challenges of rhodopsin-based optogenetics in biomedicine. *Frontiers in Neuroscience*, 16. <https://www.frontiersin.org/articles/10.3389/fnins.2022.966772>
- Zhang, J.-N., Michel, U., Lenz, C., Friedel, C. C., Köster, S., d'Hedouville, Z., Tönges, L., Urlaub, H., Bähr, M., Lingor, P., & Koch, J. C. (2016). Calpain-mediated cleavage of collapsin response mediator protein-2 drives acute axonal degeneration. *Scientific Reports*, 6, 37050. <https://doi.org/10.1038/srep37050>

- Zhang, J., Yang, H., Wu, J., Zhang, D., Wang, Y., & Zhai, J. (2022). Recent progresses in novel in vitro models of primary neurons: A biomaterial perspective. *Frontiers in Bioengineering and Biotechnology*, 10. <https://www.frontiersin.org/articles/10.3389/fbioe.2022.953031>
- Zhang, L.-G., Zhong, D.-H., Li, C.-Z., Kisaalita, W., & Wu, Z.-Z. (2014). A microwell pattern for C17.2 cell aggregate formation with concave cylindrical surface induced cell peeling. *Biomaterials*. <https://doi.org/10.1016/j.biomaterials.2014.07.046>
- Zhang, Z., O'Laughlin, R., Song, H., & Ming, G. L. (2022). Patterning of brain organoids derived from human pluripotent stem cells. *Curr Opin Neurobiol*, 74, 102536. doi:10.1016/j.conb.2022.102536
- Zhao, H., Kim, Y., Wang, H., Ning, X., Xu, C., Suh, J., Han, M., Pagan, G., Liu, W., Li, H., Bai, W., Aydın, O., Park, Y., Wang, J., Yao, Y., He, Y., Saif, M., Huang, Y., & Rogers, J. (2021). Compliant 3D frameworks instrumented with strain sensors for characterization of millimeter-scale engineered muscle tissues. *Proceedings of the National Academy of Sciences*, 118, e2100077118. <https://doi.org/10.1073/pnas.2100077118>
- Zhao, Z., Chen, X., Dowbaj, A. M., Sljukic, A., Bratlie, K., Lin, L., Fong, E. L. S., Balachander, G. M., Chen, Z., Soragni, A., Huch, M., Zeng, Y. A., Wang, Q., & Yu, H. (2022). Organoids. *Nature Reviews. Methods Primers*, 2, 94. <https://doi.org/10.1038/s43586-022-00174-y>
- Zhou, G., Wang, Z., Han, S., Chen, X., Li, Z., Hu, X., Li, Y., & Gao, J. (2022). Multifaceted Roles of cAMP Signaling in the Repair Process of Spinal Cord Injury and Related Combination Treatments. *Frontiers in Molecular Neuroscience*, 15, 808510. <https://doi.org/10.3389/fnmol.2022.808510>
- Zhu, C.-H., Mouly, V., Cooper, R. N., Mamchaoui, K., Bigot, A., Shay, J. W., Di Santo, J. P., Butler-Browne, G. S., & Wright, W. E. (2007). Cellular senescence in human myoblasts is overcome by human telomerase reverse transcriptase and cyclin-dependent kinase 4: Consequences in aging muscle and therapeutic strategies for muscular dystrophies. *Aging Cell*, 6(4), 515-523. <https://doi.org/10.1111/j.1474-9726.2007.00306.x>
- Ziegler, L., Segal-Ruder, Y., Coppola, G., Reis, A., Geschwind, D., Fainzilber, M., & Goldstein, R. S. (2010). A human neuron injury model for molecular studies of axonal regeneration. *Experimental Neurology*, 223(1), 119-127. <https://doi.org/10.1016/j.expneurol.2009.09.019>
- Zimmer, J., & Gahwiler, B. H. (1984). Cellular and connective organization of slice cultures of the rat hippocampus and fascia dentata. *J Comp Neurol*, 228(3), 432-446.
- Zisimopoulou, P., Evangelakou, P., Tzartos, J., Lazaridis, K., Zouvelou, V., Mantegazza, R., Antozzi, C., Andreetta, F., Evoli, A., Deymeer, F., Saruhan-Direskeneli, G., Durmus, H., Brenner, T., Vaknin, A., Berrih-Aknin, S., Frenkian Cuvelier, M., Stojkovic, T., DeBaets, M., Losen, M., ... Tzartos, S. J. (2014). A comprehensive analysis of the epidemiology and clinical characteristics of anti-LRP4 in myasthenia gravis. *Journal of Autoimmunity*, 52, 139-145. <https://doi.org/10.1016/j.jaut.2013.12.004>